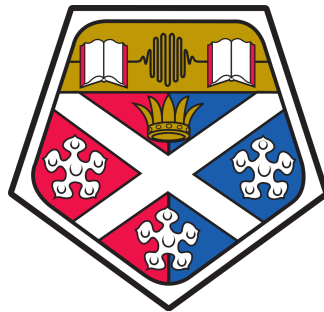


Dynamics in many-body quantum systems with long-range interactions

Araceli Venegas-Gómez

A thesis submitted for the degree of
Doctor of Philosophy

Department of Physics and SUPA
UNIVERSITY OF STRATHCLYDE



August 2020

This thesis is the result of the author's original research. It has been composed by the author and has not been previously submitted for examination which has led to the award of a degree.

The copyright of this thesis belongs to the author under the terms of the United Kingdom Copyright Acts as qualified by University of Strathclyde Regulation 3.50. Due acknowledgement must always be made of the use of any material contained in, or derived from, this thesis.

Signed:

Date:

“Every real story is a never ending story.”

Michael Ende, *The Neverending Story*

“Imagination is more important than
knowledge. Knowledge is limited.
Imagination encircles the world.”

Albert Einstein

Abstract

The ability to realise quantum simulation experimentally at extremely low temperature provides the capability to microscopically control macroscopic quantum phenomena. The control over cold atoms in optical lattices offers an excellent platform to study the out-of-equilibrium behaviour of strongly correlated systems, especially spin physics that can be realised with multicomponent gases. In this field a major ambition is to observe sensitive many-body phenomena such as quantum magnetism.

This thesis contains theoretical and numerical studies of many-body dynamical phenomena of spin models with two-component bosonic atoms in optical lattices. Firstly, beginning from a state with all effective magnetic spins in the same direction, we investigate dynamics of spin-spin correlations, and how they behave for different spin models. Most of the results explored in this thesis use reduced Hilbert space techniques, based on the Density Matrix Renormalisation Group, and the representation of Matrix Product States and Matrix Product Operators. Using numerical methods in 1D we compute non-equilibrium dynamics, ground states, and thermal states for these systems. We also study and compare their behaviour in terms of spin correlation functions and induced currents. We find in some cases, where the current is non-decaying for the ground state, a decay for the rotated state with time, since the decay of the long-range correlations becomes important. Furthermore, we explore changes that occur when we add long-range interactions to the models, and analyse how the correlations can be affected by the presence of disorder. We found that in the regime of short and intermediate range interactions, the correlations are affected by the disorder, whereas these effects were suppressed for long-range interactions.

One of the challenges in ongoing experiments remains reaching the low temperatures/entropies necessary for some particularly sensitive interacting states. We investigate the magnetically ordered quantum states that can be engineered in these two-species bosonic models, studying techniques to prepare states with a very low entropy using adiabatic and near-adiabatic protocols. We compute the corresponding dynamics, modelling these techniques for realistic experimental parameters. We also show how the same models can give rise to entanglement that is potentially useful for quantum enhanced metrology, and characterise the states we can prepare in terms of their Quantum Fisher Information. Lastly, we analyse the effect of dissipation in these models.

Our results provide an interesting experimental perspective to probe the difference between mean-field spin states and the true ground states for effective spin models. In summary, our studies offer innovative new results to study spin models in optical lattices, which should be feasible with current experimental techniques.

Acknowledgements

It was 2013, I was working full time at Airbus in Germany and doing a Master in Medical Physics in my free time. It is when I bumped into quantum physics. It came across my life as a hurricane, swallowing the rest of my free time, my holidays, and my future. And it is the best thing that could ever happen to me. Through an online course I asked Charles Clark for advice, and he put me in touch with my supervisor, Andrew Daley. I cannot thank you enough Andrew, not only for offering me the MRes, and the opportunity to continue with the PhD, but for everything else. I had the chance to collaborate with amazing people, and spent time in one of the top universities in the world. Moreover, I have built a new career, connections, and this is thanks to your support. Thanks for giving me the chance to spend time doing so many other activities, and travel across the globe, besides my research.

I would like to thank my viva committee: Beatriz Olmos and Elmar Haller for their comments and suggestions.

Thanks to our collaborators, it has been a great pleasure to work with you all!

I arrived in Glasgow feeling an old student, but I could not feel more younger again, than being surrounded by this group of people, who made me laugh, and go crazy, but people I could count on if I needed to complain about something. Thanks to the bunch of the QOQMS group: Alex, Francois D., Guanglei, Jorge, Rosaria, Tomohiro, Saubhik, Suzanne... Thanks to the rest of the Glaschu group, you guys made this a funny odyssey! Thanks to Anton and Johannes for their patience teaching me, answering my questions, and for all of the jokes in between.

Thanks to all those people who were telling me I could do it. People from Spain, from Germany, from France, and from everywhere else I have met during this journey!

Thanks to my family, my parents and my brother, being always there for me, and supporting me on each new adventure. ¡Gracias de verdad!

And of course to my partner, François, who changed his life to follow me to pursue this PhD, and for being there every single day, standing at my side, in my ups and my downs. Merci mon amour!

I could not have made it without you all!

Contents

| | | |
|----------|---|-----------|
| 1 | Introduction | 1 |
| 1.1 | Short background and overview | 1 |
| | <u>Quantum simulation</u> | 2 |
| | <u>Optical lattices</u> | 3 |
| | <u>Quantum magnetism</u> | 3 |
| | <u>Numerical methods</u> | 4 |
| | <u>Thesis overview</u> | 5 |
| 1.2 | Thesis outline | 6 |
| | <u>Contributions during PhD</u> | 7 |
| 2 | Cold atoms in optical lattices | 10 |
| 2.1 | Optical Lattices | 10 |
| 2.1.1 | Atoms interaction with a light field | 11 |
| | Spin dependent lattices | 13 |
| 2.1.2 | Energy bands | 14 |
| 2.2 | The Bose-Hubbard model | 15 |
| 2.2.1 | Superfluid to Mott Insulator transition | 17 |
| | $J \gg U$: Superfluid (SF) phase | 17 |
| | $U \gg J$: Mott Insulator (MI) phase | 18 |
| | Phase transition | 18 |
| 2.3 | Experiments with optical lattices: state of the art and outlook | 19 |
| 2.4 | Summary | 20 |
| 3 | Spin models with ultracold atoms | 21 |
| 3.1 | Quantum Magnetism | 22 |
| 3.1.1 | Superexchange | 23 |
| 3.2 | Bose-Hubbard model for two bosonic components | 23 |
| 3.2.1 | From Bose-Hubbard to spin models | 25 |
| | <u>n=2: Spin-1 model</u> | 25 |
| | <u>n=1: Spin-1/2 model</u> | 27 |
| 3.2.2 | Ground state magnetic ordering | 28 |
| 3.3 | Summary | 30 |
| 4 | Numerical Simulation | 31 |
| 4.1 | Exact Diagonalisation | 32 |
| 4.2 | Density Matrix Renormalisation Group (DMRG) | 34 |
| | <u>The area law</u> | 35 |

| | | |
|----------|--|-----------|
| 4.2.1 | Matrix Product States (MPS) | 36 |
| | Singular Value Decomposition (SVD) | 37 |
| | The Schmidt Rank | 37 |
| | Matrix Product Operators MPO | 40 |
| 4.2.2 | Variational search for the ground state | 41 |
| 4.2.3 | Time evolution algorithms: TEBD, TDVP | 42 |
| | 4.2.3.1 Time-Evolving Block Decimation Algorithm (TEBD) | 42 |
| | 4.2.3.2 Time Dependent Variational Principle (TDVP) | 44 |
| 4.2.4 | Finite temperature algorithm: The Ancilla method | 46 |
| 4.3 | Open quantum systems | 48 |
| | 4.3.1 The Master Equation | 49 |
| | 4.3.2 Quantum Trajectories and the quantum jump approach | 50 |
| 4.4 | Summary | 52 |
| 5 | Engineering magnetic ordering of rotated spin states and probing dynamics in quantum simulators | 53 |
| 5.1 | Preparation of spin rotated states | 54 |
| 5.2 | Comparison of the rotated state with the ground state | 55 |
| 5.3 | Exploring properties of states by out-of-equilibrium dynamics | 56 |
| 5.4 | Thermal states | 59 |
| | 5.4.1 Background: Statistical Mechanics | 60 |
| | 5.4.2 Results for thermal states | 62 |
| | 5.4.3 Rotated states as thermal states | 64 |
| | 5.4.4 Thermalisation dynamics | 67 |
| 5.5 | Probing the states with spin currents | 71 |
| | 5.5.1 Study of the currents on the rotated state | 72 |
| | 5.5.1.1 Initial state | 72 |
| | 5.5.1.2 Time evolution of the spin currents | 73 |
| | 5.5.1.3 Spin-spin correlations | 74 |
| | 5.5.2 Comparison with the ground state | 74 |
| | 5.5.2.1 Dynamical results | 75 |
| | 5.5.2.2 Energy difference after “kick” | 81 |
| | 5.5.3 Critical velocity and excitation spectrum | 83 |
| 5.6 | Summary and discussion | 84 |
| 6 | Adiabatic state preparation and metrology with cold atoms in optical lattices | 86 |
| 6.1 | Introduction to adiabatic state preparation | 87 |
| 6.2 | Antiferromagnetic state preparation using adiabatic ramps | 90 |
| | 6.2.1 Model with a staggered magnetic field | 91 |
| | 6.2.2 Model with a tilted magnetic field | 93 |
| | 6.2.2.1 Study of the energy gap | 94 |
| | 6.2.2.2 Resulting ramps | 94 |
| 6.3 | Study of an XY-ferromagnet | 96 |
| | 6.3.1 Adiabatic ramps for the spin-1/2 model | 97 |
| 6.4 | Spin models and metrology | 98 |
| | 6.4.1 Quantum Fisher Information | 98 |

| | | |
|----------|--|------------|
| 6.4.2 | Characterising the ground state: useful entanglement for metrology | 100 |
| 6.4.2.1 | Case with negative interactions | 102 |
| 6.4.3 | Adiabatic State Preparation | 103 |
| 6.4.3.1 | Ramp in $\Delta \neq 0$: Optimal Control | 105 |
| 6.4.3.2 | Ramp to $\Delta = 0$ | 109 |
| 6.4.4 | Effects of dissipation | 111 |
| 6.5 | Summary and Outlook | 113 |
| 7 | Spin dynamics in the presence of long-range interactions and disorder | 115 |
| 7.1 | Long-Range Interactions | 115 |
| 7.1.1 | Results | 116 |
| 7.1.2 | Transition studies in different regimes | 121 |
| 7.2 | Presence of disorder | 123 |
| 7.2.1 | Results | 124 |
| 7.3 | Summary and discussion | 126 |
| 8 | Conclusions & Outlook | 129 |
| | Appendices | 132 |
| A | Convergence studies | 133 |
| A.1 | Time evolution for a large number of spins | 133 |
| A.1.1 | Spin-1 model time evolution | 133 |
| A.1.2 | Spin-1/2 model time evolution | 136 |
| A.2 | Finite temperature calculations | 138 |
| A.2.1 | Spin-1 model finite temperature calculations | 138 |
| A.2.2 | Spin-1/2 model finite temperature calculations | 139 |
| A.3 | Spin currents | 140 |
| | Bibliography | 141 |

Chapter 1

Introduction

“ *Those who are not shocked when they first come across quantum theory cannot possibly have understood it.* ”

Niels Bohr,

Essays 1932-1957 on Atomic Physics & Human Knowledge

1.1 Short background and overview

From the foundations of quantum mechanics at the beginning of the twentieth century, to the cutting edge research for applications in quantum technologies, the field of Atomic Molecular and Optics (AMO) physics has a continued history. After the 1960s, with the development of the laser, the ability to use light to control matter at the quantum level has enabled us with the tools to unfold new theoretical and experimental methods to expand our understanding of physical phenomena in an unprecedented way.

The following development of experimental techniques to cool atoms to ultracold temperatures led to Nobel-prize winning discoveries, such as to W. D. Phillips, S. Chu, and C. Cohen-Tannoudji in 1997 “for development of methods to cool and trap atoms with laser light” [1–3], and E. Cornell, C. Wieman, and W. Ketterle in 2001 “for the achievement of Bose-Einstein condensation in dilute gases of alkali atoms, and for early fundamental studies of the properties of the condensates” [4–6].

This ability to realise experiments at extremely low temperatures provide physicists the capability to microscopically control macroscopic quantum phenomena. The importance

of realising these regimes with atomic gases is that the level of microscopic control and first principles understanding was particularly high, because of the techniques developed over the course of many decades. In the ensuing years, this generated the ability to engineer new Hamiltonians, leading to the research field of quantum simulation.

Quantum simulation

The concept of a quantum simulator can be summarised as “the intentional engineering of the quantum characteristics of a physical model using a particularly controllable quantum system”. This definition came from Richard Feynmann’s famous article [7] after his seminal lecture “Simulating Physics with Computers”. The enormous advances in isolating, controlling and detecting quantum systems since then has transformed quantum simulation into a rich field where new insights into many-body physics can be gained. Quantum simulators can be applied to solve problems in different fields, such as spectroscopy applications [8], the understanding of high temperature superconductivity in condensed-matter physics [9], studies in high-energy physics [10], or quantum chemistry [11].

The motivation for quantum simulation is to tackle the complexity and difficulty of classically simulating quantum systems computationally. The design of a quantum simulator starts with the proper mapping of the Hamiltonian of the system to be simulated. The exponential growth of the Hilbert space with system size creates the difficulty of simulating these many-body Hamiltonians on a classical computer, mainly due to the large amount of memory needed to store a quantum state, and the amount of operations required to simulate its evolution in time [12, 13]. Understanding many-body quantum systems can be hard, even using state-of-the-art numerical techniques on the largest classical supercomputers. Thus, to investigate models or effects in condensed matter physics which are hard to access via classical computers, quantum simulators provide a particularly interesting alternative to study dynamical phenomena in many-body systems.

Currently, there are several experimental platforms for quantum simulation, such as ion traps [14, 15], superconducting circuits [16], quantum photonics systems [17], and ultracold neutral atoms [18]. The macroscopic control over cold atoms in optical lattices offers an excellent platform to investigate out-of-equilibrium dynamics of strongly correlated systems, such as spin models, which are usually motivated by solid state physics. In this thesis, we use optical lattices as the interface between ultracold atoms and condensed matter.

Optical lattices

Optical lattices are periodic potentials created by a pair of counter-propagating laser beams far detuned from an optical transition. This potential is formed via the AC-Stark effect, and it provides access to study many-body physical phenomena. Optical lattices provide a platform to realise experimentally simplified models of condensed matter, as an instrument to understand physical phenomena, such as high-temperature superconductivity, which is an example of strongly correlated quantum matter.

Many examples for strongly correlated systems are based in different types of Hubbard models, first proposed to describe how electrons move in a crystalline structure [19]. Although electrons are fermions, in the lab, these experiments are possible with both fermions and bosons. Quantum degenerate gases of fermions are particularly well suited to the simulation of solid-state systems, as they obey Fermi–Dirac statistics, where the behaviour of the electrons in a solid can be simulated directly. With the realisation of Bose-Einstein Condensation, and some advantages in cooling bosons to low temperatures, the Bose-Hubbard model was realised first. Today these kind of experiments are possible with different kind of both bosonic and fermionic species (for a review on quantum simulation of the Hubbard model with ultracold fermions in optical lattices see for example [20]). The phase diagram of this Bose-Hubbard model was presented theoretically by Fischer et al. [21], and a proposal for implementation of this with cold atoms was first proposed by Jaksch et al. [22].

The first experimentally realised phase transition in ultracold atoms between the Mott insulator and the superfluid regime in a weakly interacting Bose gas was observed in an optical lattice by Greiner et al. [23]. This first realisation was made just by varying the lattice depth, which changes the ratio between interactions and tunnelling (kinetic energy) in the system. These days the possibility to use Feshbach resonances for some atomic species [24] provides independent control over interactions. This offers new opportunities to observe sensitive many-body processes, such as quantum magnetism, when introducing more than one atomic spin state.

Quantum magnetism

Quantum magnetism is at the heart of many fundamental phenomena in condensed matter physics. In ultracold atoms it can be described by quantum many-body states of spins coupled by interactions. In cases where we have only on-site interactions between particles, the magnetic ordering of spins is driven by the critical energy for superexchange, the antiferromagnetic coupling between neighbouring spins [25, 26].

In order to observe magnetic correlations, the motional temperature has to be lower than this effective spin-spin coupling energy, or superexchange, which is in the nanokelvin range. The first observation of superexchange in a double-well potential was experimentally achieved in 2008 [27]. In the last years incredible progress has been made in the field. A review of some of the most promising implementations to study quantum magnetism can be found in [28].

The behaviour of a gas at temperatures close to absolute zero depends on whether the atoms in the gas are fermions or bosons. Latest advances in the field of degenerate Fermi gases now offer the possibility of loading ultracold fermionic gases into optical lattices. Furthermore, antiferromagnetic magnetic ordering has been recently observed in optical lattices [29–32].

Probing many-body quantum systems is now a reality thanks to diverse experimental techniques and the possibility to use quantum microscopes to detect and study atoms in optical lattices at the single-particle level [33–35]. These new opportunities offer an unprecedented control of many-body physics [18, 36].

However, the challenge in ongoing experiments still remains to reach the low temperatures/entropies necessary for some of the most interesting phenomena [37], such as pairing of itinerant particles in analogy with high-temperature superconductors. In the case of magnetic ordering with bosons in optical lattices, there are still many open questions, both theoretically and experimentally. The main research of this thesis focusses in answering several questions in this field. To achieve this level of accuracy in the study of quantum many-body states and their dynamical properties theoretically, we use specific numerical methods to solve these complicated calculations.

Numerical methods

The study of quantum many-body systems is related to Hamiltonians whose exact solution is very difficult to tackle due to the exponential growth of the Hilbert space \mathcal{H} with the system size. Just to calculate the ground states in these systems it is necessary to diagonalize a matrix of $\dim(\mathcal{H}) \cdot \dim(\mathcal{H})$, and the evolution will be a matrix exponential, requiring large matrix multiplications.

Considering a spin-1/2 chain with a local dimensional $d = 2$ and M sites, the total Hilbert space will have a dimension of $\dim(\mathcal{H}) = 2^M$. For a system with 50 spins, the dimension is thus $\dim(\mathcal{H}) = 2^{50} \approx 10^{15}$, requiring a memory on the order of tens of thousands of terabytes. Although this could be possible using supercomputers, adding some more spins would result in a hard task to be performed.

One approach will be by using specific symmetries and parallelism, which is the basis of optimisation in the implementation of the Exact Diagonalisation (ED) technique [38]. Another solution is to find numerical methods that, by using approximations, can still capture the most relevant features of these cold many-body systems with a reasonable computational cost.

The density matrix renormalization group (DMRG), introduced by S. R. White [39, 40], transformed the way ground states of large one-dimensional systems were calculated. DMRG relies on the idea of truncating the Hilbert space by keeping the most important basis states, based on the amount of bipartite entanglement in the system, without a significant change of the physical features. Subsequently, these methods provide an accurate representation for low excited states in one-dimensional systems with gapped Hamiltonians.

The efficient representation of these ground states was generalised by applying Matrix Product States (MPS) [41, 42], also used to study the time evolution of these systems, as the Time Evolving Block Decimation algorithm (TEBD) introduced by Vidal [43, 44].

New methods have since been designed to study specific systems, mainly using the extension of Matrix Product States to operators, Matrix Product Operators (MPO) [42, 45, 46]. Some of the methods used in this thesis include additionally Hamiltonians with long-range interactions [47], and finite temperature calculations [48].

Furthermore, we can now perform calculations also when these systems are coupled to an environment, by simulating the dynamics of the master equation using quantum trajectories techniques [49–51].

In summary, we have seen how experimental advances with ultracold atomic gases allow us to construct strongly correlated many-body systems. This means that the Hamiltonians can be engineered experimentally. Thus, we are now in the era of quantum engineering, where systems can be designed, controlled and manipulated in unprecedented ways, allowing us to study the systems and physics of interest.

Quantum simulations and its applications run from quantum information to quantum metrology, on both a theoretical and experimental level [36, 52, 53].

Thesis overview

The generalised Bose-Hubbard model for two-component bosons on an optical lattice is used to investigate the physics that is associated with a variety of spin models.

The main focus of this thesis is to study the quantum many-body physics and dynamics of these spin models for realistic experimental realisations. This objective is addressed for four major topics:

1. dynamics of many-body quantum states and probing methods,
2. adiabatic state preparation of specific magnetic ordered quantum states,
3. Quantum Fisher Information and metrology,
4. long-range interactions and the effects of disorder on spin dynamics.

The results are simulated for realistic parameters using numerical methods based on Matrix Product States.

1.2 Thesis outline

This thesis is organised into three main parts. The first two parts contain all of the theoretical background material (chapters 2 and 3) and numerical methods (chapter 4) which are required to obtain and discuss the results which are presented in the subsequent remaining part (chapters 5-7).

Chapter 2 provides an introduction to the field of ultracold atoms. Specifically, this chapter introduces the procedures that allow experimentalists to trap and manipulate atoms in optical lattices.

Chapter 3 completes this introduction with a description of the general Bose-Hubbard model. Next, the model studied for the research projects in this thesis, the Bose-Hubbard model for two-component of bosons, is introduced. From it, we derive the effective spin models in the regime of strong interactions, basis for the study of specific quantum magnetic states.

In the second part, chapter 4 is dedicated to presenting the different numerical techniques for the simulation of quantum many-body systems used to obtain the research results. We start by simulating the entire Hilbert space with the Exact Diagonalisation method. We then focus on reduced Hilbert space techniques, in particular de Density Matrix Renormalisation Group, and the use of Matrix Product States and Matrix Product Operators. These methods will be used, in particular, for the out-of-equilibrium dynamics studied in the following chapters. To simulate these dynamics, we present different methods, principally algorithms based on the Time Evolving Block Decimation

and the Time Dependent Variational Principle. In addition, we describe the numerical methods used for thermal state calculations, and for systems with long-range interactions. Lastly we devote a section to open quantum systems and the evolution of the master equation using quantum trajectories techniques.

The following three chapters describe the three research projects that compose the results for this dissertation. Additionally, we include a conclusion chapter at the end where we provide some final comments and outlook.

Chapter 5 presents results for a mean-field approach to prepare a XY-ferromagnet, and compare it with the true ground state of the Hamiltonian. We then study the non-equilibrium many-body dynamics, and evaluate thermalisation in the systems. Lastly, we include an approach to probe the dynamics based on the study of the spin currents.

In Chapter 6 the possibility to adiabatically prepare magnetically ordered quantum states is described. Additionally, we characterise specific states that are useful for metrology in terms of their Quantum Fisher Information.

Chapter 7 studies the existence of different interaction regimes and their consequences in the out-of-equilibrium dynamics of the systems. Furthermore, we investigate the effect of adding disorder into the models.

The thesis concludes with a summary and outline of future directions for this work in chapter 8.

Contributions during PhD

◇ Publications

1. A. Venegas-Gomez, A. S. Buyskikh, J. Schachenmayer, W. Ketterle, and A. J. Daley, *Dynamics of rotated spin states and magnetic ordering with two-component bosonic atoms in optical lattices*, published in Physical Review A [54].

The author of this thesis performed all of the calculations for the models, wrote most of the article, and produced all of the plots. This is described in chapter 5.

2. A. Venegas-Gomez, J. Schachenmayer, A. S. Buyskikh, W. Ketterle, M. L. Chiofalo, and A. J. Daley, *Adiabatic preparation of entangled, magnetically ordered states with cold bosons in optical lattices*, ArXiv **cond-mat/2003.10905** [55], accepted in Quantum Science and Technology.

The author of this thesis performed all of the calculations for the models, wrote most of the article, and produced all of the plots. This is described in chapter 6.

3. I. Dimitrova, N. Jepsen, A. S. Buyskikh, A. Venegas-Gomez, J. Amato-Grill, A. J. Daley, and W. Ketterle, *Enhanced Superexchange in a Tilted Mott Insulator*, [56], Physical Review Letters **124**:043204, Jan 2020.

The author of this thesis contributed to the calculations for the adiabatic state preparation of the model. This is described in chapter 6, section 6.4.3.

◇ Prizes

1. Best poster award at the workshop *Quantum Simulation & Computation: Advantage, Scalability, and Verification*, 12-16.02.2018, Bilbao, Spain, issued by John Wiley & Sons, Inc., Wiley Editorial and Publishing.
2. Best poster award at the 9th *SU2P Annual Symposium*, 21-22.05.2018, Glasgow, Scotland, UK, issued by Optos PLC.

◇ Conference talk presentations¹

- *IONS Paris 2017*, 14–17.06.17, Ecole Polytechnique & Université Paris-Sud, Palaiseau, France.
- *CCPQ 2017: Workshop on Dynamics of Complex Quantum Systems*, 31.07 – 04.08.17, Cumberland Lodge, Windsor, UK.
- *CMD27, The 27th Edition of the Condensed Matter Division Conference*, 11-16.03.2018, Berlin, Germany.
- *DesOEQ Meeting 2018*, 09.04.2018, Cambridge, UK.
- *CLEO/EUROPE-EQEC 2019*, 23–27.06.2019, Munich, Germany.

◇ Scientific visits

The author of this thesis gave at least 1 talk in each of these research visits.

- Visit *QUTIS Group*, hosted by Dr. Mikel Sanz and Prof. Enrique Solano, 7-21.02.2018, Bilbao, Spain.
- Scientific stay and collaboration with Dr. Monika Schleier-Smith's group, 01.07-03.08.2018, Stanford University, California, USA.

Research focussed on Rydberg atoms.

¹Conference poster presentations not included

- Visit *UK Quantum Technology Hub for Sensors and Metrology*, hosted by Prof. Kai Bongs, 07.12.2018, Birmingham, UK.
- Visit Prof. Maria Luisa Chiofalo, 01-02.04.2019, Pisa, Italy.
- Visit Dr. Johannes Schachenmayer, 01.07.2019, Strasbourg, France.
- Visit Prof. Wolfgang Ketterle's group, 09.09.2019, MIT, Boston, USA.
- Visit Prof. Alán Aspuru-Guzik's group, 12.09.2019, Toronto, Canada.

Chapter 2

Cold atoms in optical lattices

In the previous chapter we discussed how ultracold atoms in optical lattices provide a platform to engineer specific Hamiltonians, and study phenomena in the field of strongly correlated many-body physics. Experimentally this is possible thanks to the possibility to tune the parameters according to the models to be simulated.

Most importantly, atoms in an optical lattice potential are particularly clean systems, hence providing the closest idea to an ideal crystalline lattice, with a corresponding band structure. This makes these systems excellent quantum simulators. Disorder can be added by using a superlattice (arrays of double wells [57]) or a laser speckle pattern [58], enabling new theoretical models to be studied.

In this chapter, we will outline the theoretical background of optical lattices in section 2.1. We will give an overview of the band structure of atoms in the lattices, equivalent to the energy bands of electrons in real solids, providing information about the material's features, such as whether they are insulators or conductors. In ultracold atoms we are confined in the lowest energy band, and we can then derive the motion of bosonic (fermionic) atoms in the lattice with the Bose-Hubbard (Hubbard) model, as we do in section 2.2. In the last section, 2.3, we present some of the experimental achievements and challenges in the field.

2.1 Optical Lattices

The idea of using standing light waves to confine atoms goes back to Letokhov [59] but it was not until twenty years later that was experimentally achieved [60]. The interest emerged at the end of the 90s when the idea of using cold atoms in optical lattices as a toolbox to study strong correlated regimes was suggested by Jaksch et al. [22].

The physics of cold atoms in optical lattices relies on the use of periodic potentials created by external laser beams, which is described next.

2.1.1 Atoms interaction with a light field

We consider an electric field with angular frequency ω_L as $\mathcal{E}(\mathbf{r}, t) = \mathcal{E}_0(\mathbf{r})\boldsymbol{\varepsilon}e^{-i\omega_L t} + \mathcal{E}_0^*(\mathbf{r})\boldsymbol{\varepsilon}^*e^{i\omega_L t}$, where \mathcal{E}_0 contains the spatial dependence of the field and $\boldsymbol{\varepsilon}$ is the vector of polarization. The interaction between an atom and an electric field is usually given in the dipole approximation [61, 62], by

$$\hat{\mathcal{H}}_{\text{dip}} = \hat{\mathbf{d}}(\mathbf{r}, t) \cdot \mathcal{E}(\mathbf{r}, t), \quad (2.1)$$

with $\hat{\mathbf{d}}$ the electric dipole moment.

The effect of this interaction in the atom, being in a non-degenerate ground state $|g\rangle$ with energy E_g , is considered by expanding the spectrum of the Hamiltonian by a set of eigenstates $\{|n\rangle\}$ with eigenenergies E_n . We compute the effects of a weak field on the atomic ground state as a perturbation.

The first term of the expansion vanishes:

$$\Delta E^{(1)}(\mathbf{r}) = -\langle 0 | \hat{\mathbf{d}}_0(\mathbf{r}) \mathcal{E}_0(\mathbf{r}) \boldsymbol{\varepsilon} | 0 \rangle = 0. \quad (2.2)$$

The second order term takes the form

$$\Delta E^{(2)}(\mathbf{r}) = \alpha(\omega_L) |\mathcal{E}_0(\mathbf{r})|^2, \quad (2.3)$$

where $\alpha(\omega_L)$ is the atomic polarizability [63]

$$\alpha(\omega_L) = \sum_{n \neq 0} |\langle 0 | \hat{\mathbf{d}}_0(\mathbf{r}) \boldsymbol{\varepsilon} | n \rangle|^2 \left(\frac{1}{E_0 - E_n + \hbar\omega_L} + \frac{1}{E_0 - E_n - \hbar\omega_L} \right). \quad (2.4)$$

Eq. 2.3 describes the Stark effect [64], or light shift, defined as a change in the energy levels of an atom exposed to a laser light with frequency ω_L .

We restrict now to the case where ω_L is close to one of the atomic transitions, where we neglect all other transitions. We denote this atomic transition ω_0 as

$$\omega_0 = \frac{E_e - E_g}{\hbar}, \quad (2.5)$$

where E_g and E_e are the energies for the ground state $|g\rangle$ and excited state $|e\rangle$, respectively. We can then rewrite the polarizability as

$$\alpha(\omega_L) = \frac{1}{\hbar\delta} |\langle g | \hat{\mathbf{d}}_0(\mathbf{r}) \boldsymbol{\varepsilon} | e \rangle|^2, \quad (2.6)$$

where

$$\delta = \omega_L - \omega_0, \quad (2.7)$$

is the laser detuning. In our two level system we refer to as red detuned with $\delta < 0$ and blue detuned with $\delta > 0$ (see Fig. 2.1).

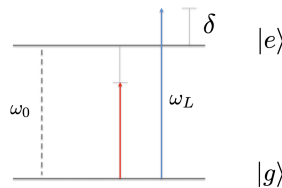


FIGURE 2.1: Schematic diagram of a two level atom with an atomic transition frequency ω_0 interacting with a standing wave of light with frequency ω_L . The detuning of the laser from resonance is δ . We show two lasers, one red detuned, and one blue detuned.

We introduce the Rabi frequency as

$$\Omega_{\text{RABI}}(\mathbf{r}) = \frac{\langle g | \hat{\mathbf{d}}_0(\mathbf{r}) \mathcal{E}_0(\mathbf{r}) \boldsymbol{\varepsilon} | e \rangle}{\hbar}. \quad (2.8)$$

Thus, the energy shift in Eq. 2.3 can be also described as

$$\Delta E^{(2)}(\mathbf{r}) = \frac{\hbar |\Omega_{\text{RABI}}(\mathbf{r})|^2}{4\delta} \propto \frac{I(\mathbf{r})}{\delta}, \quad (2.9)$$

with $I(\mathbf{r})$ the intensity of the laser field. This implies that a neutral atom in the ground state feels an optical potential proportional to the intensity of the laser, a fundamental effect for the optical trapping and manipulation of neutral atoms:

$$V_{\text{opt}}(\mathbf{r}) \propto \frac{I(\mathbf{r})}{\delta}. \quad (2.10)$$

To make a lattice potential, the electric field must be periodic in space, which can be created by using several laser beams. When two counter-propagating laser beams of the same frequency overlap, they will create an interference pattern. Hence, the lattice potential will be

$$V_{\text{opt}}(x) = V_0 \sin^2(k_L x), \quad (2.11)$$

with $k_L = 2\pi/\lambda$, where λ is the wavelength of the laser light, and V_0 is the depth of the potential proportional to the laser intensity. The sign of δ will hence indicate if the

atoms are trapped in the intensity maxima (the red detuned case), or repelled from the intensity maxima (the blue detuned case).

The lattice spacing is defined as

$$a_L = \frac{\lambda}{2}. \quad (2.12)$$

In the limit of a deep lattice, the optical potential for the atom can be approximated by a harmonic potential with trapping frequency

$$\omega_T = 2 \frac{\sqrt{V_0 E_R}}{\hbar}, \quad (2.13)$$

and the recoil energy, indicating the kinetic energy imparted to an atom at rest when it absorbs a photon of momentum $\hbar k_L$, will be

$$E_R = \frac{\hbar^2 k_L^2}{2m}, \quad (2.14)$$

with m the atomic mass. This is the most natural energy scale in the lattice.

Additional lasers can generate potential in higher dimensions [65] as depicted in Fig. 2.2.

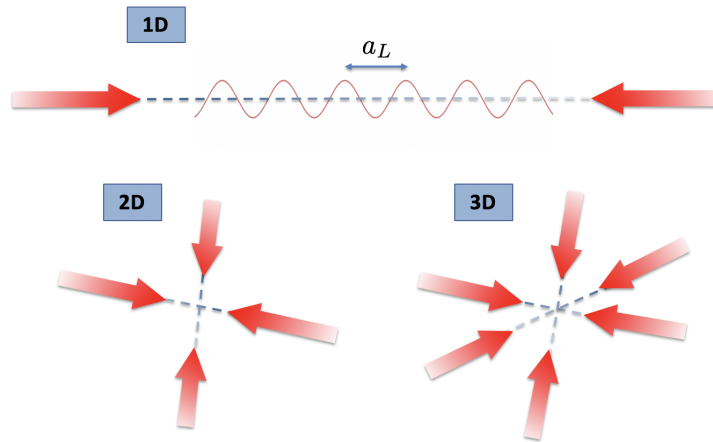


FIGURE 2.2: Optical lattices formed by counter-propagating laser beams, with the arrows as the directions of the laser beams. The standing waves represent the resulting periodic potential.

Spin dependent lattices

Different potentials for different spin states can be realised using spin-dependent optical lattices, on an optical lattice with a wavelength close to the transition of an atom, with a detuning of the order of the hyperfine splitting. In that configuration, the dipole force felt by a given spin state is generally dependent on the light polarization. Basically, the idea is to use counter-propagating laser beams with linear polarization forming an angle

θ [66–68]. The two lattice potentials for the two spin states with polarisations σ^+ and σ^- will be in a relative position to each other. By controlling the polarization of the optical lattice, one can control the potential for each of the spin states. Such a technique is often used to control interactions between atoms, without using Feshbach resonances.

2.1.2 Energy bands

We will now define the band structure for the optical lattice. We start considering the Hamiltonian for a single atom of mass m and momentum p in a one-dimensional standing wave (on time scales where spontaneous emission is negligible) as

$$\hat{\mathcal{H}} = \frac{\hat{p}^2}{2m} + V_0 \sin^2(k_L x), \quad (2.15)$$

with $k_L = 2\pi/\lambda = \pi/a_L$. The eigenstates of this Hamiltonian are called Bloch functions (also called Bloch waves). In our quantum simulator, the link to solid-state physics is that Bloch waves are often used to describe an electron in a crystal [69]. The Schrödinger equation is

$$\left[\frac{\hat{p}^2}{2m} + V_0 \sin^2(k_L x) \right] \Phi_q^{(n)}(x) = E_q^{(n)} \Phi_q^{(n)}(x), \quad (2.16)$$

where the Bloch eigenstates will then be

$$\Phi_q^{(n)}(x) = e^{iqx} u_q^{(n)}(x), \quad (2.17)$$

with $u_q^{(n)}(x)$ having the same periodicity as the potential, where q is the quasimomentum in the first Brillouin zone $(-\pi/a_L, \pi/a_L]$, a quantum number representative of the translational symmetry of the periodic potential [53]. The eigenenergies $E_q^{(n)}$ will form the spectrum of energy bands separated by the energy band gaps.

Bloch waves are delocalised in position space, and localised in quasimomentum space, which means that they are relatively easy to compute in Fourier space. Depending on the depth of the lattice, the particles in the lowest bands will be in the bound states of the potential, whereas free particles will appear in the higher bands ($E_q^{(n)} > V_0$).

It is particularly useful to give a local representation to the Bloch functions by using Wannier functions, a complete set of orthogonal basis states. The Wannier functions represent how much of the wavefunction of a particle is confined in one site, and are given by the following relation to the Bloch functions:

$$w_n(\mathbf{x} - \mathbf{x}_i) = \sqrt{\frac{a_L}{2\pi}} \int_{-\pi/a_L}^{\pi/a_L} e^{-iq\mathbf{x}_i/\hbar} \Phi_q^{(n)}(x) dq, \quad (2.18)$$

where \mathbf{x}_i is the position on the lattice site i and a_L the lattice spacing. As these functions are localised on particular sites, they are useful to describe local interactions between particles [70]. In the limit of very deep lattices, the Wannier functions can be very well approximated, for the purposes of computing on-site properties of the system, by harmonic oscillator wavefunctions with trapping frequency ω_T (as in Eq. 2.13). By using Wannier functions we will next derive the Bose-Hubbard model for ultracold atoms in optical lattices.

2.2 The Bose-Hubbard model

We start with the many-body Hamiltonian describing bosons in a periodic potential, in second quantization [70, 71]:

$$\hat{\mathcal{H}} = \int_{-\infty}^{+\infty} d^3\mathbf{r} \hat{\psi}^\dagger(\mathbf{r}) \left[\frac{\hbar^2}{2m} \nabla^2 + V_0 \sin^2(\mathbf{k}_L \mathbf{r}) + V_T(\mathbf{r}) \right] \hat{\psi}(\mathbf{r}) + \frac{g}{2} \int_{-\infty}^{+\infty} d^3\mathbf{r} \hat{\psi}^\dagger(\mathbf{r}) \hat{\psi}^\dagger(\mathbf{r}) \hat{\psi}(\mathbf{r}) \hat{\psi}(\mathbf{r}), \quad (2.19)$$

where $\hat{\psi}(\mathbf{r})$ [$\hat{\psi}^\dagger(\mathbf{r})$] is the bosonic field operator for the annihilation [creation] of a bosonic particle at position $\mathbf{r} = (x, y, z)$. The first term denotes the kinetic energy and the interaction with an external potential, which is formed by the periodic potential of the laser fields and some extra potential $V_T(\mathbf{r})$ associated with external fields. The second term contains the contact interaction where

$$g = \frac{4\pi\hbar^2 a}{m}, \quad (2.20)$$

is the coupling constant with a the scattering length, used to describe a pseudopotential involving the interatomic potential. Here, where we have atom-atom interactions at lower temperatures, only s-wave scattering is significant [63, 72]. The external potential will be the periodic one created by the laser fields plus an extra non-uniform potential associated with additional external fields V_T .

From now on, and assuming the potential can be factorised as well, we consider only the x component in the state function, thus $\hat{\psi}(x)$. Then, by working with sufficiently deep lattices, the band gap to the excited band is $\Delta_g \approx \hbar\omega_T$, and as long as the energy scales are smaller than that value, we can keep only the lowest states [22]. That is, the model is valid when the energy per atom for atom-atom interaction is small compared to Δ_g . We now expand the bosonic field operators in terms of the Wannier functions,

$$\hat{\psi}(x) = \sum_i \hat{b}_i w(x - x_i), \quad (2.21)$$

with \hat{b}_i the bosonic annihilation operator of a particle at site i , obeying the corresponding commutation relations

$$[\hat{b}_i, \hat{b}_j] = [\hat{b}_i^\dagger, \hat{b}_j^\dagger] = 0, \quad \forall i, j, \quad (2.22)$$

$$[\hat{b}_i, \hat{b}_j^\dagger] = \delta_{i,j}. \quad (2.23)$$

Replacing the operators in the Hamiltonian, we obtain the generalised Bose-Hubbard model

$$\hat{\mathcal{H}} = -\sum_{\langle i,j \rangle} J_{ij} \hat{b}_j^\dagger \hat{b}_i + \frac{U}{2} \sum_i \hat{n}_i (\hat{n}_i - 1) + \sum_i \epsilon_i \hat{n}_i, \quad (2.24)$$

where $\hat{n} = \hat{b}_i^\dagger \hat{b}_i$ will count the number of bosons at a given lattice site i , and $\langle i, j \rangle$ denotes nearest-neighbours site i and j .

The tunnelling matrix element or hopping, between adjacent sites i and j , is given by

$$J_{ij} = -\int_{-\infty}^{+\infty} w^*(x - x_i) \left(-\frac{\hbar^2}{2m} \nabla^2 + V_0 \sin^2(k_L x) \right) w(x - x_j) dx, \quad (2.25)$$

with $w(x)$ the lowest-band Wannier functions.

U is the on-site interaction energy of having two atoms in one site:

$$U = g \int_{-\infty}^{+\infty} dx |w(x)|^4. \quad (2.26)$$

The last term of Eq. 2.24 symbolises the external trapping potential, that is, gives a site-dependent energy offset

$$\epsilon_i = \int_{-\infty}^{+\infty} dx w(x - x_i)^2 V_T(x). \quad (2.27)$$

If we restrict the physics to the lowest band, with a very deep lattice potential, and well-localised Wannier functions on each lattice site, we can approximate the model to a tight-binding model from condensed matter physics, where a state at any given site only couples to neighbouring sites. [69, 73], In this limit, only nearest neighbours tunnelling matrix elements are retained, where the tunnelling term J depends on the overlap of the localized wavefunctions.

In the next section we will describe the quantum phases in the context of bosons in optical lattices in the limiting cases, where either the hopping or the interaction energy will dominate.

2.2.1 Superfluid to Mott Insulator transition

Being the energy for atom-atom interaction small compared to the energy spacing between the bands, we can treat the model as a competition between hopping (kinetic energy) and interaction energy. In this case, we should expect quantum phase transitions which are either localised or delocalised.

The phase diagram for the Bose-Hubbard model at zero temperature was first investigated by Fischer et al. [21], and the first proposal to realise a phase transition in an optical lattice experimentally appeared almost ten years later by Jaksch et al. [22]. Finally, the first observation of this transition was first demonstrated by Greiner et al. in 2002 [23], where they used time of flight experiments to measure a posteriori the occupation of the lattice sites, allowing for the determination of the phases of the atomic system.

Next, we are going to give an overview of the two different quantum phases, which depend on the ratio of U/J in the ground state of the system [53, 65, 74, 75]. This ratio can be changed by varying the laser intensity, hence the depth of the lattice, or the interactions by Feshbach resonances (i.e. where the effective interaction is a function of the magnetic field) [24]. Furthermore, the number of atoms at each site, i.e. the filling fraction of the lattice, is a crucial factor in determining the properties, that is, the phase of the model. In the next two sections, we describe the two main phases of the Bose-Hubbard model, appearing respectively for $J \gg U$ and $J \ll U$.

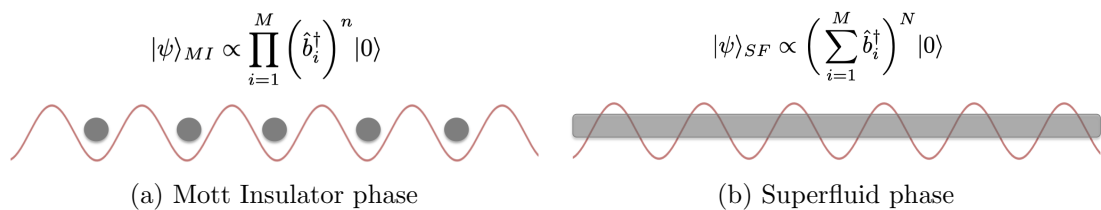


FIGURE 2.3: Mean-field picture of the two quantum phases in the Bose-Hubbard model. (a) Mott Insulator phase in the limit of strong interactions, where the atoms are completely localized on lattice site, and the many-body wave function is given by a product of on-site Fock states. (b) In the non-interacting limit, we have the superfluid phase, where each atom is delocalized over the entire lattice, and the many-body wave function is a product of delocalized single-particle states.

$J \gg U$: Superfluid (SF) phase

In this case, the hopping dominates the on-site interaction, and the many-body wave function is a product of delocalized single-particle states, see Fig. 2.3(a), where each atom is delocalised over the entire lattice, and in the limit $U/J \rightarrow 0$, the state can be

given by

$$|\psi\rangle_{SF} \propto \left(\sum_{i=1}^M \hat{b}_i^\dagger \right)^N |0\rangle, \quad (2.28)$$

where $|0\rangle$ is the vacuum, M the number of sites, and N the number of bosons in the lattice. This state is locally a coherent state with Poisson statistics (a superposition of different atom numbers). The superfluid state throughout the whole phase is compressible, that is, there are large local number fluctuations, and a vanishing energy gap in the thermodynamic limit ($M, N \rightarrow \infty$ with M/N held constant).

$U \gg J$: Mott Insulator (MI) phase

When the system is dominated by the interaction between particles, the wavefunctions are localised with an integer average number of atoms $n = N/M$ per lattice site, see Fig. 2.3(b), and in the limit $U/J \rightarrow \infty$, all phase coherence disappears. This state can be written as

$$|\psi\rangle_{MI} \propto \prod_{i=1}^M \left(\hat{b}_i^\dagger \right)^n |0\rangle, \quad (2.29)$$

which is a product of local Fock states, i.e. states with well-defined number of particles. The Mott Insulator in general is incompressible, with an energy gap in the excitation spectrum.

Phase transition

At zero temperature in 1D the quantum phase transition between the SF and the MI is characterised by the decay of the off-diagonal elements of the single particle density matrix $\langle \hat{b}_i^\dagger \hat{b}_{i+j} \rangle$. The SF phase exhibits divergent correlation lengths, as the off-diagonal elements decay algebraically. The MI phase has finite correlation length, where the off-diagonal elements decay exponentially.

In the last section of this chapter we describe how this phase transition was observed experimentally. We also highlight some of the experimental techniques to detect atoms in optical lattices, and how the results in the following chapters can be applied using these techniques.

2.3 Experiments with optical lattices: state of the art and outlook

We have mentioned that the first time the quantum phase transition between the superfluid and the Mott Insulator phase was observed was by Greiner et al. in 2002 [23]. They used time of flight experiments to measure momentum distributions. This is a standard technique for probing atoms in optical lattices, to measure interference between all waves from the lattice sites. The release of atoms from the lattice allows measurement of momentum distributions [76].

Experimentally, the phase transition was observed by the measurement on the change of coherence properties. In the SF phase the condensate will show sharp matter-wave interference peaks when the quantum gas is released from the optical lattice, due to the long-range phase coherence. In the MI phase, as the system is comprised of pure Fock states of integer on-site density, no interference pattern is observed.

Next, the MI lobes were experimentally observed using atomic clocks shifts [77]. Later, quantum gas microscopes were developed to further enhance the level of single-particle and single-lattice site measurement and control in these systems. For the first time, it was possible to combine single particle detection and control in strongly correlated many-body systems. This allows precise in-situ measurements and dynamics study. A quantum microscope works by fluorescence detection of atoms, illuminating the atoms with near-resonant light and collecting the emitted photons with a microscope objective. The possibility to image the Mott insulators lobes, as Jaksch predicted in [22], was finally possible at the single-atom level [35, 78]. Until 2015, single-atom-resolved detection and manipulation in optical lattices were realised for bosonic species only [34, 79], but from 2015 it was also possible to use fermions (see, for example, [80]).

Last but not least, it is important to mention that atoms in optical lattices can be relatively well isolated from their environment, offering excellent platforms to probe coherent dynamics, such as the observation of an effective light cone that bounds the propagation speed of correlations in a quantum many-body system [81].

Although some experimental difficulties still remain, such as heating and lost of atoms via dissipation [37], the way ahead of research of quantum many-body physics with ultracold atoms in optical lattices looks very interesting.

Some of the ideas to extend these experimental techniques are tackled in this thesis, such as:

- the use of further atomic species: we focus on the Bose-Hubbard model for two bosonic component (or species), which will be introduced in the next chapter;
- new cooling techniques: we present two different techniques to prepare states with very low entropy (temperature), in chapters 5 and 6;
- different range of interactions: in chapter 7 we study models with short, intermediate, and long-range interactions.

2.4 Summary

In this chapter we have introduced the background theory for cold atoms in optical lattices, starting with the description of the interaction of atoms with a light field. We then derived the Bose-Hubbard model, by describing bosons in a periodic potential. We have also described the two quantum phases of the model, the superfluid and the Mott Insulator phase, and how the transition between these phases was first observed experimentally.

Even though these models are particularly important for condensed matter physics [82], there are other applications for optical lattices. The study of formation of molecules [83, 84], or even gate operations for quantum computation [85–87] are just a couple of examples.

We can realise different many-body Hamiltonians using ultracold atoms in optical lattices. In the next chapter we present the methodology to obtain spin models out of a Bose-Hubbard Hamiltonian. We explain how, in the limit of strong interactions, when we have one or few atoms per lattice site, we can then implement spin models, by using perturbation theory. We also describe how we can then study quantum magnetism in quantum simulators. These are the crucial theoretical elements needed to obtain the different research results in the following chapters of this thesis.

Chapter 3

Spin models with ultracold atoms

In the previous chapter, we have discussed how cold atoms in optical lattices offer an excellent resource for quantum simulation, as they present the possibility to study complex many-body physics with very controllable models. Spin systems realised with cold atoms in optical lattices are an example of such models [88], and allow for the investigation of complex many-body physics. One of these interesting physical phenomena is quantum magnetism, lying at the core of condensed matter physics. In order to study quantum magnetism, we model the magnetic ordering governed by specific spin Hamiltonians.

Effective magnetic properties and phenomena in ultracold atoms in optical lattices are driven by a short-range interaction process between spins called superexchange. On one hand, superexchange interactions lead to a state-dependent energy shift which can favour certain magnetically ordered states. This energy sets a time-scale for the dynamics. Also, it defines how fast the system can rearrange itself in order to react to external perturbations (changes to the Hamiltonian). In general, this energy scale is small, leading to very low entropies/temperatures being necessary to observe superexchange. This is the crucial difficulty to experimentally realise sensitive phenomena on a superexchange energy scale [89, 90].

We start this chapter with a general introduction to quantum magnetism in section 3.1, and explain how cold atoms in optical lattices can realise spin models via the process of superexchange. The Bose-Hubbard Hamiltonian for two components is discussed in section 3.2, where we present how this can be mapped to the two effective spin models which we will focus on in the rest of this thesis.

3.1 Quantum Magnetism

In order to investigate quantum magnetism we study magnetic ordering governed by specific spin Hamiltonians. Spin systems have a role as being excellent simple models to explain complex physical phenomena. Starting with the idealised Ising model, spin models provide the framework to study different critical phenomena in many-body physics, such as quantum phase transitions and collective quantum behaviour.

To describe strongly correlated systems and as one potential model for high- T_c superconductivity, the t-J model was derived in the 1980s [91], where in the limit of large interactions, reduces to a Heisenberg spin model. This is an example of spin systems being used as simplified models to capture the properties of real materials. Associated with condensed matter and solid state physics, we are interested in long range antiferromagnetic ordering, as it is directly linked to cuprate ceramics and high temperature superconductors.

Cold atom platforms can be used in this context. However, there are some differences between condensed matter systems and an experiment with ultracold gases [92, 93]. Firstly, the electrons in real materials are fermions, but the collisions necessary to rethermalise atoms, and thus cooling down the system, are more likely between bosons, making them the preferable options for some experiments, especially in magnetic spin models where the exchange properties of the particles are unimportant. Secondly, experiments in materials are carried out at constant temperature, via a thermal reservoir. In ultracold atoms the systems are isolated from the environment, and changes in the parameters (e.g. interactions, hopping) of the system induce changes on the gas temperature. The invariant variable in these experiments is more often the entropy S of the system, provided that the changes are made slowly so that excitations are avoided, making the process adiabatic.

Nowadays, different Hamiltonians can be realised with both bosonic and fermionic platforms. Bosonic systems favour ferromagnetic phases in the ground state, whereas fermions tend to have antiferromagnetic ordering. Nonetheless, an advantage of bosons over fermions in experimental platforms [89] is that lower entropies have been more readily realised. Some recent experiments include the observation of antiferromagnetic magnetic ordering in optical lattices with fermions [29–32], and the investigation of superexchange mediated magnetization dynamics in pseudospin-1/2 bosons in a 2D lattice [94]. We explain in the next section the concept of superexchange in more detail.

3.1.1 Superexchange

We derived in the last chapter the generalised Bose-Hubbard model

$$\hat{\mathcal{H}} = -\zeta \sum_{\langle i,j \rangle} \hat{b}_j^\dagger \hat{b}_i + \frac{U}{2} \sum_i \hat{n}_i (\hat{n}_i - 1) + \sum_i \epsilon_i \hat{n}_i. \quad (3.1)$$

with tunnelling ζ and on-site interaction U .

To understand superexchange, we start with atoms localised in individual lattice sites that can tunnel to the nearest-neighbour site. We then consider a virtual tunnelling to the neighbour lattice site with tunnelling rate ζ . This adds an energy cost U due to the on-site interaction by having the two atoms together on the same site. By energy conservation, the atom tunnels back to the original lattice site (see Fig. 3.1 for a better understanding of superexchange). The whole process results in a total energy element $J_{SE} \propto \zeta^2/U$ (the effective matrix element in perturbation theory) where J_{SE} is this critical energy or superexchange.

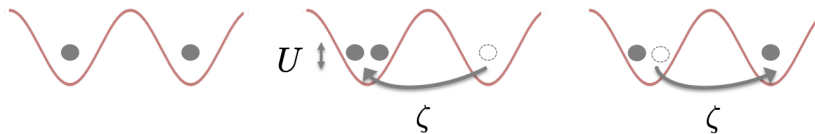


FIGURE 3.1: The process of superexchange is mediated by two virtual tunnelling events between neighbouring sites in an optical lattice.

Typical experimental values are $\zeta \sim 100\text{Hz}$ and $U \sim 0 - 10\text{kHz}$. This sets the critical temperatures to observe quantum magnetic ordering to the nanoKelvin regime. Superexchange was first observed for cold atoms in isolated double well potentials in 2008 by Trotzky et al. [27].

Now that we understand how superexchange works, we can derive effective spin models. This mapping will be done in the next section, where the core model for the results in this thesis, being the Bose-Hubbard model for two different atomic species, will be introduced.

3.2 Bose-Hubbard model for two bosonic components

A generalisation of Eq. 3.1, considering in particular the low energy model where atoms are confined to the lowest Bloch band, the Bose-Hubbard model for two bosonic species

A and B ¹, trapped independently in an optical lattice, is [95–97]

$$\begin{aligned} \hat{\mathcal{H}} = & -t_A \sum_{\langle i,j \rangle} (\hat{a}_i^\dagger \hat{a}_j + \hat{a}_j^\dagger \hat{a}_i) - t_B \sum_{\langle i,j \rangle} (\hat{b}_i^\dagger \hat{b}_j + \hat{b}_j^\dagger \hat{b}_i) + U \sum_i \hat{n}_{Ai} \hat{n}_{Bi} \\ & + \frac{1}{2} \sum_{i,\alpha=A,B} V_\alpha \hat{n}_{\alpha i} (\hat{n}_{\alpha i} - 1) - \sum_{i,\alpha=A,B} \mu_\alpha \hat{n}_{\alpha i}. \end{aligned} \quad (3.2)$$

The first two terms denote the tunnelling energies t_A and t_B for the species A and B respectively, where $\hat{a}_i^\dagger, \hat{b}_i^\dagger, \hat{a}_i, \hat{b}_i$ are the bosonic creation and annihilation operators on site i . The third term in the Hamiltonian designates the case where two atoms of different species are on the same site, with U the inter-component on-site interaction, where \hat{n}_A and \hat{n}_B are the number operators for the atomic species A and B , respectively. The fourth term describes the intra-component on-site interaction, when atoms of the same species seat on the same lattices site. The chemical potentials μ_A, μ_B will normally be different. However, here they will be considered equal and fixed, as we will focus on the case of equal populations. Lastly, $\langle i, j \rangle$ denotes nearest-neighbour sites.

Note that instead of two atomic species we could refer likewise to two different hyperfine states of the same atomic species.

With the following simplifications:

- the tunnelling energies are the same for the two components: $t_A = t_B = \zeta$;
- inter-component interaction is denoted as U_{AB} ;
- intra-component interactions are U_A and U_B , respectively;
- the chemical potential is negligible $\mu_\alpha \simeq 0$;

the Hamiltonian takes the form

$$\hat{\mathcal{H}} = -\zeta \sum_{\langle i,j \rangle} (\hat{a}_i^\dagger \hat{a}_j + \hat{b}_i^\dagger \hat{b}_j) + U_{AB} \sum_j \hat{a}_j^\dagger \hat{a}_j \hat{b}_j^\dagger \hat{b}_j + \frac{U_A}{2} \sum_j \hat{a}_j^\dagger \hat{a}_j \hat{a}_j \hat{a}_j + \frac{U_B}{2} \sum_j \hat{b}_j^\dagger \hat{b}_j \hat{b}_j \hat{b}_j. \quad (3.3)$$

In Fig. 3.2 the different terms of Eq. 3.3 are represented.

For strong interactions ($U_{AB}, U_A, U_B \gg \zeta$) the atoms become localized on individual lattice sites (if we have integer filling), as it was explained in the last chapter when we described the Mott Insulator regime. If the atoms are a mixture of two spin-components, this is effectively a system of spins which are held to a lattice, interacting by superexchange, as explained in the next section.

¹components or species are interchangeable in the text.

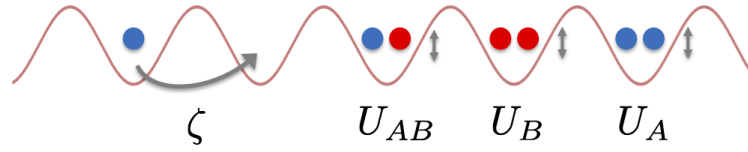


FIGURE 3.2: Bose-Hubbard model for two bosonic species in an optical lattice, where ζ denotes the tunnelling rate, U_{AB} the inter-component interaction, and U_A, U_B the intra-component interactions.

3.2.1 From Bose-Hubbard to spin models

In the Mott Insulator regime where $U_{AB}, U_A, U_B \gg \zeta$, the Hamiltonian can be highly simplified using second order perturbation theory in the tunnelling [96]. We consider a particular integer occupation n on every site, that is, the filling factor introduced in the previous chapter, in the lowest Bloch band. We also map the general spin operators in terms of the bosonic creation and annihilation operators as

$$\hat{S}_j^{x,y,z} = \frac{1}{2} \sum_{\beta=A,B} \hat{c}_{j,\beta}^\dagger \hat{\sigma}_\beta^{x,y,z} \hat{c}_{j,\beta}, \quad (3.4)$$

where $\hat{c}_{j,\beta=A,B}^\dagger, \hat{c}_{j,\beta=A,B}$ are the bosonic creation and annihilation operators for species A and B , and $\hat{\sigma}^{x,y,z}$ are the Pauli matrices [96]. Hence, we obtain, with the corresponding operators species A and B , the different spin operators

$$\hat{S}_j^z = \frac{1}{2} (\hat{a}_j^\dagger \hat{a}_j - \hat{b}_j^\dagger \hat{b}_j), \quad (3.5)$$

$$\hat{S}_j^y = -\frac{i}{2} (\hat{a}_j^\dagger \hat{b}_j - \hat{b}_j^\dagger \hat{a}_j), \quad (3.6)$$

$$\hat{S}_j^x = \frac{1}{2} (\hat{a}_j^\dagger \hat{b}_j + \hat{b}_j^\dagger \hat{a}_j). \quad (3.7)$$

Next, we are considering two different cases, where either $n = 2$ on each lattice site, or $n = 1$ on each lattice site.

n=2: Spin-1 model

We start with an integer filling with $n = n_A + n_B = 2$ atoms per site, with same number of atoms of each species ($\hat{n}_A = \hat{n}_B$). We also consider $U_A = U_B = U$.

By applying second order perturbation theory in the tunnelling, we derived all of the matrix elements for the effective Hamiltonian. All virtual tunnelling possibilities between neighbouring sites in the optical lattice are taken into account (in Fig. 3.3 we sketch this process for a better understanding).

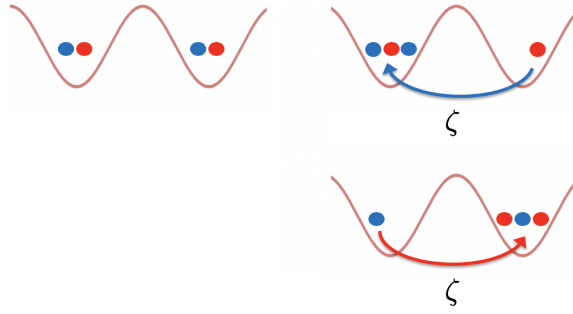


FIGURE 3.3: Hopping possibilities for the derivation of the effective spin-1 Heisenberg model from the two-species Bose-Hubbard model with $n = 2$ atoms per lattice site.

The effective Hamiltonian results in an anisotropic spin-1 Heisenberg model

$$\hat{\mathcal{H}}_{\text{SP1}} = -J \sum_{\langle j,l \rangle} \hat{\mathbf{S}}_j \hat{\mathbf{S}}_l + u \sum_l (\hat{S}_l^z)^2, \quad (3.8)$$

with

$$J = 4 \frac{\zeta^2}{U_{AB}}, \quad (3.9)$$

the superexchange term,

$$u = U - U_{AB}, \quad (3.10)$$

the anisotropy, and

$$\hat{\mathbf{S}}_j = (\hat{S}_j^x, \hat{S}_j^y, \hat{S}_j^z), \quad (3.11)$$

is a vector of the three spin-1 operators.

Hence, a model with two species of bosons with double occupation can be represented as three different spin-1 states ($|+1\rangle$, $|0\rangle$, $| -1\rangle$) (see Fig. 3.4).

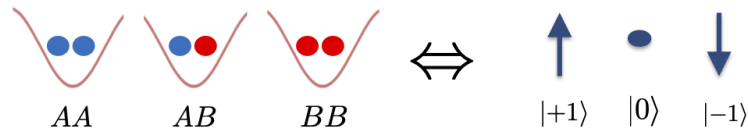


FIGURE 3.4: Spin-1 model: three states representation.

The lower energy states of the lattice for the spin ($S=1$) in the z-direction $S^z = +1, 0, -1$ are the three states:

$$\hat{a}_l^\dagger \hat{a}_l^\dagger |0\rangle, \quad (3.12)$$

$$\hat{a}_l^\dagger \hat{b}_l^\dagger |0\rangle, \quad (3.13)$$

$$\hat{b}_l^\dagger \hat{b}_l^\dagger |0\rangle, \quad (3.14)$$

respectively.

n=1: Spin-1/2 model

In the case of total filling of one particle per site ($n = 1$, $\hat{n}_A = \hat{n}_B$), by applying second order perturbation theory in the tunnelling, we derived all of the matrix elements for the effective Hamiltonian as in Fig. 3.5.

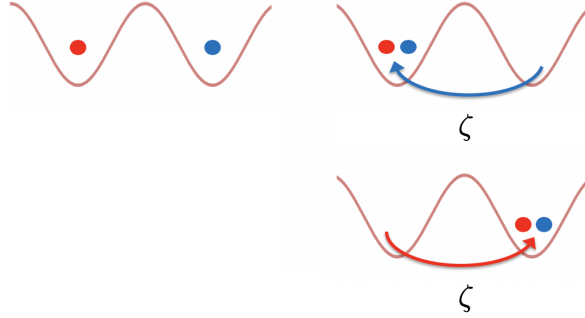


FIGURE 3.5: Hopping possibilities for the derivation of the effective spin-1/2 Heisenberg model from the two-species Bose-Hubbard model with $n = 1$ atom per lattice site.

In this case, spin $|\uparrow\rangle$ represents the atomic species A and spin $|\downarrow\rangle$ represents the atomic species B , as in Fig. 3.6.

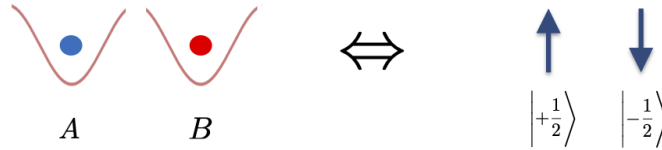


FIGURE 3.6: Spin-1/2 model: two-state representation. It is essential to mention that we are talking about spin-1/2 bosons, coming from different hyperfine state levels of integer spin.

The resulting effective Hamiltonian will be a spin-1/2 XXZ Heisenberg model

$$\hat{\mathcal{H}}_{\text{SP1/2}} = -J_{xy} \sum_{\langle j,l \rangle} (\hat{s}_j^x \hat{s}_l^x + \hat{s}_j^y \hat{s}_l^y) + J_z \sum_{\langle j,l \rangle} \hat{s}_j^z \hat{s}_l^z, \quad (3.15)$$

where

$$J_z = 4 \frac{\zeta^2}{U_{AB}} - 4 \frac{\zeta^2}{U_A} - 4 \frac{\zeta^2}{U_B}, \quad (3.16)$$

and

$$J_{xy} = 4 \frac{\zeta^2}{U_{AB}}. \quad (3.17)$$

Here, $\hat{s}_j^x, \hat{s}_j^y, \hat{s}_j^z$ are the three spin-1/2 operators.

In the limit where $U_{AB} < U_A = U_B = U$ and $\zeta = 1$, we have

$$J_{xy} = \frac{4}{U_{AB}}, \quad (3.18)$$

and

$$J_z = \frac{4}{U_{AB}} - \frac{8}{U} \rightarrow J_z < 0, \quad (3.19)$$

and the effective Hamiltonian from Eq. 3.15 becomes (taking $J = J_{xy}$)

$$\hat{\mathcal{H}}_{\text{SP1/2}} = -J \sum_{\langle j,l \rangle} \hat{\mathbf{s}}_j \hat{\mathbf{s}}_l + \Delta \sum_{\langle j,l \rangle} \hat{s}_j^z \hat{s}_l^z, \quad (3.20)$$

where

$$\Delta = J_{xy} + J_z, \quad (3.21)$$

denotes the coupling anisotropy in this XXZ Heisenberg model, and

$$\hat{\mathbf{s}}_j = (\hat{s}_j^x, \hat{s}_j^y, \hat{s}_j^z), \quad (3.22)$$

is a vector of the three spin-1/2 operators. We use this notation here to differentiate from the spin-1 operators, as we will do in the rest of the thesis.

In the next section we will analyse the magnetic ground states of both Hamiltonians depending on the value of the interactions, that is, the value of the anisotropies in the spin models.

3.2.2 Ground state magnetic ordering

Here we include a mean-field picture of the ground state phases in different regimes for the spin-1 and spin-1/2 model, depending on the value of the interactions.

The phase diagrams of the models are shown schematically in Fig. 3.7 depending on the ratio of the anisotropies u, Δ and the superexchange J [95, 98, 99].

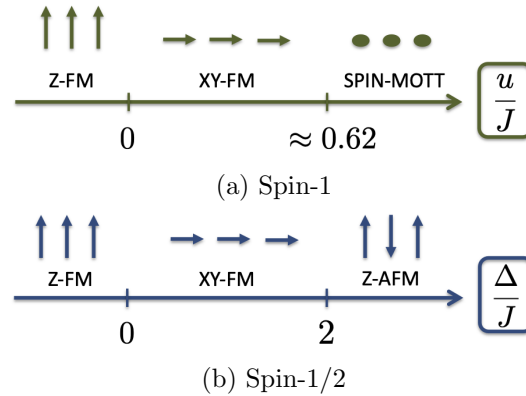


FIGURE 3.7: Simplified mean field phase diagram in the spin picture, following [98] results, for the Hamiltonians in Eq. 3.8(a) and Eq. 3.20(b), respectively.

In Fig. 3.8 we sketch the magnetic ground state of the two models. For the spin-1 model Hamiltonian (Eq. 3.8), interactions of the same order ($U_{AB} \approx U$) lead to a XY-ferromagnet in the ground state, induced by superexchange term, characterised by a superposition of total spin in z $S^z = +1, 0, -1$ on each site. By having $U_{AB} > U$, the ground state is a z-ferromagnet, that is, all spins will point up (or down, depending on the chosen basis). When $U_A = U_B = U \gg U_{AB}$, hence, very low U_{AB} compare to u/J , the ground state state will show a spin insulator or spin Mott state configuration, characterised by $S^z = 0$.

For the spin-1/2 Hamiltonian (Eq. 3.20), the ground state state will be an antiferromagnet when U_{AB} is very low compared to U . The superposition of $S^z = +1/2, -1/2$ on each site indicates interactions of the same order ($U_{AB} \approx U$) leading again to a XY-ferromagnet in the ground state. When $U_{AB} > U$, the ground state is a z-ferromagnet.

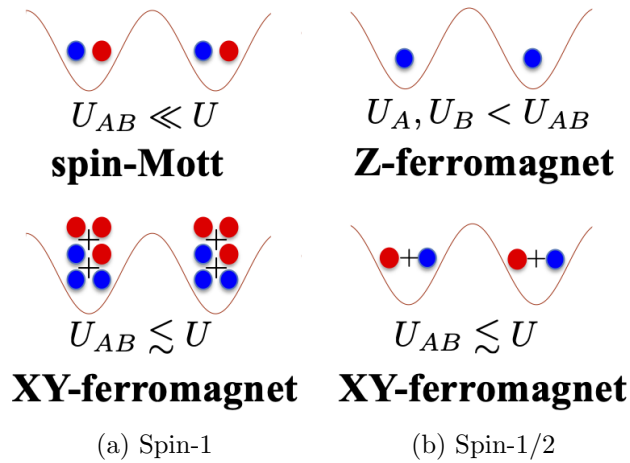


FIGURE 3.8: Ground state magnetic phases for the spin models depending on the interactions (mean-field picture). There are two cases not represented in the figure. For the spin-1, having $U_{AB} > U$, the ground state is a z-ferromagnet, that is, all spins will point up (or down, depending on the chosen basis). For the spin-1/2, the ground state state will be an antiferromagnet when U_{AB} is very low compared to U .

In the Mott phase of two species of atoms, while the net density transport is still suppressed, the counterflow (when the currents of the two species are equal in absolute values and are in opposite directions) survives, and can be nondissipative (supercounterflow) [96]. The XY-ferromagnetic Mott state can be then seen as a counterflow superfluid. We will investigate this phase in the following chapters.

In both models, changing the interactions contributes to phase transitions. This is important as we will study how to prepare specific magnetic ordering in both models where we study different regimes depending on the anisotropy values of u/J and Δ/J , respectively.

Experimentally, spin-dependent lattices can be used to adiabatically tune the system from a spin Mott regime to an XY-ferromagnet. The interactions can be tuned by using Feshbach resonances [24]. The detection of the magnetic states could be performed by measuring population difference locally between the different spin states, or using imaging techniques such as quantum microscopes or Bragg scattering [29, 100].

3.3 Summary

In this chapter we have described how quantum magnetism can be studied with ultracold atoms in optical lattices. Furthermore, the concept of superexchange, which describes magnetism induced by tunnelling and local interactions between particles, has been explained.

The Bose-Hubbard model for two bosonic components has been introduced. We have derived two different effective spin models from this Bose-Hubbard model, one for spin-1, and one spin-1/2 XXZ Heisenberg Hamiltonian. These are the core models for all of the research results presented in the next chapters.

The interactions produce particular magnetic ordering in the ground state of the models in different parameter regimes. In the coming chapters we present different approaches to prepare specific ground states. In chapter 5 we investigate the XY-ferromagnetic (or counterflow spin superfluid) phase. We also study ways to probe these states by analysing the out-of-equilibrium dynamics in the systems. Furthermore, we compute thermal states for these systems, and analyse the spin currents. In chapter 6 we use adiabatic ramps to prepare specific ground states (XY-ferromagnet and antiferromagnet) of the corresponding spin Hamiltonians. However, before presenting these results, we need to provide an overview of the numerical tools needed to investigate these quantum many-body systems. This will be the focus of the next chapter.

Chapter 4

Numerical Simulation

Nowadays, numerical simulations play a fundamental role in any theoretical research. In cold atoms in optical lattices, our field of study, analytical solutions typically rely on certain approximations that limit our ability to model realistic experimental scenarios. We can use Exact Diagonalisation, described in 4.1, to simulate these kind of systems. However, we have mentioned in previous chapters that in a system of M atoms, the size of the Hilbert space will be proportional to d^M , being d the local dimension of the system. Exact Diagonalisation (ED) then has limitations in terms of memory and computational time required for systems with more than $M = 20$ atoms. To handle this many-body problem numerically, the Density Matrix Renormalisation Group (DMRG) algorithm was introduced [39, 40]. The basic idea behind DMRG is to truncate the Hilbert space by keeping the most important basis states, without a significant change of the physical features. We provide an introduction to DMRG in section 4.2.

An efficient representation of the Hilbert space to be able to describe the system of interest and access all its properties is based on Matrix Product States (MPS) and Matrix Product Operators (MPOs). We extensively review these concepts in section 4.2.1. We are going to widely use the MPS and MPO methods presented in this chapter to simulate the dynamics of spin Hamiltonians in Chapters 5, 6 and 7.

One of the central questions for any quantum problem is to find the ground state of the Hamiltonian, and study its properties. In section 4.2.2 we present a variational ansatz to find ground states. Following the properties of the ground state, we are interested in evolving the quantum systems, and understanding dynamical phenomena. Although there are numerous algorithms to study the dynamics of quantum systems, we focus on those approaches using MPS and MPOs, as we can implement the kind of spin models we investigate in 1D for experimental system sizes. Two of these methods are Time-Evolving Block Decimation Algorithm (TEBD), in section 4.2.3.1, and Time

Dependent Variational Principle (TDVP), in section 4.2.3.2. We use these algorithms in the following chapters.

Furthermore, in section 4.2.4, we present the Ancilla method to simulate finite temperature states, which is the method we use for the results presented in section 5.4.

Beyond the previous simplified closed model, we also provide a brief overview of open quantum systems, that is, when the system interacts with its environment, and the evolution of the system is governed by the master equation (section 4.3.1). We introduce the quantum trajectory method in section 4.3.2, where the master equation is rewritten as a stochastic average over individual trajectories. This is particularly useful in our case when we consider dissipation in our lattice models, as we consider in section 6.4.4.

4.1 Exact Diagonalisation

The exact diagonalisation (ED) technique [53] relies on solving an eigenvalue problem. When analysing our quantum system we often face tasks such as solving the Schrödinger equation

$$i\hbar \frac{\partial |\psi\rangle}{\partial t} = \hat{\mathcal{H}} |\psi\rangle, \quad (4.1)$$

or finding the eigenvalues E_i and eigenvectors ψ_i (e.g. to compute the ground state) for a given Hamiltonian

$$\hat{\mathcal{H}} |\psi_i\rangle = E_i |\psi_i\rangle. \quad (4.2)$$

One way to attain larger system sizes with ED is to use symmetries, i.e., when there is a set of operators $\{O_i\}$ which commutes with the Hamiltonian. In this case the full Hamiltonian can be reduced to the diagonalisation of smaller matrices defined by the subspaces composed of the well-defined eigenvalues of the operators. To understand this better, we can write the Hamiltonian in matrix form

$$\hat{\mathcal{H}} = \begin{bmatrix} \hat{\mathcal{H}}_{11} & \dots & \hat{\mathcal{H}}_{1N} \\ \vdots & \ddots & \vdots \\ \hat{\mathcal{H}}_{N1} & \dots & \hat{\mathcal{H}}_{NN} \end{bmatrix}, \quad (4.3)$$

where the matrix elements are $\hat{\mathcal{H}}_{ij} = \langle \psi_j | \hat{\mathcal{H}} | \psi_i \rangle$. This matrix is usually sparse, with typically only $\mathcal{O}(M)$ non-zero coefficients. But the sizes are still limited. This means that large matrices can be stored in memory. The most popular algorithm for this kind of problems is the Lanczos algorithm [101], which is very accessible because to calculate the ground state energy only few iterations are needed. One of the drawbacks, however, is that it does not work so well in the middle of the spectrum.

Using the Lanczos method, we can also compute the time evolution of the Hamiltonian. These techniques are based on Krylov-space methods. The Krylov space is a sub-space of the full Hilbert space, and the low-lying states of a Hamiltonian of interest should be well approximated within it. We evaluate the matrix exponential of a Hamiltonian matrix using Krylov subspace projection.

Coming back to the Schrödinger equation in 4.1, the evolution of the state will be

$$|\psi(t)\rangle = e^{-\frac{i}{\hbar}\hat{\mathcal{H}}t} |\psi(0)\rangle. \quad (4.4)$$

where the evolution operator is (we set up $\hbar = 1$ for simplicity)

$$U(\hat{t}) = e^{i\hat{\mathcal{H}}t}. \quad (4.5)$$

We could think of evaluating explicitly this evolution at each time step, that is

$$|\psi(t + \Delta t)\rangle = (\mathbb{1} - i\hat{\mathcal{H}}\Delta t) |\psi(t)\rangle + \mathcal{O}(\Delta t^2). \quad (4.6)$$

However, we need to renormalise at each time step, due to the large time step error, and because the evolution operator $U(\hat{\Delta}t) = (\mathbb{1} - i\hat{\mathcal{H}}\Delta t)$ is not unitary. There are some methods with better robustness and scaling, such as the Crank-Nicholson methods, which relies in an intermediate step, half-evolving the state forward and backward (more details can be found in [102]).

Now, in order to use Krylov methods, we will Taylor expansion the evolution of the state

$$U(\hat{t}) = e^{-i\hat{\mathcal{H}}t} = \mathbb{1} + \frac{-i\hat{\mathcal{H}}t}{1!} + \frac{(-i\hat{\mathcal{H}}t)^2}{2!} + \frac{(-i\hat{\mathcal{H}}t)^3}{3!} + \dots, \quad (4.7)$$

that is

$$|\psi(t)\rangle = U(\hat{t}) |\psi(0)\rangle = |\psi(0)\rangle + \frac{-i\hat{\mathcal{H}}t}{1!} |\psi(0)\rangle + \frac{(-i\hat{\mathcal{H}}t)^2}{2!} |\psi(0)\rangle + \dots, \quad (4.8)$$

and we truncate the evolution after n terms (normally for sparse matrices, n values are much smaller than the dimension of $\hat{\mathcal{H}}$)

$$|\psi(t)\rangle = |\psi(0)\rangle + \alpha_1(\hat{\mathcal{H}}t) |\psi(0)\rangle + \alpha_2(\hat{\mathcal{H}}t)^2 |\psi(0)\rangle + \dots + \alpha_n(\hat{\mathcal{H}}t)^n |\psi(0)\rangle + \mathcal{O}(t^{n+1}), \quad (4.9)$$

with coefficients

$$\alpha_n = -\frac{(i)^n}{n!}. \quad (4.10)$$

The truncated Krylov subspace is

$$\mathcal{K} = (\hat{\mathcal{H}}t, |\psi(0)\rangle) = \{|\psi(0)\rangle, (\hat{\mathcal{H}}t)|\psi(0)\rangle, (\hat{\mathcal{H}}t)^2|\psi(0)\rangle, \dots, (\hat{\mathcal{H}}t)^n|\psi(0)\rangle\}, \quad (4.11)$$

spanned by non-orthonormal vectors (making the coefficients not certainly the best coefficients). The algorithm relies on finding the optimal linear combination in the Krylov subspace to represent the state.

The techniques described above are the key elements for matrix diagonalisation and time evolution, in functions such as *eig* built in *MATLAB*[®], and *expv* from *Expokit* [103]. These are essential functions used for small systems results in the following chapters.

Unfortunately, in order to simulate many-body physics we need system sizes representing what can be done in the experiments. For a system of M atoms in an optical lattice, the total Hilbert space will increase exponentially with the number of atoms

$$\dim(\hat{\mathcal{H}}) = \dim\{\hat{\mathcal{H}}_1 \otimes \hat{\mathcal{H}}_2 \otimes \dots \otimes \hat{\mathcal{H}}_M\} = d^M. \quad (4.12)$$

We provide an idea why a standard diagonalisation where all matrix elements are stored faces difficulties for a classical computer. Considering a system of N spins (bosons in our models) in an optical lattice of M sites, the dimension of the Hilbert space is

$$\dim(\hat{\mathcal{H}}) = \frac{(N + M - 1)!}{N!(M - 1)!}. \quad (4.13)$$

From now on, we consider the case where $N = M$. Giving specific values, for a system of size $M = 12$, the $\dim(\hat{\mathcal{H}}) \simeq 1352078$, and for $M = 24$ $\dim(\hat{\mathcal{H}}) \simeq 16.12 \times 10^{12}$, respectively. In terms of memory, and a system with $M = 12$ spin-1/2 atoms, the requested memory capacity will be 256Mb to store all complex numbers. For a system size $M = 24$, more than 4000Tb are needed. To operate with such a high memory requirement, ED is not sufficient, even if we use some symmetries and sparse matrices, which means that we need other methods for the simulation of larger systems. We could build a quantum computer, or we could employ Reduced Hilbert Space Techniques. The latter will be the core of the next section, where different algorithms based on MPS techniques will be presented.

4.2 Density Matrix Renormalisation Group (DMRG)

In certain systems, only a small subset of the possible states are actually important for the calculation of most quantities of interest. In 2D and 3D this is only true for small systems. In 1D, we are interested in ground states and low-lying excited states

of many-body quantum systems, which belong to a low-entangled subset of the whole Hilbert space. This means that we do not need to represent the full Hilbert space, and that we should be able to truncate our Hilbert space by removing the long-range entanglement that is not involved in the ground state nor in the time evolution of the system. The effectiveness of these methods will be depending on how reliable this truncation is. The renormalisation technique applied to one-dimensional quantum systems was introduced in the 90s by White [39, 40], the Density Matrix Renormalisation Group (DMRG). DMRG allows for the calculation of ground states of spin models in 1D at zero temperature for all gapped Hamiltonians with finite-range interactions.

The area law

We have mentioned that we are interested in a subset of the full Hilbert space with low entanglement. To understand the success of DMRG in 1D, we need to explain the so-called area law, where the area of the boundary is independent of the system size, and so is the entanglement entropy, where the Hamiltonian is local [104]. In Fig. 4.1 we sketch this idea of the subspace, within the Hilbert space, where our interest relies, containing the ground states and the low-lying excited states of the Hamiltonians.

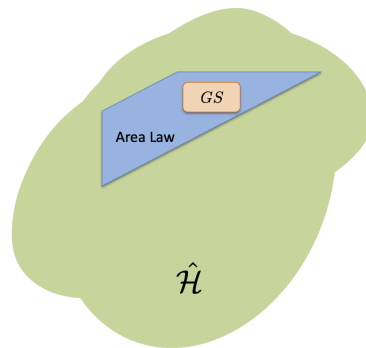


FIGURE 4.1: Sketch of the full Hilbert space and the small subset where states obey the area law, including the ground state. By effectively representing these states, we can reduce the size of the Hilbert space we need to compute, thus, reducing the memory needed and increasing the efficiency of the simulations.

For ground states of short-ranged Hamiltonians with a gap to excited states the entanglement entropy is proportional to the size of the boundary. In 1D this boundary is constant, hence the entanglement, meaning that it does not grow with system size, as in Fig. 4.2(a). For 2D, the entanglement entropy grows with the size of the system, as in Fig. 4.2(b). For this reason, the effectiveness of DMRG in 2D will fail even for relatively small systems.

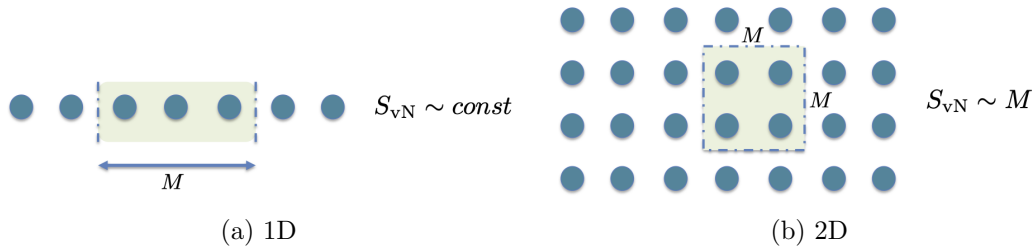


FIGURE 4.2: Area Law for a (a) one-dimensional and a (b) two-dimensional system of atoms. The von Neumann entropy (or entanglement entropy) grows with the size of the boundary in 2D, while it remains constant for 1D. This is the success of DMRG methods for the Hamiltonians of one-dimensional quantum systems.

The following step in the development of these powerful numerical tools was to find an efficient representation for this low-entangled subspace. The idea of using Matrix Product states to represent DMRG ground states was introduced by Ostlund and Rommer [105, 106]. In the next section we describe Matrix Product States, based on tensor networks, including all of the ingredients we need to present the different algorithms we use for the calculation of ground states, thermal states, and time evolution in our systems.

4.2.1 Matrix Product States (MPS)

We explained how the Hilbert space of a quantum mechanical many-body system grows exponentially with system size. We also said that the one-dimensional relevant states we want to investigate will have an entanglement entropy independent of system size. An efficient representation of these low entanglement states is called Matrix Product States (MPS). The *optimal representation* is the same as in DMRG: the eigenstates of the reduced density matrix with the largest eigenvalues are retained. We now explain why this is the case.

We represent a state in the complete Hilbert space, spanned in local basis $\{|i\rangle\}$, of a one-dimensional Hamiltonian of interest with dimension d^M as

$$|\psi\rangle = \sum_{i_1, \dots, i_M}^d C_{i_1, \dots, i_M} |i_1, \dots, i_M\rangle. \quad (4.14)$$

We now arrange these coefficients as

$$C_{i_1, \dots, i_M} = A_{[1]}^{i_1} A_{[1],[2]}^{i_2} \dots A_{[M-1],[M]}^{i_{M-1}} A_{[M]}^{i_M}, \quad (4.15)$$

where each A^{i_m} is a matrix depending on the local state $|i\rangle_m$. Thus, we obtain a generic Matrix Product State

$$|\psi\rangle = \sum_{i_1 \dots i_M} A_{[1]}^{i_1} A_{[1],[2]}^{i_2} \dots A_{[M-1],[M]}^{i_{M-1}} A_{[M]}^{i_M} |i_1, \dots, i_M\rangle. \quad (4.16)$$

So far we have performed a rearrangement of terms, the power of the method will come with the truncation. In order to understand how the truncation is performed, we need to recall some concepts from linear algebra.

Singular Value Decomposition (SVD)

To perform the truncation, i.e. choosing the optimal state represented with fewer parameters, we use Single Value Decomposition (SVD) [42, 47, 107].

For any rectangular matrix M of dimensions $m \times n$, with $k = \min(m, n)$ we can have the following decomposition

$$M = USV^\dagger, \quad (4.17)$$

where

- U has dimensions $m \times k$, with orthonormal columns (left singular vectors), satisfying $U^\dagger U = \mathbb{1}$, and unitary when $m \leq n$.
- S has dimensions $k \times k$, and is diagonal. The values on the diagonal are real and non-negative, and are called the singular values s . The number of positive s values, and smaller than k , is called the Schmidt Rank.
- V^\dagger has dimensions $k \times n$, with orthonormal rows (right singular vectors), where $V^\dagger V = \mathbb{1}$. When $m \geq n$, is also unitary.

The Schmidt Rank

We can relate this now to a bipartite quantum state residing in the Hilbert space $\hat{\mathcal{H}}$, composed of two subspaces A (sites 1 through m) and B (sites $m+1$ through M), with dimensions d_A and d_B , that is $\hat{\mathcal{H}} = \hat{\mathcal{H}}_A \otimes \hat{\mathcal{H}}_B$. The quantum state can be denoted as

$$|\psi_{AB}\rangle = \sum_i \sum_j^{d_B} C_{i,j} |i\rangle_A \otimes |j\rangle_B, \quad (4.18)$$

with $|i\rangle_A$ and $|j\rangle_B$ being the subsystems orthonormal basis. We decompose $C_{i,j}$ via Singular Value Decomposition as

$$C = USV^\dagger, \quad (4.19)$$

or as

$$C_{i,j} = \sum_k^{D_{AB}} U_{i,k} S_{k,k} V_{k,j}^\dagger, \quad (4.20)$$

where S is a diagonal matrix of dimension $d_A \times d_B$ and singular values $s_{k,k}$, and we define D_{AB} as the minimum of the two dimensions, thus $D_{AB} = \min(d_A, d_B)$. Here

The Schmidt coefficients are $\lambda_k \equiv s_{k,k}$ and satisfy

$$\sum_l \lambda_k^2 = 1, \quad (4.21)$$

where the number of non-zero λ_k defines the Schmidt rank, which quantifies the amount of entanglement between subsystems A and B [42, 47, 107]. If there is more than one non-zero Schmidt value, the two parts of the system are entangled. Another way to quantify this bipartite entanglement is by calculating the von Neumann entropy of the subsystems. We have for the subsystems

$$S_{vN}(\rho_A) = -\text{Tr} \rho_A (\log_2 \rho_A) = -\text{Tr} \rho_B (\log_2 \rho_B) = S_{vN}(\rho_B), \quad (4.22)$$

where Tr denotes the trace, with $\rho_A = \text{Tr}_B |\psi\rangle_{AB} \langle\psi|_{AB}$ and $\rho_B = \text{Tr}_A |\psi\rangle_{AB} \langle\psi|_{AB}$ the reduced density matrices of the subsystems A and B .

Hence the von Neumann entropy becomes

$$S_{vN} = - \sum_k^{D_{AB}} \lambda_k^2 (\log_2 \lambda_k^2). \quad (4.23)$$

and will be $0 \leq S_{vN} \leq \log_2(D_{AB})$. We can relate D_{AB} with the bond dimension, that is, the dimension of the common index between every two matrices $A_{[i]}$ in Eq. 4.16 . D_{AB} can be used to measure the entanglement of the system, and will be an important parameter for all further analyses done with numerical simulations in this thesis. The state $|\psi_{AB}\rangle$ from Eq. 4.18 can now be represented with the Schmidt coefficients as

$$|\psi_{AB}\rangle = \sum_{k=1}^{D_{AB}} \lambda_k |\Phi_k^A\rangle \otimes |\Phi_k^B\rangle, \quad (4.24)$$

where

$$|\Phi_k^A\rangle \equiv \sum_{i=1}^{d_A} U_{i,k} |i\rangle_A, \quad (4.25)$$

and

$$|\Phi_k^B\rangle \equiv \sum_{j=1}^{d_B} V_{k,j} |j\rangle_B, \quad (4.26)$$

are the Schmidt vectors from orthonormal basis in the subsystems A and B , and $U_{i,k}, V_{k,j}$ come from the SVD. The Matrix Product State that best represents a given state can be built this way, by applying singular value decompositions (see Fig. 4.3), based on the real positive singular values of the Schmidt coefficients.

$$A = U S V^\dagger$$

FIGURE 4.3: Singular Value Decomposition of matrix A , where shaded regions denote the relevant part in the systems.

The way it works is by building blocks, starting from a block with just one site, and add site by site. With a maximum number D of states for a block description, assuming we have the block A described above, we take a block of length $m - 1$, with basis $\{|a_{m-1}\rangle\}$, and add site m , having

$$|a_m\rangle = \sum_{a_{m-1}, i_m} \langle a_{m-1}, i_m | a_m \rangle |a_m\rangle |a_{m-1}\rangle |i_m\rangle \equiv \sum_{a_{m-1}, i_m} A_{a_{m-1}, a_m}^{i_1} |a_{m-1}\rangle |i_m\rangle. \quad (4.27)$$

Now we can iterate all of the coefficients to obtain

$$|a_m\rangle = \sum_{i_1 \dots i_m} (A^{i_1} A^{i_2} \dots A^{i_m})_{1, a_m} |i_1, i_2, \dots, i_m\rangle. \quad (4.28)$$

We now have MdD^2 coefficients, in comparison to the exponential coefficients d^M , and we can represent any MPS using tensor network graphical notation, where the bond dimension D is the maximum linear dimension of any of the matrices $A_{[m]}^{i_m}$. In Fig. 4.4 we represent the state as a product of matrices, a Matrix Product State. The error per

$$|\psi\rangle = \text{[Diagram showing contraction of tensors]} \longrightarrow \text{[Diagram showing contracted MPS bar]}$$

FIGURE 4.4: Tensor network representation of a Matrix Product State for the state $|\psi\rangle$, where d^M coefficients are now represented with $d \cdot M$ matrices, where D is the bond dimension. Each tensor has a number of indices (represented as legs). Closed links mean contraction over those indices here, as we see on the right hand side of the figure.

bond in the truncation comes from the Schmidt coefficients condition in Eq. 4.21 and it will be

$$\epsilon_k = \sum_{i_k}^{D_k} (\lambda_{i_k}^{[k]})^2. \quad (4.29)$$

A Matrix Product State representation of states is not unique. There is a gauge freedom [42, 47, 107] for MPS, both for the general state decomposition and the block procedure. If we begin SVD building blocks from the left, adding blocks to the right, we will have *left-normalised* matrices with

$$\sum_{i_m} A^{i_m \dagger} A^{i_m} = \mathbb{1}, \quad (4.30)$$

and if we start building blocks from the right, adding blocks to the left,

$$\sum_{i_m} B^{i_m} B^{i_m \dagger} = \mathbb{1}, \quad (4.31)$$

the matrices are similarly called *right-normalised*. This gauge freedom leads to the mixed canonical forms of MPS, performing SVD from both the left and the right side, and hence simplifying most of the algorithms. As an example, if we want to evaluate the expectation value of a local operator \hat{O}_m on site m , all orthonormal tensors on the left and on the right will produce identities after being contracted from the edges. The expression with MPS is

$$\langle \psi | \hat{O}^{[m]} | \psi \rangle = \sum_{i_m, i'_m=1}^{D_m} (A_{i'_m}^{[m]})^\dagger O_{i_m, i'_m} A_{i_m}^{[m]}, \quad (4.32)$$

with O the matrix representation of the operator in the basis $|i_m\rangle$.

Until now, in our description of the MPS we considered open boundary conditions, where the bond dimensions at the boundaries $D_{i_1} = D_{i_M} = 1$. If we want to use periodic boundary conditions in our models, that is, we have all tensors connected in a ring, then the representation of the MPS on a lattice with M sites will be

$$|\psi_{PBC}\rangle = \sum_{i_1, \dots, i_M=1}^D \text{Tr}(A_{[1]}^{i_1} \dots A_{[M]}^{i_M}) |i_1, \dots, i_M\rangle. \quad (4.33)$$

Here, the condition for the bond dimensions at the boundaries $D^{[1]} = D^{[M]}$ is not valid any longer.

Matrix Product Operators MPO

The generalisation of MPS to represent operators with tensor networks is called Matrix Product Operator, or MPO [42, 47, 107, 108]. The most general MPO on m sites is

$$\hat{O} = \sum_{\{i\}} \sum_{\{i'\}} A^{i_1 i'_1} A^{i_2 i'_2} \dots A^{i_M i'_M} |i_1, \dots, i_M\rangle \langle i'_1, \dots, i'_M|. \quad (4.34)$$

Graphically, we can represent an MPO the same way we do with MPS, as a product of local tensors, as depicted in Fig. 4.5(a). We also show the application of a Matrix Product Operator to a Matrix Product State, with the corresponding contraction in Fig. 4.5(b).

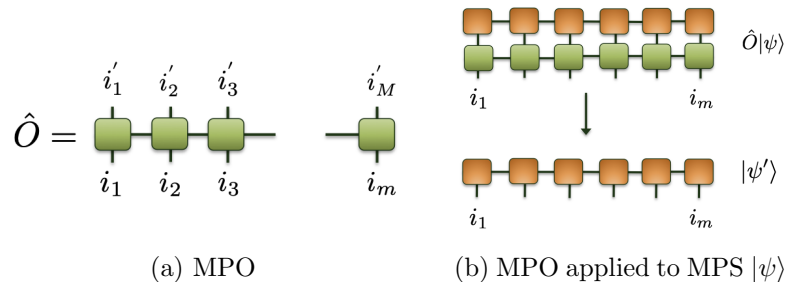


FIGURE 4.5: (a) Tensor network representation of a Matrix Product Operator for the operator \hat{O} . (b) Application of a Matrix Product Operator to a Matrix Product State, where all connected lines contract.

The use of MPOs is very effective for example to represent one-dimensional Hamiltonians, or for some time evolution algorithms, as we will see in the coming sections. Next, we present how to find the ground state of a Hamiltonian using MPS.

4.2.2 Variational search for the ground state

We use Matrix Product States as a variational ansatz for the eigenstates of a Hamiltonian expressed as a Matrix Product Operator [47]. The ground state is found by minimising the energy of the system as

$$E = \min_{|\psi\rangle} \frac{\langle \psi | \hat{\mathcal{H}} | \psi \rangle}{\langle \psi | \psi \rangle}, \quad (4.35)$$

with respect to the parameters of $|\psi\rangle$. The way the algorithm works is by introducing a Lagrange multiplier that we call Λ , that is, we need to find the minimum of the equation

$$\langle \psi | \hat{\mathcal{H}} | \psi \rangle - \Lambda \langle \psi | \psi \rangle. \quad (4.36)$$

Now we define the orthogonality center $C^{[m]}$ on site m , which we call the *active site*. We start with the expectation value $\langle \psi | \hat{\mathcal{H}} | \psi \rangle$, and optimise it to the tensor on the site m . To do so, we look for zeros to the derivative with respect to the tensor

$$\frac{\partial}{\partial C^{[m]}} (\langle \psi | \hat{\mathcal{H}} | \psi \rangle - \Lambda \langle \psi | \psi \rangle) = 0. \quad (4.37)$$

In Fig. 4.6 we show graphically the algorithm on one site. After this site is optimised, thus the minimum is found, then we do the same in the next site, and like that to all sites, finding the global minimum after one or several sweeps throughout the system, finding the ground state with energy $\Lambda \equiv E_0$.

Suzuki-Trotter decomposition [109]. We start by expressing our Hamiltonian as a sum over two-site Hamiltonians

$$\hat{\mathcal{H}}_{\text{NN}} = \sum_m^{M-1} \hat{h}_{m,m+1}. \quad (4.39)$$

The evolution operator will be ($\hbar = 1$)

$$\hat{U}_{\text{NN}}(\Delta T) = e^{-i\hat{\mathcal{H}}_{\text{NN}}\Delta T} \simeq e^{-i \sum_m^{M-1} \hat{h}_{m,m+1} \Delta T}, \quad (4.40)$$

and can be expressed as a product of individual nearest-neighbours gates

$$\hat{U}_{m,m+1}(\Delta T) = e^{-i\hat{h}_{m,m+1}\Delta T} = \prod_m e^{-i\hat{h}_{m,m+1}\Delta T} + \mathcal{O}(\Delta T^2), \quad (4.41)$$

with the error coming from the fact that the neighbours Hamiltonian do not commute with each other.

As an example, if we use the first-order Trotter decomposition as in Eq. 4.39, we will have

$$e^{(\hat{h}_m + \hat{h}_{m+1})\Delta t} \approx e^{\hat{h}_m \Delta t} e^{\hat{h}_{m+1} \Delta t}. \quad (4.42)$$

If we evolve in time by Δt , and then evolve backwards by Δt , we do not return to the initial state. To rectify this, we use the second order decomposition

$$e^{(\hat{h}_m + \hat{h}_{m+1})\Delta t} \approx e^{\hat{h}_m \frac{\Delta t}{2}} e^{\hat{h}_{m+1} \frac{\Delta t}{2}}. \quad (4.43)$$

We can always decompose $e^{\hat{h}_m + \hat{h}_{m+1}\Delta t}$ into a product of more exponential obtaining higher order Trotter expansions.

The application of TEBD to our state will be done in the same way. Two neighbouring sites are contracted on sites m and $m + 1$. We continue applying to next sites back and forth to have a second order Trotter expansion as in Eq. 4.43, depicted in Fig. 4.7. The resulting tensor on neighbouring sites is then reshaped into a matrix of dimensions $dD_L^{[m]} \times dD_R^{[m]}$ m being L and R the left and right side, respectively. Then we perform the truncation using SVD as it was explained in section 4.2.1 (see Fig. 4.8 for a representation of a single step in the algorithm).

TEBD allows time dependent simulations of large 1D quantum systems, for a Hamiltonian with local operations. This means that we can use it for our spin-1 and spin-1/2 models, introduced in chapter 3, with nearest-neighbours interactions. The main sources

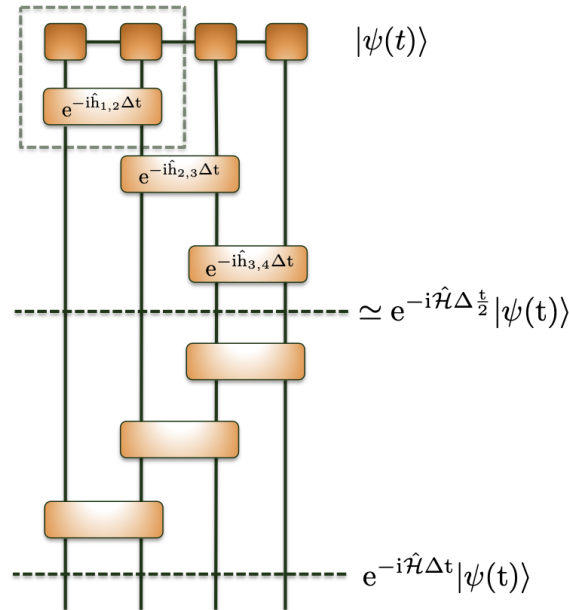


FIGURE 4.7: TEBD algorithm using Suzuki-Trotter decomposition on neighbouring sites.

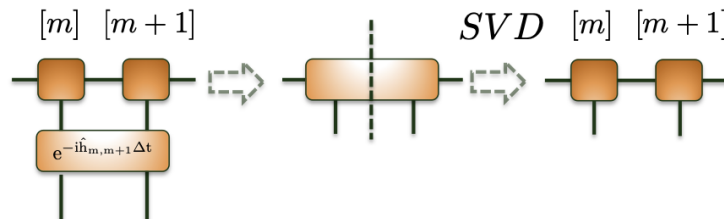


FIGURE 4.8: Two neighbouring sites are contracted, resulting in a tensor that will be reshaped to a matrix where SVD will be performed.

of error for this kind of methods come from the truncation of the Schmidt decomposition or from the Trotter expansion of the Hamiltonian, but both can be controlled and monitored.

In the next sections we will present other methods to simulate time evolution of quantum states and the application for thermal states calculations.

4.2.3.2 Time Dependent Variational Principle (TDVP)

An alternative algorithm to simulate time evolution is the Dirac-Frenkel Time-Dependent Variational Principle (TDVP) method [48], developed to avoid the Trotter errors we encounter with TEBD, mainly truncation errors when selecting the largest Schmidt coefficients (Eq. 4.29). This method also provides a solution to other kind of problems, such as thermal states, presented in the next section, and systems with long-range interactions.

The TDVP algorithm relies on the manifold interpretation of uniform matrix product states, and, in particular, the concept of a tangent space. We start with a MPS tensor time dependent $|\psi(A(t))\rangle$, where $A(t)$ is a time dependent parameter, and the state ψ belongs to a manifold of the Hilbert space, the tangent space (see Fig. 4.9). On the

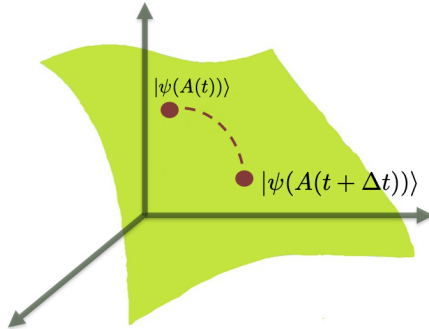


FIGURE 4.9: Sketch of the manifold where the time dependent MPS tensor lies, a subspace of the Hilbert space.

other hand, the time evolution of such a state is given by the Schrödinger equation is

$$i \frac{\partial |\psi(A(t))\rangle}{\partial t} = \hat{\mathcal{H}} |\psi(A(t))\rangle. \quad (4.44)$$

If contained in the manifold, the left-hand side is a tangent vector

$$i \frac{\partial |\psi(A(t))\rangle}{\partial t} = |\Phi(\dot{A}; A)\rangle, \quad (4.45)$$

where $\dot{A}(t)$ is a highly non-linear differential equation for the MPS tensor

$$\dot{A}(t) = f(A(t)), \quad (4.46)$$

but the right-hand side is out of the manifold. This is corrected with TDVP, where we project the time evolution into the tangent space

$$i\hbar \frac{\partial |\psi(A(t))\rangle}{\partial t} = P_{|\psi(A(t))\rangle} \hat{\mathcal{H}} |\psi(A(t))\rangle, \quad (4.47)$$

thus

$$|\Phi(\dot{A}; A)\rangle = -iP_{|\psi(A(t))\rangle} \hat{\mathcal{H}} |\psi(A(t))\rangle. \quad (4.48)$$

Eventually, we want to find $|\Phi(\dot{A}; A)\rangle$ that minimises the function

$$\left\| iP_{|\psi(A(t))\rangle} \hat{\mathcal{H}} |\psi(A(t))\rangle - |\Phi(\dot{A}; A)\rangle \right\|, \quad (4.49)$$

which surprisingly is very similar to the way we calculated ground states in section 4.2.2.

The most successful application of TDVP is the idea of using a Trotter decomposition of the projector on the tangent space $P_{|\psi(A(t))\rangle}$ defined as a MPO. Here, we use imaginary-time evolution corresponding to a steepest-descent optimization scheme using the tangent-space gradient. This process is very similar to what was explained in section 4.2.2. The Hamiltonian will be the effective Hamiltonian reshaped after removal of the site m , and where we evolve the vector ν_m in time as

$$\nu_m(t + \Delta t) = e^{-i\hat{\mathcal{H}}_{\text{EFF}}\Delta t}\nu_m(t). \quad (4.50)$$

In Fig. 4.10 we sketch the whole process for a better understanding of how the algorithm works.

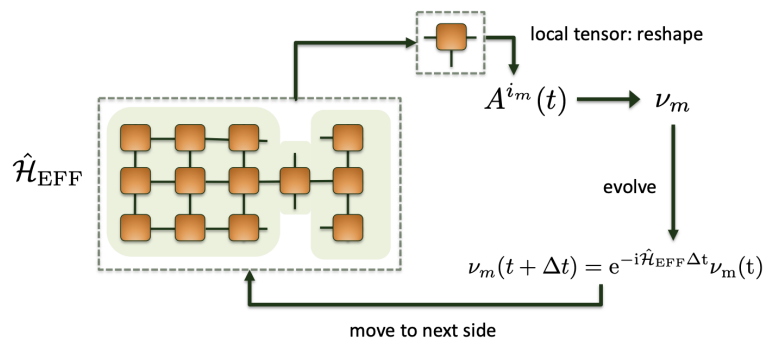


FIGURE 4.10: Representation of the TDVP algorithm to evolve in imaginary time evolution the reshaped vector ν_m from a local site m . This method relies in the same principles as the variational search for the ground state explained in section 4.2.2.

We have now presented the background on MPS and MPOs, introduced a method to find the ground state of the Hamiltonian, and described two different time evolution algorithms with MPS and MPOs. Another example of time-dependent algorithm that we used for some calculations is the application of Runge-Kutta-like method with MPS [110]. However, we do not go into details as we found in some preliminary results, for our particular problems, that with Runge-Kutta there was not satisfactory convergence with the corresponding ED results. Next, we will apply TDVP to simulate thermal states, which will be used for the results in section 5.4.2.

4.2.4 Finite temperature algorithm: The Ancilla method

The approach we use to calculate thermal states involves the evolution of initial infinite temperature density matrix to finite temperatures by means of the Time-Dependent Variational Principle (TDVP) method described in the previous section. It is called the Ancilla method [47, 111] based on purification [45, 112].

At finite temperature, the quantum system state is given by the thermal density matrix

$$\hat{\rho}_{\text{th}} = \frac{e^{-\beta\hat{H}}}{Z}, \quad (4.51)$$

with Z the partition function. We start by defining the density matrix in MPO form. At the initial point of the evolution the system is considered at infinite temperature, i.e. its density matrix is proportional to the identity

$$\rho_0 \propto \mathbb{1}, \quad (4.52)$$

where all states have equal probability of occupation. Then, the next step is to evolve the density matrix to finite temperatures

$$\hat{\rho}(\beta) \propto e^{-\beta\hat{H}}. \quad (4.53)$$

We use a purification technique to preserve positive semi-definiteness (all eigenvalues have to be ≥ 0) of the density matrix ($\hat{\rho}(\beta) = \hat{\rho}(\beta)^\dagger$), and this technique rewrites $\hat{\rho}$ as

$$\hat{\rho}(\beta) \propto e^{-\beta\hat{H}/2} \rho_0 e^{-\beta\hat{H}/2}. \quad (4.54)$$

The purification technique relies in reshaping the density matrix (MPO) into a pure state (MPS), and since

$$\hat{\rho}_0 = \hat{\rho}_0^2 = \hat{\rho}_0 \hat{\rho}_0^\dagger, \quad (4.55)$$

only one side of the above expression needs to be evolved, thus

$$\bar{\rho}(\beta) \equiv \frac{e^{-\beta\hat{H}/2}}{\sqrt{Z}} \hat{\rho}_0. \quad (4.56)$$

We perform our numerical simulations by performing an evolution on β in the formula from Eq. 4.51, with the state

$$|\psi(\beta)\rangle = e^{-\beta\hat{H}/2} |\psi(0)\rangle. \quad (4.57)$$

The evolution of the physical sites is realized via TDVP methods with imaginary time evolution, as described in the previous section. In Fig. 4.11 we summarised the process for this method. The thermal expectation value of an arbitrary operator \hat{O} can be then obtained as

$$\langle \hat{O} \rangle_\beta = \frac{\text{tr}[\hat{O} \bar{\rho}(\beta) \bar{\rho}^\dagger(\beta)]}{\text{tr}[\bar{\rho}(\beta) \bar{\rho}^\dagger(\beta)]}. \quad (4.58)$$

We have all elements to understand how the time evolution of a state can be done using MPS and MPOs. In this section we have applied imaginary time evolution using the

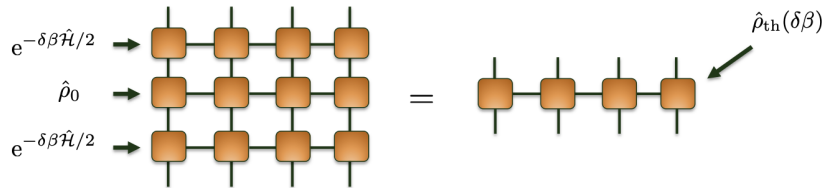


FIGURE 4.11: We reshape the density matrix (MPO) into a MPS and evolve in imaginary time evolution the contracted vector for each local site. Then we evolve using Trotter gates to the next site. This method relies in the same method described in section 4.2.3.2.

TDVP algorithm to evolve thermal states and calculate thermal expectation values. We can also use TDVP methods in Hamiltonians with long-range interaction, as we will see in Chapter 7.

Until now we have discussed numerical algorithms for closed quantum systems which means that these systems are isolated from the environment. In reality, however, systems are not fully isolated, and we must consider its interaction with the environment. Last section of this chapter is devoted to open quantum systems and a very successful numerical tool to capture the physics of quantum systems in the presence of dissipation into the environment, quantum trajectories.

4.3 Open quantum systems

When describing the coupling of a quantum system with its environment, we typically consider the system much smaller than the environment. When we describe a global system of our system and its environment, the Hamiltonian contains three terms

$$\hat{\mathcal{H}} = \hat{\mathcal{H}}_{\text{SYS}} + \hat{\mathcal{H}}_{\text{ENV}} + \hat{\mathcal{H}}_{\text{INT}}, \quad (4.59)$$

where $\hat{\mathcal{H}}_{\text{SYS}}$ describes the quantum system, $\hat{\mathcal{H}}_{\text{ENV}}$ the environment, and $\hat{\mathcal{H}}_{\text{INT}}$ the interaction, that we assume to be a weak coupling between the two. In Fig. 4.12(a) we show a diagram of an open quantum system.

We denote the state of our system, a pure state, as

$$|\psi\rangle = |\psi\rangle_{\text{SYS}} \otimes |\psi\rangle_{\text{ENV}}. \quad (4.60)$$

We are interested in the dynamics of the quantum system, and therefore we trace out the environment, obtaining the density matrix for the system

$$\hat{\rho}_{\text{SYS}} = \text{Tr}_{\text{ENV}}(|\psi\rangle \langle\psi|), \quad (4.61)$$

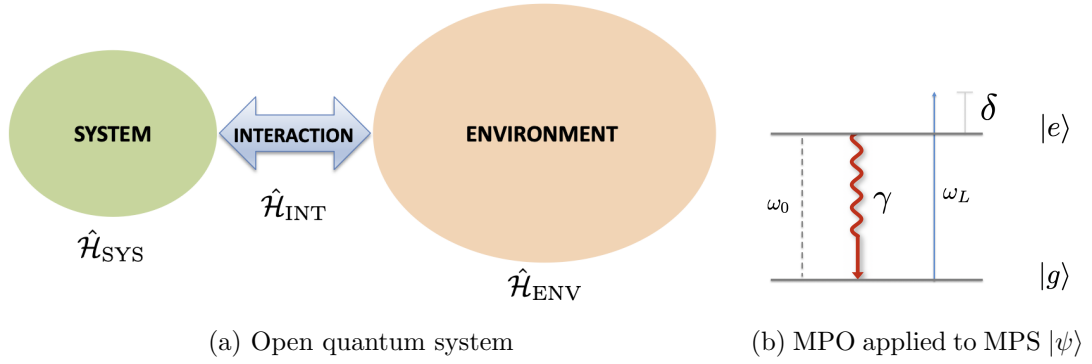


FIGURE 4.12: (a) Full diagram of an open quantum system showing the different terms in the Hamiltonian. (b) In a two level system, the interaction with the environment occurs with an amplitude γ , with $\gamma \ll \omega_0$, being ω_0 the atomic transition. In this scheme, the external field is ω_L and δ is the detuning.

which will become mixed. Next, we introduce the master equation to describe the evolution of our open quantum system.

4.3.1 The Master Equation

Without going into the details of the derivation of the general master equation for open quantum systems [49, 113], a summary of the approximations used in quantum optics is provided:

- Rotating wave approximation (RWA): the non-conserving energy terms can be neglected.
- Born approximation: The coupling between the system and the environment is typically weak, loosely speaking: $\|\hat{\mathcal{H}}_{\text{INT}}\| \ll \|\hat{\mathcal{H}}_{\text{ENV}}\|, \|\hat{\mathcal{H}}_{\text{SYS}}\|$. Therefore, the coupling is weak in comparison with the system and environment energy scales.
- Markov Approximation: The environment relaxes back to its thermodynamical equilibrium and provides a response to the system before any other event takes place in the system. Hence, the environment is unchanged in time.

The resulting markovian master equation in Lindblad form will be (here $\hat{\rho} \equiv \hat{\rho}_{\text{SYS}}$ for simplification)

$$\frac{d}{dt}\hat{\rho} = -\frac{i}{\hbar}[\hat{\mathcal{H}}, \hat{\rho}] - \mathcal{L}[\hat{\rho}], \quad (4.62)$$

with \mathcal{L} the Lindbladian operator with a set of “jump operators” acting on the system coupling it with the environment. Expanding the Lindbladian operator we get

$$\frac{d}{dt}\hat{\rho} = -\frac{i}{\hbar}[\hat{\mathcal{H}}, \hat{\rho}] - \frac{1}{2} \sum_m \gamma_m [\hat{C}_m^\dagger \hat{C}_m \rho + \rho \hat{C}_m^\dagger \hat{C}_m - 2\hat{C}_m \rho \hat{C}_m^\dagger], \quad (4.63)$$

with γ_m the dissipation rate on site m (although we could consider dissipation processes affecting more than one site, here we study local processes), and \hat{C}, \hat{C}^\dagger the “jump operators”.

The computation of the master equation is extremely heavy, as the density matrix has a dimension $\dim(\hat{\rho}) = \dim(\hat{\mathcal{H}}) \times \dim(\hat{\mathcal{H}})$. We use a method based on quantum trajectories to overcome this issue, and it will be described next.

4.3.2 Quantum Trajectories and the quantum jump approach

The idea of quantum trajectories [50] is based on mapping the evolution of the open quantum system into an stochastic process. These techniques involve rewriting the master equation as a stochastic average over individual trajectories of pure states, evolved in time numerically [51]. Thus, we do not evolve the density matrix using the master equation, but instead we simulate probabilistic events (i.e. “quantum jumps”) by computing a state $|\phi(t)\rangle$ evolved under a non-Hermitian Hamiltonian. Firstly, we rewrite Eq. 4.63 as ($\hbar = 1$)

$$\frac{d}{dt}\hat{\rho} = -i(\hat{\mathcal{H}}_{\text{eff}}\hat{\rho}(t) - \hat{\rho}(t)\hat{\mathcal{H}}_{\text{eff}}^\dagger) + \sum_m \gamma_m \hat{C}_m \hat{\rho} \hat{C}_m^\dagger, \quad (4.64)$$

where the effective non Hermitian Hamiltonian for the dissipative system is

$$\hat{\mathcal{H}}_{\text{eff}} = \hat{\mathcal{H}} - \frac{i}{2} \sum_m \gamma_m \hat{C}_m^\dagger \hat{C}_m. \quad (4.65)$$

We start constructing the stochastic process by expanding the master equation to first order in a time step δt . We will then evolve individual trajectories of $|\phi(t)\rangle$. To evaluate the value of any observable, we will average over the trajectories.

Step 1: evolve the state $|\phi(t)\rangle$ according to the effective Hamiltonian for a small time δt :

$$|\phi_1(t + \delta t)\rangle = e^{-i\hat{\mathcal{H}}_{\text{eff}}\delta t} |\phi(t)\rangle. \quad (4.66)$$

In order to normalise the state (as $\hat{\mathcal{H}}_{\text{eff}}$ is not hermitian), as δt is small

$$\begin{aligned} \langle \phi_1(t + \delta t) | \phi_1(t + \delta t) \rangle &\approx \langle \phi(t) | (\mathbb{1} + i\hat{\mathcal{H}}_{\text{eff}}^\dagger \delta t) (\mathbb{1} - i\hat{\mathcal{H}}_{\text{eff}} \delta t) | \phi(t) \rangle \\ &\approx \langle \phi(t) | \phi(t) \rangle - i\delta t \langle \phi(t) | \hat{\mathcal{H}}_{\text{eff}} - \hat{\mathcal{H}}_{\text{eff}}^\dagger | \phi(t) \rangle \\ &= 1 - \delta p, \end{aligned} \quad (4.67)$$

assuming the initial state $|\phi(t)\rangle$ was normalised, and with

$$\delta p = i\delta t \langle \phi(t) | \hat{\mathcal{H}}_{\text{eff}} - \hat{\mathcal{H}}_{\text{eff}}^\dagger | \phi(t) \rangle = \delta t \sum_m \gamma_m \langle \phi(t) | \hat{C}_m^\dagger \hat{C}_m | \phi(t) \rangle = \sum_m \delta p_m, \quad (4.68)$$

where δp_m is the probability that the action of \hat{C}_m will take place at this time step.

Also, δt needs to be small enough so that $e^{-i\hat{\mathcal{H}}_{\text{eff}}\delta t} \approx \mathbb{1} - i\hat{\mathcal{H}}_{\text{eff}}\delta t$ and $\delta p \ll 1$.

Step 2: The ‘‘Gedanken’’ experiment of a possible quantum jump, introducing the stochastic aspect of the method.

Firstly, we choose a random number

$$0 \leq \epsilon \leq 1, \quad (4.69)$$

if $\delta p \geq \epsilon$ (probability $1 - \delta p$, thus, mostly of the times): No jump occurs. We normalise the state:

$$|\phi(t + \delta t)\rangle = \frac{|\phi_1(t + \delta t)\rangle}{\sqrt{1 - \delta p}}, \quad (4.70)$$

if $\delta p < \epsilon$ (probability δp): A jump occurs.

$$|\phi(t + \delta t)\rangle = \frac{\hat{C}_m |\phi(t)\rangle}{\sqrt{\delta p_m / \gamma_m \delta t}}. \quad (4.71)$$

Then we can proceed to the next time step and apply step 1 onto the state $|\phi(t + \delta t)\rangle$.

Now, having $N \gg 1$ copies $|\phi_n(t)\rangle$ of the state $|\phi(t)\rangle$, with a chosen random number for each ($\epsilon_n \in [0, 1]$), we will get N' times a jump and $N - N'$ times no jump. Then, as $N \rightarrow \infty$,

$$\frac{N'}{N} \rightarrow \frac{\delta p}{1} = \delta p, \quad (4.72)$$

that is, δp is the probability that a jump happens.

We repeat the steps above until we covered the whole time range $t = n\delta t$, and the evolution is the quantum trajectory.

By doing the same procedure L times, we get L trajectories. and the result averaged over all trajectories is exactly the evolution described by the master equation with the corresponding reduced density operator

$$\hat{\rho}(t) = \frac{1}{L} \sum_{k=1}^L |\phi_k(t)\rangle \langle \phi_k(t)|. \quad (4.73)$$

4.4 Summary

In this chapter we have described the computational methods that we use to calculate the main results provided in this thesis. We have seen that Exact Diagonalisation is constrained to smaller systems. To attain larger system sizes we need to use powerful numerical techniques, and one of the most flexible and effective algorithms is the Density Matrix Renormalisation Group (DMRG). The combination of DMRG with tensor network representation using MPS and MPOs have made numerically possible the computation of ground states and time evolution of one-dimensional quantum systems. In the last years a lot of progress has been made to develop numerical tools to simulate quantum systems in higher dimensions, such as Projected Entangled Pairs States (PEPS) [41] or Multi-scale Entanglement Renormalisation Ansatz (MERA) [114].

In chapter 5, we calculate the energy of the ground state of both the spin-1 and the spin-1/2 model, and we compare it with the energy of a quenched state, in section 5.2. We use the variational search method to evaluate these calculations in larger systems. This approach is used to evaluate ground states also in chapter 6, both for the initial and target states of the adiabatic ramps, and the evaluation of the Quantum Fisher Information in section 6.4.

We evaluate the dynamics of these systems in chapter 5, where we use the TEBD algorithm in section 5.3. Furthermore, in section 5.4, we also study finite temperature states where we implement the Ancilla method based on imaginary time evolution and TDVP. Another example of calculations done with the TDVP algorithm is the simulation of spin currents to probe the quantum states at the end of chapter 5, in section 5.5. Additionally, TDVP is also used to simulate systems with long-range interactions in chapter 7.

Additionally, ED is normally sufficient for small systems. However, TEBD is implemented for bigger number of atoms in most of the ramps evaluated in chapter 6. We have also introduced the methodology of using quantum trajectories to evolve the master equation in open quantum systems. This approach is used when we consider dissipation in our systems, at the end of chapter 6, in section 6.4.4.

Chapter 5

Engineering magnetic ordering of rotated spin states and probing dynamics in quantum simulators

In this chapter¹ we explore the properties and dynamics of non-equilibrium states by applying a rotation to the spins from a low-entropy initial state with all spins initially aligned. We want to study the XY-ferromagnet, to see how different it is from a mean-field description when the spins are in the xy-plane. Furthermore, we want to quantify how far this mean-field description is from the ground state as a function of the anisotropy (consequence of inter-species interactions) in the effective spin models. We compare the energy of the rotated state with that of the ground state, the correlation length in a thermal state, and the out-of-equilibrium dynamics. We also evaluate alternative ways to probe the state by investigating the behaviour of the spin current.

We start with all of the spins up and rotate them into the xy-plane, in the so-called counterflow superfluid regime. When the anisotropy is 0, interactions are equal in all directions. In these regimes sometimes we obtain a XX model that can be transformed to non-interacting fermions. At a higher anisotropy the characteristics of the spin superfluid will be more visible, and this is exactly our focus.

In the spin-1/2 model for $\Delta/J > 0$, irrespective of the value, the system remains in the ferromagnetic phase. However, in the case of the spin-1, the ferromagnetic phase exists until a critical value of u/J , where we enter the spin-Mott phase. These phase diagrams were discussed in section [3.2.1](#).

¹This work is taken in part from the publication [\[54\]](#), but with additional data and some restructuring of the presentation. The author of this thesis performed all of the calculations for the models and produced all of the plots.

In this chapter, we will first discuss the preparation of the spin-rotated states, and then study their differences to true XY-ferromagnetic ground states in section 5.2. Secondly, in 5.3, we study the dynamics of the system and analyze the dynamically prepared states, as function of the anisotropies. In section 5.4 we compare the dynamically prepared states to the corresponding thermal states and we analyse where thermalisation occurs in the systems. Lastly, we discuss methods to probe these states by observing spin currents of bosons in an optical lattice in section 5.5.

For all following sections, the Hamiltonians are the ones presented in chapter 3:

$$\hat{\mathcal{H}}_{\text{SP1}} = -J \sum_{\langle j,l \rangle} \hat{\mathbf{S}}_j \hat{\mathbf{S}}_l + u \sum_l (\hat{S}_l^z)^2, \quad (5.1)$$

for the spin-1, and

$$\hat{\mathcal{H}}_{\text{SP1/2}} = -J \sum_{\langle j,l \rangle} \hat{\mathbf{s}}_j \hat{\mathbf{s}}_l + \Delta \sum_{\langle j,l \rangle} \hat{s}_j^z \hat{s}_l^z, \quad (5.2)$$

for the spin-1/2.

5.1 Preparation of spin rotated states

In a classical picture, the XY-ferromagnet could be prepared by beginning with all of the spins aligned along the z-axis ($|\psi_0\rangle = |\uparrow\uparrow\uparrow\uparrow\uparrow\uparrow\dots\rangle$), and then rotating that state locally towards the xy-plane, on every atom simultaneously.

We want to study the quantum case, defining the rotation operator as

$$\hat{R}_x = \prod_j e^{-i\frac{\pi}{2}\hat{S}_j^x}, \quad (5.3)$$

so that the rotated state will be

$$|\psi_r\rangle = \hat{R}_x |\psi_0\rangle, \quad (5.4)$$

where all spins will point along the y-axis. This rotation operation is calculated analogously for the spin-1/2 with operator \hat{s}_j^x . Fig. 5.1 illustrates the idea of this rotation operation.

The goal is to evaluate how close the state obtained by this procedure is to the ground state of the anisotropic model.

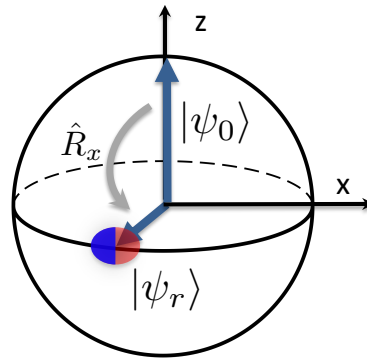


FIGURE 5.1: In the Bloch Sphere, a rotation from the z-axis towards the xy-plane is represented by the rotation operator $\hat{R}_j = e^{-i\hat{S}_j^x \phi}$ with $\phi = \frac{\pi}{2}$.

5.2 Comparison of the rotated state with the ground state

As notated in the introduction to this chapter, we would like to study a XY-ferromagnet, to see how different it is from a mean-field when they are in the xy-plane. Furthermore, we want to quantify how far this mean-field picture is from the ground state depending on the values of the anisotropies u/J and Δ/J , respectively.

The energy difference between the rotate state $|\psi_r\rangle$ and the ground state of the system is computed as $\Delta E = E_r - E_{GS}$ per spin of the two states, using MPS representation.

It is important to notice that the Hamiltonians (spin-1 and spin-1/2) are significantly different and therefore their energy scales are difficult to compare directly. Fig. 5.2 shows ΔE for various values of the anisotropy (u/J and Δ/J) for spin-1 and spin-1/2, respectively. There is no energy difference for a zero anisotropy (this is expected, as the rotated state belongs to the highly degenerate ground state manifold), and the result gives something very close to the ground state for small values of $u/J, \Delta/J$ in each case. The energy difference increases with the anisotropy. Furthermore, the difference of energy per spin for a given anisotropy decreases until it converges to a constant for sufficiently large lattice sizes. It is important to notice that the energy difference in spin-1/2 is five times the one for the spin-1.

Naturally, the energy difference only gives us a first indication of similarities or differences between the rotated state and the ground states. In the next sections we will study the evolution of the correlation functions, and the behaviour of spin currents induced in the system.

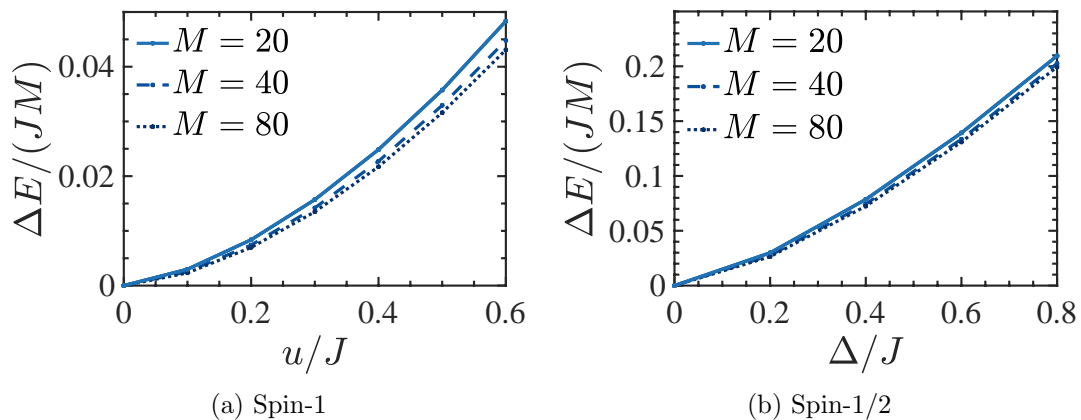


FIGURE 5.2: Energy difference per particle between the reference state (rotated state) and the ground state of the Hamiltonian, for different systems sizes M and different anisotropy $u/J, \Delta/J$, for the effective (a) spin-1 and (b) spin-1/2 models of two-component bosons on an optical lattice. As the anisotropy increases, the energy difference increases, in both models. This is expected as for a zero anisotropy, the rotated state belongs to the highly degenerate ground state manifold. [The bond dimension used for the MPS calculations was $D = 64$, with open boundary conditions.]

5.3 Exploring properties of states by out-of-equilibrium dynamics

One interesting question for probing the properties of the model in out-of-equilibrium dynamics could be to evaluate the difference of a specific magnetic model to the mean-field approximation of the same model. In the previous work done by Barnettler et al. in [116], they start with a perfect Néel state evolving under a Heisenberg antiferromagnet Hamiltonian. As a result of the dynamics, the magnetic ordering decays exponentially.

We now study the out-of-equilibrium dynamics after a preparation of $|\psi_r\rangle$ as in Eq 5.4, in particular we will focus on the dynamics of spin-spin correlations in the system. The quench dynamics in this system, in which all spins are initially prepared aligned along the z-axis, followed by having a product state of spins rotated into the xy-plane (say, $|\rightarrow\rangle$), is an easily realisable experimental sequence. Then the dynamics are allowed to proceed under the Hamiltonians 5.1 and 5.2.

We are able to compute the dynamics using exact diagonalisation for small chain lengths. For larger systems there are different ways to compute the time evolution of a Hamiltonian. To handle this many-body problem numerically, a Density Matrix Renormalisation Group (DMRG) code is implemented, by using Matrix Product States (MPS) representation. To keep the time-scale required for the numerical calculations manageable, we truncate it by defining a maximum value bond dimension D . The method used here for the time evolution is the Time Evolving Block Decimation (TEBD) algorithm, which is a specific time-dependent DMRG method (for more details about this algorithm see

section 4.2.3.1). For these calculations, the convergence in the MPS bond dimension D and time step Δt was tested to ensure accuracy of the calculations. All calculations were performed with fourth order Trotter expansion of the time evolution operator. The convergence studies for these results are summarised in Appendix A.

In figures 5.3 and 5.4 (for spin-1 and spin-1/2, respectively), we evaluate different spin-spin correlations, as well as the bipartite entanglement entropy, that is, the half-chain entanglement entropy, during the evolution, defined as

$$S_{\text{vN}}(\hat{\rho}_{M/2}) = -\text{Tr} \hat{\rho}_{M/2} (\log_2 \hat{\rho}_{M/2}), \quad (5.5)$$

where $\hat{\rho}_{M/2} = \text{Tr}_{M/2} |\psi\rangle \langle \psi|$ is the reduced density matrix for the half of the system.

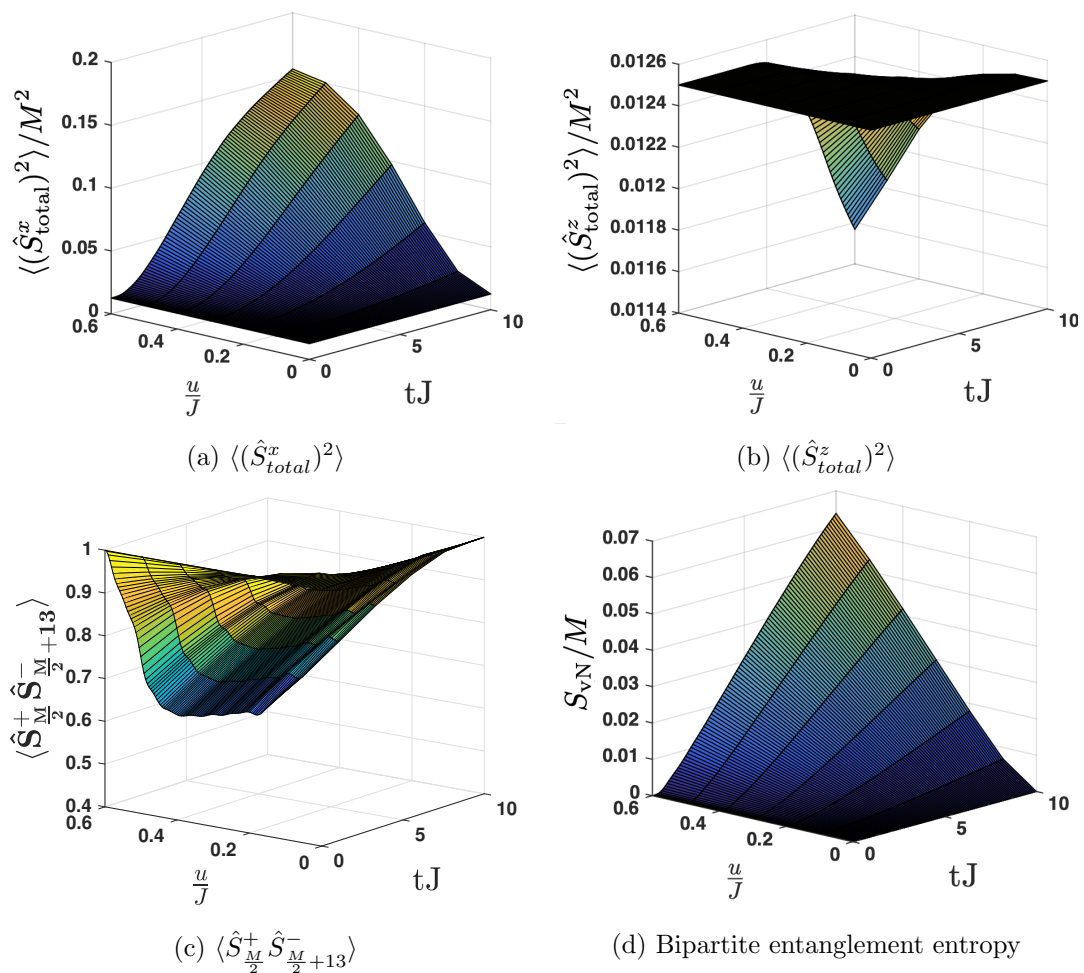


FIGURE 5.3: Spin-1 model: Evolution of different observables for $M = 40$ and different values of the anisotropy u/J . (a) The $\langle (\hat{S}_{\text{total}}^x)^2 \rangle$ correlations increase with time, being more noticeable at higher anisotropy values. (b) The total $\langle (\hat{S}_{\text{total}}^z)^2 \rangle$ correlations only show a small decrease at the end of the evolution, for $u \geq 0.2$. (c) The value of the $\langle \hat{S}_{M/2}^+ \hat{S}_{M/2+13}^- \rangle$ correlations show a decay with time, and more accentuated as the anisotropy increases. (d) The von Neumann entropy per particle increases linearly with time, showing a smooth monotonic increase. [Numerical parameters are $Jdt = 0.1$ and $D = 128$.]

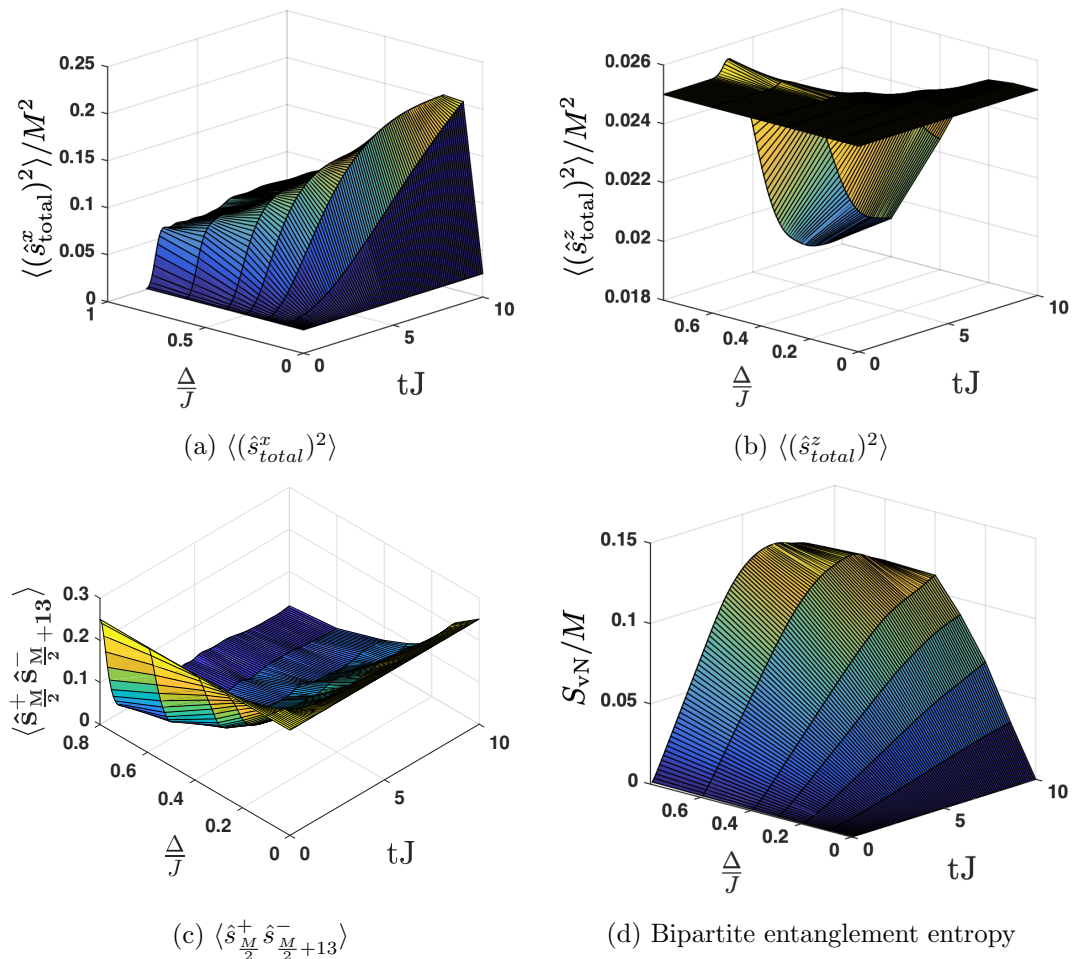


FIGURE 5.4: Spin-1/2 model: Evolution of different observables for $M = 40$, and different values of the anisotropy Δ/J . (a) The $\langle (\hat{s}_{total}^x)^2 \rangle$ correlations increase with time, and the steepness decreases with higher values of the anisotropy. (b) The total $\langle (\hat{s}_{total}^z)^2 \rangle$ correlations decrease at the end of the evolution, for $\Delta \geq 0.2J$. (c) The value of the $\langle \hat{S}_{M/2}^+ \hat{S}_{M/2+13}^- \rangle$ correlations show a decay with time, more noticeable as the anisotropy increases. (d) The von Neumann entropy increases linearly with time and anisotropy. The maximum value of the von Neumann entropy per particle remains the same from $\Delta = 0.4J$ with a value of $S/M \simeq 0.125$. [Numerical parameters are $Jdt = 0.1$ and $D = 256$.]

For the $\langle (\hat{S}_{total}^x)^2 \rangle$ correlations, in the spin-1 model, we see an increase with both anisotropy and time. For the spin-1/2 this increase is accentuated for small anisotropies with time. The $\langle (\hat{S}_{total}^z)^2 \rangle$ correlations decrease with time and anisotropy in both models. We evaluate the $S^+ \hat{S}^-$ from the middle of the system and taking away the boundaries, hence the $\langle \hat{S}_{M/2}^+ \hat{S}_{M/2+13}^- \rangle$. These correlations decay to only $\approx 50\%$ of the initial value at high anisotropy for the spin-1. However, for the spin-1/2 case, the correlations scramble really quickly, faster for a higher Δ/J . This also corresponds with the previous results where we looked at the energy difference, showing that the spin-1/2 is much farther from the ground state with the anisotropy. The von Neumann entropy of the subsystem increases linearly with time for both models. For the spin-1/2 we see the effect of

the quasi-oscillations that grow with entanglement. This behaviour is explained as the group velocity of quasiparticle excitations in the system will have a maximum giving rise to the so called Lieb-Robinson bound [117], defining an effective light cone for spatial correlations, outside of which the correlations are exponentially suppressed [118]. At larger system sizes ($M \geq 30$) the boundary “echos” of this light cone appear later and therefore the oscillations disappear, that is why we see this monotonic behaviour at larger anisotropies.

Then we study how the correlations evolve with distance, in different snapshots in time. We evaluate the correlation functions calculated as

$$\Theta_j = |\overline{\langle S_i^+ S_{i+j}^- \rangle}| = \frac{1}{M - 2b - j} \sum_{i=1+b}^{M-b-j} |\langle \hat{S}_i^+ \hat{S}_{i+j}^- \rangle|, \quad (5.6)$$

where i denotes the index of the site, j is the distance or number of sites, and $b = M/5$ is a number of sites at the boundary that we omit to reduce the open boundary effects. The operation is calculated analogously for the spin-1/2 with operators $\hat{s}_i^+, \hat{s}_{i+j}^-$.

Fig. 5.5 shows the correlation function as a function of distance at different times, together with the correlations in the ground state for the time evolution of a lattice of 100 sites. In both models, the correlations decay faster in time with increasing anisotropy. However, in the spin-1/2 this decrease of the correlations occurs much faster, and for $\Delta = 0.8J$ the magnetic ordering vanishes very quickly. In the spin-1 case, for $u = 0.2J$ the decay of the correlations at $tJ = 4$ is minimal, indicating that for a small value of the anisotropy u/J the magnetic order remains under time evolution. For $u = 0.6J$, in contrast, the correlations decay faster with time, but still preserve the magnetic ordering at long distances. In the spin-1/2 case, even for a small value of the anisotropy $\Delta/J = 0.2$ we can see how the correlations decrease quickly on the time-scale of a few tunnelling times. For $\Delta/J = 0.8$, the spin-ordering vanishes rapidly to zero. From these results, we realised that the effect of the out-of-equilibrium dynamics is much more accused for the spin-1/2 model. Again, we consider this is due to the fact that the spin-1 model is closer to the classical model than the spin-1/2 one.

5.4 Thermal states

Before presenting the results for the corresponding thermal states, we introduce some general concepts from Statistical Mechanics, which are necessary to understand how the correlation lengths and entropies in the models are calculated.

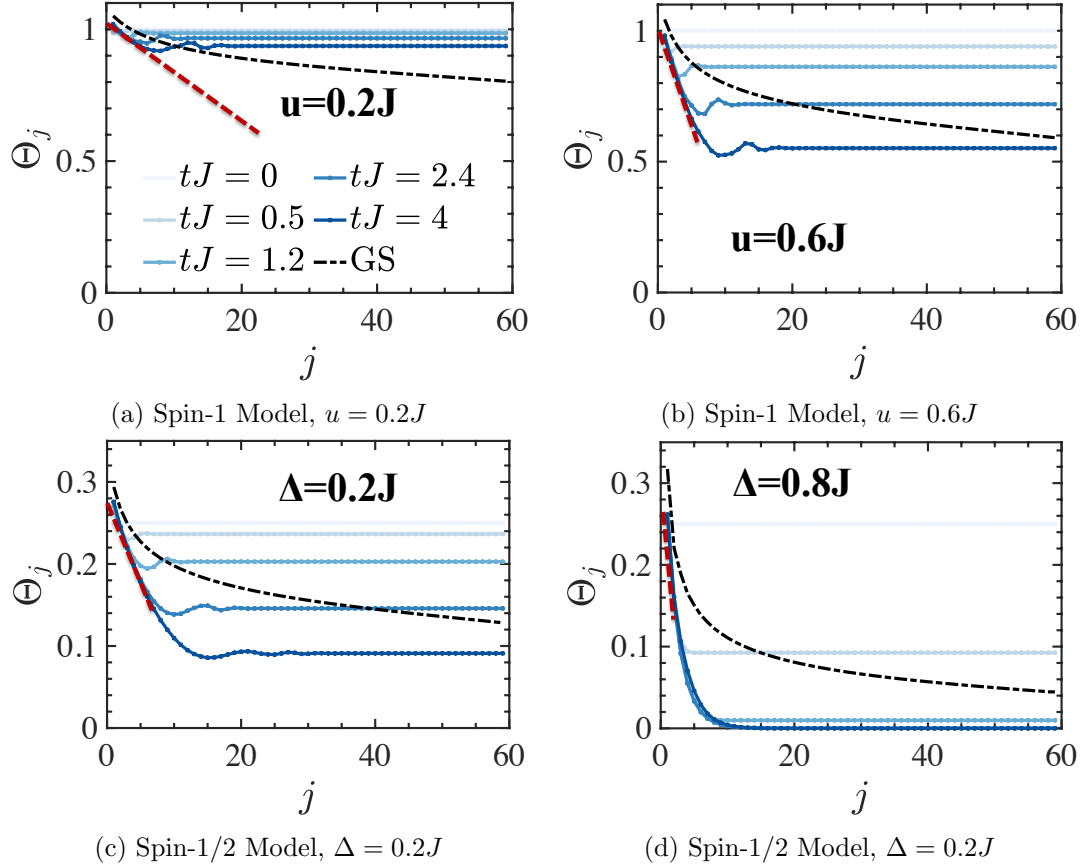


FIGURE 5.5: Comparison of the decay of the correlations with distance at different snapshots in the time evolution ($tJ = 0$, $tJ = 0.5$, $tJ = 1.2$, $tJ = 2.4$, $tJ = 4$). The black dash-dotted line indicates the value of the correlations for the ground state (GS) of the corresponding Hamiltonian. Results are for the spin-1 (a,b) and spin-1/2 (c,d) model, respectively. The different panels contrast the evolution for different anisotropies. The dashed black lines indicate the algebraic decay of the correlations in the ground state. The red dashed lines indicate a fit to the initial decay of the corresponding thermal states with the correlation lengths calculated in Fig. 5.11. The calculation were done for a system size $M = 100$, bond dimension for the MPS calculations $D = 128$, and open boundary conditions.

5.4.1 Background: Statistical Mechanics

For a closed system in contact with a heat bath at temperature T , the probability of finding the system in a given micro-state of energy E_i is proportional to the Boltzmann factor [119]

$$p(E_i) \propto e^{-\frac{E_i}{k_B T}} = e^{-\beta E_i}, \quad (5.7)$$

with k_B the Boltzmann constant, and $\beta = 1/(k_B T)$.

The absolute probability can be found by normalising the Boltzmann factor over the sum of all possible micro-states

$$p(E_i) = \frac{e^{-\beta E_i}}{Z}, \quad (5.8)$$

where Z is the partition function

$$Z = \sum_i e^{-\beta E_i}, \quad (5.9)$$

which describes the statistical properties of a system in thermodynamic equilibrium, representing a particular statistical ensemble (with a particular free energy).

Individual states with lower energy will always have a higher probability of being occupied than the ones with higher energy.

The entropy of the ensemble will be

$$S = -k_B \sum_i P_i \ln P_i, \quad (5.10)$$

where P_i is simply the probability of the ensemble being in the i th microstate.

The maximum entropy possible in any system is at infinite temperature, when all states are equally probable. In our spin-1/2 system, we have 2^M states, hence this will occur with probability $\frac{1}{2^M}$ at infinite temperature, thus

$$S = - \sum_{i=1}^{2^M} P_i \ln P_i = - \sum_{i=1}^{2^M} \left(\frac{1}{2^M}\right) \ln\left(\frac{1}{2^M}\right) = M \ln 2. \quad (5.11)$$

Therefore, by calculating the entropy per spin, we know that the largest possible entropy per spin is $\ln 2 = 0.6931$ for spin-1/2. For the spin-1 model, we have 3^M states, with probability $\frac{1}{3^M}$ at infinite temperature and largest possible entropy per spin $\ln 3 = 1.0986$ for spin-1.

When the distance r between spins is very small, the interaction between them can generally induce correlations, such that for an ideal XY-ferromagnetic ground state we expect algebraically decaying correlations. However, this effect will be destroyed by thermal effects: at high temperatures, spin orientations become randomized, and we generally expect correlations which exponentially decrease with increasing distance r ,

$$\langle \hat{S}_i^+ \hat{S}_{i+j}^- \rangle \propto e^{-\frac{r}{\xi(T)}}, \quad (5.12)$$

with ξ the correlation length, which tells us how fast the correlation function vanishes. The operation is calculated analogously for the spin-1/2 with operators $\hat{s}_i^+, \hat{s}_{i+r}^-$.

The density matrix is defined as

$$\hat{\rho} = \sum_i P_i |\psi\rangle_i \langle \psi|_i. \quad (5.13)$$

At finite temperature, the state of a quantum system is given by the thermal density matrix

$$\hat{\rho}_{\text{th}} = \frac{e^{-\beta\hat{H}}}{Z}. \quad (5.14)$$

We can then calculate the correlations by using the relation

$$\langle \hat{O} \rangle = \text{tr}(\hat{O}\hat{\rho}_{\text{th}}) = \sum_i P_i \langle \psi |_i \hat{O} | \psi \rangle_i, \quad (5.15)$$

where \hat{O} is an operator, in our case, the $\hat{S}_i^+ \hat{S}_{i+r}^-$ correlations.

To calculate the entropy S we use the standard formula from statistical mechanics:

$$F = U - TS, \quad (5.16)$$

where F is the free energy

$$F = -k_B T \ln Z, \quad (5.17)$$

and U the internal energy

$$U = -\frac{\partial}{\partial \beta} \ln Z. \quad (5.18)$$

We investigate here the regimes where the correlation functions decay exponentially, characterising a thermal state. In our analysis we study the correlation length ξ as a function of the entropy (temperature) of the system, for different number of spins.

5.4.2 Results for thermal states

Our approach for calculating thermal states involves imaginary time evolution of initial infinite temperature density matrix to finite temperatures. Specifically, we use the Ancilla Method described by Wall and Carr [47, 48] where we perform our numerical simulations by using the Dirac-Frenkel Time-Dependent Variational Principle (TDVP) method [48, 120–122], by giving β different values. The details of these methods are described in sections 4.2.3.2 and 4.2.4.

We find that the Time-Dependent Variational Principle (TDVP) algorithm is the most optimal integrator for time-propagation at finite temperatures in terms of the balance between the speed and accuracy, however other methods might win in terms of accuracy, for instance Runge-Kutta [102].

The accuracy of the method is verified by comparing the numerical calculations with the exact solution (using exact diagonalisation methods) in the case of smaller systems. For bigger system sizes the convergence of numerical results to the exact solution is checked by increasing the bond dimension D . We verified the validity of all our results

by comparing the convergence of this method with respect to the observables we are interested in, and we confirm the convergence in the bond dimension by running multiple calculations with increasingly large D . The convergence study is summarised in Appendix A.

In figures 5.6 and 5.7 we observe the behaviour of some observables during the temperature evolution, for a system size of $M = 40$, for spin-1 and spin-1/2 respectively. Again, we evaluate the $S^+ \hat{S}^-$ from the middle of the system and taking away the boundaries, hence the $\langle \hat{S}_{\frac{M}{2}}^+ \hat{S}_{\frac{M}{2}+13}^- \rangle$. For the spin-1 model, in Fig. 5.6(a) we see that with higher anisotropies the correlations converge to the same value, when the temperature decreases. This could be explained as with higher anitropy in the spin-1 model we enter into the spin-Mott regime. This is the opposite behaviour as with the spin-1/2 model, where the initial correlations value decreased with the anisotropy, where we do not have an insulating phase.

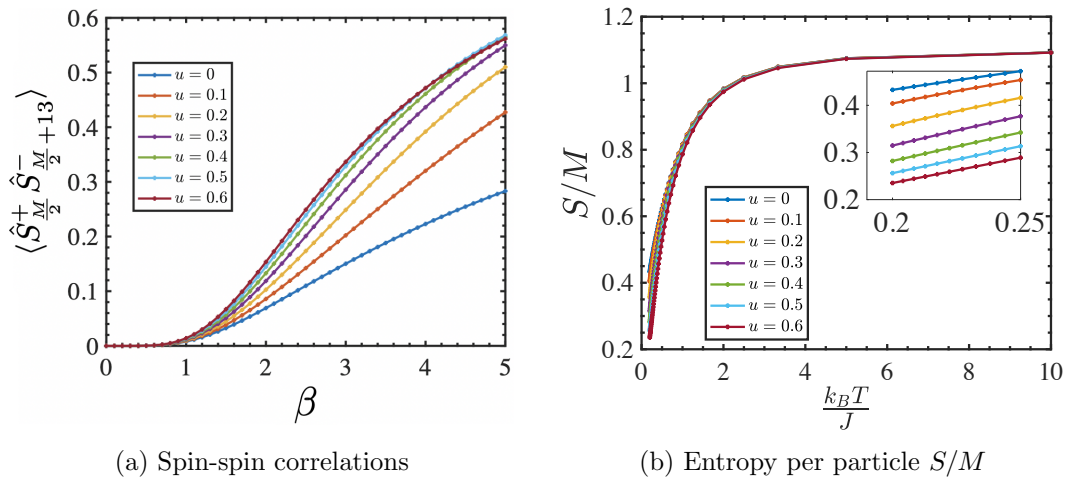


FIGURE 5.6: Spin-1: Different observables during the evolution in temperature (β), for $M = 40$, and different anisotropy u . (a) At higher temperatures $\langle \hat{S}_{\frac{M}{2}}^+ \hat{S}_{\frac{M}{2}+13}^- \rangle$ correlations increase with u/J . (b) The entropy S per particle is increased with temperature, converging asymptotically to its maximum as discussed in Eq. 5.19. [Numerical parameters for the MPS calculations are $D = 64$ and $\beta_{step} = 1$.]

In figures 5.8 and 5.10 the correlation length ξ as a function of temperature and entropy S per spin is depicted, for different values of $u/J, \Delta/J$, for the spin-1 and spin-1/2 model, respectively. We can see that, as $T \rightarrow 0$, the correlation length increases in both models.

For spin-1, the results in Fig. 5.8 are very similar to the case of $M = 40$, since for bigger system sizes, we get a finite correlation length value, and at higher sizes we observe that ξ does not change anymore. This behaviour is expected as we are working with finite temperature, so long as the correlation length is substantially smaller than the system size, and what finite temperature does is to provide an exponential decay of the

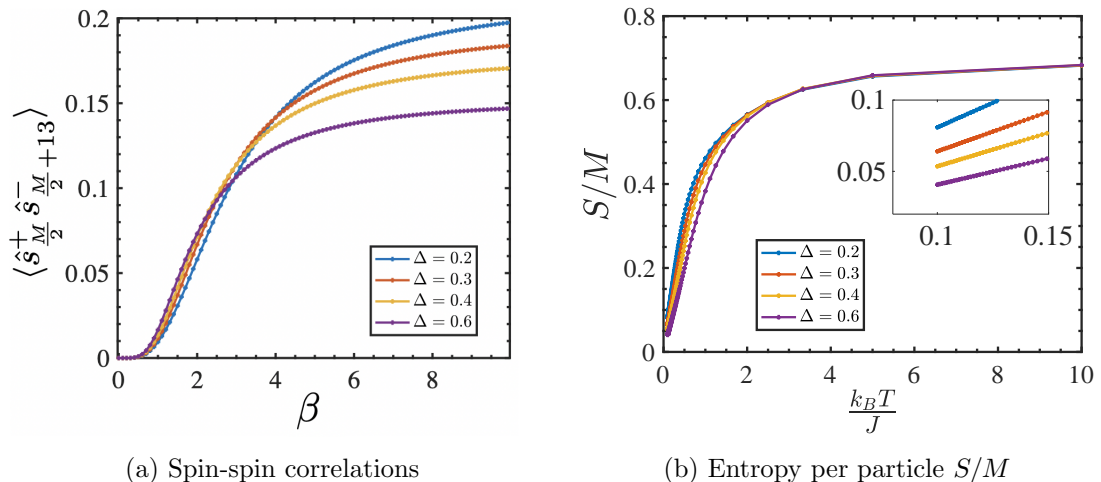


FIGURE 5.7: Spin-1/2: Different observables during the evolution of temperature (β), for $M = 40$, for various anisotropy values Δ/J . a) At higher temperatures $\langle \hat{s}_{M/2}^+ \hat{s}_{M/2+13}^- \rangle$ correlations decrease with Δ/J . Thus, having the opposite behaviour as in the spin-1. (b) The entropy S per particle increases with temperature, converging asymptotically to its maximum as discussed in Eq. 5.19. [Numerical parameters for the MPS calculations are $D = 64$ and $\beta_{step} = 1$.]

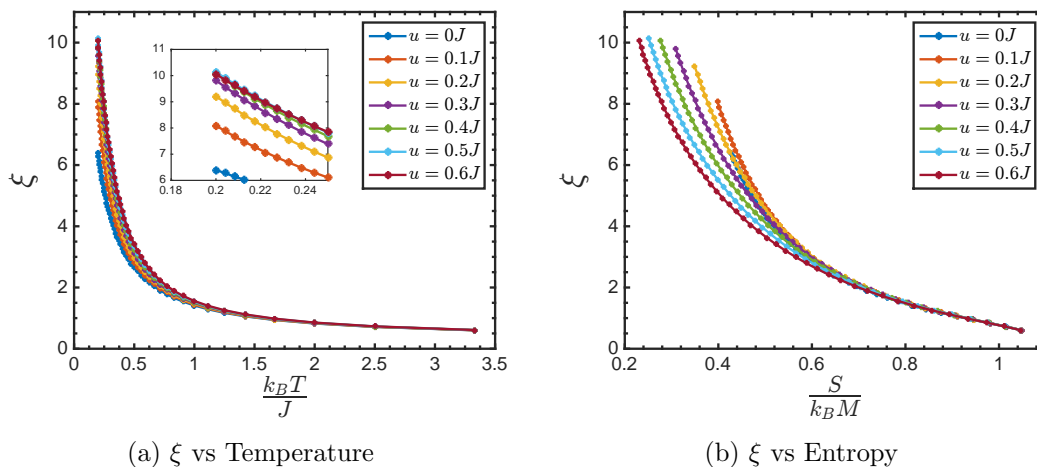


FIGURE 5.8: Spin-1: Correlation length ξ as a function of temperature T and entropy S per spin, for $M = 60$ and different values of u/J , for open boundary conditions. The insets provide a zoom as $T \rightarrow 0$, for a better understanding of the convergence. As u/J increases, higher values of ξ are obtained.

correlations. To have a better understanding, in Fig. 5.9 we evaluate the agreement for different M but the same value of u/J .

5.4.3 Rotated states as thermal states

We investigate here the regimes where the correlation functions decay exponentially, and we evaluate the correlation length and thermal entropy for the rotated state at different values of the anisotropy.

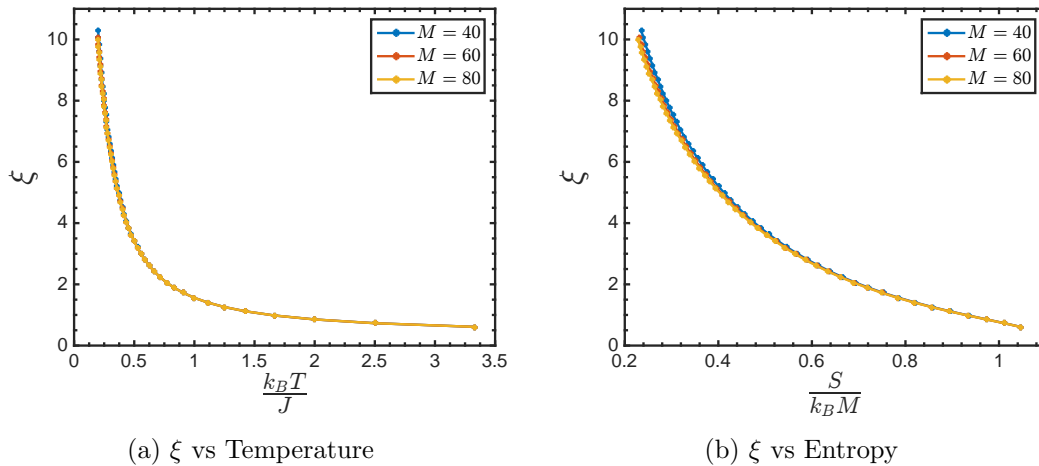


FIGURE 5.9: Spin-1: Correlation length ξ as a function of temperature T and entropy S per spin, for different M and with $u/J = 0.6$, for open boundary conditions. The figures show that for bigger system sizes we get a finite correlation length value, observing that at higher sizes ξ does not change anymore. It is important to notice the convergence for the maximum value of entropy ($\ln 3$) per spin for all values of M and u/J . In our spin-1 system, we have 3^M states, hence this will occur with probability $1/3^M$ at infinite temperature.

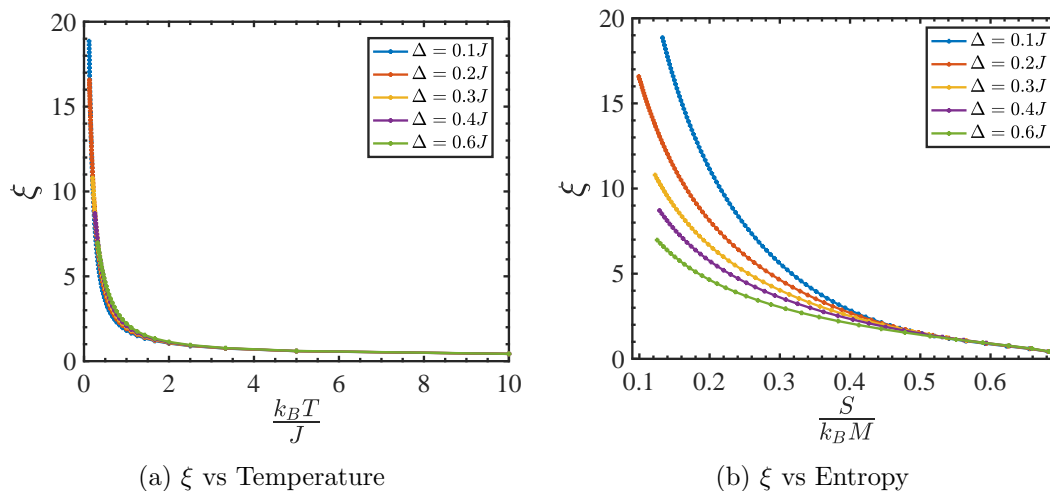


FIGURE 5.10: Spin-1/2: Correlation length ξ as a function of temperature T entropy S per spin, for $M = 40$ and different values of Δ/J , for open boundary conditions. For higher temperature/entropy there is convergence for all anisotropy values. However, as Δ/J increases, the maximum correlation length derived by the exponential decay of the correlations decreases. Similar behaviour is observed with the entropy.

We compare the evolution of the state that looks like mean-field in the first place (rotated state), and ask if we get something similar to the ground state or something more analogous to the thermal state. We have seen in Fig. 5.5 the difference with the ground state. For a thermal state, we can know the corresponding β that gives us the same correlations.

In this section, we now compare the dynamically obtained states to a thermal state $\hat{\rho}_{\text{th}} \propto \exp(-\beta\hat{\mathcal{H}})$ with an inverse temperature $\beta = 1/T$ ($k_B \equiv 1$) such that the energy of the thermal state matches the energy of the rotated state. Considering all of the energy above the ground state for the rotated state was thermalised, we compute the thermal state that would be obtained. Having the energy of the rotated state, we compute a thermal state at a temperature β such that the energy expectation value is the same,

$$\langle E \rangle_{\beta} = \text{tr}(\hat{\rho}_{\text{th}}\hat{\mathcal{H}}) = E_r. \quad (5.19)$$

and we can then obtain the corresponding density matrix $\hat{\rho}_{\text{th}}$.

We consider here the regimes where the correlation functions decay exponentially, and we investigate the correlation length for the rotated state at different values of the anisotropy. We can also quantify the amount of thermal entropy produced by being non-adiabatic in the rotation, for each value of the anisotropy. In order to ensure we are into an exponential regime, we fit the correlations into a semi-logarithmic plot for different temperature values and take only the ones where there is an exact fit outside the boundaries. The properties of the thermal states corresponding to the energies of the rotated states are summarized in Fig. 5.11.

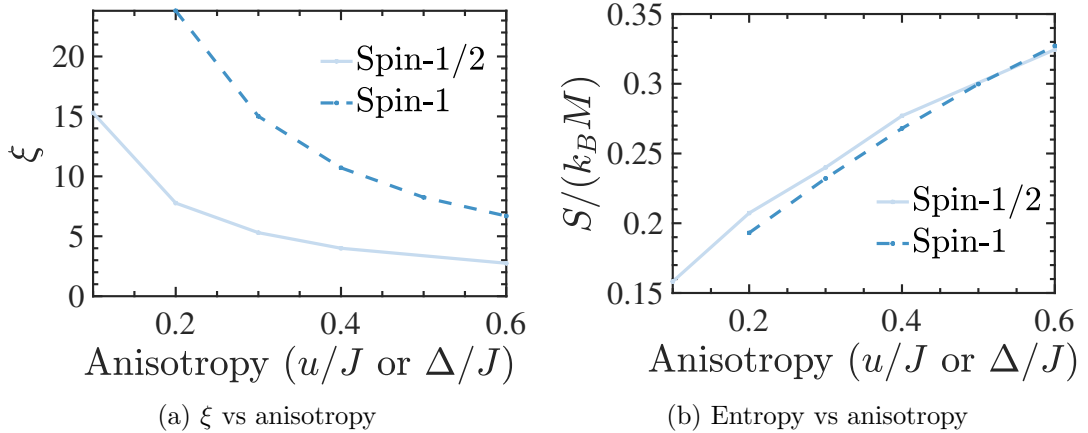


FIGURE 5.11: Properties of thermal states with identical energy as the rotated state for both the spin-1 and spin-1/2 model. (a) Correlation length ξ obtained from an exponential fit to the decay of $\langle \hat{S}_i^+ \hat{S}_{i+r}^- \rangle$ with r (Eq. 5.12). Shown is ξ as a function of the anisotropies u/J and Δ/J . Here, $M = 40$, correlations calculated as in Eq. 5.6. (b) Entropy per particle, $S/(k_B M)$, as function of the anisotropies, $M = 40$. The bond dimension used for these MPS calculations was $D = 64$, with open boundaries.

In both models the correlation length decreases with the anisotropy. For the spin-1 model, we find that a large correlation length is attained for smaller anisotropy, demonstrating that for a thermal state (in the long-time limit) a state with significant correlations may be stabilized for small u/J . In contrast, for the spin-1/2 case we find that except for very small Δ/J the correlation lengths obtained are shorter.

Note that in the numerical method described above, the exponential instability towards the ground state makes the thermal state unreliable for large β . Thus, in our calculation for thermal states, the calculations become inaccurate in the low-temperature limit, here limiting us to the regime of $u \gtrsim 0.2J$ for the spin-1 model. However, we see in Fig. 5.11 that the spin-1 model shows a long correlation length already at $u = 0.2J$, and it is reasonable that for smaller u/J the correlation length will further drastically increase, leading ultimately to an algebraic decay in the limit where the rotated state becomes the true ground state.

5.4.4 Thermalisation dynamics

In general, we expect closed quantum systems to thermalise in the long-time limit. This is meant in the sense that local observables in a small subsystem appear to be described by a thermal density matrix $\hat{\rho}_{\text{th}} \propto \exp(-\beta\hat{\mathcal{H}})$, with the (inverse) temperature set by the energy matching condition with the initial state, $\langle\psi_0|\hat{\mathcal{H}}|\psi_0\rangle = \text{tr}(\hat{\rho}_{\text{th}}\hat{\mathcal{H}})$. In general, this thermalisation behaviour is expected for Hamiltonians without simple/local conserved degrees of freedom (integrable models) and in situations without disorder. The mechanism behind such thermalisation can be explained, e.g., via the well-studied eigenstate thermalisation hypothesis [123–127]. It states that the expectation value of an observable $\langle\hat{O}\rangle$ in an eigenstate $|\psi_\alpha\rangle$ with energy E_α is equal to the thermal (microcanonical ensemble) average of that observable with the same mean energy [128]:

$$\langle\psi_\alpha|\hat{O}|\psi_\alpha\rangle = \langle\hat{O}\rangle_{\text{microc}}(E_\alpha). \quad (5.20)$$

While the ETH and quantum thermalisation appear to apply to a large class of closed quantum systems, not all quantum systems thermalise, as in the limit of vanishing anisotropies ($u, \Delta \rightarrow 0$) in our case, where the models become integrable.

Considering a subsystem which is a small fraction of the full closed system, then thermalisation means that at long times the state of this subsystem is as if it was in thermal equilibrium in contact with a reservoir, provided by the remainder of the closed system [129]. This feature of quantum systems to act as their own reservoirs is the key in equilibrium quantum statistical mechanics. If the dynamics satisfy this property, we say the system thermalises.

Furthermore, for closed systems, the dynamics will be unitary. We consider thermalisation as the equilibration towards a state that is locally indistinguishable from a thermal equilibrium state proportional to $e^{-\beta\hat{H}}$ for some inverse temperature $\beta > 0$ [130]. For initially prepared far-from-equilibrium states, this means that they evolve in time to a state that appears locally as if it is in thermal equilibrium.

To identify regimes, in particular, where a system does not thermalise, we investigate the behaviour of few-particle observables at long times. We then analyse whether the few-particle observables are the same as in the thermal state.

In order to see if there is thermalisation, the difference between the subsystem at infinite time and the corresponding thermal state shall be minimal, and being expressed as a distance, should be close to zero:

$$D = \left\| |\hat{\rho}_S(t \rightarrow \infty)\rangle - |\hat{\rho}(\beta)\rangle \right\|^2 \rightarrow 0. \quad (5.21)$$

To analyze in which regimes such thermalisation might or might not occur in our system, we consider the time dependent expectation value of the correlations, here $\langle \hat{O}_j \rangle = \langle \hat{S}_i^+ \hat{S}_{i+j}^- \rangle$ (analogously for the spin-1/2 with operators $\hat{s}_i^+, \hat{s}_{i+j}^-$). If the system relaxes to a steady state, this state should be identical to the infinite-time average,

$$\overline{\langle \hat{O}_j \rangle}_\infty = \lim_{T \rightarrow \infty} \frac{1}{T} \int_0^T dt \langle \psi(t) | \hat{O}_j | \psi(t) \rangle \quad (5.22)$$

$$\approx \sum_{\alpha} |c_{\alpha}|^2 \langle \alpha | \hat{O}_j | \alpha \rangle, \quad (5.23)$$

where for the last line we have expanded the time-dependent states into the Hamiltonian eigenbasis with eigenvalues $\{E_{\alpha}\}$ and eigenstates $\{|\alpha\rangle\}$, with

$$|\psi(t)\rangle = \sum_{\alpha} c_{\alpha} |\alpha\rangle \exp(-i\hat{E}_{\alpha}t), \quad (5.24)$$

(here, $\hbar \equiv 1$ and we assumed non-degenerate eigenstates) [131], denoting the expectation value in a “diagonal ensemble”. We want to test if the correlations averaged over our simulation times and the infinite time-average (given by the diagonal ensemble) can be described by a thermal density matrix [132, 133].

In order to see if the thermalisation occurs, we compare the steady state with the thermal state. If the relative difference is zero, we consider that the system does thermalise, hence, that the ETH hypothesis is valid in those regimes. The relative difference between

the steady state and the thermal state is calculated as:

$$\Delta \langle \hat{O}_j \rangle_\infty = \frac{|\langle \hat{O} \rangle_{t \rightarrow \infty} - \langle \hat{O} \rangle_{\text{th}}|}{\langle \hat{O} \rangle_{\text{th}}}. \quad (5.25)$$

Numerically it is difficult to simulate systems with large M to very long times, but we can investigate the behaviour for small system sizes, where the whole spectrum can be numerically computed, and then extrapolate to larger systems. We compute $\langle \hat{O}_j \rangle$ averaged over a time-scale $t \in [0, t_0]$, $\overline{\langle \hat{O}_j \rangle}_{t_0}$, and compare the result to a thermal state with the energy of the initial state, $\hat{\rho}_{\text{th}}$, and we then evaluate

$$\Delta \langle \hat{O}_j \rangle_{\text{th}} = \frac{|\overline{\langle \hat{O}_j \rangle}_{t_0} - \text{tr}(\hat{O}_j \hat{\rho}_{\text{th}})|}{|\text{tr}(\hat{O}_j \hat{\rho}_{\text{th}})|}. \quad (5.26)$$

The results are summarized in Fig. 5.12 (a-b) for spin-1 and spin-1/2.

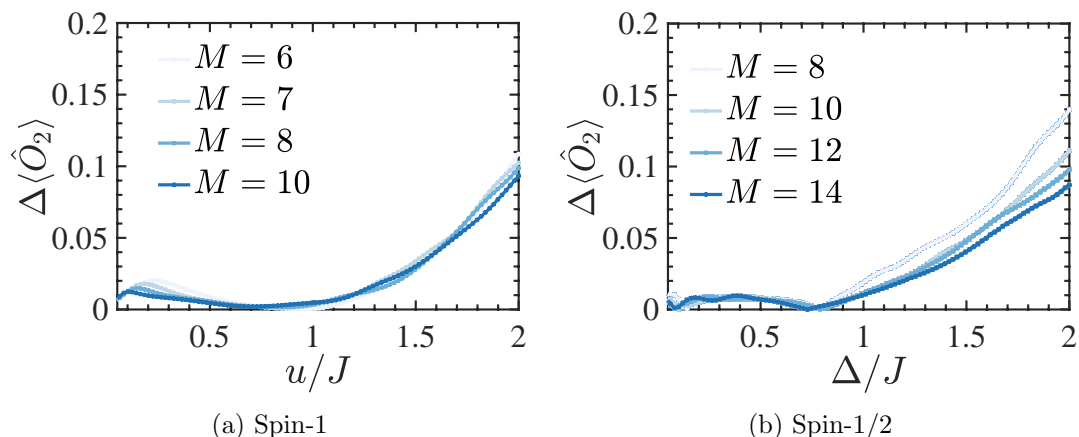


FIGURE 5.12: thermalisation behaviour of correlations for both the spin-1 (a) and spin-1/2 (b) model. Shown are differences of long-time averages values with those of expected thermal states of energy E_r . Panels show results from a long-time average up to $t_0 = 10$, Eq. 5.26. A value of zero indicates dynamics towards a thermal state. As observable we consider the correlations \hat{O}_j as in Eq. 5.6 with $b = 2$. The difference is shown as function of the anisotropies and for various system sizes. All calculations are done with exact diagonalisation methods and for periodic boundaries.

One of the first questions raised by the above results is the following: how can we be sure that the average results in time are sufficient to simulate the behaviour at long times?

We compared different time scales and see if there was convergence. Also we considered the average by ignoring small anisotropies, as we expect the effect of the small anisotropies to be very weak.

Furthermore, we compare the infinite time-average, i.e. the diagonal expectation value, to the thermal one by computing

$$\Delta \langle \hat{O}_{d.e.} \rangle = \frac{\left| \overline{\langle \hat{O}_j \rangle}_{d.e.} - \text{tr}(\hat{O}_j \hat{\rho}_{\text{th}}) \right|}{|\text{tr}(\hat{O}_j \hat{\rho}_{\text{th}})|}, \quad (5.27)$$

by projecting into all of the eigenstates, where $\langle \hat{O}_{d.e.} \rangle = |C_n|^2 \langle \psi_n | \hat{O}_j | \psi_n \rangle$. Thus, observables can be described as the diagonal ensemble when the effective density matrix takes a diagonal form in the basis low-lying energy eigenstates. The diagonal ensemble results are shown in Fig. 5.13.

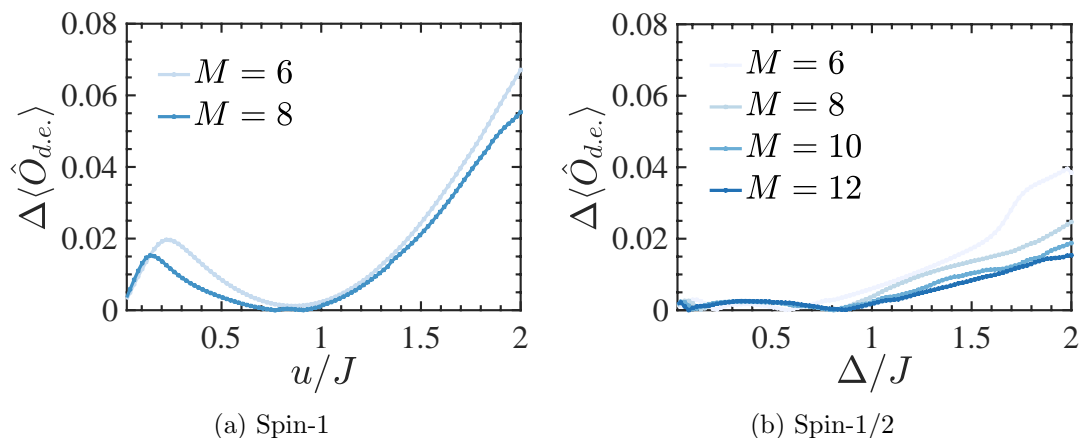


FIGURE 5.13: thermalisation behaviour of correlations for both the spin-1 (a) and spin-1/2 (b) model. Shown are differences of diagonal expectation values with those of expected thermal states of energy E_r . Panels show the differences from the diagonal ensemble, Eq. 5.27. A value of zero indicates dynamics towards a thermal state. As observable we consider the correlations \hat{O}_j as in Eq. 5.6 with $b = 2$. The difference is shown as function of the anisotropies and for various system sizes. All calculations are done with exact diagonalisation methods and for periodic boundaries.

Strikingly, for anisotropies larger than 1, both the diagonal ensemble expectation value and the finite time average differ clearly from thermal states in both models. For smaller anisotropies, within finite size effects the states obtained have expectation values of the chosen observables that are consistent with the thermal state. In all cases, we observe that around $\Delta, u = 0.8J$ the lack of thermalisation starts to be clearly shown. We expect that the lack of thermalisation for larger anisotropies is related to increasing interactions between magnons, which will lead to integrability in 1D.

5.5 Probing the states with spin currents

We study different ways to characterise (through measurements) the properties of the states, finding those measurements that give qualitatively different signatures for different parameter regimes, and also allow us to clearly distinguish between the real ground state and the rotated state.

We study new ways to probe the resulting state, by investigating the behaviour of spin currents [134] in an optical lattice. To do so, we should be able to see a reaction of the state and how it behaves if you try to excite it, and what we do is to move the lattice in a spin-dependent way and see how the system responds.

If a finite current is induced to the system so that the quasi-momentum distribution is shifted by a small amount, then we expect the resulting behaviour to depend on the superfluidity of the state, so that the current will remain constant in the superfluid regime. For an ideal, non-interacting, superfluid, we would expect no decay of the current, but interactions will lead to a decay of the current once we exceed a critical strength of the kick.

We begin with the initial state where all of the spin pointing along z , then we apply the rotation towards the xy -plane, and then consider an acceleration applied in order to produce a finite current [135].

In our case the following “kick” operator is applied to the rotated state

$$\hat{\kappa}(\Omega) = \prod_l^M e^{-i\hat{S}_l^z \Omega}, \quad (5.28)$$

with Ω a quasi-momentum or “kick-strength”. Experimentally we can realise this by applying a magnetic field gradient for a short time, which induces a spin current.

In our spin model the spin current \hat{C} will have the form:

$$\hat{C} = \frac{1}{M} \sum_l \hat{c}_l, \quad (5.29)$$

with

$$\hat{c}_l = -\frac{1}{2i} \left(\hat{S}_l^+ \hat{S}_{l+1}^- - \hat{S}_l^- \hat{S}_{l+1}^+ \right), \quad (5.30)$$

which satisfies the continuity equation [136, 137]:

$$\frac{d}{dt} \hat{S}_l^z = \left[i\hat{\mathcal{H}}, \hat{S}_l^z \right] = \hat{c}_{l+1} - \hat{c}_l. \quad (5.31)$$

The operation is calculated analogously for the spin-1/2 with operators $\hat{s}_l^+, \hat{s}_{l+j}^-, \hat{s}_l^z$.

In comparison to [135], where the infinite TEBD (iTEBD) algorithm [138] was used, in our simulations we use finite TEBD. In our case we defined the “kick” operator as an MPO and we performed the calculations with two different algorithms: Runge-Kutta [110] and TDVP [48]. We found that preliminary results with Runge-Kutta do not show good correspondence with ED results, and the current decay very fast even at high dimensions. This could have been affected by the way we define the observable in the algorithm, but a much more extensive study has to be done to understand how the algorithm worked in this case. However, TDVP works with both open and periodic boundary conditions, reproducing the results obtained from ED calculations on small systems.

Note that in contrast to single particle current measurements [139], the spin-currents correspond to relative momentum distributions of the two species, and correlations between this could be probed via noise correlation measurements [140, 141].

The stability of superfluid currents in a system of strongly interacting bosons in a lattice has been studied before [142, 143], and depends on the magnitude of the quasi-momentum, and the strength of the interactions. It will also depend on the dimensionality of the system, where for 1D there is a crossover, and in 3D a sharp discontinuity.

We expect here to see this behaviour for our one-dimensional systems, as a function of the magnitude of the strength of the “kick” and the anisotropy $u/J, \Delta/J$ for the spin-1 and spin-1/2 model respectively.

5.5.1 Study of the currents on the rotated state

The convergence study for all spin currents is summarised as part of Appendix A.

5.5.1.1 Initial state

For both of our models, we begin with the ground state of our Hamiltonian, and then apply an acceleration in order to produce a finite current, as in 5.28.

Firstly, we consider the time immediately after the application of the “kick” $t = 0^+$, in Fig. 5.14, where we show the spin currents for different momenta Ω/π and various values of the anisotropies $u/J, \Delta/J$, for periodic boundary conditions. The current is proportional to the kick as $\langle C \rangle \propto \sin(\Omega\pi)$, which can be calculated from the quasi-momentum distribution, as in [135].

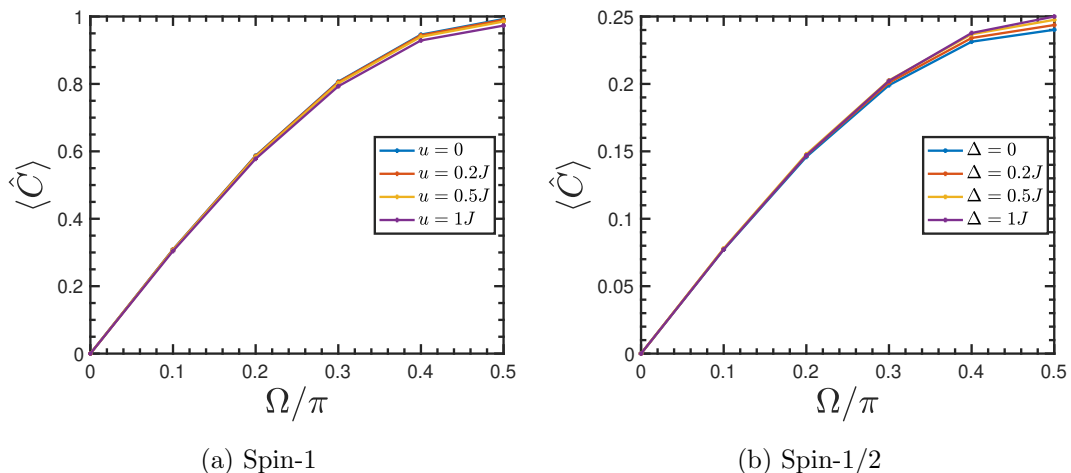


FIGURE 5.14: Spin current \hat{C} after the “kick” is imparted on the ground state (time= 0^+) for the (a) spin-1 and (b) spin-1/2 model, for $M=40$ and PBC. In both models, in the limit of non interactions, the current is exactly $\langle C \rangle = J \sin(\Omega\pi) = 0$. With higher anisotropy values we have $\langle C \rangle \propto u \sin(\Omega\pi)$ for the spin-1 and $\langle C \rangle \propto \frac{\Delta}{4} \sin(\Omega\pi)$

5.5.1.2 Time evolution of the spin currents

Now we want to study the current stability with time for our models. We should see non-decaying currents when we are in the superfluid (XY-ferromagnetic) phase, up to boundary effects.

In Fig. 5.15 the current evolution for the spin-1, for different anisotropy values and “kick-strength”, up to a time $TJ = 2$, is depicted.

The currents are constant for small gradients and small value of the anisotropy and slightly decaying as this increases. The change in the current behaviour in the crossover can be clearly observed, as even for smaller momenta the currents decay.

In Fig. 5.16 we show the current evolution for the spin-1/2, for different anisotropy values and “kick-strength”, up to a time $TJ = 3$.

In this case we are always in the XY-ferromagnetic phase, and only when we induce a strong “kick” can we see the currents decay. For $\Delta = 1J$ we see no decay of the currents as this XX model can be mapped to non-interacting fermions. The small decay at longer times is due to the fact that the most robust currents occur for larger anisotropy, where there is a bigger difference between the rotated state and the ground state, with a faster decay of the correlations.

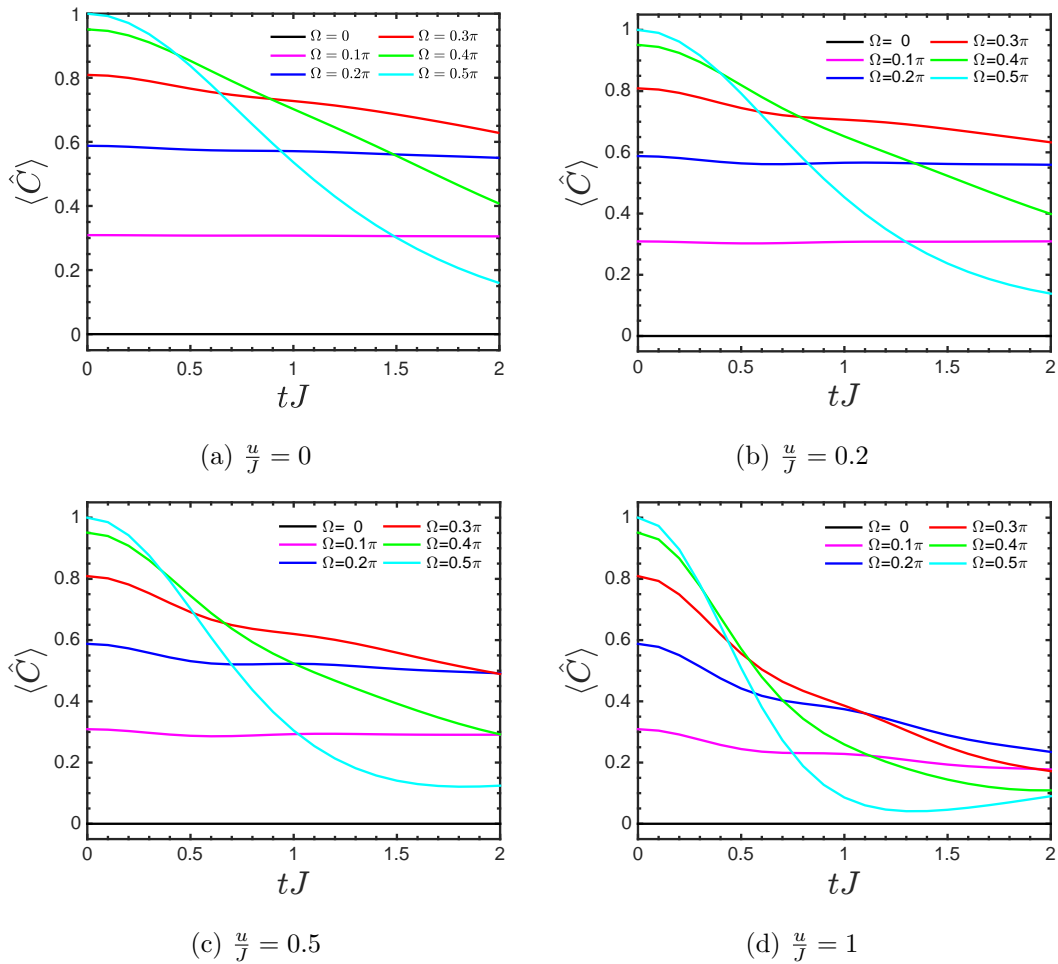


FIGURE 5.15: Spin-1: Time evolution of the spin current \hat{C} for different values of the anisotropy u/J and gradient Ω , for PBC.

5.5.1.3 Spin-spin correlations

In order to evaluate the out-of-equilibrium dynamics, in Fig. 5.17 we consider the spin-spin correlations evolution for different momenta strength during the time evolution of a lattice of 40 sites, for both models.

First of all we can see that as the anisotropy and the “kick-strength” increase the correlations decay faster, for both models. However, this effect is again much more noticeable in the spin-1/2 model.

5.5.2 Comparison with the ground state

In this section we are going to compare the results for both models, as well as the differences in the current behaviour between the ground state and the rotated state.

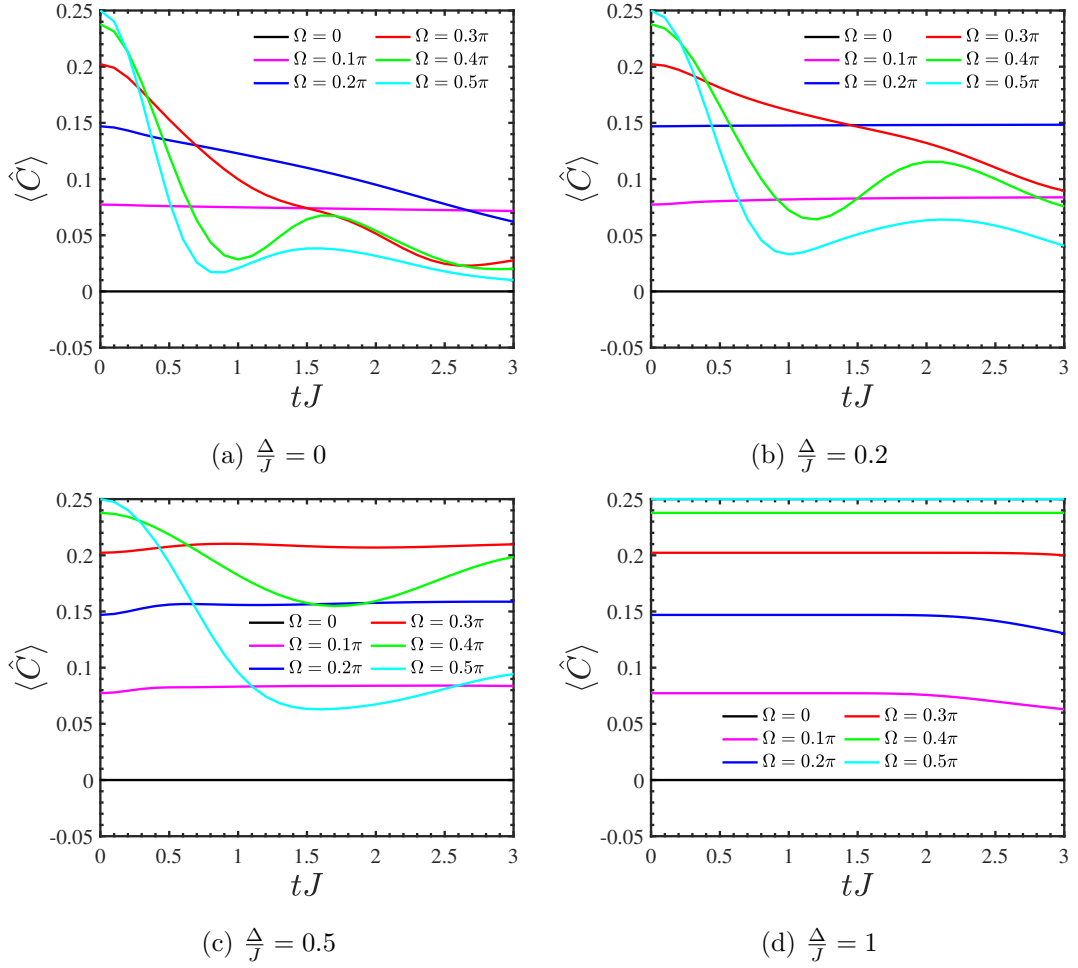


FIGURE 5.16: Spin-1/2: Time evolution of the spin current \hat{C} for different values of the anisotropy Δ/J and gradient Ω , with PBC.

5.5.2.1 Dynamical results

We compute the currents for spin-1/2 and spin-1, in each case considering the behaviour of the current in the ground state and the rotated state. We perform calculations by applying the “kick” operator as an MPO to a MPS representation of our state, and computing the corresponding time evolution. We show the evolution of the currents for different values of the anisotropies and momenta Ω/π in Fig. 5.18, for both spin-1 and spin-1/2, and for the ground states (on the left hand side of the figure) and rotated states (on the right hand side of the figure). We can clearly distinguish the crossovers between the regimes where the currents are stable (superfluid phase, or XY-ferromagnetic phase) and unstable.

To more clearly study the dependence of the stability of currents on the anisotropy and Ω , in figures 5.19 to 5.21 we plot the relative difference between the current after short time evolutions at different times during the evolution and at the beginning of the

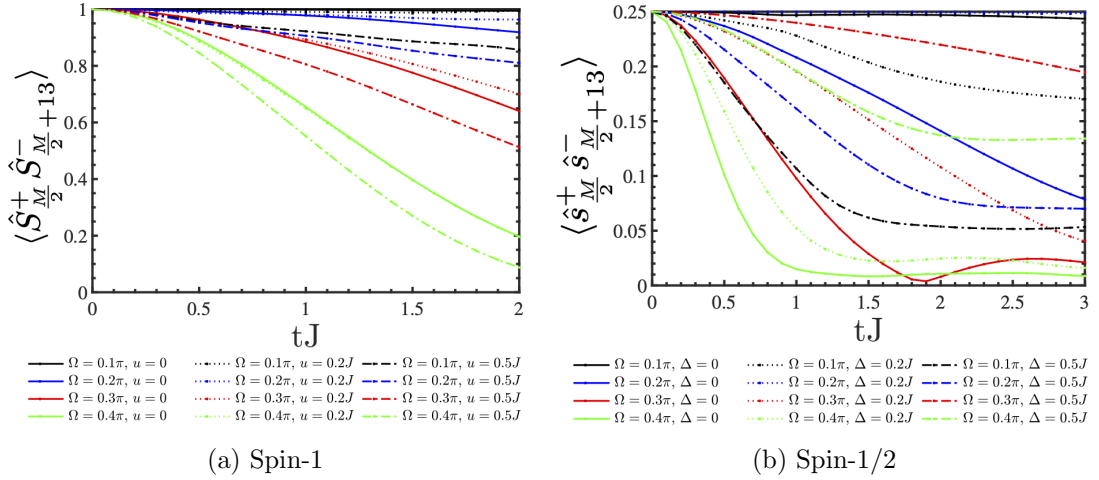


FIGURE 5.17: Decay of the spin-spin correlations with time for different anisotropies and momenta strength for the (a) spin-1 and (b) spin-1/2 model, for $M = 40$.

evolution,

$$\Delta \langle \hat{C} \rangle = \frac{|\langle \hat{C} \rangle_{tJ} - \langle \hat{C}_{tJ=0+} \rangle|}{\langle \hat{C}_{tJ=0+} \rangle}. \quad (5.32)$$

We find that also when the “kick” is applied to the rotated states, we can clearly quantify a crossover between two regimes of persistent and decaying currents, in both models.

For the spin-1 model in 1D, we expect a crossover between persistent currents in a spin superfluid (XY-ferromagnet) regime, to a rapid decay as the system becomes strongly anisotropic, in analogy to spin currents for bosons in a 1D Bose-Hubbard model [135, 142–144]. For infinitesimal “kick-strength” $\Omega \rightarrow 0$, we expect the currents to remain constant in the XY-ferromagnetic phase regime, and start to decay once entering into the spin-Mott phase. This can be seen along the vertical axis in Fig. 5.19 for the rotated state. The currents remain constant for small values of the anisotropy small gradients, and slightly decaying as u/J increases. The change in the current behaviour as we cross the phase transition ($u > 0.6J$) can be clearly observed.

For a larger Ω , as we go towards the isotropic point, the current will still decay after a certain critical Ω value is reached. This value decreases to zero as we go towards the critical value of u/J to enter the spin-Mott phase. Again, as in the 1D case for currents in a Bose-Hubbard model [135], this is not a sharp transition, but rather a gradual crossover.

In contrast, for spin-1/2 in Fig. 5.20, we are always in the XY-ferromagnetic phase, so we expect the currents to remain constant for any infinitesimal “kick-strength” Ω , except exactly at the isotropic point. We know at the same time that the critical value of Ω increases from zero with increasing anisotropy Δ/J , and we see that the value of Ω

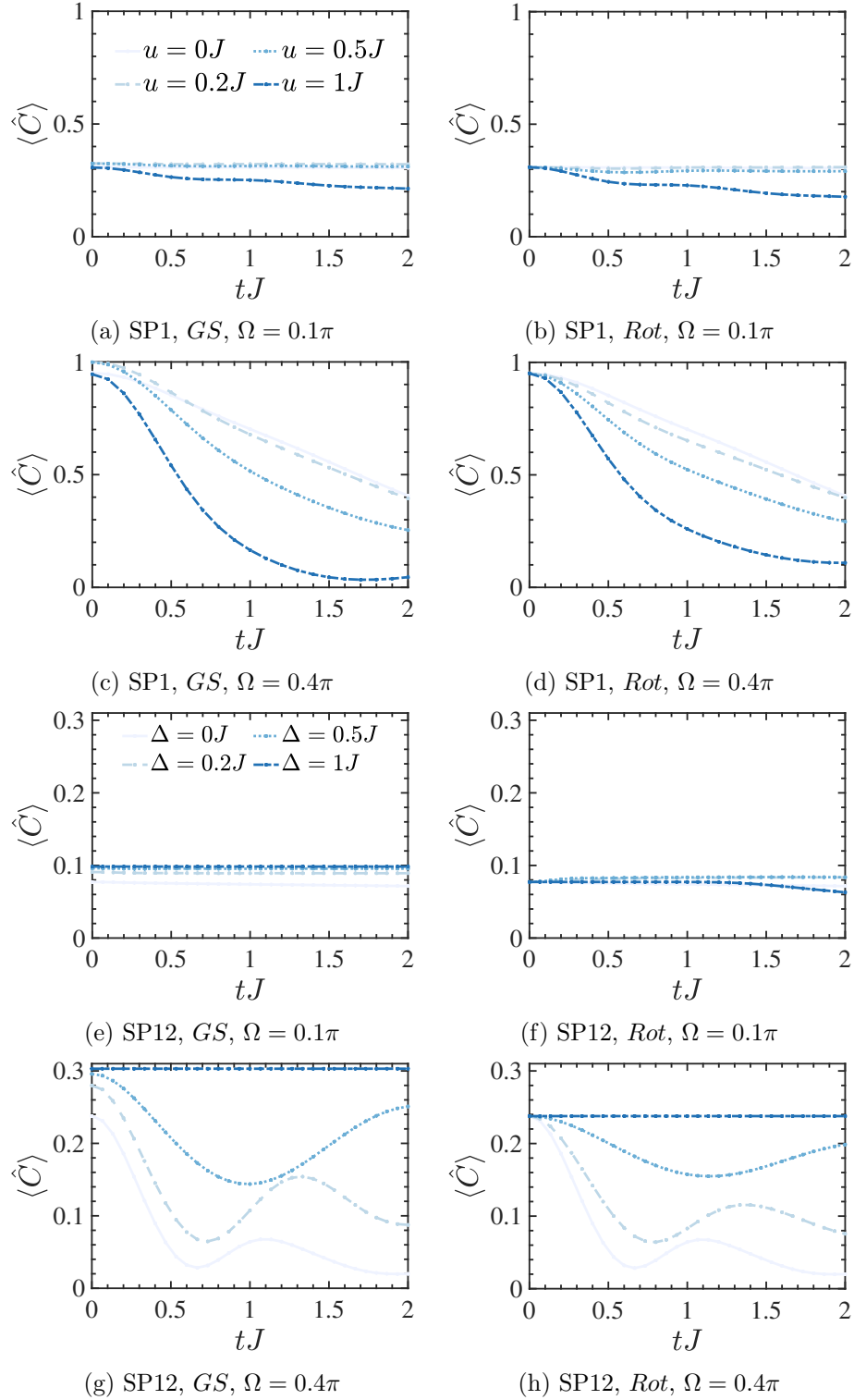


FIGURE 5.18: Spin current time-evolution after a momentum Ω is imposed onto the state for different values of the anisotropies u/J and Δ/J in the spin-1 (a-d) and spin-1/2 (e-h) case. The initial momentum is either small $\Omega = 0.1\pi$ [panels (a/b,e/f) for the ground state and the rotated state, respectively] or large $\Omega = 0.4\pi$ [panels (b/d,g/h) for the ground state and the rotated state, respectively]. The calculations were done for a system size $M = 40$, with bond dimension for the MPS calculations $D = 256$, and periodic boundary conditions.

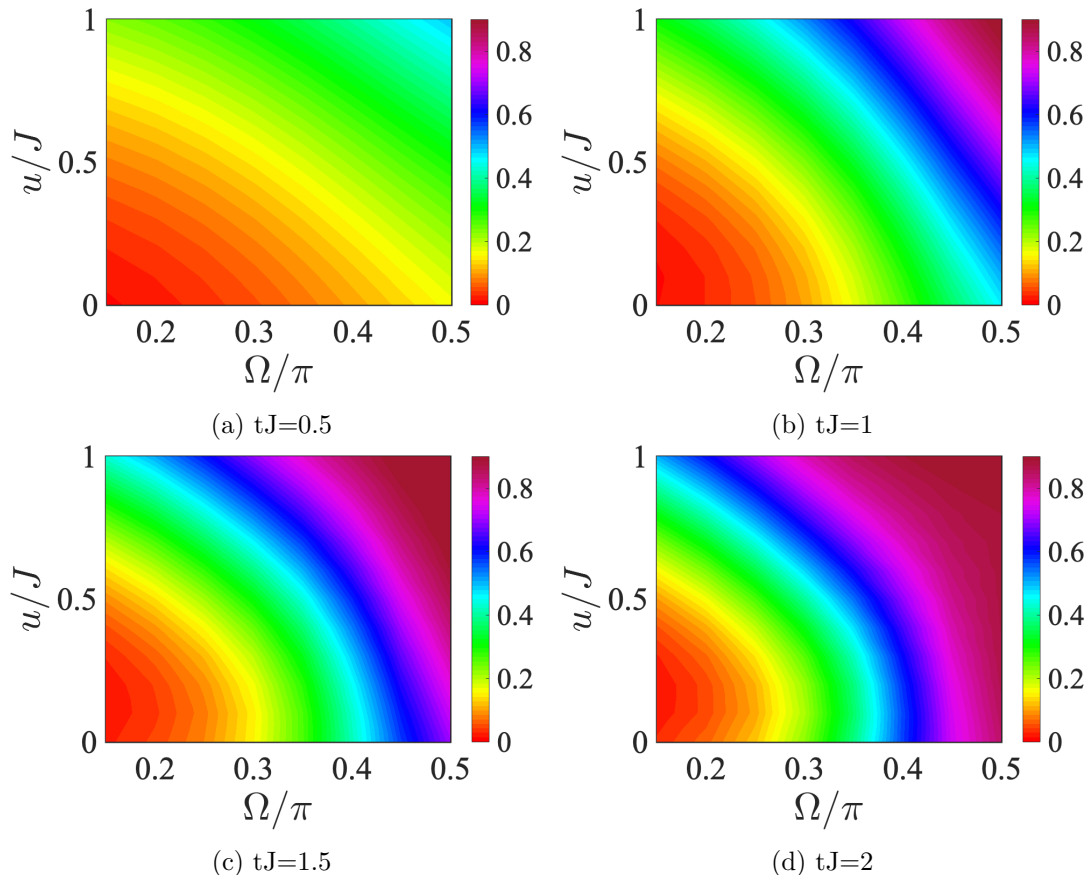


FIGURE 5.19: Spin-1 Model. Relative difference $\Delta \langle C \rangle$ between the spin current at different time steps in the evolution, and at the beginning of the evolution, Eq. (5.32). The figures show the time evolution after a quasi-momentum Ω of various strength is imposed onto the rotated state for different anisotropy u/J . All calculations are performed for $M = 40$, and with periodic boundaries. The bond dimension used for these MPS calculations was $D = 256$.

above which we observe substantial decay of the current increases with increasing Δ/J . For $\Delta = J$, we see essentially non-decaying currents at any time and “kick-strength” from the ground state, which we expect as the model can be mapped to non-interacting fermions.

A comparison between the ground state and the rotated state for both models at $tJ = 1.5$ is depicted in Fig. 5.21.

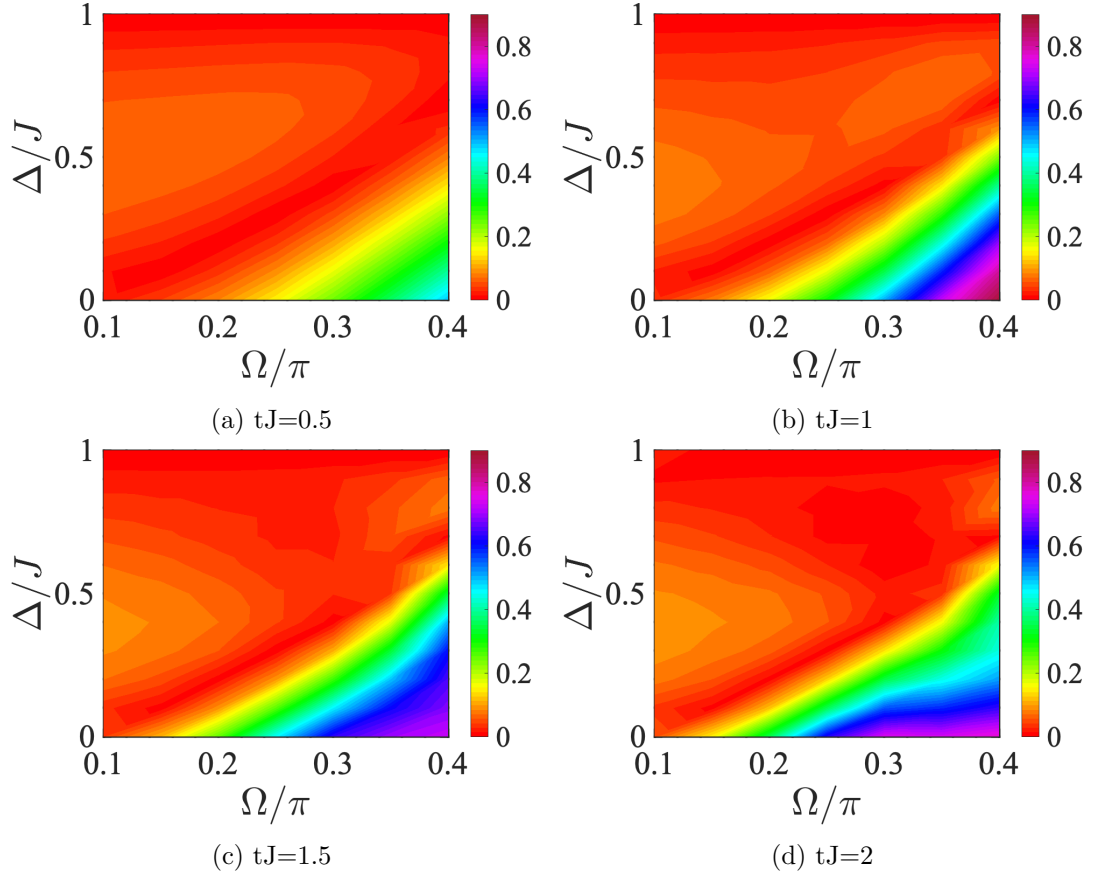


FIGURE 5.20: Spin-1/2 Model. Relative difference $\Delta \langle C \rangle$ between the spin current at different time steps in the evolution, and at the beginning of the evolution, Eq. (5.32). The figures show the time evolution after a quasi-momentum Ω of various strength is imposed onto the rotated state for different anisotropy Δ/J . All calculations are performed for $M = 40$, and with periodic boundaries. The bond dimension used for these MPS calculations was $D = 256$.

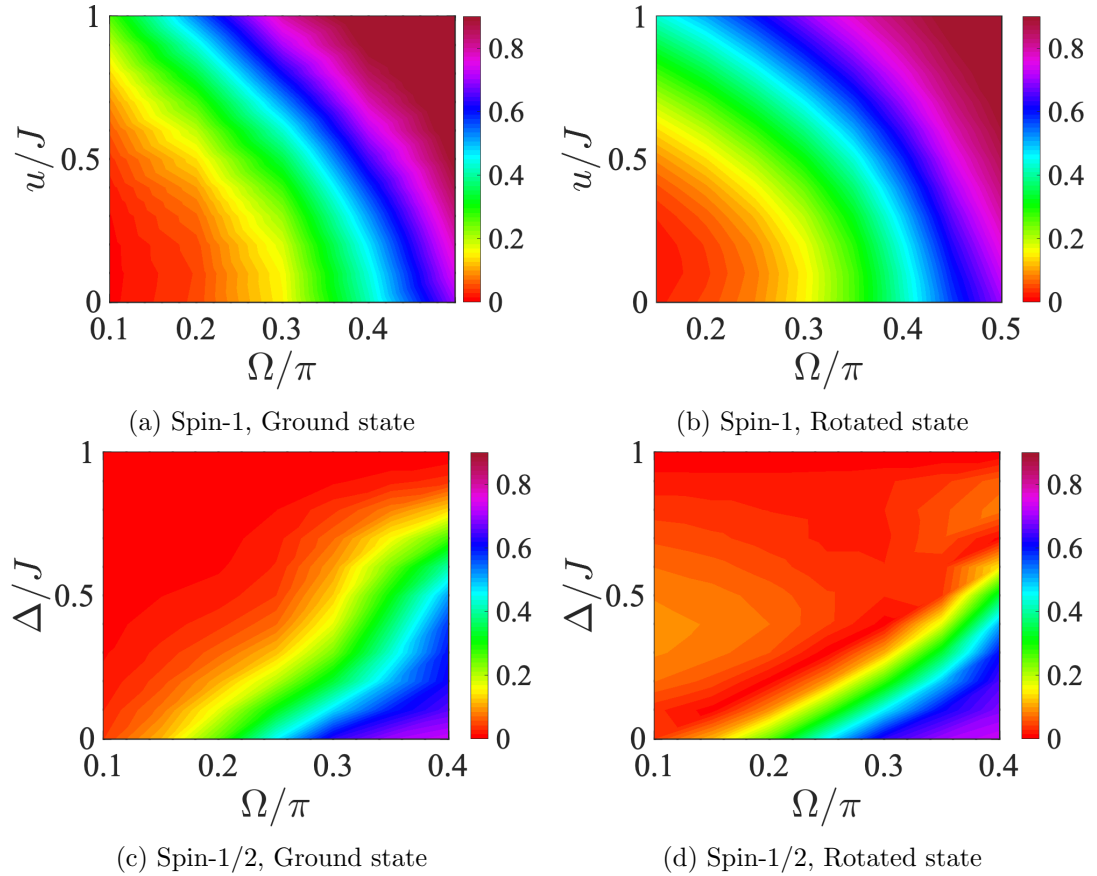


FIGURE 5.21: Relative difference $\Delta \langle C \rangle$ between the spin current at $tj = 1.5$ and at the beginning of the evolution, Eq. (5.32). The figures show the time evolution after a quasi-momentum Ω of various strength is imposed onto the ground state (a,c) and the rotated state (b,d) for different anisotropy u/J in the spin-1 model (a,b) and Δ/J in the spin-1/2 (c,d). All calculations are performed for $M = 40$, and with periodic boundaries. The bond dimension used for these MPS calculations was $D = 256$.

5.5.2.2 Energy difference after “kick”

One of the questions we could ask to distinguish between the rotated state and the ground state is the amount of energy that we are adding into the system by the “kick” in both cases.

In Fig. 5.22 we show the absolute energy difference added to the system with the “kick” operator between the rotated state and the ground state, for given values of the anisotropy for the spin-1 and spin-1/2 in the XY-ferromagnetic phase.

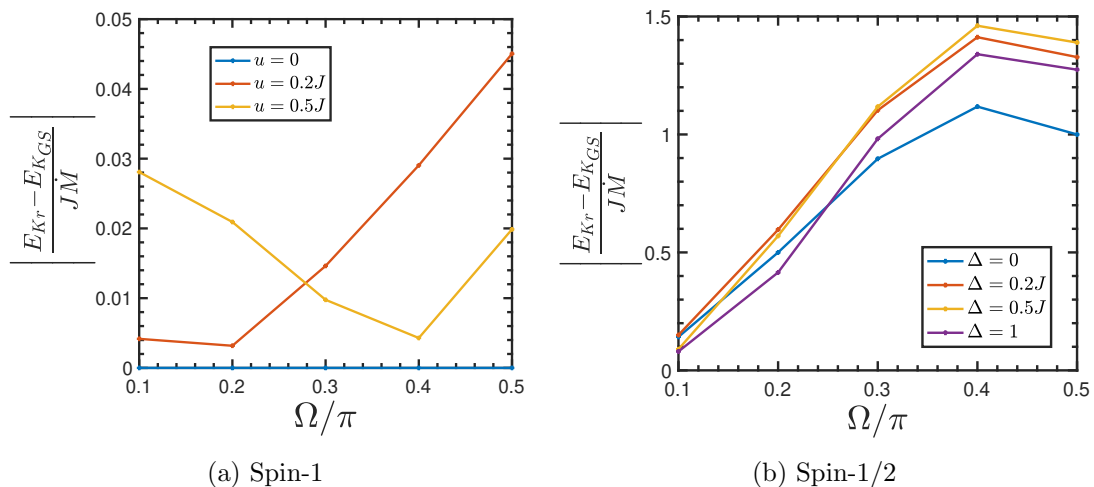


FIGURE 5.22: (a) Spin-1 model: Energy difference per spin after the “kick” between the ground state and the rotate state, for different values of u/J and Ω/π , for $M=40$. There is no energy difference with the “kick” for zero anisotropy, and small variations for increasing anisotropies and different Ω/π values. (b) Spin-1/2 model: Energy difference per spin after the “kick” between the ground state and the rotate state, for different values of Δ/J and Ω/π , for $M=40$. Here the energy difference increases with the “kick-strength”, except from $\Omega = 0.4\pi$ to $\Omega = 0.5\pi$.

How could we measure this energy difference experimentally? By investigating the quasi-momentum distribution we can see the redistribution after the “kick”, in both models and for different parameter values.

We define the quasi-momentum bosonic operators related to the spin operators as

$$\hat{S}_j^+ = \frac{1}{\sqrt{M}} \sum_q e^{-iqj} \hat{S}_q^+, \quad (5.33)$$

and

$$\hat{S}_j^- = \frac{1}{\sqrt{M}} \sum_q e^{-iqj} \hat{S}_q^-, \quad (5.34)$$

with q the quasi-momentum. The operation is calculated analogously for the spin-1/2 with operators \hat{s}_j^+, \hat{s}_j^- .

The quasi-momentum distribution is defined as

$$m_q = \langle \hat{S}_q^+ \hat{S}_q^- \rangle, \quad (5.35)$$

which is depicted in Fig. 5.23 for the two models. In each of the plots we can see the quasi-momentum distribution m_q right before and after the “kick”, and at the end of the evolution for a time $TJ = 10$.

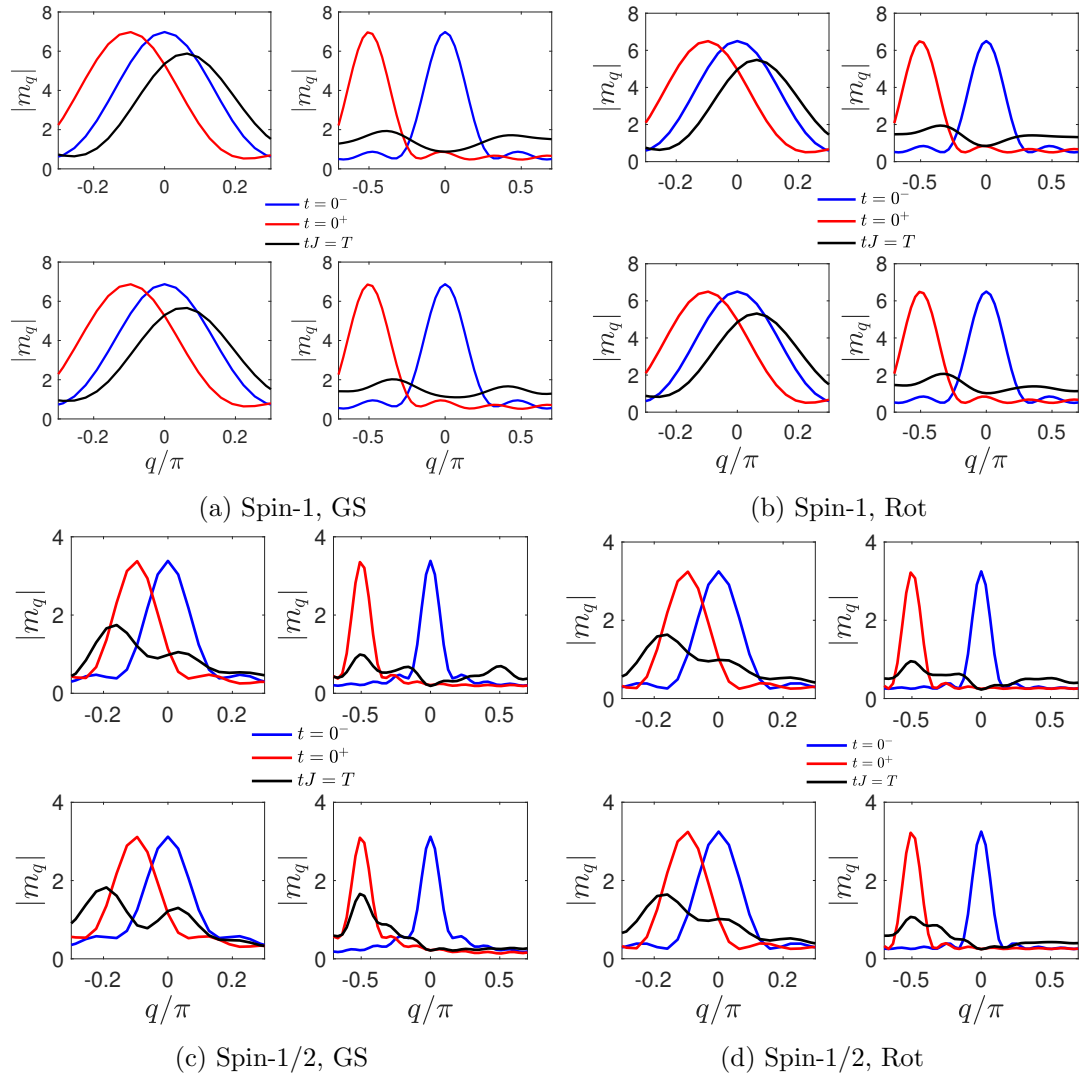


FIGURE 5.23: The figures show the quasi-momentum distribution right before and after the “kick”, and at the end of the evolution for a time $TJ = 10$, for various “kick-strength” ($\Omega = 0.2\pi$ for odd columns and $\Omega = 0.5\pi$ for even columns) imposed onto the ground state (a/c) and rotated state (b/d) for different anisotropies ($u, \Delta = 0.2J$ odd rows, $u, \Delta = 0.5J$ even rows) for spin-1 (a/b) and spin-1/2 (c/d), respectively. All calculations are performed for $M = 6$ for the spin-1 and $M = 12$ for spin-1/2, and with periodic boundaries.

One of the main differences between the two spin models is that there is a higher quasi-momentum value in the case of the spin-1. We can see that in all cases at time $t = 0^-$ the quasi-momentum distribution is peaked around $q = 0$, as we expect from a superfluid

state. The effect of the ‘kick’ is to broaden the distribution at the end of the evolution, which practically disappears for $\Omega = 0.5\pi$ in the spin-1 case.

5.5.3 Critical velocity and excitation spectrum

For the spin-1/2, or XXZ model, we study the excitation spectrum, in particular for the XY-ferromagnetic or counterflow superfluid regime, where we want to show the effect of the anisotropy in the critical velocity.

For a weakly interacting gas the critical velocity is linear. In a superfluid with an elementary excitation spectrum the flow velocity at the point will follow the Landau criterion as in Fig. 5.24.

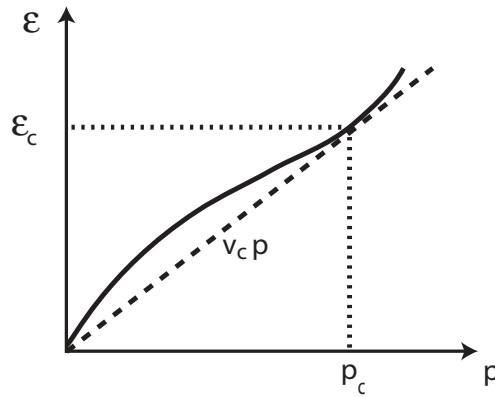


FIGURE 5.24: The slope of the dashed line is the critical velocity v_c according to the Landau criterion. Redrawn from [145].

To derive the excitation spectrum, we begin with our Hamiltonian:

$$\hat{\mathcal{H}} = -J \sum_{\langle i \rangle} (\hat{s}_i^x \hat{s}_{i+1}^x + \hat{s}_i^y \hat{s}_{i+1}^y) - (J - \Delta) \sum_{\langle i \rangle} \hat{s}_i^z \hat{s}_{i+1}^z, \quad (5.36)$$

and then rewrite it in terms of \hat{s}^+ and \hat{s}^- operators (with $\{\hat{s}_i^-, \hat{s}_j^+\} = \delta_{ii'}$) as

$$\begin{aligned} \hat{\mathcal{H}} &= -\frac{J}{4} \sum_i ((\hat{s}_i^+ + \hat{s}_i^-) (\hat{s}_{i+1}^+ + \hat{s}_{i+1}^-) - (\hat{s}_i^+ - \hat{s}_i^-) (\hat{s}_{i+1}^+ - \hat{s}_{i+1}^-)) \\ &\quad - (J - \Delta) \sum_i (2\hat{s}_i^+ \hat{s}_i^- - 1)(2\hat{s}_{i+1}^+ \hat{s}_{i+1}^- - 1) \\ &= -\frac{J}{2} \sum_i (\hat{s}_i^+ \hat{s}_{i+1}^- + \hat{s}_i^- \hat{s}_{i+1}^+) - (J - \Delta) \sum_i \hat{s}_i^+ \hat{s}_i^- \hat{s}_{i+1}^+ \hat{s}_{i+1}^- + 4(J - \Delta) \sum_i \hat{s}_i^+ \hat{s}_i^- - (J - \Delta) \\ &= -\frac{J}{2} \sum_i (\hat{s}_i^+ \hat{s}_{i+1}^- + \hat{s}_i^- \hat{s}_{i+1}^+) - (J - \Delta) \sum_i \hat{s}_i^+ \hat{s}_i^- \hat{s}_{i+1}^+ \hat{s}_{i+1}^- + (J - \Delta)(N^\dagger - \frac{1}{4}), \end{aligned} \quad (5.37)$$

where $N^\dagger = \hat{s}_i^+ \hat{s}_i^-$.

We then define the Fourier transform

$$\hat{s}_l^- = \int_{-\pi/a}^{\pi/a} dk e^{ikal} \hat{s}_k^- \equiv \sum_k e^{ikal} \hat{s}_k^-, \quad (5.38)$$

and by taking into account Bogoliubov theory [146] in terms of the fermions operators, the excitation spectrum can be calculated with the final Hamiltonian:

$$\begin{aligned} \hat{\mathcal{H}} = & -(J - \Delta) \frac{N^\dagger}{4} - J \sum_k \cos(k) \hat{s}_k^+ \hat{s}_k^- + (J - \Delta) \sum_k \cos(k) \hat{s}_k^+ \hat{s}_k^- \\ & - \frac{(J - \Delta)}{N^\dagger} \sum_{k_1+k_2-k_3-k_4=0} \cos(k_1 - k_4) \hat{s}_{k_1}^+ \hat{s}_{k_2}^+ \hat{s}_{k_3}^- \hat{s}_{k_4}^-. \end{aligned} \quad (5.39)$$

More detailed analysis is performed in [147] for ferromagnetic XXZ-chains. A further analysis could be done for the spin-1 model following a similar approach, investigating the excitations as a function of the anisotropy.

5.6 Summary and discussion

We have studied a XY-ferromagnet, and how different the ground state is from a product state of spins rotated into the xy-plane. We also quantified how far this product state is as a function of the anisotropy in two different effective spin models (spin-1 and spin-1/2) from the Hubbard Model for two bosonic components in an optical lattice.

We have compared both models, and by controlling the out-of-equilibrium dynamics, we have probed that for the spin-1/2 case the correlations decrease rapidly in time, faster for a higher anisotropy. Furthermore, correlation lengths and thermal entropies have been calculated using Tensor Networks techniques for thermal states.

Lastly, to probe the states we have also evaluated the short time evolution of the spin currents, for the ground state and the rotated state, and for both models. For spin-1/2 currents are more stable for higher anisotropy. At longer times, we begin to see decay of currents for the rotated states that occur earlier than for the ground states, where the influence of the correlation decay becomes significant in the dynamics. For the spin-1 model, we observed a cross-over between regions where the currents were stable (counterflow superfluid regime, or XY-ferromagnet) and unstable (towards a spin-Mott state).

These techniques are directly relevant for ongoing experiments to investigate the dynamics of strongly-correlated models in optical lattices.

An open question, which is not addressed here, is the robustness of these techniques to classical noise on the lattice and spontaneous emission, which is significant in current experiments. Also, an experimental approach in higher dimensions will be interesting to provide an interesting basis for further investigation of spin superfluidity in multi-component bosonic lattice models.

Chapter 6

Adiabatic state preparation and metrology with cold atoms in optical lattices

In this chapter¹ we study new techniques to engineer states with a very low entropy using adiabatic state preparation, especially investigating the magnetically ordered quantum states (XY-ferromagnet, antiferromagnet) that can be engineered using these techniques, within the parameter regimes of current experiments. Tuning the inter-component interactions via Feshbach resonances [24] or adjusting the relative positions of spin-dependent lattices allows us to adiabatically connect different many-body states [144, 148–153].

External magnetic fields can be used in these systems to tune the interactions between atoms [154, 155]. We study if it is possible to produce specific magnetic states by appropriate time variation of these fields. Under various conditions we determine the fidelity of magnetically ordered states that can be engineered.

The models that we study can give rise to entanglement that is useful for quantum enhanced metrology. We characterise the states we can prepare in terms of their Quantum Fisher Information (QFI) for collective measurements with Ramsey spectroscopy [156–163]. Interferometry is the archetype for precision measurements, and for cases where particles are not entangled, the measurement precision is bounded by the Standard Quantum Limit (*SQL*) or shot noise limit $1/\sqrt{M}$, with M the number of particles. There have been various experimental and theoretical proposals to beat the classical precision limit using highly entangled states such as Dicke states or twin-Fock states

¹This work is taken in part from a publication, to be submitted. The author of this thesis performed all of the calculations for the models and produced all of the plots.

[164–168]. We calculate the QFI of adiabatically prepared quantum states near a quantum phase transition point in our models, discuss their usefulness for metrology, and investigate their robustness to experimental noise.

We start this chapter with a general introduction to the concept of adiabatic state preparation in section 6.1. Next, we apply adiabatic ramps to prepare interesting magnetic states, antiferromagnet in 6.2 and XY-ferromagnet in 6.3. The second half of the chapter focusses on the application of these techniques to specific states that are useful for metrology, in terms of their QFI, in section 6.4, where we study the characterisation and preparation of specific magnetic states as well as the effect of dissipation.

6.1 Introduction to adiabatic state preparation

The concept of adiabaticity in quantum mechanics has allowed for the experimental study of non-trivial many-body quantum states leading to profound insights into fundamental physics [169–171]. An example of an extensively implemented experimental realisation is *STIRAP* (Stimulated Raman Adiabatic Passage) [172], which allows efficient and selective population transfer between two quantum states, via at least two coherent electromagnetic (light) pulses.

The original form of the term adiabatic in quantum theory was coined in 1928 by Born and Fock [173]. We will now explain the adiabatic concept and then derive the adiabatic condition for a quantum system [174–176].

When the conditions on a quantum mechanical system are changed rapidly, the process is considered diabatic (or non-adiabatic), meaning that the spatial probability density remains unchanged. On the other hand, when the parameters of a quantum mechanical system are changed very slowly, so that the system can readjust, this process is called adiabatic evolution. At the beginning of the evolution the initial state corresponds to one of the energy eigenstates, and at the end it corresponds to the same energy eigenstate, but potentially a different physical state, as the Hamiltonian has been changed.

The Hamiltonian will depend on a parameter $X(t)$ which is function of time (such as Rabi frequencies or detunings, experimentally). The goal will be the integration of the time dependent Schrödinger Equation ($\hbar = 1$) for a slow change of $X(t)$:

$$i \frac{d}{dt} |\psi(t)\rangle = \hat{\mathcal{H}}(X(t)) |\psi(t)\rangle. \quad (6.1)$$

We now expand in the instantaneous eigenstates of the time-dependent Hamiltonian,

$$\hat{\mathcal{H}}(X(t)) |n(X(t))\rangle = E_n(X(t)) |n(X(t))\rangle, \quad (6.2)$$

considering $E_n(X(t))$ the energy eigenvalues of the Hamiltonian. The state of the system can be written as

$$|\psi(t)\rangle = \sum_n a_n(t) |n(X(t))\rangle, \quad (6.3)$$

with

$$a_n(t) = \langle n(X(t)) | \psi(t) \rangle. \quad (6.4)$$

To generate the adiabatic wave function $|\psi(t)\rangle$, we solve the Schrödinger Equation ($\hbar = 1$) and substitute

$$\begin{aligned} i \frac{d}{dt} |\psi(t)\rangle &= \hat{\mathcal{H}}(t) |\psi(t)\rangle, \\ i \frac{d}{dt} \sum_n a_n(t) |n(X(t))\rangle &= \hat{\mathcal{H}}(t) \sum_n a_n(t) |n(X(t))\rangle, \\ \rightarrow i \sum_n \left(\frac{d}{dt} a_n(t) |n(X(t))\rangle + a_n(t) \frac{d}{dt} |n(X(t))\rangle \right) &= \hat{\mathcal{H}}(t) \sum_n a_n(t) |n(X(t))\rangle, \\ \rightarrow \langle m(X(t)) | \sum_n i \frac{d}{dt} a_n(t) |n(X(t))\rangle &= \langle m(X(t)) | \hat{\mathcal{H}}(t) \sum_n a_n(t) |n(X(t))\rangle \\ &\quad - \langle m(X(t)) | \sum_n a_n(t) i \frac{d}{dt} |n(X(t))\rangle. \end{aligned} \quad (6.5)$$

Then,

$$i \frac{d}{dt} a_m(t) = E_m(t) a_m(t) - \sum_n \langle m(X(t)) | i \frac{d}{dt} |n(X(t))\rangle a_n(t). \quad (6.6)$$

With $m \neq n$

$$\begin{aligned} \langle m(X(t)) | \frac{d}{dt} |n(X(t))\rangle &= \frac{\langle m(X(t)) | \frac{d}{dt} \hat{\mathcal{H}}(X(t)) |n(X(t))\rangle}{E_n(t) - E_m(t)}, \\ \rightarrow i \frac{d}{dt} a_m(t) &= \left(E_m(t) - \langle m(X(t)) | i \frac{d}{dt} |m(X(t))\rangle \right) a_m(t) \\ &\quad - \sum_{m \neq n} \frac{\langle m(X(t)) | \frac{d}{dt} \hat{\mathcal{H}}(X(t)) |n(X(t))\rangle}{E_n(t) - E_m(t)} a_n(t). \end{aligned} \quad (6.7)$$

For the adiabatic approximation, we drop the coupling terms, having then

$$i \frac{d}{dt} a_m(t) \approx \left(E_m(t) - \langle m(X(t)) | i \frac{d}{dt} |m(X(t))\rangle \right) a_m(t), \quad (6.8)$$

and the condition to say that $\hat{\mathcal{H}}(t)$ is changing very slowly will be

$$\left| \langle m(X(t)) | \frac{d}{dt} \hat{\mathcal{H}}(X(t)) | n(X(t)) \rangle \right| \ll |E_n(t) - E_m(t)|, \quad (6.9)$$

that is, as the Hamiltonian is modified, the system will remain in the same adiabatic eigenstate, provided that we vary the Hamiltonian in this sense slowly on timescales given by energy differences between the eigenstates.

There will be a finite probability of coupling to excited states depending on the separation of the eigenvalues. For a two-level system, this is now known as the Landau-Zener tunnelling effect [169]. The adiabatic derivation for a multilevel system was derived more than fifty years later in [170].

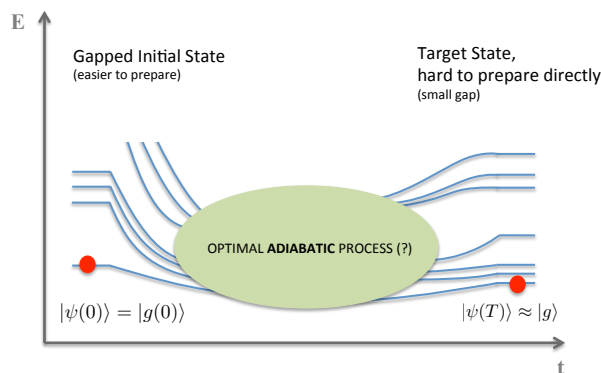


FIGURE 6.1: Adiabatic state preparation conceptual representation. We start with a state easy to prepare and with a big energy gap between the ground state and the first excited state. We let the Hamiltonian evolve in time slow enough that no excitation to the excited states will occur, and try to reach the target state (generally a state with a very small energy gap) with the highest fidelity.

As can be seen in Fig. 6.1, where an adiabatic ramp is represented, the gap between the ground state and the first excited state should be maximised at the beginning, to avoid any coupling to the excited states (e.g. a gapped state like a spin Mott). We are normally interested in final states with small gap, that is why they are so difficult to prepare.

It is critical to understand the scaling of the gap with the system size, in order to determine an optimal path for a specific adiabatic evolution. Some references using adiabatic state preparation in a similar context can be found for ultracold spinor atoms loaded in optical superlattices [177], polar molecules or Rydberg atoms in deep optical lattices [151], bosonic atoms in optical lattices [153, 178, 179], and fermionic atoms in optical lattices [148, 149, 152].

As noted in the work, e.g. of Sørensen et al. in [150], it is not only possible to connect ground states, but also gapped excited states via adiabatic state preparation. The time

scale is set by the gap between energy states, irrespective of whether we are dealing with the ground state or an excited state.

6.2 Antiferromagnetic state preparation using adiabatic ramps

As we have mentioned previously in the description of our models, two-component Hamiltonians can be realised by using two atomic species. However, experimentally two different hyperfine states of the same atom could be employed instead.

We consider particles loaded into an optical lattice in the regime where the lattice is sufficiently deep so that tunnelling can be neglected on experimental time scales.

In this section we are interested in creating an antiferromagnet in the case of attractive interactions in the spin model [99], for example, with ^7Li . In order to change the anisotropy for Rb, we need to be able to control the interactions by shifting the two different spin states apart (e.g. in a spin dependent-lattice), whereas for ^7Li we can already control the interactions (we can choose to work on a combination of states that are not magnetically sensitive). The extreme tuneability of ^7Li [180] opens up a very interesting field of research, where attractive interactions are achieved by Feshbach resonances (see Fig. 6.2).

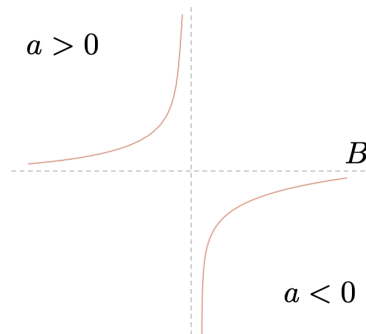


FIGURE 6.2: The inter-atomic interaction can be widely varied with a magnetic Feshbach resonance, via tunability of a magnetic field B , where a is the scattering length.

The **target** state will be the antiferromagnetic ground state of the following spin-1/2 XXZ Hamiltonian ($\hbar = 1$):

$$\hat{\mathcal{H}}_{AFM} = J \sum_{\langle i,j \rangle} (\hat{s}_i^x \hat{s}_j^x + \hat{s}_i^y \hat{s}_j^y) + (J + \Delta) \sum_{\langle i,j \rangle} \hat{s}_i^z \hat{s}_j^z. \quad (6.10)$$

An antiferromagnet is a state which is not easy to prepare directly, because of the small energy gap in the ground state. However, if we start with an initial state where all

our spins are up (i.e. $|\psi_0\rangle = |\uparrow\uparrow\uparrow\uparrow\uparrow\uparrow\dots\rangle$), we could use adiabatic ramps to achieve our target state. This initial state is very easy to prepare, as only optical pumping is needed. In order to study whether this protocol can be realised, two different proposals are investigated.

6.2.1 Model with a staggered magnetic field

The model Hamiltonian used for this simulation is:

$$\hat{\mathcal{H}}_{\text{ST}} = \hat{\mathcal{H}}_{\text{AFM}} + \hat{\mathcal{H}}_B + \hat{\mathcal{H}}_\Omega + \hat{\mathcal{H}}_\Gamma, \quad (6.11)$$

where

$$\hat{\mathcal{H}}_B = -h \sum_i \hat{s}_i^z, \quad (6.12)$$

with h a magnetic field in the z axis to ensure that in the initial state all spins are up (i.e. $|\psi_0\rangle = |\uparrow\uparrow\uparrow\uparrow\uparrow\uparrow\dots\rangle$),

$$\hat{\mathcal{H}}_\Omega = -\frac{\Omega}{2} \sum_i \hat{s}_i^x, \quad (6.13)$$

with Ω an anisotropy (weak magnetic field) in the x direction, and

$$\hat{\mathcal{H}}_\Gamma = \Gamma \sum_i (-1)^i \hat{s}_i^z, \quad (6.14)$$

with Γ a weak staggered magnetic field in z , following previous studies in [150, 152]. Hence, the total Hamiltonian will take the form:

$$\hat{\mathcal{H}}_{\text{ST}} = J \sum_{\langle i,j \rangle} (\hat{s}_i^x \hat{s}_j^x + \hat{s}_i^y \hat{s}_j^y) + (J + \Delta) \sum_{\langle i,j \rangle} \hat{s}_i^z \hat{s}_j^z - h \sum_i \hat{s}_i^z - \frac{\Omega}{2} \sum_i \hat{s}_i^x + \Gamma \sum_i (-1)^i \hat{s}_i^z. \quad (6.15)$$

The initial values for the parameters in the Hamiltonian are $h(0) \approx 17J$, $\Omega(0) = 3J$, and $\Gamma(0) \approx 3J$, and we apply the ramps for values of $\Delta/J \in [0.001, 1]$, and $J = 1$.

For an adiabatic ramp, the time evolution of the Hamiltonian is described as:

$$|\psi(t)\rangle = e^{-\frac{i}{\hbar} \hat{\mathcal{H}}_{\text{ST}} t} |\psi(0)\rangle. \quad (6.16)$$

We ramp the different additional terms (h, Ω, Γ) step by step, calculating the fidelity between the ground state for the target state at $t = T$, or $|\psi_{\text{targ}}\rangle$, and the final state of the evolution $|\psi(T)\rangle$, defined as:

$$F = |\langle \psi(T) | \psi_{\text{targ}} \rangle|^2. \quad (6.17)$$

The procedure of the total adiabatic ramp for this model consists of three parts.

Step 1: ramp $h/J \rightarrow 0$, by sweeping the detuning of an RF coupling between the two spins to zero.

This is an exponential ramp with a duration of $T_1 J = 20$.

Step 2: ramp $\Omega/J \rightarrow 0$. Here we will adiabatically turn off the effective magnetic field in x , by sweeping the Rabi frequency to zero.

Evidently, the Hamiltonian for this second evolution does not have the term in h/J , as this term has been ramped to zero in the first step. Our initial state will be the final state of the first ramp. This second time evolution is linear, and has a duration of $T_2 J = 7.5$.

Step 3: ramp $\Gamma/J \rightarrow 0$.

The Hamiltonian for this third evolution does not have the term in Ω/J , as this term has been ramped to zero in the second step. Our initial state will be the final state of the second ramp. The time evolution is also exponential, and has a duration of $T_3 J = 10$. The results for the fidelity at the end of the last ramp, $F_3 = |\langle \psi(T_3) | \psi_{\text{targ}} \rangle|^2$, are shown in Fig. 6.3.

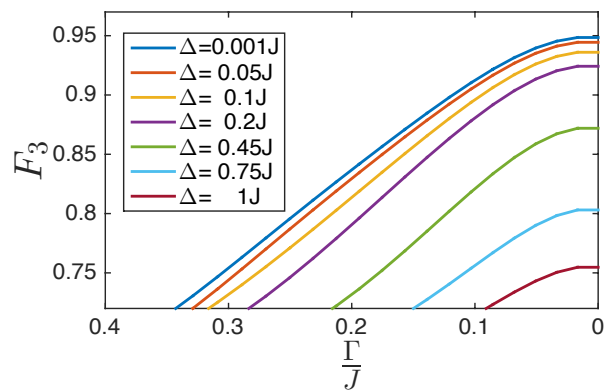


FIGURE 6.3: Fidelities, $F_3 = |\langle \psi(T_3) | \psi_{\text{targ}} \rangle|^2$, between the ground state at the end of the third ramp $|\psi_{\text{targ}}\rangle$ and the final state of the evolution $|\psi(T_3)\rangle$, for $M = 8$, and different values of Δ/J .

The fact that high fidelities, in this case with smaller values of the anisotropy Δ/J , are attained proves satisfactorily that the true ground state of the Hamiltonian can be achieved through an adiabatic path. Here we only study small system sizes using Exact Diagonalisation.

We can also calculate the spin-spin correlations and investigate the magnetic ordering, as in Fig. 6.4.

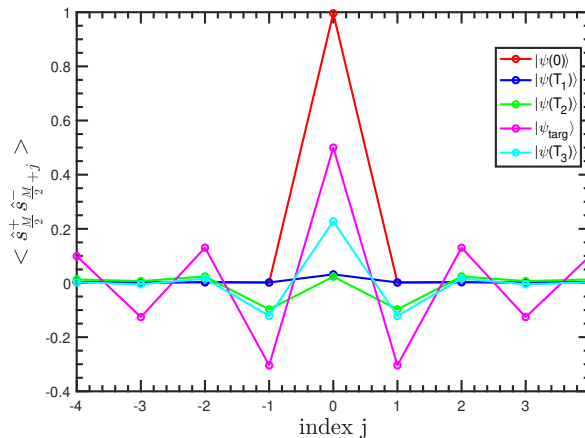


FIGURE 6.4: Spin-spin correlations, for $M = 8$, and $\Delta/J = 0.001$, with periodic boundary conditions.

The $\langle \hat{s}_i^+ \hat{s}_{i+j}^- \rangle$ correlations are calculated at the initial state $|\psi(0)\rangle$ (algebraic decay of the correlations), at the end of the first ramp $|\psi(T_1)\rangle$, at the end of the second ramp $|\psi(T_2)\rangle$, at the target state $|\psi_{\text{targ}}\rangle$, and at the end of the third ramp $|\psi(T_3)\rangle$, for $\Delta/J = 0.001$. The antiferromagnetic behaviour can be observed in the figure, where the spins point in different directions (alternating signs in the correlations) in the target state and in the final state at the end of the evolution (with faster decay of the correlations than in the target state).

An extension of this work would be to optimise the ramps and investigate the behaviour for bigger systems.

6.2.2 Model with a tilted magnetic field

Next we would like to prepare an antiferromagnetic state with the following Hamiltonian:

$$\hat{\mathcal{H}}_{\text{TILT}} = J \sum_{\langle i,j \rangle} (\hat{s}_i^x \hat{s}_j^x + \hat{s}_i^y \hat{s}_j^y) + (J + \Delta) \sum_{\langle i,j \rangle} \hat{s}_i^z \hat{s}_j^z - h \sum_i \hat{s}_i^z - \Omega \sum_i \hat{s}_i^x + W \sum_i i \hat{s}_i^z. \quad (6.18)$$

The difference with Eq. 6.15 is the magnetic field gradient in z (much easier to prepare experimentally than a staggered field) where W/J denotes the gradient strength.

Similarly to the previous model, we start with all of the spins up and we ramp each of the parameters to zero. The target state is again the ground state of Eq. 6.10.

Next, we will first study the ground-state properties of this model, with open boundary conditions, which will give us a deep understanding of the energy gap for the dynamical preparation process. We will then study the time dependence of this system starting

from a many-body state where all of the spins are up, and investigate the adiabatic preparation of antiferromagnetic states as the parameters are modified.

The question now is whether the parameters h/J , Ω/J and W/J can be time dependently ramped to zero, or close to zero, getting a final antiferromagnetic state. For that, we consider next trajectories in the $\Omega - W$ plane, for different values of h/J , to adiabatically transfer the initial state to an antiferromagnetic state.

6.2.2.1 Study of the energy gap

Firstly, we evaluate viable paths for the adiabatic transfer based on the size of the energy gap ΔE between the ground state and excited states. During the adiabatic ramps, ΔE has to remain as large as possible to restrain couplings (non-adiabatic transitions) to excited states of the effective model. The first step is to consider regions in the small scale of values for Ω/J and W/J , with a very small h/J , where we should get our antiferromagnetic target state in the ground state.

The next step is to identify the initial state, where we will have a paramagnet, as it is caused by the alignment with the magnetic field in z . In Table. 6.1 we summarise the choice of parameters in the initial and final steps of the adiabatic protocol.

TABLE 6.1: Summary of parameters regime for the initial and final state.

| Parameter | Initial state (paramagnet, PM) | Target state (antiferromagnet, AFM) |
|---------------------------------|--------------------------------|---|
| Δ/J (anisotropy) | Any Δ/J | $\Delta \simeq 0.5J$ (smaller Δ/J will lead to smaller gaps). We consider a final ramp in Δ/J to 0. |
| h/J (magnetic field in z) | Large ($h \geq 30J$) | Small ($h \in [0, 2.5J]$) |
| Ω/J (weak field in x) | $\Omega \geq 4.5J$ | $\Omega \in [0, 1J]$ |
| W/J (field gradient in z) | $W \geq 1J$ | $W \simeq 0J$ |

Fig. 6.5 shows the energy gap ΔE between the ground and the first excited state, for the Hamiltonian in Eq. 6.18, for a system size of $M = 14$, as a function of the parameters Ω/J and W/J , for a fixed value of $\Delta = 0.5J$, and $h = 0$, respectively. We consider our **target state** as the ground state for small Ω/J and W/J , with h/J between 0 and $2.5J$, and $\Delta = 0.5J$ (the final point of the third white line in Fig. 6.5).

6.2.2.2 Resulting ramps

In order to achieve an antiferromagnet at the end of the adiabatic passage, four different ramps are necessary. The total procedure of the total adiabatic ramp is summarised below.

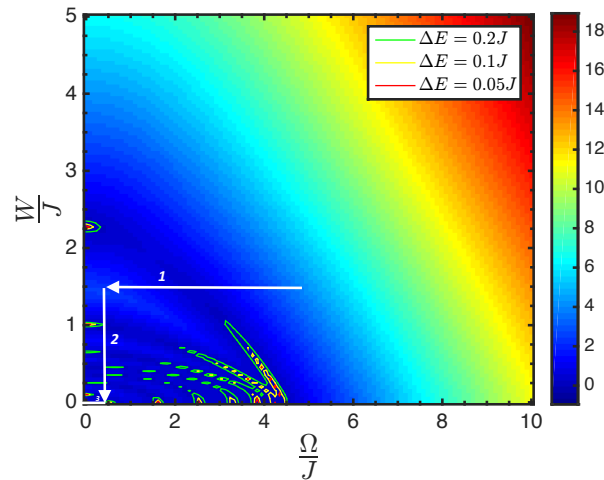


FIGURE 6.5: Energy gap ΔE between the ground state of the Hamiltonian and the first excited state, for $M = 14$, $\Delta = 0.5J$, and $h = 0$, as a function of Ω/J and W/J . Lines of constant energy gap ($\Delta E = 0.05J, 0.1J, 0.2J$) are marked in the plot. The white arrows indicate the segments of an adiabatic passage providing an antiferromagnetic ground state.

Step 1: ramp $h/J \rightarrow 0$, at a constant $\Omega(0) = 5J$ and $W(0) = 1.5J$, with $h(0) \simeq 50J$.

After an extensive study for different kinds of ramps, an exponential ramp is the most favourable one, with a total ramp time $T_1J = 20$.

Step 2: $\Omega \rightarrow 0.4J$, at a constant $W(0) = 1.5J$.

Our initial state will be the final state of the first ramp $|\psi(T_1)\rangle$. This will be a quadratic ramp with a total ramp time of $T_2J \simeq 200$.

Step 3: $W/J \rightarrow 0$, at a constant $\Omega = 0.4J$.

Our initial state will be the final state of the second ramp $|\psi(T_2)\rangle$. This ramp is also exponential with a total ramp time of $T_3J \simeq 2000$. This slow ramp is necessary due to the small energy ramp in this region, as we identified in our study.

Step 4: $\Omega/J \rightarrow 0$.

Our initial state will be the final state of the third ramp $|\psi(T_3)\rangle$. This ramp is linear, with a duration of $T_4J = 400$.

Furthermore, we investigate the results of an additional ramp in the anisotropy Δ/J .

Step 5: $\Delta/J \rightarrow 0$.

Our initial state will be the final state of the previous ramp $|\psi(T_4)\rangle$. This final ramp is also linear, with a total ramp time of $T_5J \simeq 700$.

We characterise the magnetic behaviour by evaluating the spin-spin correlations, in Fig. 6.6, as the end of the final ramp, where the alternating signs in the correlations show the antiferromagnetic ordering in the final state.

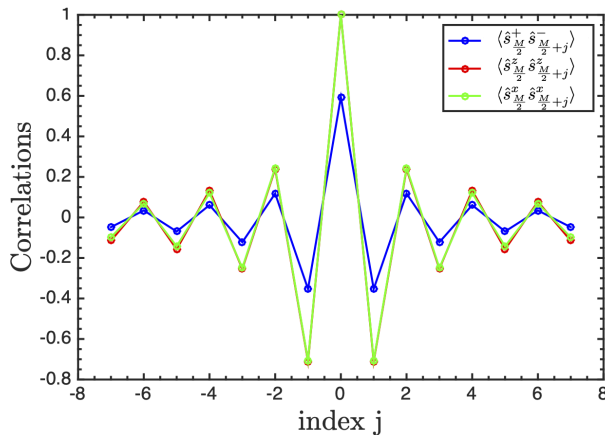


FIGURE 6.6: $\langle \hat{s}_{M/2}^+ \hat{s}_{M/2+j}^- \rangle$, $\langle \hat{s}_{M/2}^z \hat{s}_{M/2+j}^z \rangle$, and $\langle \hat{s}_{M/2}^x \hat{s}_{M/2+j}^x \rangle$ correlations, for $M = 14$, at the end of the final ramp, where all parameters are ramped to 0. The antiferromagnetic behaviour can be clearly observed.

As it has been demonstrated that the study works for small systems, next step is to analyse larger systems, closer to the system sizes used in experiments. To handle this many-body problem numerically, a DMRG could be implemented, by using Matrix Product States (MPS) representation. Furthermore, it would be important to investigate different approaches to be able to use ramps with a duration which could be realised in practise in experimental platforms with cold atoms in optical lattices. For example, in this case we also tried to ramp different parameters to 0 at the same time, and even all parameters at once, but unfortunately, the fidelities reached were very low.

6.3 Study of an XY-ferromagnet

We consider we work with a system where we can change U_{AB} relative to U_A and U_B . One specific experimental implementation to prepare magnetic states is by using spin dependent lattices. In this case, the two lattices are shifted relatively to each other allowing the tuning of the inter-component interaction, by changing the overlap of the spin-component's wavefunction on a lattice site [65]. This is the case of Rubidium, where we have combinations of hyperfine states that are magnetically sensitive.

In this section we study the preparation of XY-ferromagnetic states for the spin-1/2, by using adiabatic ramps. Adiabatic state preparation was considered previously for the spin-1 model in [153].

6.3.1 Adiabatic ramps for the spin-1/2 model

In the previous chapter, the rotation was done instantaneously, but in reality there would be a time involved. Experimentally, the symmetry break can be done by a transverse magnetic field. In this section, an adiabatic process in which the spins are rotated slowly in the presence of the interaction terms is evaluated. Experimentally, we suggest to create a spin-1/2 model with ^{87}Rb from a single component Mott insulator as a low entropy starting point. The model Hamiltonian used for the calculations is the following

$$\hat{\mathcal{H}}_{\text{XY}} = -J \sum_{\langle i,j \rangle} (\hat{s}_i^x \hat{s}_j^x + \hat{s}_i^y \hat{s}_j^y) - (J - \Delta) \sum_{\langle i,j \rangle} \hat{s}_i^z \hat{s}_j^z - h \sum_i \hat{s}_i^z - \frac{\Omega}{2} \sum_i \hat{s}_i^x. \quad (6.19)$$

For values of $\Delta \in [0.001, 1]$, and $J=1$, we apply:

a) magnetic field in the z-axis, h/J , to ensure that in the initial state all spins are up (i.e. $|\psi_0\rangle = |\uparrow\uparrow\uparrow\uparrow\uparrow\uparrow \dots\rangle$). Thus, the first step will be to adiabatically turn off this effective magnetic field in z (by sweeping the detuning of an RF coupling between the two spins to zero).

b) an anisotropy (very weak magnetic field) in the x direction, Ω . Here we will adiabatically turn off the effective magnetic field in x , by sweeping the Rabi frequency to zero.

The initial values for the parameters are $h = 50J$ and $\Omega = 1.1J$. The procedure of the total adiabatic ramp consists then in two parts:

Step 1: ramp $h/J \rightarrow 0$.

This ramp is linear and has a total time $T_1 J = 500$.

Step 2: ramp $\Omega/J \rightarrow 0$.

We start with the state value of the final state of the first ramp $|\psi(T_1)\rangle$. This second time evolution is also linear, and has been computed for different ramp durations. The results are summarised in Fig. 6.7, for different anisotropy values, and a system of $M = 20$ spins, calculated using Matrix Product State techniques.

Fig. 6.7 shows that at the end of the ramps fidelities closer to 1 are attained for $\Delta > 0.5J$.

In the next section we introduce the concept of Quantum Fisher Information in metrology and how we can apply it to our models. We also considered alternative approaches to have durations for the ramps within experimental parameters.

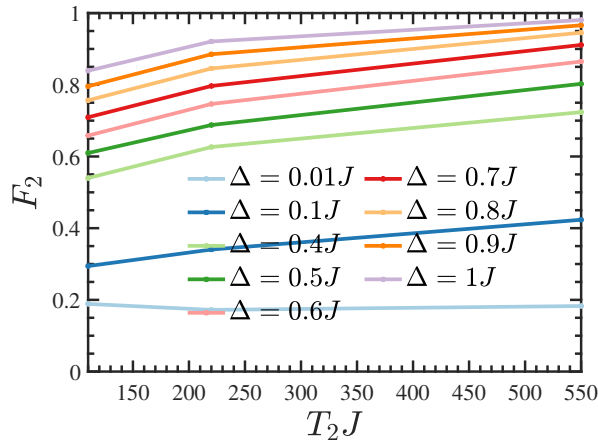


FIGURE 6.7: Fidelities between the target state $|\psi_{\text{targ}}\rangle$, the ground state at the end of the second ramp, and the final state of the evolution $|\psi(T_2)\rangle$, for $M = 20$, and different values of Δ and ramp times. The calculations were done with bond dimension for the MPS calculations $D = 128$.

6.4 Spin models and metrology

We now show how the models can give rise to entanglement that is useful for quantum enhanced metrology, and characterise the states we can prepare in terms of their QFI for collective measurements with Ramsey spectroscopy.

6.4.1 Quantum Fisher Information

Arising from interferometry, the Quantum Fisher information determines the optimal sensitivity (with the right measurement choice) of a state to a given transformation \hat{G} . It corresponds to the upper bound of the Fisher Information over all possible generalised quantum mechanical measurements, providing a tool to measure many-body entanglement.

In order to provide a definition for it, the simplest way is to consider a more general concept of Fisher information \mathcal{I} , arising from the context of Quantum Estimation Theory [181, 182]. Having a given state, described by a density operator $\hat{\rho}$, we perform a measurement generated by \hat{G} , so that the state transforms as $\hat{\rho}(\theta) = e^{-i\theta\hat{G}}\hat{\rho}e^{i\theta\hat{G}}$, with the phase shift θ that we would like to measure. We can define an estimator $\theta_{\text{est}}(\vec{\mu})$ which is a function of the outcomes $\vec{\mu} = \mu_1, \dots, \mu_m$ with m the number of measurements performed. The error associated with this estimator is subject to the Cramér-Rao bound [183, 184]:

$$\Delta\theta_{\text{est}} \geq 1/\sqrt{m\mathcal{I}}, \quad (6.20)$$

where $\Delta\theta_{\text{est}}$ is the variance of our estimator, and the classical Fisher information is

$$\mathcal{I} = \sum_{\mu_i} \frac{1}{p(\mu_i|\theta)} \left(\frac{\partial p(\mu_i|\theta)}{\partial \theta} \right)^2, \quad (6.21)$$

with $p(\mu_i|\theta)$ the conditional probability of measuring the value μ_i with the phase shift produced by the transformation in θ .

By maximizing \mathcal{I} over the total set of m measurements we obtain the QFI $\mathcal{I}_{\mathcal{Q}}$:

$$\mathcal{I}_{\mathcal{Q}}[\hat{\rho}, \hat{G}] = 2 \sum_{k,k'} \frac{(\alpha_k - \alpha_{k'})^2}{\alpha_k + \alpha_{k'}} |\langle k|\hat{G}|k'\rangle|^2, \quad (6.22)$$

with $\hat{\rho} = \sum_k \alpha_k |k\rangle\langle k|$ and the sum only including terms that fulfil $\alpha_k + \alpha_{k'} > 0$.

Then, we can restate the Cramér-Rao bound as:

$$\Delta\theta \geq 1/\sqrt{m\mathcal{I}} \geq 1/\sqrt{m\mathcal{I}_{\mathcal{Q}}}. \quad (6.23)$$

In the models described in this work, where we have many spins, in order to describe an ensemble of M spins, we can introduce the collective spin vector $\hat{\mathbf{J}} = \{\hat{J}_x, \hat{J}_y, \hat{J}_z\}$, where [184]

$$\hat{J}_\mu = \frac{1}{2} \sum_{l=1}^M \hat{\sigma}_\mu^{(l)}, \quad (6.24)$$

with $\hat{\sigma}^{(l)}$ the Pauli operator for the particle l and $\mu = x, y, z$ axis.

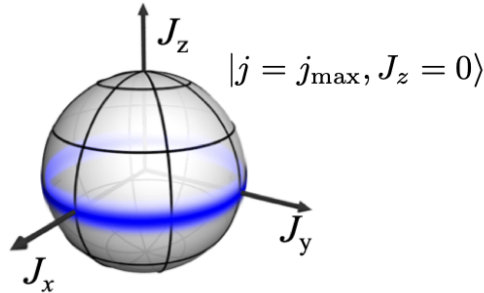


FIGURE 6.8: The final state completely symmetric in spin (or Dicke state), around the equator of the Bloch sphere (representation for the spin-1/2 case), it is a good candidate for interferometry beyond the shot noise limit.

Imposing the condition that our state lies in the equator of the Bloch Sphere (Fig. 6.8) with $J_z = 0$, a possible transformation would be a coherent spin-flip from the xy -plane, whose generator is basically a collective spin operator in x :

$$\hat{G} = \hat{J}_x = \frac{1}{2} \sum_{l=1}^M \hat{\sigma}_x^{(l)}. \quad (6.25)$$

With pure states we only need to compute the variance of the expectation value of the operator of our given transformation [183], and thus in our case

$$\mathcal{I}_Q = 4\Delta\hat{G} = 4\Delta\hat{J}_x. \quad (6.26)$$

That is, we compute the QFI in our models as

$$\mathcal{I}_Q = 4(\langle\hat{J}_x^2\rangle - \langle\hat{J}_x\rangle^2) = 4\left(\sum_{l,l'}\langle\hat{S}_l^x\hat{S}_{l'}^x\rangle - \sum_l\langle\hat{S}_l^x\rangle^2\right). \quad (6.27)$$

The QFI is calculated analogously for the spin-1/2 with operator \hat{s}_l^x .

In these schemes, the sensitivity on the phase estimation is restricted to the shot noise limit, with $\Delta\theta \geq 1/\sqrt{mM}$, being M the total number of spins. However, these can be overcome by the introduction of entanglement in the system up to the Heisenberg scaling with $\Delta\theta \geq 1/\sqrt{mM}$, affecting the scaling of \mathcal{I}_Q , from $\mathcal{I}_Q \sim M$, in the shot noise regime, to $\mathcal{I}_Q \sim M^2$ for the Heisenberg scaling.

We use \mathcal{I}_Q as a tool to measure many-body entanglement. Thus, \mathcal{I}_Q will increase if the system cannot be factorised and for a larger Hilbert space (larger M).

The expression for the maximum QFI that we expect for a given system size M will then be, using angular momentum theory

$$\mathcal{I}_{Q_{\max}} = \frac{J(J+1)}{2}, \quad (6.28)$$

and for the respective models

$$\mathcal{I}_{Q_{\max}}^{\text{SP12}} = M\left(\frac{M}{2} + 1\right), \quad (6.29)$$

and

$$\mathcal{I}_{Q_{\max}}^{\text{SP1}} = 2M(M+1). \quad (6.30)$$

The question now is how close we are to $\mathcal{I}_{Q_{\max}}$ in both models, and whether we have indeed useful entanglement, and go beyond the shot noise limit.

6.4.2 Characterising the ground state: useful entanglement for metrology

We know that final states completely symmetric in spin are good candidates for interferometry beyond the shot noise limit, and we want to show that these systems can be prepared with bosons in optical lattices.

As a tool to probe the final state, we evaluate the QFI for different values of the anisotropies $u/J, \Delta/J$ in the spin-1 and spin-1/2 model, with Hamiltonians

$$\hat{\mathcal{H}}_{\text{SP1}} = -J \sum_{\langle j,l \rangle} \hat{\mathbf{S}}_j \cdot \hat{\mathbf{S}}_l + u \sum_l (\hat{S}_l^z)^2, \quad (6.31)$$

for the spin-1, and

$$\hat{\mathcal{H}}_{\text{SP1/2}} = -J \sum_{\langle j,l \rangle} \hat{s}_j \cdot \hat{s}_l + \Delta \sum_{\langle j,l \rangle} \hat{s}_j^z \hat{s}_l^z, \quad (6.32)$$

for the spin-1/2, respectively. We also study how \mathcal{I}_Q scales with the system size M . A large \mathcal{I}_Q will justify a better accuracy, and thus less uncertainty in the characterisation of the ground state.

For both models the QFI has been calculated for different anisotropy values ($\Delta/J, u/J$ in each case), in Fig. 6.9.

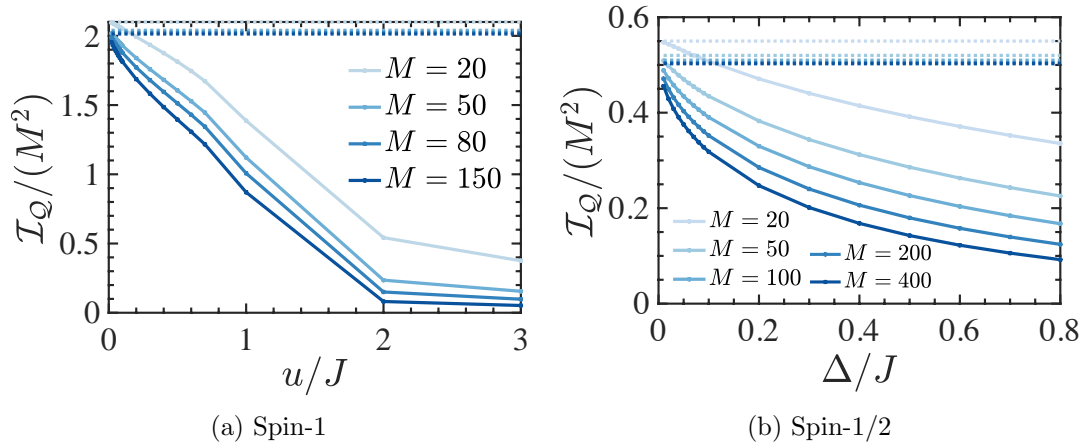


FIGURE 6.9: Quantum Fisher Information \mathcal{I}_Q versus anisotropy for the ground state of the Hamiltonian for the (a) spin-1 and (b) spin-1/2 model, for different number of spins. As the anisotropy decreases we get closer to the maximum QFI value ((6.30), dotted lines). The values are calculated for different system sizes by using MPS. The bond dimension for the MPS calculations was $D = 128$ for $M \leq 200$, and $D = 256$ for bigger systems, with open boundary conditions.

For the spin-1/2 we are in the same regime when $\Delta/J > 0$. However, for the spin-1 case, once we enter in the spin-Mott regime at $u \simeq 0.62J$, as the particles are localised, increasing u/J decreases much more the value of \mathcal{I}_Q .

We have also evaluated the scaling by fitting the values of \mathcal{I}_Q for different system sizes to a curve of the form

$$\mathcal{I}_Q \propto A \cdot M^\alpha + C, \quad (6.33)$$

being α the scaling factor and A, C constants.

In Fig. 6.10, we show that the fit obtained has very low errors for all systems, having the highest final scaling factor α . We present here just the application to the spin-1/2 model, because the case for spin-1 is completely equivalent. We also take a small value of the anisotropy $\Delta = 0.01J$, as we already know smaller anisotropy gets closer to the Heisenberg scaling.

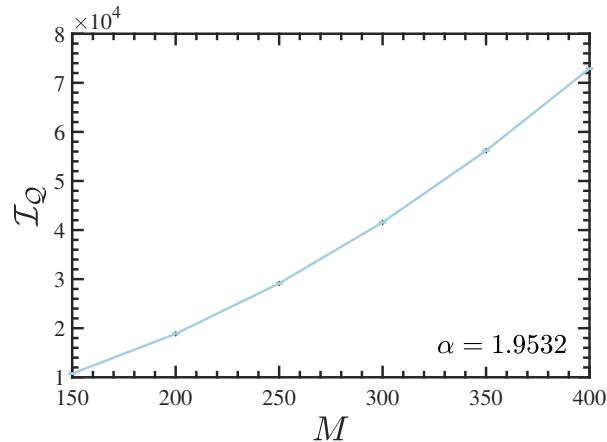


FIGURE 6.10: Spin-1/2 Model. Fitting of the scaling function $A \cdot M^\alpha + C$ for an anisotropy $\Delta = 0.01J$. The data points are the black dots, and the fitting is light blue.

The results for both models are summarised in Fig. 6.11, where we show the scaling with system size and the equivalent scaling parameter α . In the regime where we have larger nearest-neighbours interactions (smaller anisotropy), we see a larger value of \mathcal{I}_Q , getting closer to the classical picture. We also get closer to the Heisenberg scaling in the limit of anisotropies $u/J, \Delta/J \rightarrow 0$. At larger anisotropies, we found less precision and thus more uncertainty.

6.4.2.1 Case with negative interactions

In this section we investigate the QFI for the spin-1/2 case with negative interactions, thus an antiferromagnet AFM in the ground state.

The results are shown in Fig. 6.12. As in the spin-Mott, we see that \mathcal{I}_Q is very small. However, as we increase the Δ/J , we “turn-on” the interactions and that is why we see a slight increase in \mathcal{I}_Q . Here there is no entanglement, and therefore the scaling with system size will not give any useful information.

An open question remains to investigate other types of measurement, or transformation, that could be made with antiferromagnetic states that are useful for metrology.

In the next sections we will focus on the study of regimes with high Quantum Fisher Information, which implies useful entanglement for practical applications.

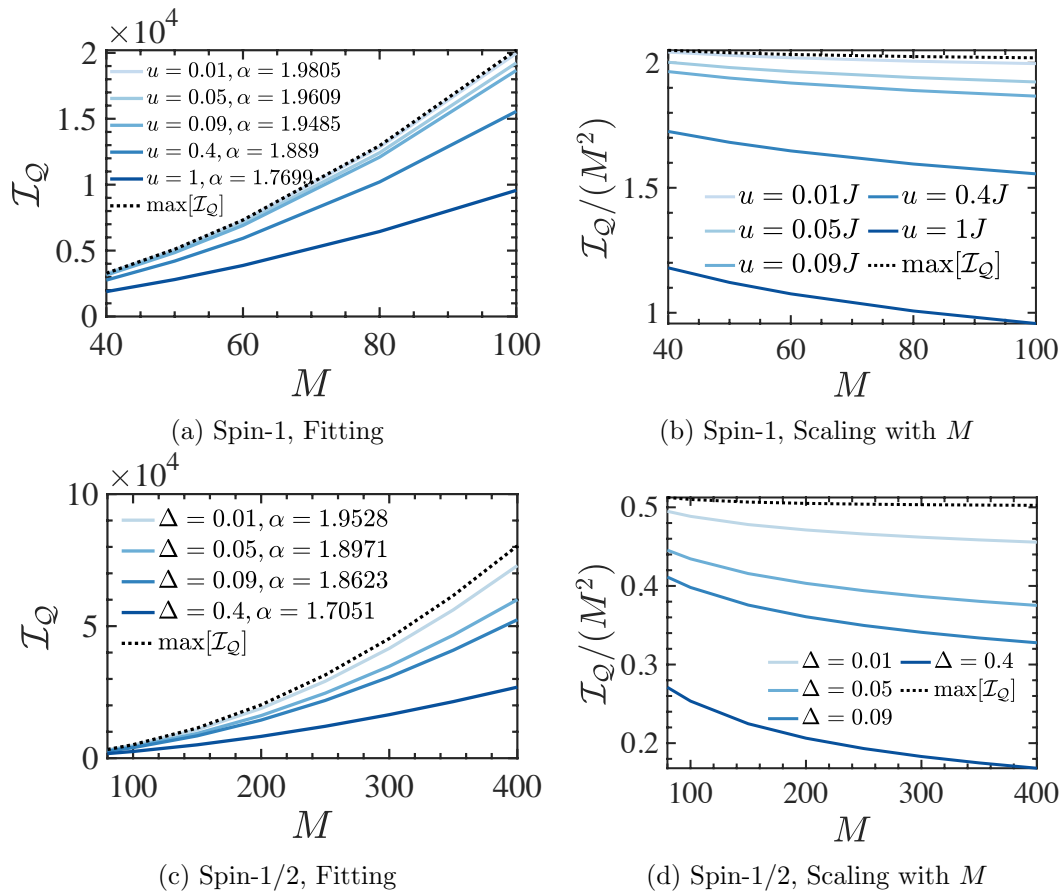


FIGURE 6.11: Scaling of \mathcal{I}_Q for the ground state of the Hamiltonian for the (a,b) spin-1 and (c,d) spin-1/2 model. In (a,c) we show the resulting fitted curves of the QFI versus system size, where we can see that the changing scaling factor α indicates a different scaling for different anisotropy. The maximum QFI is depicted as black dashed lines. In (b,d) we clearly see that as the anisotropy $\Delta/J, u/J \rightarrow 0$ the scaling is closer to the Heisenberg scaling, that is, $\alpha \rightarrow 2$ and $\mathcal{I}_Q \sim M^2$. The bond dimension for the MPS calculations was $D = 128$ for $M \leq 200$, and $D = 256$ for bigger systems, with open boundary conditions.

6.4.3 Adiabatic State Preparation

As we have seen earlier in the chapter, we can prepare our target states by starting with low entropy states with a large energy gap ramps and then ramp to states with a much smaller gap. However, it is critical to understand the scaling of the gap with the system size, and thus it is convenient to find an optimal path for a specific adiabatic evolution. Understanding the gap in many-body systems and the limit of adiabaticity has been a remaining open question [185]. The use of different kinds of ramps in order to choose the optimal one is a recurrent method, in order to achieve ramp times that are feasible experimentally [186].

In order to have a successful ramp useful for metrology, we aim at a duration of the experiment between 0.5 and 0.75 seconds. For our systems, where we have cold atoms

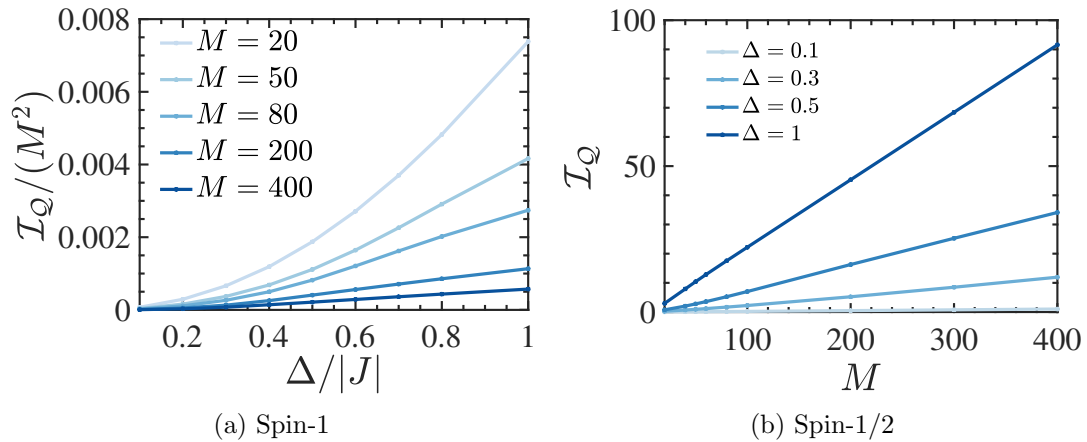


FIGURE 6.12: (a) Quantum Fisher Information \mathcal{I}_Q for the antiferromagnetic ground state of the Hamiltonian (spin-1/2 model) with negative interactions, vs different values of the anisotropy Δ/J . (b) \mathcal{I}_Q versus system size, where we see the scaling is linear (thus the parameter α will be closer to the shot noise limit). The bond dimension for the MPS calculations was $D = 128$ for $M \leq 200$, and $D = 256$ for bigger systems, with open boundary conditions.

in optical lattices, typically the tunnelling for the atomic species used in the experiments we are interested (K, Rb, and different for other species such as Cs) is of the order or $1 - 5$ ms ($t \simeq 1000$ Hz). In our model with a very low tunnelling in comparison with the interactions (otherwise perturbation theory would not work) we are talking of a ratio of around $t \simeq 1/8$ to $1/10 U$.

The superexchange will be of the order of 10 ms, that is, we are considering ideal theoretical times of $tJ = 0.5 \cdot 100 = 50$. In the experiments, we expect small differences with the theory. There are ways to be faster in the experiment (e.g. lighter atoms, shallower lattice), but here we want to investigate theoretical approaches to reach those experimental time scales.

This control is essential for the development of quantum technologies [187]. However, it is not always easy to find a ramp sufficiently slow to maintain adiabaticity and at the same time within experimental limitations. One approach is to use shortcuts to adiabaticity, an alternative providing a trade-off between the speed of the ramp and the energetic cost [188–190]. Unfortunately, the complexity of many-body physics with many degrees of freedom can be difficult to control.

Another alternative is the use of optimal control techniques, which have been used in chemistry and physics for a number of years [191, 192]. It is indeed this control at the quantum scale, at the atomic and molecular level, where numerous groups have targeted their efforts, [193–195], which pioneered new ways to apply time-dependent density matrix renormalisation group algorithms to quantum simulations, [196], and/or quantum trajectories, [197].

In the next section we present some alternative optimisation methods, to obtain an adiabatic ramp in realistic experimental times ².

From now on, and in the rest of the chapter, we focus on the spin-1/2 model, as we mentioned that adiabatic state preparation (without the Fisher Information) was considered previously for the spin-1 model in [153]. Further, despite having studied different regimes, we concentrate now on the XY-ferromagnetic regime. Following other works [179, 198], an alternative approach focuses on the adiabatic preparation and the study of many-body dynamics for the generation of antiferromagnetically ordered states.

6.4.3.1 Ramp in $\Delta \neq 0$: Optimal Control

We investigate the preparation of the ground state of the spin-1/2 XXZ model with a small number of spins, represented by the Hamiltonian in Eq. 3.15.

Beginning with all spins in a superposition of

$$\prod_i \frac{|\uparrow\rangle_i + |\downarrow\rangle_i}{\sqrt{2}}, \quad (6.34)$$

with a large coefficient of Ω/J (magnetic field in the x direction) in \hat{s}^x , we want to decrease this coefficient to zero, at a fixed non-zero anisotropy Δ/J . Experimentally, the effective magnetic field in x will be turned off adiabatically, by sweeping the Rabi frequency to zero.

That is, we start with the following Hamiltonian:

$$\hat{\mathcal{H}}'_{\text{SP1/2}} = -J \sum_{\langle i,j \rangle} (\hat{s}_i^x \hat{s}_j^x + \hat{s}_i^y \hat{s}_j^y) - (J - \Delta) \sum_{\langle i,j \rangle} \hat{s}_i^z \hat{s}_j^z - \Omega \sum_i \hat{s}_i^x, \quad (6.35)$$

and we want to ramp $\Omega \rightarrow 0$ with a ramp time within experimental limitations.

We tried different ramps (linear, exponential, polynomial) but none of them worked in a relatively short time, or times relevant for experiments, as we always got ramps of $TJ \approx 200 - 300$.

The Hamiltonian can be expressed in terms of the eigenstates:

$$\hat{\mathcal{H}}'_{\text{SP1/2}} |\phi_l\rangle = E_l |\phi_l\rangle, \quad (6.36)$$

considering E_l the energy eigenvalues of $\hat{\mathcal{H}}$.

²Part of the work in this section contributed to the publication [56].

The non-adiabatic transitions states are the eigenstates of the instantaneous Hamiltonian:

$$|\psi\rangle = \sum_l C_l(t) |\phi_l(t)\rangle. \quad (6.37)$$

From the adiabaticity condition, we say that if $\hat{\mathcal{H}}'_{\text{SP1/2}}(t)$ is changing very slowly such that

$$|\langle \phi_j(t) | \frac{d}{dt} \hat{\mathcal{H}}'_{\text{SP1/2}}(t) | \phi_l(t) \rangle| \ll |E_l(t) - E_j(t)|, \quad (6.38)$$

then there will be no coupling between different energy eigenstates. As the Hamiltonian is modified, the system will remain in the same state.

Now, considering the coefficients as

$$C_l(t) = \frac{\langle \phi_j(t) | \frac{d}{dt} \hat{\mathcal{H}}'_{\text{SP1/2}}(t) | \phi_l(t) \rangle}{E_l(t) - E_j(t)}, \quad (6.39)$$

we want to find a function $g(t)$ proportional to this energy gap ΔE .

We know that the energy gap is very small when Ω/J gets very small. The first thing is to study the energy gap as a function of Ω/J , and we show this study for $M = 20$ using Matrix Product States in Fig. 6.13.

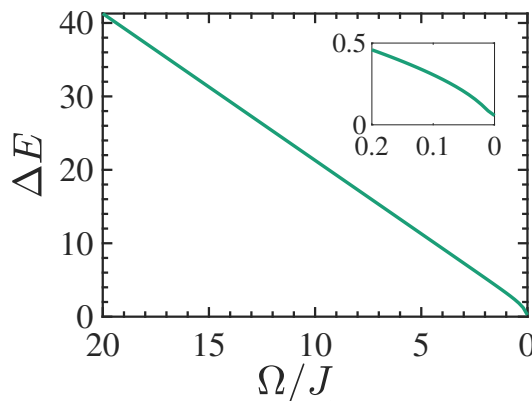


FIGURE 6.13: Energy gap ΔE between the ground state of the Hamiltonian and the first excited state, for $M = 20$, $\Delta = 0.8J$ and different values of Ω/J . The inset shows the behaviour for smaller values of Ω/J . The smallest value of the gap here for $\Omega = 0$ is $\Delta E = 0.057$. For smaller anisotropy it gets even smaller, and for $\Delta = 0.1J$ the gap is $\Delta E = 0.0056$.

Now that we know how the energy gap behaves, we want to find the control function $g(t)$ which will satisfy

$$\frac{\frac{d}{dt}g(t)}{\Delta E} \sim \text{constant}, \quad (6.40)$$

thus,

$$\int_{g(t_1)}^{g(t_2)} \frac{1}{\Delta g(t)} dg = \int_{t_1}^{t_2} dt. \quad (6.41)$$

We start by mapping our energy gap and write a function such as

$$g(t + dt) = g(t) + dt \cdot C \cdot \Delta g(t), \quad (6.42)$$

where C is a constant, satisfying

$$\frac{d}{dt}g(t) = -C\Delta g(t), \quad (6.43)$$

and with $g(0) = 1$ and $g(TJ) = 0$, we start running the function, from $C = 1$ until we get a value of C where $g(TJ = 0) \simeq 0$.

We run the algorithm for different ramp times and different number of atoms, and we summarise the results in Fig. 6.14. As we can see in the figure, we still need to use longer ramps to attain high fidelities in systems of experimental system sizes.

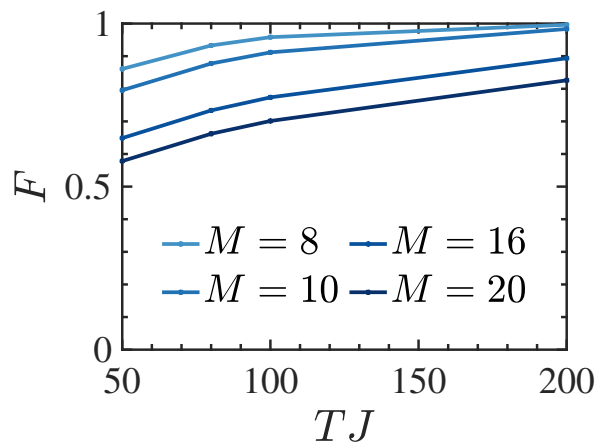


FIGURE 6.14: Fidelity achieved in the Ω/J ramp, for different system size M , and different ramp times, using the optimised ramp $g(t)$ proportional to the energy gap. All these results are for $\Delta = 2J$. Eventually, even for bigger system sizes the reached fidelity will be closer to 1, but the times will be extremely long, not attainable experimentally.

We then decided to use optimal control by evaluating a set of functions such that

$$g(t) = \sum_l C_l f_l(t, \Theta_l), \quad (6.44)$$

with Θ_l a parameter and f_l the optimal control functions, where we fixed the duration of the evolution, i.e. the length of the ramp. To do this, we parameterise our time-dependent ramp as $\Omega(t) = \Omega_0 g(t)$ with an initial $\Omega_0 = 10J$. For our optimisation the optimal control functions are based on Legendre polynomials, which are a type of Fourier series that form a complete orthogonal system over the interval $[-1, 1]$. We use a basis of 10 Legendre polynomials and the nonlinear optimisation function *fmincon* in *MATLAB*[®].

The figure of merit with which we quantify success in this case is the fidelity between the ground state (target state) of $\hat{\mathcal{H}}'_{\text{SP1/2}}$, or $|\psi_{\text{targ1}}\rangle$, and the final state of the evolution $|\psi(T_1)\rangle$ at $t = T_1$, defined as:

$$F = |\langle \psi(T_1) | \psi_{\text{targ1}} \rangle|^2. \quad (6.45)$$

In the algorithm we specify the sensitivity of the result, implying that the final fidelity must be greater than a certain value, and we specify $F \geq 0.9$.

Firstly, we study the algorithm for small system and compare with the previous results. We can see this comparison for small systems in Fig. 6.15, for two different values of Δ/J and a ramp duration of $TJ = 50$, and where we have:

- in purple results for a linear ramp,
- in orange results for a ramp proportional to the energy gap (as discussed above),
- in green results for this new approach using optimal control based on Legendre polynomials.

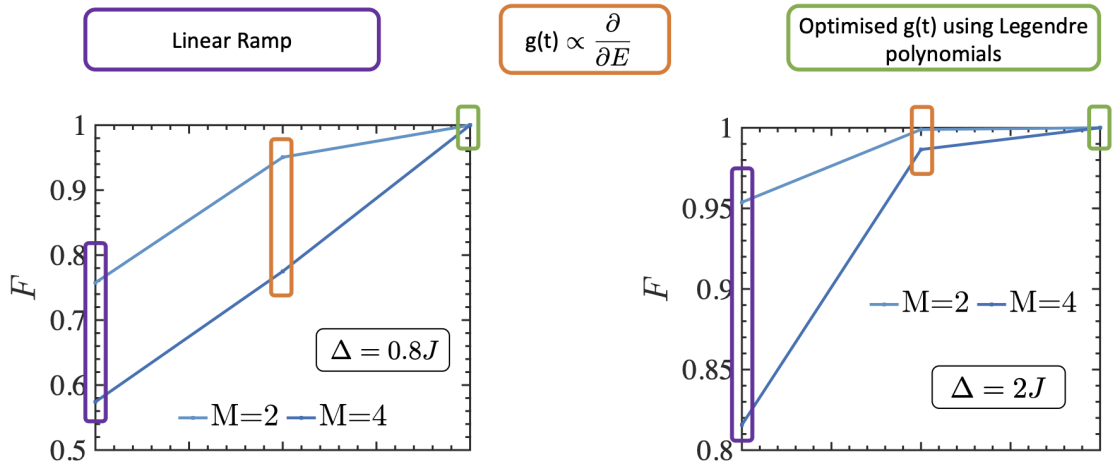


FIGURE 6.15: Fidelity results for different kind of ramps for the spin-1/2 Hamiltonian where we ramp $\Omega \rightarrow 0$, for two different values of the anisotropy (a) $\Delta = 0.8J$ and (b) $\Delta = 2J$, for different system sizes M , and ramp time of $TJ = 50$.

We see a clear improvement with the last optimisation algorithm, and next we will apply it to bigger system sizes.

We call the optimal ramp g_{opt} , and we show the results in Fig. 6.16 for different system sizes and two anisotropy values Δ/J (high values in order to attain higher fidelities with this protocol). It works so well because some excited states are populated during the quick evolution and land exactly on the ground state at the final moment of time. However, the cost of this is quite enormous, and we do not show the ramp for $M = 20$ and $\Delta = 0.8J$, as the time needed to find the optimal ramp exceeded our limitation.

We believe the explanation is that it grows because the Hilbert space grows as well as the number of solutions.

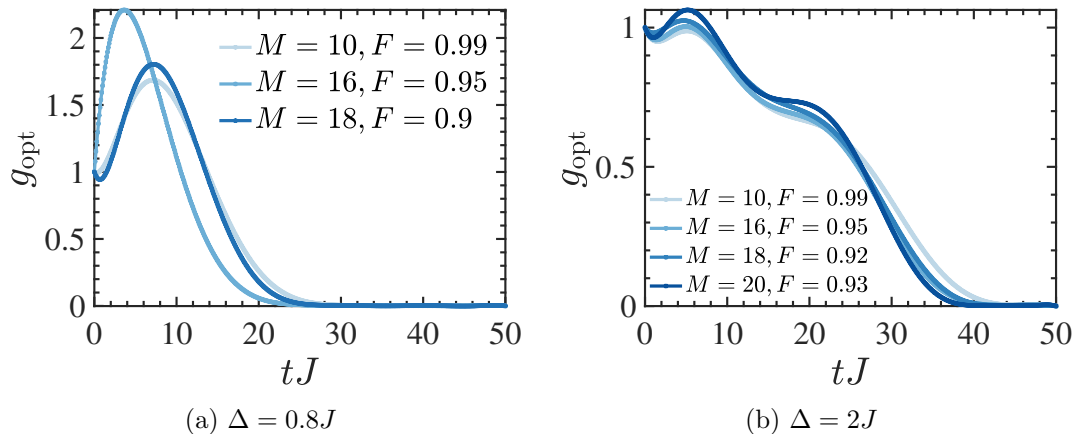


FIGURE 6.16: Optimised ramps for the Hamiltonian in 6.35 where we ramp the magnetic field in the x direction Ω/J to 0, for two different values of the anisotropy (a) $\Delta = 0.8J$ and (b) $\Delta = 2J$, for different system sizes M .

6.4.3.2 Ramp to $\Delta = 0$

We are interested in evaluating the perfect XY-ferromagnet in the presence of a very small anisotropy Δ/J , as we know from section 6.4.2 that is the regime close to the Heisenberg scaling, which is useful for metrology.

Here we ramp the anisotropy Δ/J and we evaluate the fidelity and the Quantum Fisher Information \mathcal{I}_Q during the ramp. We start with the ground state $|\psi_0\rangle$ of the Hamiltonian in (3.15) with a specific value of Δ/J , which will be prepared following the protocol described in the last section. We then ramp the anisotropy linearly, as $\Delta(t) = \Delta - \beta t$, from Δ/J at $tJ = 0$ to Δ_T/J at time $t = T$, for different values of β , and different final values of the anisotropy Δ_T .

The fidelity between the target state $|\psi_{\text{targ}}\rangle$ (the ground state of the Hamiltonian where $\Delta = \Delta_T$) and the final state of the evolution $|\psi(T)\rangle$ will then be:

$$F_{\Delta_T} = |\langle \psi(T) | \psi_{\text{targ}} \rangle|^2. \quad (6.46)$$

In Fig. 6.17 we evaluate the final fidelity for different ramp times and different system sizes M , for two particular initial and final values of the anisotropy Δ_T/J . In agreement with the adiabatic theorem, the time scale required for the ramp to be adiabatic depends on the size of the system. Furthermore, we identified how trying to reach lower final anisotropies becomes much harder with the system size. However, for typical experimental ramp times and system sizes we can still reach high fidelities up to a value of Δ_T

where we know from Fig. 6.9 the scaling is close to the Heisenberg limit, which means we can still prepare these high entangled states useful for precision measurements with high fidelity.

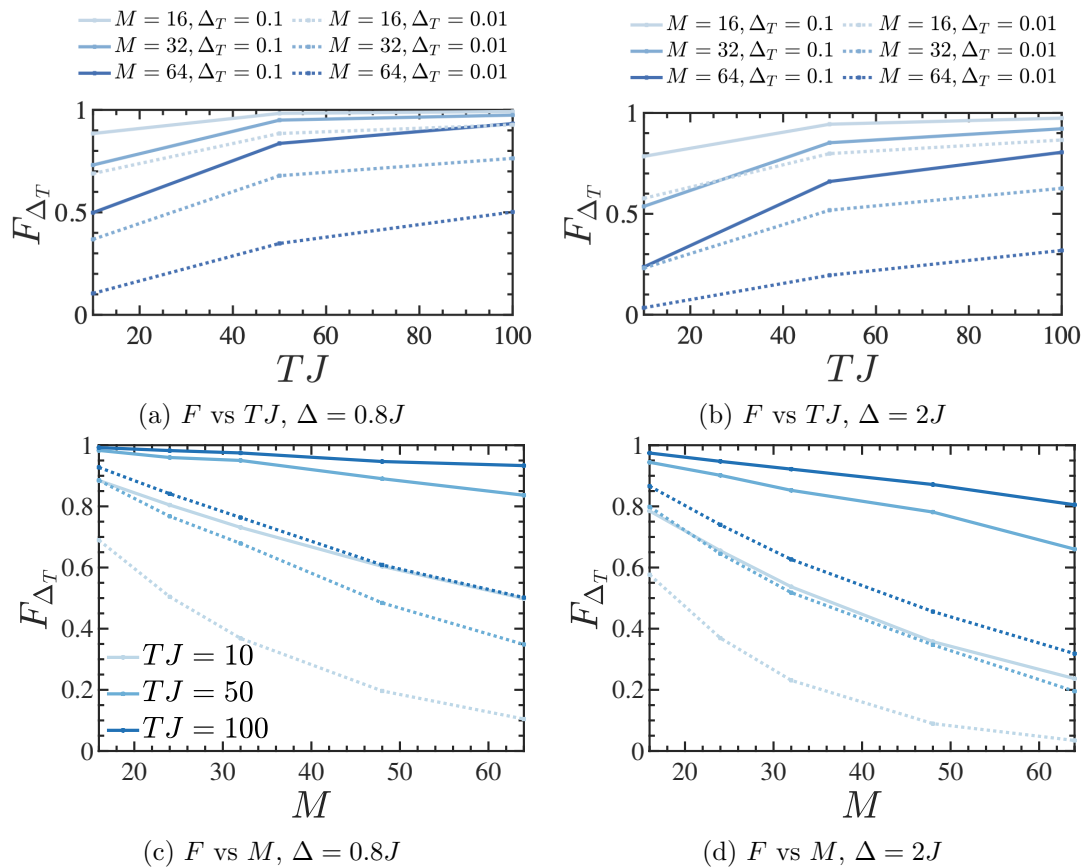


FIGURE 6.17: Fidelities between the ground state at the end of the ramp in the anisotropy Δ/J for the spin-1/2 model. We consider two different initial anisotropy values (a,c) $\Delta = 0.8J$ and (b,d) $\Delta = 2J$. We also evaluate the ramps with two different final values of Δ_T/J (solid lines $\Delta_T = 0.1J$, dotted lines $\Delta_T = 0.01J$), for different ramp times TJ and system sizes M . We can see that the highest value of the fidelity at the end of the ramp happens with the largest ramp, being $TJ = 100$, following the adiabatic theorem. We also show how it is harder to target a lower Δ_T , and how the final fidelity decreases with system size. The calculations were done with bond dimension for the MPS calculations $D = 128$, and open boundary conditions.

We also evaluate the QFI as in (6.27) (compared with its maximum value (6.30)) in Fig. 6.18, where we identify that, contrary to the result with the fidelity, the final anisotropy has an insignificant role on the behaviour of \mathcal{L}_Q with ramp time and system size. However, we again see that the ramps are more robust with an initial fidelity $\Delta = 0.8J$. Thus, we believe the procedure of preparing the Hamiltonian with $\Delta = 0.8J$ in (6.35), followed by a ramp in Δ/J to a final value of $\Delta = 0.1J$, will prepare an XY-ferromagnet with a high entangled ground state that can be used for measurement schemes such as Ramsey spectroscopy.

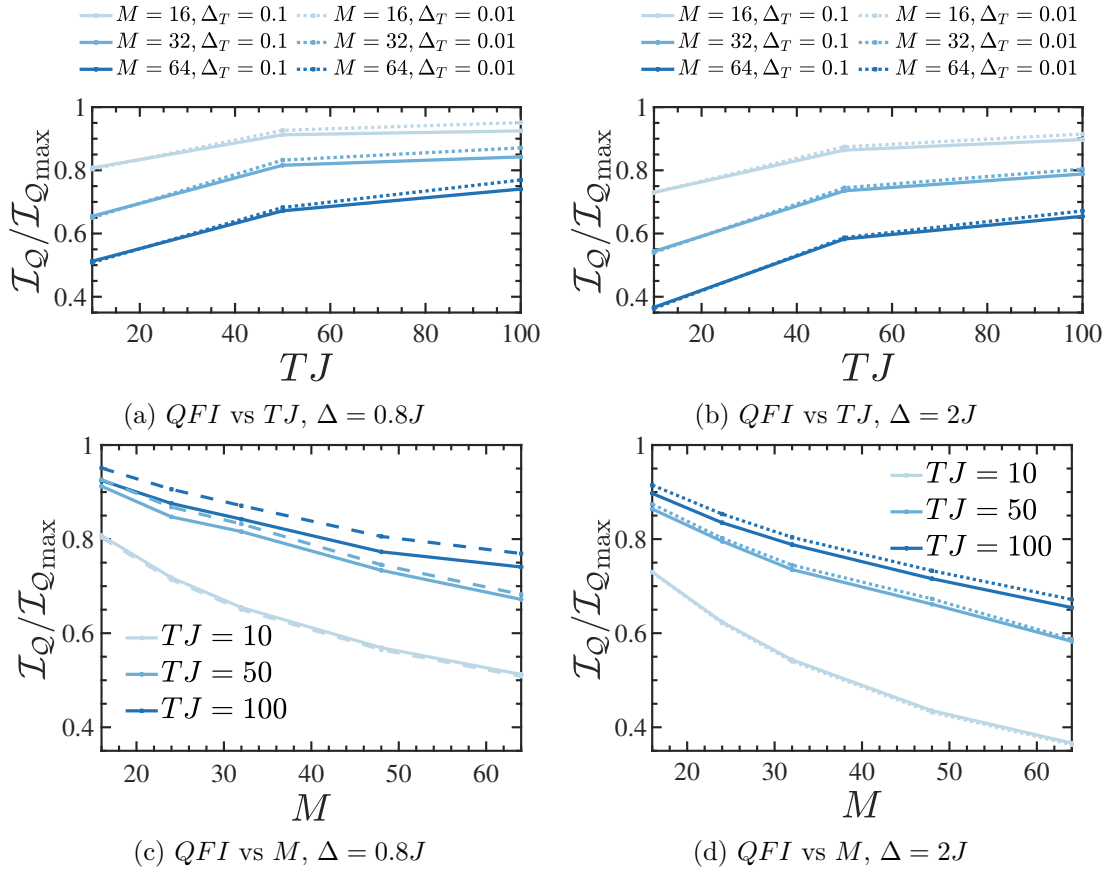


FIGURE 6.18: We evaluate the ratio of the QFI with its maximum value $\mathcal{I}_Q/\mathcal{I}_{Q_{\max}}$ at the end of the ramp in the anisotropy Δ/J for the spin-1/2 model. We consider two different initial anisotropy values (a,c) $\Delta = 0.8J$ and (b,d) $\Delta = 2J$. We consider different system sizes M and different ramp times TJ . The flat lines are for a final anisotropy value $\Delta_T = 0.1J$ and the dotted lines for $\Delta_T = 0.01J$. The decrease of the QFI with increasing system size is independent of the final value of Δ_T/J , for a specific ramp time TJ . The calculations were done with bond dimension for the MPS calculations $D = 128$, and open boundary conditions.

In the next section we discuss the stability of the states when we add dissipation into the system, which is key for any experimental realisation.

6.4.4 Effects of dissipation

We mentioned before that one of the challenges in using adiabatic state preparation is the trade-off between the speed of the ramp and the energetic cost of natural heating, being in the form of spontaneous dissipation in experiments with spin-dependent lattices [199].

We have seen in chapter 4 that for open quantum systems the resulting markovian master equation in Lindblad form will be [113]

$$\frac{d}{dt}\hat{\rho} = -\frac{i}{\hbar}[\hat{\mathcal{H}}, \hat{\rho}] - \frac{\Gamma}{2} \sum_m [\hat{C}_m^\dagger \hat{C}_m \hat{\rho} + \hat{\rho} \hat{C}_m^\dagger \hat{C}_m - 2\hat{C}_m \hat{\rho} \hat{C}_m^\dagger], \quad (6.47)$$

with Γ the dissipation rate.

In our case, the master equation will be

$$\frac{d}{dt}\hat{\rho} = -\frac{i}{\hbar}[\hat{\mathcal{H}}_{\text{SP1/2}}, \hat{\rho}] - \frac{\Gamma}{2} \sum_{i,\kappa=A,B} \left[\hat{C}_{i,\kappa}^\dagger \hat{C}_{i,\kappa} \hat{\rho} + \hat{\rho} \hat{C}_{i,\kappa}^\dagger \hat{C}_{i,\kappa} - 2\hat{C}_{i,\kappa} \hat{\rho} \hat{C}_{i,\kappa}^\dagger \right], \quad (6.48)$$

where the jump operators are the projectors on the $|\uparrow\rangle$ and $|\downarrow\rangle$ state

$$\begin{aligned} \hat{C}_{i,A} &= \frac{\mathbb{1} + \hat{s}^z}{2}, \\ \hat{C}_{i,B} &= \frac{\mathbb{1} - \hat{s}^z}{2}, \end{aligned} \quad (6.49)$$

on site i , for species A and B , respectively.

In order to solve this master equation numerically, we employ quantum trajectory techniques, which involve rewriting the master equation as a stochastic average over individual trajectories, which can be evolved in time numerically as pure states, as was explained in section 4.3.2. The effective Hamiltonian for the spin-1/2 model with two species will then have the form

$$\hat{\mathcal{H}}_{\text{eff}} = \hat{\mathcal{H}}_{\text{SP1/2}} - \frac{i}{2}\Gamma \sum_i \left[\hat{C}_{i,A} + \hat{C}_{i,B} \right]. \quad (6.50)$$

In Fig. 6.19 we plot the fidelity and the QFI (calculated as before) at the end of the ramp for different ramp times and different values of the dissipation Γ/J , within experimental time ranges. Here we show just the results with initial anisotropy $\Delta = 0.8J$.

We show how there is a trade-off between using slow ramps to improve adiabaticity and using faster ones to avoid dissipation. For large heating rates the final fidelities go to zero. However, these effects are less highlighted in the QFI, which means that if we are interested in high entangled states useful for metrology we can still prepare them in the presence of dissipation.

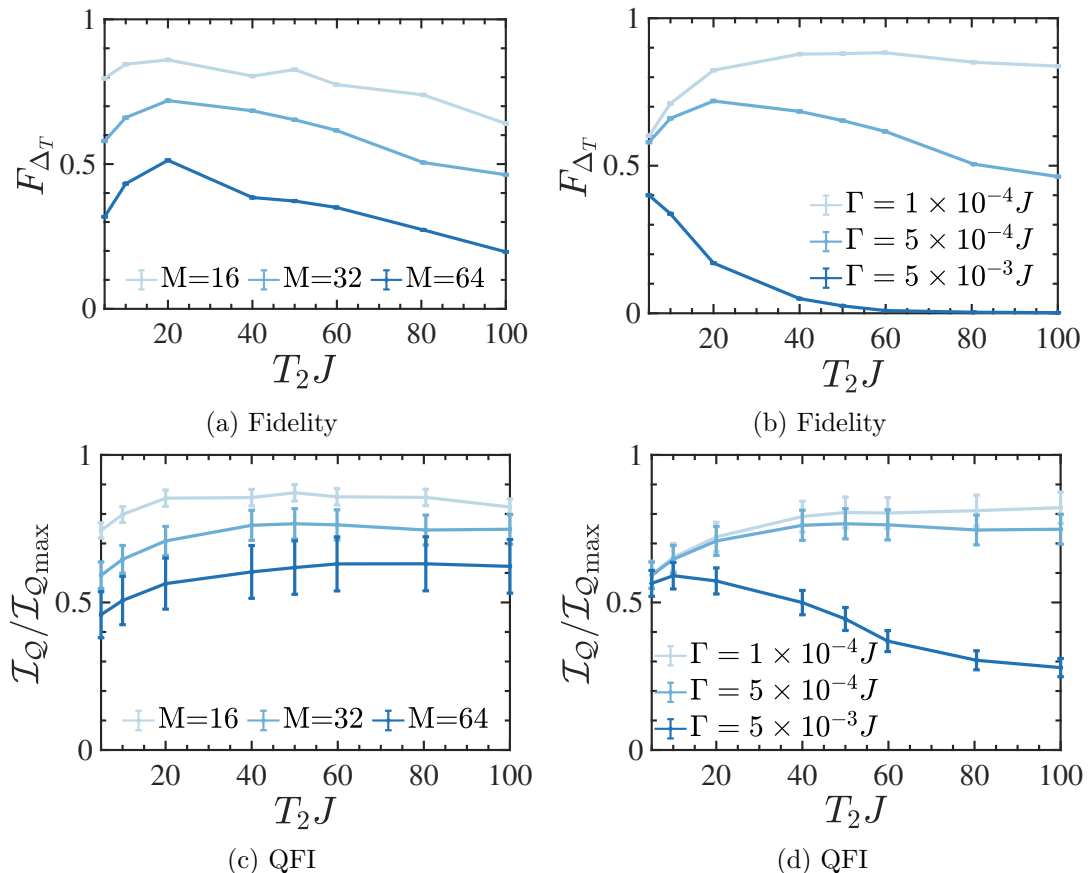


FIGURE 6.19: Averaged fidelities F [panels (a-b)] and Quantum Fisher Information [panels (c-d)] at the end of the ramp in Δ including dissipation, for initial and final anisotropy $\Delta = 0.8J$ and $\Delta_T = 0.1J$, respectively. (a) Averaged fidelities for different system sizes, ramp times, and a value of the dissipation $\Gamma = 5 \times 10^{-4}J$. (b) Averaged fidelities for different dissipation rates and ramp times, for a ramp of size $M = 32$. (c) $\mathcal{I}_Q/\mathcal{I}_{Q_{\max}}$ shown for different system sizes, ramp times, and a value of the dissipation $\Gamma = 5 \times 10^{-4}J$. (d) $\mathcal{I}_Q/\mathcal{I}_{Q_{\max}}$ shown for different dissipation rates and ramp times, for a ramp of size $M = 32$. These calculations were performed with 200 trajectories (statistical error bars are shown on the plots) and a bond dimension for the MPS calculations $D = 128$, with open boundary conditions.

6.5 Summary and Outlook

In this chapter we have demonstrated that high fidelities can be reached using adiabatic ramp evolutions, making it possible to prepare desired states with specific magnetic ordering. These techniques are directly relevant for ongoing experiments, and fundamentally interesting in terms of their non-equilibrium dynamics.

First, we introduced theoretically the concept of adiabatic state preparation and the adiabatic theorem, and how the adiabaticity depends on the energy gap of our system, and that this gap decreases with the size of the system. We then applied different ramps to prepare specific magnetic states in the spin-1/2 model. We started with the preparation of antiferromagnetic states for small systems by employing two different

approaches, and we showed how we can reach high fidelities at the end of the ramp, by comparing the evolved state with the target state. We also show the behaviour of the correlations and how we can use it to characterise the magnetic order of our final state. A further investigation with larger system sizes could be implemented using Matrix Product States.

Furthermore, we study the preparation of XY-ferromagnetic states and show how the times needed to reach high fidelities were outside the scope of experimental realisations. Next, we explained how our models can give rise to entanglement that is useful for quantum enhanced metrology. After an introduction to the concept of Quantum Fisher Information QFI (\mathcal{I}_Q), we then used it to characterise the ground states of both the spin-1 and the spin-1/2 model. We also compared with the maximum QFI value, where we showed that in the limit of very small anisotropies we are very close to the Heisenberg scaling where $\mathcal{I}_Q \sim M^2$, which is the maximum scaling possible, and the regime where we could use our highly entangled states for metrology.

We then used optimisation techniques to find optimal ramps within experimental times, focusing on the spin-1/2 model, and obtained high fidelities for bigger system sizes, and with high QFI values. Finally, we studied the robustness of our models to experimental noise, in the form of spontaneous emission, by using quantum trajectory techniques, and demonstrated that there are regimes where the useful properties of these states survive dissipation. This implies that the generation of entanglement should be generally more robust to heating than by looking at the state fidelity.

As a perspective for further studies, it would be interesting to investigate of the effects of other sources of noise and dissipation, and the implementation of actual experimental data.

Chapter 7

Spin dynamics in the presence of long-range interactions and disorder

The phenomenon of synchronisation has been investigated in a plethora of physical topics, and in particular, in systems with long-range interactions [200, 201].

In this chapter, beginning from a state with all effective magnetic spins in the same direction, we investigate the dynamics of the spin-spin correlations, and how they behave in situations with different interaction ranges and for different total spin. We show in some cases that this leads to synchronisation between the spins.

We start in section 7.1 considering the possibility of having different regimes of interactions, from long-range to the nearest-neighbour regime, being able to classify the behaviour of correlation spreading in the spin models into different patterns. We also analyse any transition points from long to short-range interactions in the models by investigating the dynamics of the spin-spin correlations. Then, in section 7.2 we investigate the stability of the correlations by adding a quenched disorder into the systems.

7.1 Long-Range Interactions

The experimental realisations with Rydberg atoms [202, 203], polar molecules [204], and especially with ion traps [14, 205] in recent years have improved the way to control and engineer platforms to study interactions that decrease following a power law. This opens up a rich research field to investigate how dynamics change in the presence of long-range interactions, making them attractive for quantum simulation.

In previous chapters we focussed on models with only nearest-neighbours interactions. Now, in addition, we consider the possibility of long-range interactions (LRI), where we are able to classify the behaviour of correlation spreading in both spin-1 and spin-1/2 models into different regimes as a function of the decay exponent α , with power law interactions decaying as $1/r^\alpha$, where r is the separation distance between spins. The models will then have the form

$$\hat{\mathcal{H}}_{\text{SP1}_{\text{LRI}}} = -\sum_{i>j} \frac{J}{|i-j|^\alpha} \hat{\mathbf{S}}_i \hat{\mathbf{S}}_j + u \sum_i (\hat{S}_i^z)^2, \quad (7.1)$$

for the spin-1 system and

$$\hat{\mathcal{H}}_{\text{SP1/2}_{\text{LRI}}} = -\sum_{i>j} \frac{J}{|i-j|^\alpha} (\hat{s}_i^x \hat{s}_j^x + \hat{s}_i^y \hat{s}_j^y) - \sum_{i>j} \frac{J-\Delta}{|i-j|^\alpha} \hat{s}_i^z \hat{s}_j^z, \quad (7.2)$$

for the spin-1/2 system.

In a quantum system with short-range interactions we expect the generic correlations to propagate with a light cone with a finite velocity, known as the Lieb-Robinson bounds [117], whereas we expect no sharp cone in the long-range interactions regime as the propagation of entanglement is suppressed. One of the main questions is the behaviour of the light cone with the propagation of correlators in the system, when we enter an intermediate interaction regime [118, 206–208].

The values of α will indicate the range of the interactions where in a system of dimension D :

- (a) $\alpha > D + 1$: regime of short-range interactions,
- (b) $\alpha < D$: regime of long-range interactions,
- (c) Intermediate-range if $D < \alpha < D + 1$.

In the next section we investigate the decay of the correlations as a function of time and distance for different values of α for long-range interactions, and compare with the behaviour with nearest-neighbour interactions.

7.1.1 Results

We study the same quench dynamics as in 5.1 where we start with all spins initially prepared aligned along the z-axis, followed by having a product state of spins rotated into the xy-plane, and then dynamically evolve under the Hamiltonians 7.1 and 7.2.

We investigate how long-range interactions persist with time and whether there is a transition point where the behaviour changes for different values of α .

For moderate times and bigger systems sizes we apply Time-Dependent Variational Principle (TDVP) techniques with Matrix Product Operator representation of the Hamiltonian, discussed in section 4.2.3.2.

The correlations are calculated as in 7.3:

$$\Theta_j = |\overline{\langle S_i^+ S_{i+j}^- \rangle}| = \frac{1}{M - 2b - j} \sum_{i=1+b}^{M-b-j} |\langle \hat{S}_i^+ \hat{S}_{i+j}^- \rangle|, \quad (7.3)$$

where i denotes the index of the site, j is the distance or number of sites, and $b = M/5$ is a number of sites at the boundary that we omit to reduce the open boundary effects. The correlations are calculated analogously for the spin-1/2 with operators $\hat{s}_i^+, \hat{s}_{i+j}^-$.

In Fig. 7.1 we show the correlations as a function of distance, at the end of a time evolution $TJ = 3$, for the spin-1 model, for different parameter values.

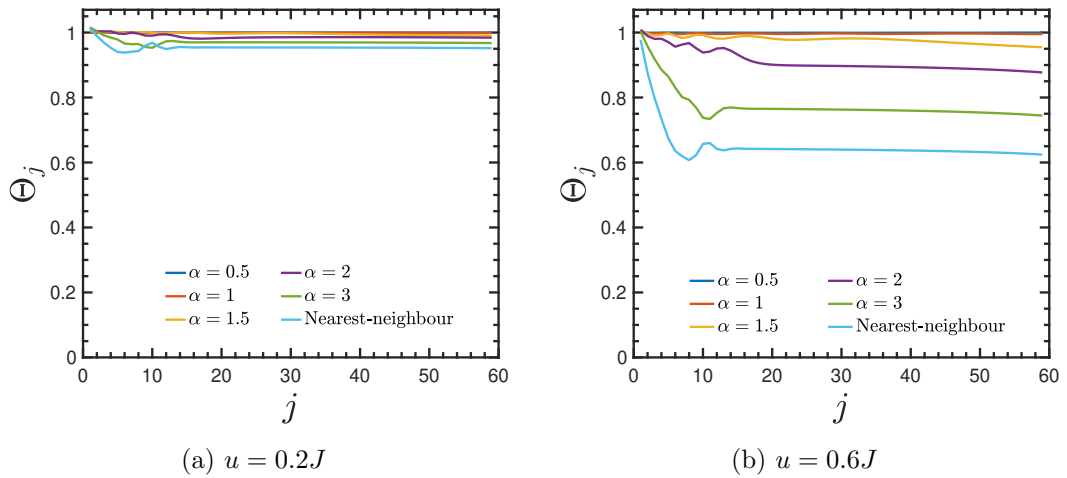


FIGURE 7.1: Comparison of the decay of the correlations as a function of distance for the spin-1 model with $M = 80$, for different α values at $TJ = 3$. The decay of the correlations with time starts when entering in the regime of intermediate interactions ($\alpha > 1$). The spreading of the light cone is only visible when entering in a regime of short-range interactions ($\alpha = 2$). We can also see that only in this regime the correlations decay as a function of distance, and that this behaviour is more pronounced with a higher anisotropy. The MPS calculations were done with bond dimension $D = 128$ and open boundary conditions.

In Fig. 7.2 we study the decay of the correlations as a function of distance at the end of the evolution ($TJ = 3$) for different values of α and nearest-neighbour interactions for the spin-1/2 model.

The results are shown on a logarithmic scale for $\Delta = 0.8J$ in 7.3, to analyse better whether there is either an algebraic or exponential decay.

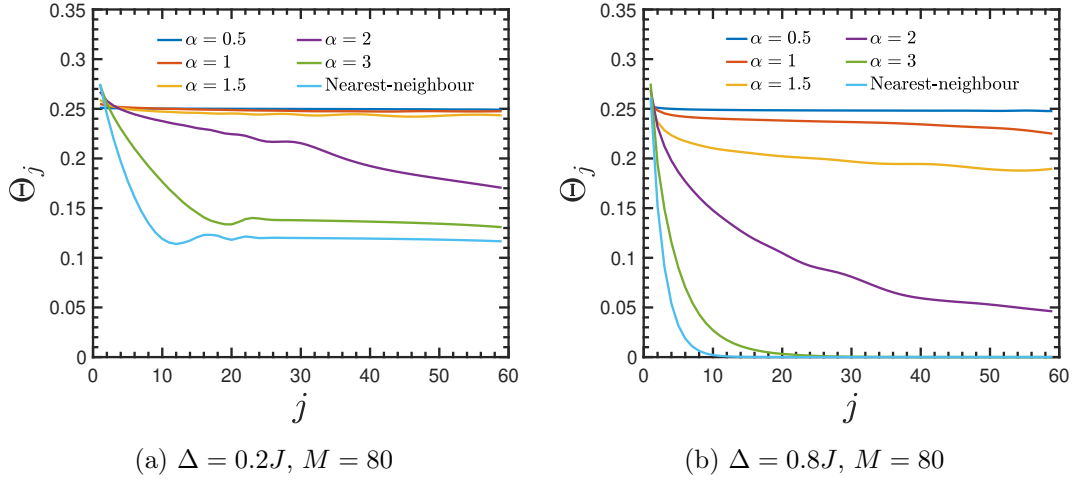


FIGURE 7.2: Comparison of the decay of the correlations as a function of distance for the spin-1/2 model with $M = 80$, for different α values at $TJ = 3$. There is a clear change in the correlations behaviour in the intermediate range of interactions ($\alpha > 1$). In this case we can see different behaviour in each of the interactions regimes. For long-range there is no decay of the correlations. In the intermediate regime we have a power law decay, and an exponential decay of the correlations (vanishing with time) for short-range interactions. The MPS calculations were done with bond dimension $D = 128$ and open boundary conditions.

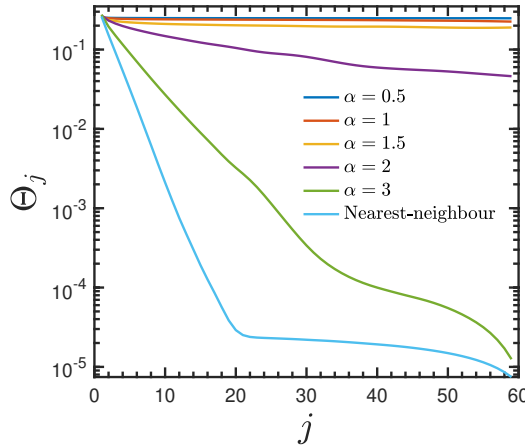


FIGURE 7.3: Correlations as a function of distance for the spin-1/2 model at $TJ = 3$, for different values of α and nearest-neighbour interactions in a semi-logarithmic scale, and $\Delta = 0.8J$. We see a transition from a power law decay of the correlations to an exponential decay in the short-range interactions regime. Size of the system $M = 80$.

We have seen how the correlations behave differently with respect to time and distance, depending on the interaction regime. In figures 7.4 and 7.5 we summarise these results for a fixed distance to evaluate the behaviour in time, for different values of α , for both models.

As we mentioned before, one of the questions that arises is whether we can observe the light cone of the correlations spreading with time and distance. In the previous figures

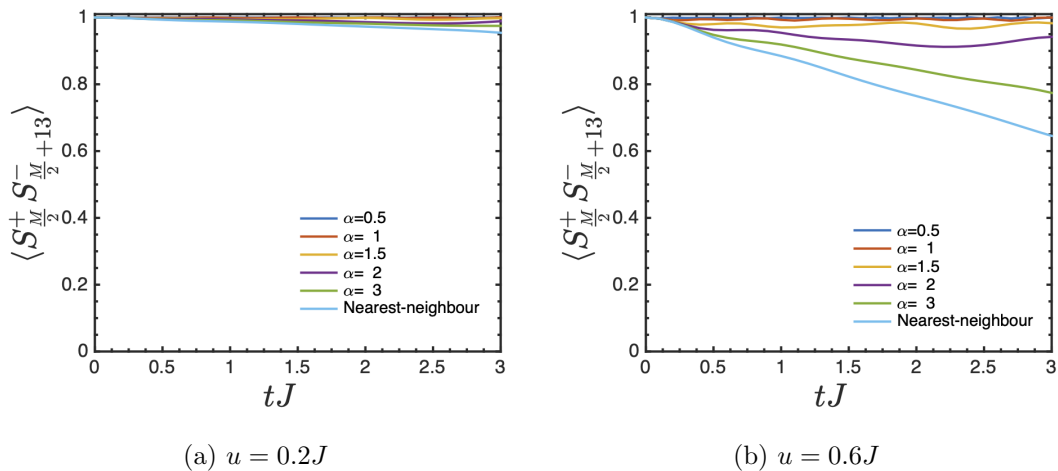


FIGURE 7.4: Spin-1: Comparison of the decay of the correlations with time for a fixed distance, for two anisotropy values, in a system of $M = 80$ spins. The correlations decay when entering in the intermediate regime of the interactions, and this effect is much more pronounced for higher anisotropy. This decay is exponentially fast in the short-range regime. The calculation for the MPS calculations were done with bond dimension $D = 128$ and open boundary conditions.

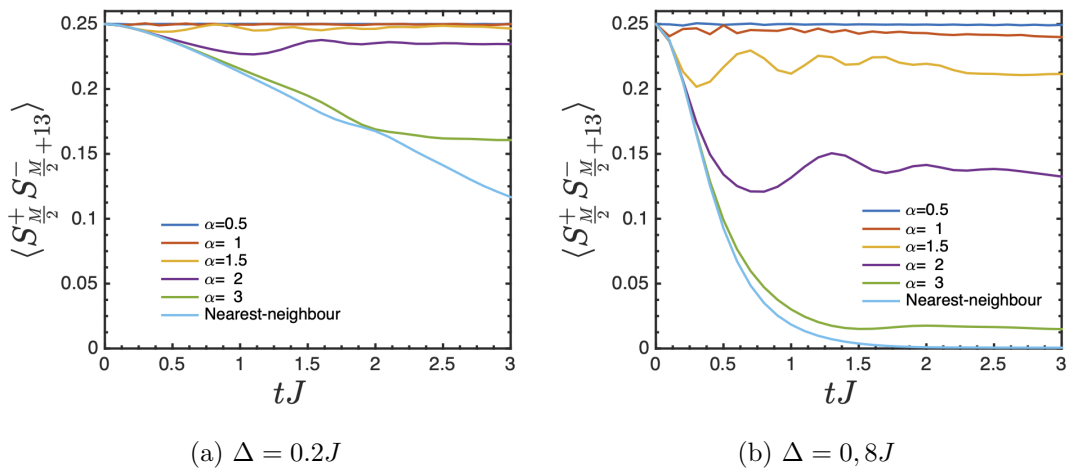


FIGURE 7.5: Spin-1/2: Comparison of the decay of the correlations with time for a fixed distance, for two anisotropy values, and a system size $M = 80$. The correlations decay when entering in the intermediate regime of the interactions, and this effect is much more pronounced for higher anisotropy. This decay is exponentially fast in the short-range regime, for both models. The calculation for the MPS calculations were done with bond dimension $D = 128$ and open boundary conditions.

we saw that the oscillations at smaller distances indicate the presence of a light cone, and we analyse this in detail next.

For spin-1 we focus on a high value of the anisotropy u/J and show in plots in 7.6 the appearance of the light cone in the short-range interactions regime. We observe that at $t = 0$ the correlations have a value $\Theta_j = 1$, due to the particular initial state (the rotated state), and the choice of correlations.

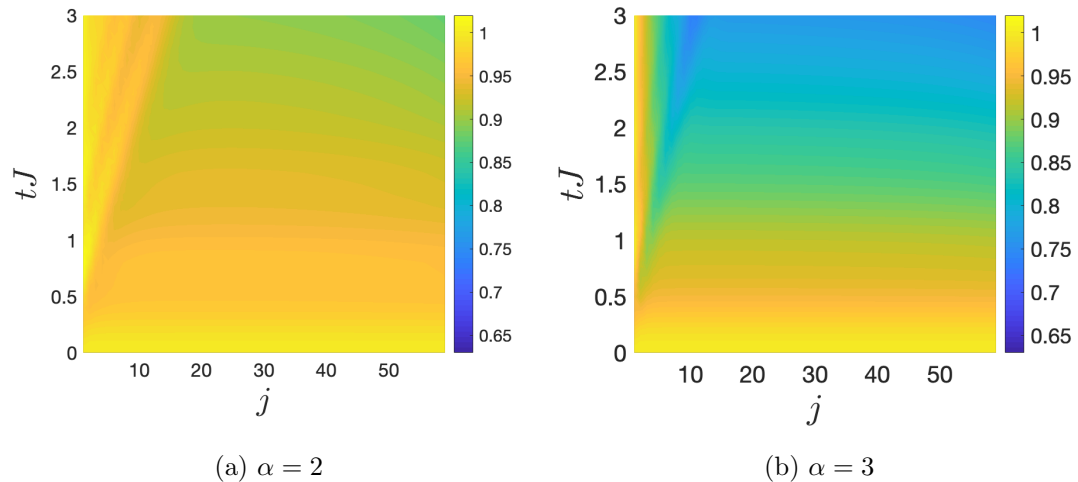


FIGURE 7.6: Correlations Θ_j with time and distance for the spin-1 model with $M = 80$ and $u = 0.6J$. In (a) with $\alpha = 2$ the edge of the light cone is not as sharp as in (b) with $\alpha = 3$ where the light cone in the dynamics is clearly visible.

For spin-1/2 we divided our study for different anisotropy value. For $\Delta = 0.2J$ we want to see the emergence of the light cone in the short-range regime, as in 7.7.

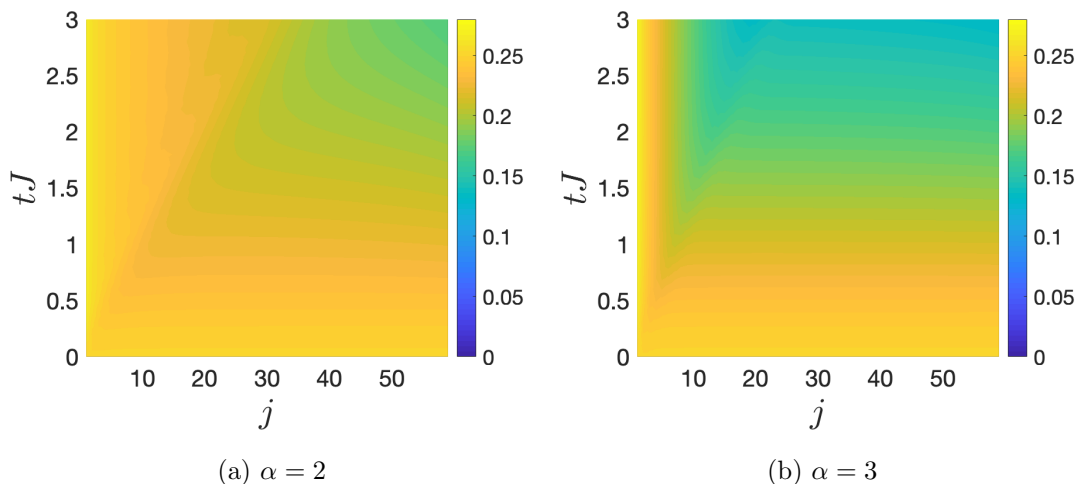


FIGURE 7.7: Correlations Θ_j with time and distance for the spin-1/2 model with $M = 80$ and $\Delta = 0.2J$. In (a) with $\alpha = 2$ the spreading of the light cone at longer and longer distances can be observed. For $\alpha = 3$ in (b) besides the light cone, we observe that at longer distances the plateau of synchronised spins as these spins were initially correlated, and the magnetic order saturates with distance.

For $\Delta = 0.8J$ the correlations vanished very quickly, but we can observe interesting behaviour for smaller α in the intermediate regime in 7.8.

In a regime of intermediate and short-range interactions the correlations decay with distance, faster with a higher anisotropy value. It is only in this regime where the spreading of the light cone is visible. This light cone is the effect of the finite-range interactions at the beginning. However, at longer distances there are fewer fluctuations and that is why we see that the correlations decrease more slowly.

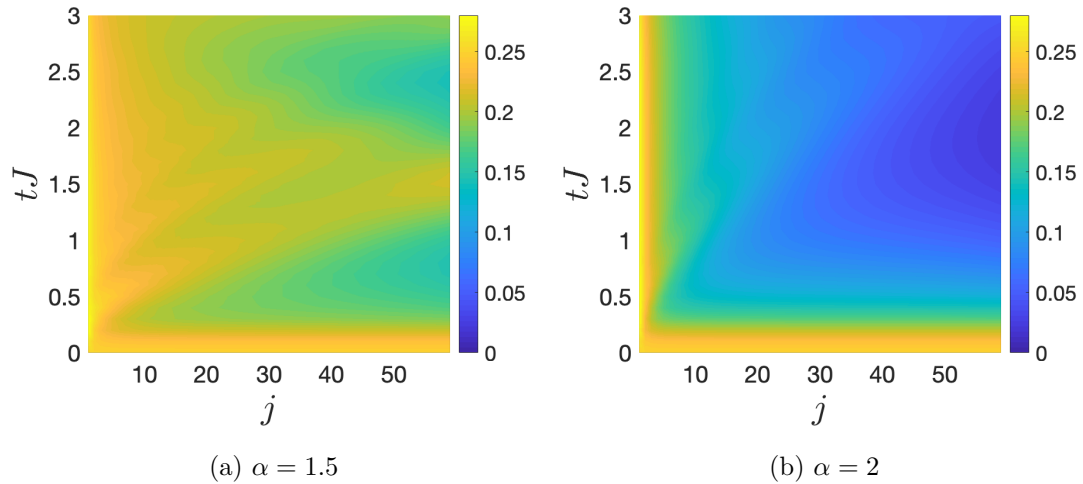


FIGURE 7.8: Correlations Θ_j with time and distance for the spin-1/2 model with $M = 80$ and $\Delta = 0.8J$. (a) With $\alpha = 1.5$ there is no light cone and we can observe the power law decay of the correlations with time. (b) In the regime with $\alpha = 2$ the dynamics is much faster, clearly starting to show the exponential decay of the correlations.

In this analysis we found a quantitative change around $\alpha = 1$, entering the intermediate regime of the correlations, and a qualitative difference around $\alpha = 2$. In the next section we analyse this transition in detail.

7.1.2 Transition studies in different regimes

We start by studying the transition at the end of the evolution ($TJ = 3$) around $\alpha = 2$ for the spin-1 model in Fig. 7.9 where there is no such a strong decay of the correlations as in the spin-1/2 case.

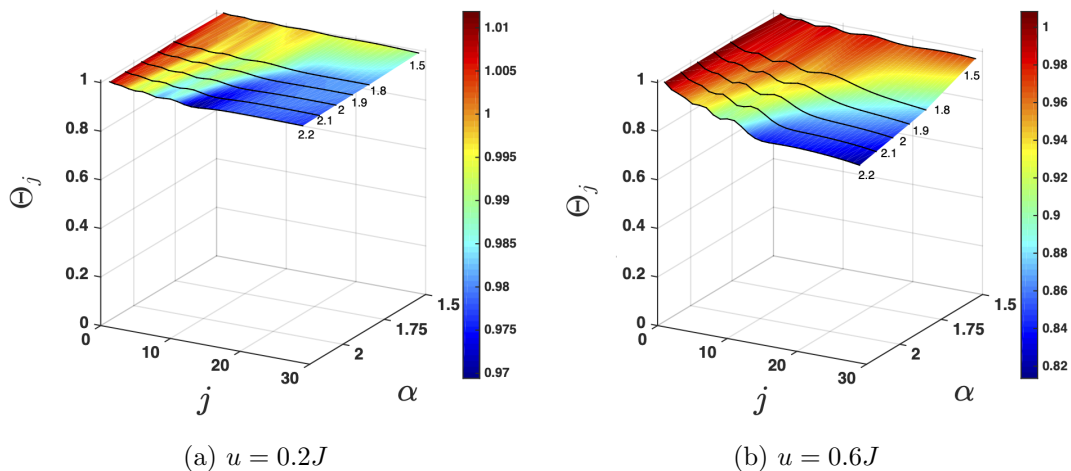


FIGURE 7.9: Correlations as a function of distance at $TJ = 3$ and different α values for the spin-1 ($M = 40$) model showing the transition around $\alpha = 1.8$.

We investigate the behaviour at the end of the evolution ($TJ = 3$) in the intermediate regime for spin-1/2 model and a high anisotropy in Fig. 7.10, and the change around $\alpha = 2$ in Fig. 7.11, showing a clear transition around $\alpha = 1.8$.

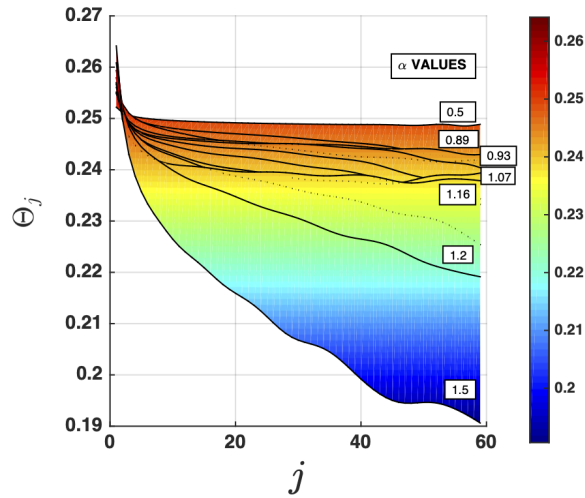


FIGURE 7.10: Correlations as a function of distance at $TJ = 3$ and different α values for the spin-1/2 model ($M = 80$) showing a smooth transition around $\alpha = 1$.

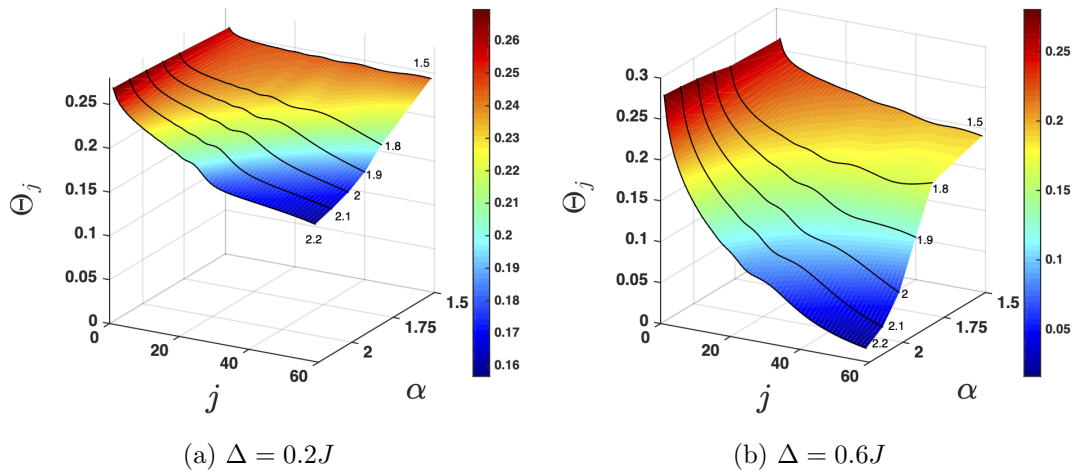


FIGURE 7.11: Correlations as a function of distance at $TJ = 3$ and different α values for the spin-1/2 model ($M = 80$) showing the transition around $\alpha = 1.8$.

To summarise, we have seen that in the regime of long-range interactions the spins are correlated. With intermediate and short-range interactions the magnetic ordering saturates with distance and this synchronisation transition occurs faster for smaller values of α .

In the next section, we study the same correlations in the presence of disorder in the system. In this case, we consider quenched disorder, which is static in time, in the spin component in the z -direction on each site.

7.2 Presence of disorder

Disorder in many-body physics can be represented in various forms. The presence of disorder in materials by lattice defects or impurities can affect the properties of a many-body system [209]. Disordered potentials can give rise to Anderson localisation in non-interacting particles and many-body localisation (MBL) in the case of a many-body system of interacting particles [210, 211].

Dynamical behaviour of many-body physics in the presence of disorder has been studied in a variety of models, such as polar molecules in 2D in [212, 213] with a mean-field approach. In our case we considered random noise in the lattice, static in time. We investigate the effect of this disorder in our 1D spin models.

We study how the interactions behave with time by adding disorder into the system.

The Hamiltonian after adding disorder in the spin-1 model will be

$$\hat{\mathcal{H}}_{\text{SP1}_{\text{dis}}} = -\sum_{i>j} \frac{J}{|i-j|^\alpha} \hat{\mathbf{S}}_i \hat{\mathbf{S}}_j + u \sum_i (\hat{S}_i^z)^2 + \sum_i \kappa_i \hat{S}_i^z, \quad (7.4)$$

and for the spin-1/2

$$\hat{\mathcal{H}}_{\text{SP1/2}_{\text{dis}}} = -\sum_{i>j} \frac{J}{|i-j|^\alpha} (\hat{s}_i^x \hat{s}_j^x + \hat{s}_i^y \hat{s}_j^y) - \sum_{i>j} \frac{J-\Delta}{|i-j|^\alpha} \hat{s}_i^z \hat{s}_j^z + \sum_i \kappa_i \hat{s}_i^z, \quad (7.5)$$

with noise κ_i being random at each site, and at each disorder iteration realisation. We use an uniform distribution with

$$\kappa_i \in [-1, 1] \propto \sigma, \quad (7.6)$$

where σ defines the strength of the disorder. We then take the average of these quantities over a set of disorder realisations.

Experimentally, this kind of disorder could be realised by using an off-resonant pumping laser through a diffuser to create a random intensity distribution. The generated speckle pattern reflects a truly random potential [53, 214].

We investigate the decay of the correlations as a function of time and distance for different values of α and different disorder strengths, and compare with the case where there is no disorder. We focus on the long-range and intermediate regime, as with short-range the decay of the correlations was already fast without any disorder.

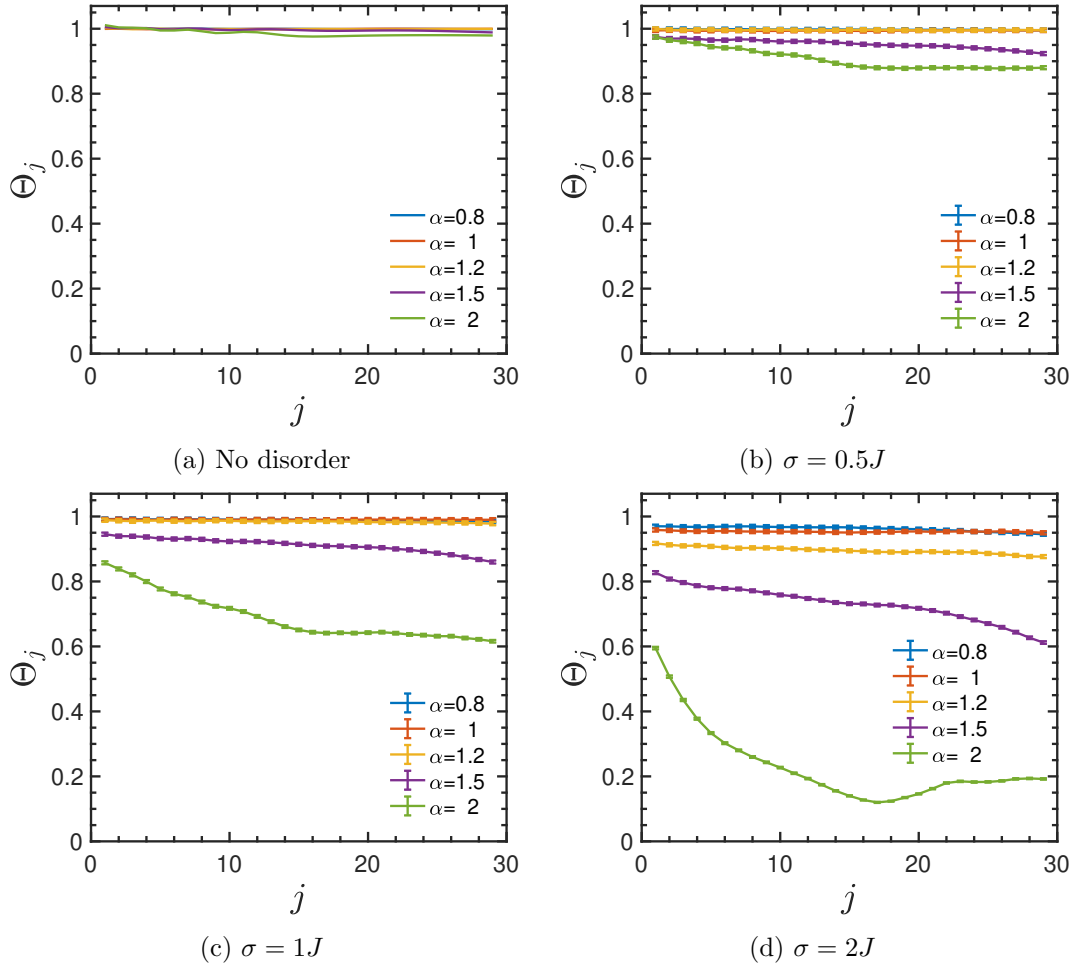


FIGURE 7.12: Spin-1: Correlations as a function of distance (at $TJ = 3$) for $u = 0.2J$ and different α , in the case of no disorder and adding disorder with different strength σ . Size of the system $M = 40$. The effect of the disorder is clearly noticeable with increasing strength. However, even with the strongest disorder there is no effect in the long-range interactions regime. The calculation for the MPS calculations were done with bond dimension $D = 128$ and open boundary conditions.

7.2.1 Results

As in the previous section, we investigate the correlations as in 7.3 for both models. We want to study if the long-range interactions persist again with time or whether there is any effect induced by the disorder. In this case, we consider values of α mostly in the long-range and intermediate regime. We incremented the number of disorder realisations until we get minimal mean statistical errors. All results shown are calculated with 100 disorder realisations.

We start with the case of the spin-1 model for two different anisotropy values, $u = 0.2J$ in Fig. 7.12 and $u = 0.6J$ in 7.13. Similar behaviour occurs for both anisotropies, where we see that even when adding weak disorder the correlations decay in the intermediate

regime of the interactions, and this effect increases with the disorder strength. However, at all disorder strengths we see that the long-range interactions persist.

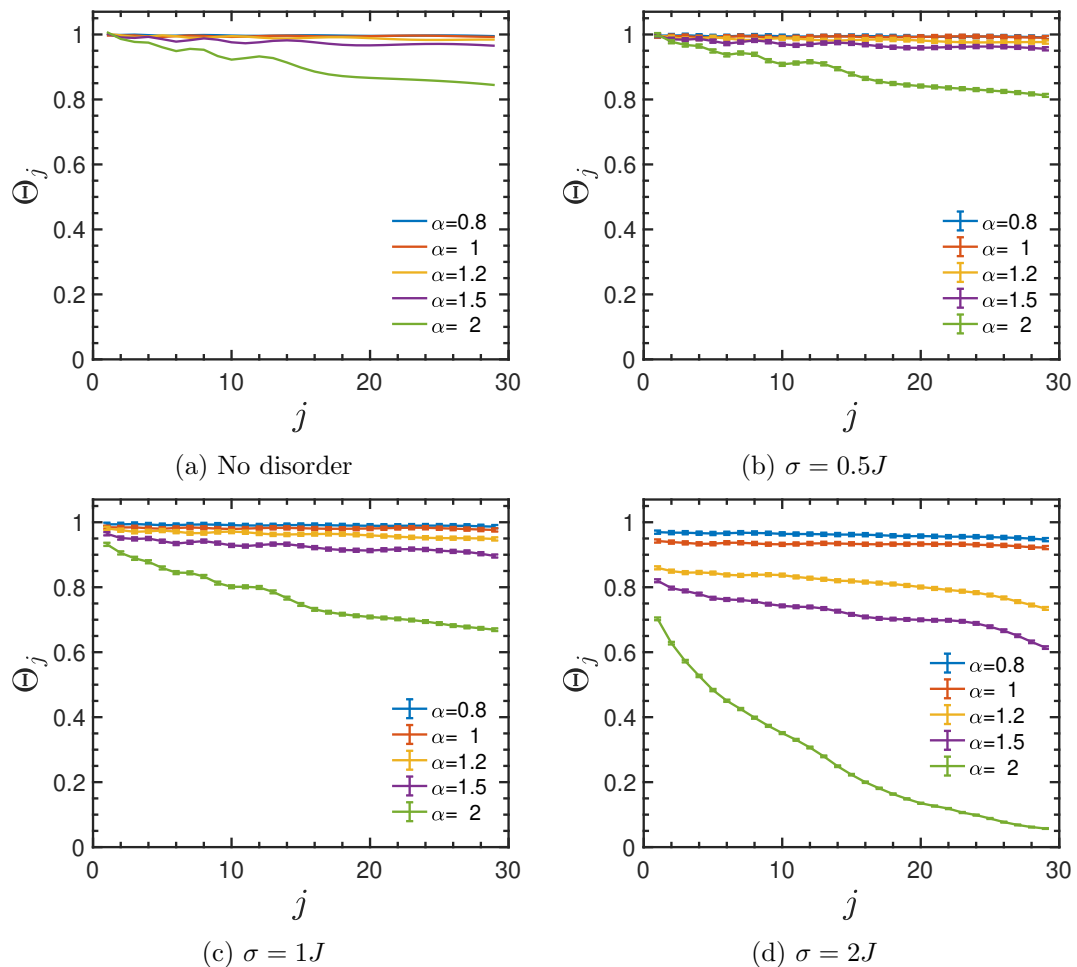


FIGURE 7.13: Spin-1: Correlations as a function of distance (at $TJ = 3$) for $u = 0.6J$ and different α , in the case of no disorder and adding disorder with different strength σ . Size of the system $M = 40$. We see an increase in the decay of the correlations with strong disorder, especially in the short-range regime. In the intermediate regime, some finite sizes effects appear at longer distances. The calculation for the MPS calculations were done with bond dimension $D = 128$ and open boundary conditions.

For the spin-1/2, in figures 7.14 and 7.15, we can distinguish a similar pattern as in the spin-1.

We found that adding disorder into the system affects the correlations in the intermediate and short-range interactions regime, for both models. This effect is also more pronounced with a larger anisotropy value, being u/J for the spin-1 or Δ/J for the spin-1/2.

In the short-range interactions regime, even a very weak disorder ($\sigma = 0.5J$) will have an effect on how the correlations decay as a function of distance. In the long-range interactions regime, however, we find that there is no effect from the disorder, independently of its strength.

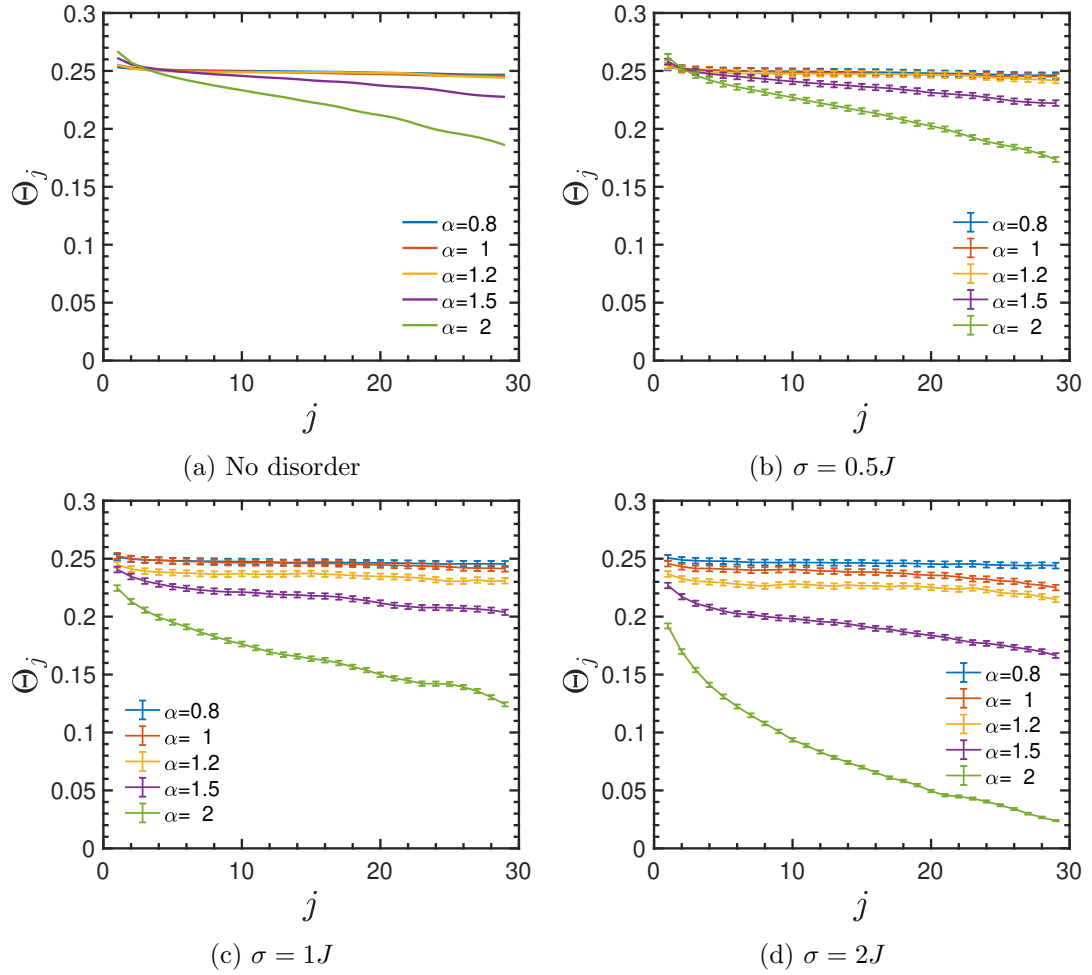


FIGURE 7.14: Spin-1/2: Correlations as a function of distance (at $TJ = 3$) for $\Delta = 0.2J$ and different α , in the case of no disorder and adding disorder with different strength σ . Size of the system $M = 40$. We see an increase in the decay of the correlations with strong disorder in the intermediate and short-range regime. For long and intermediate interactions, some finite size effects appear at longer distances. The calculation for the MPS calculations were done with bond dimension $D = 128$ and open boundary conditions.

Nonetheless, we consider that at any regime, there should be a value of disorder strength where we expect decay of the correlations, even in the long-range regime. One open question, for when this value is found, is whether the transition will then be sharp or more of a crossover. To see it clearly, a follow up study with a constant ratio M/σ with different system sizes and periodic boundary conditions will be needed.

7.3 Summary and discussion

We have investigated the effect of having power-law decay of correlations in our models, and how the correlations behave depending on the interactions regime, being long-range,

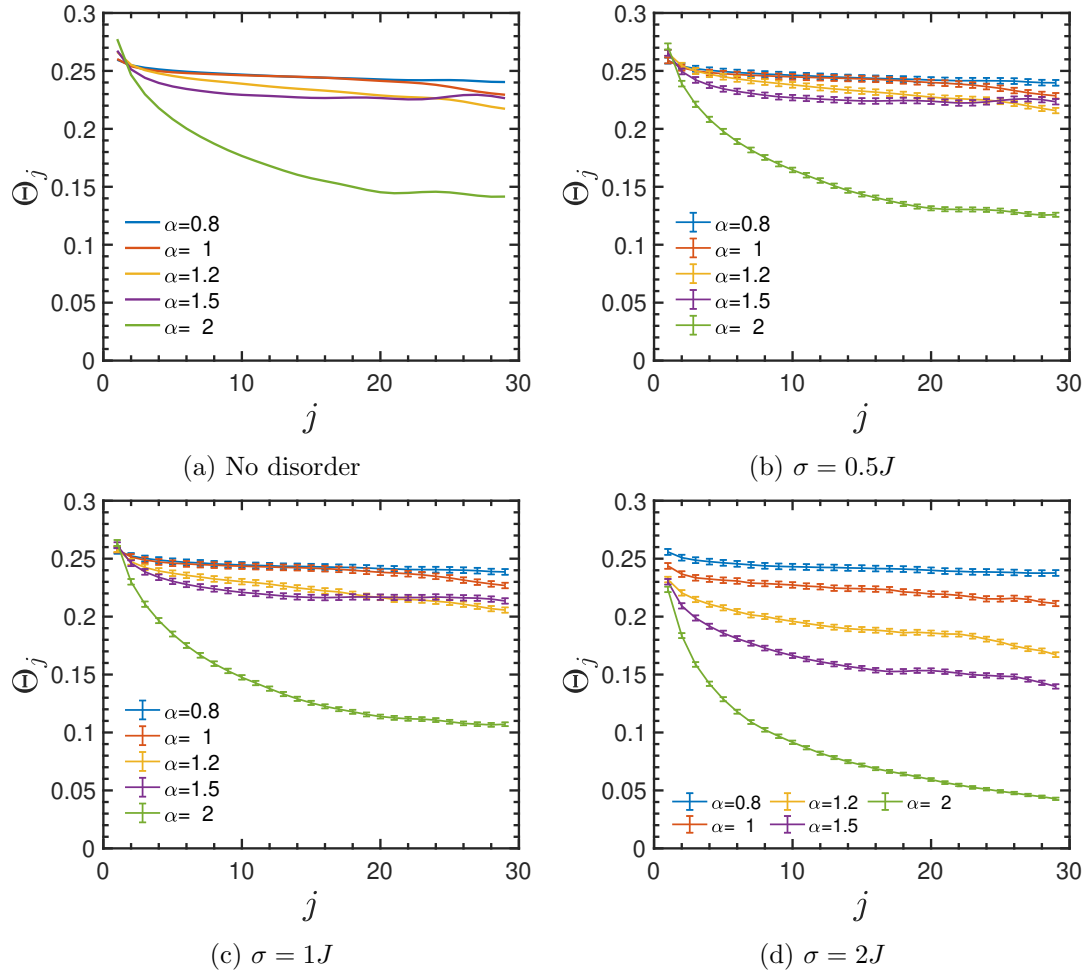


FIGURE 7.15: Spin-1/2: Correlations as a function of distance (at $TJ = 3$) for $\Delta = 0.6J$ and different α , in the case of no disorder and adding disorder with different strength σ . Size of the system $M = 40$. In this case the effect of the disorder in the intermediate regime is even visible with weak disorder. The effect is stronger as α increases. The calculation for the MPS calculations were done with bond dimension $D = 128$ and open boundary conditions.

intermediate, and short-range, and compared it with the nearest-neighbour interactions results previously evaluated in 5.3.

Likewise, we have identified the light-cone spreading with short range interactions. For the intermediate regime the behaviour shows clearly no light-cone, but a further analytical study could tell us more about the spreading of correlations here.

Moreover, we have also evaluated the transition where the correlations start to behave qualitatively different in the intermediate regime, and we found a transition point around $\alpha = 1.8$ for both models, independently of the anisotropy. Again, an analytical study with spin-wave theory (using Holstein-Primakoff approximation) [118, 215] will add further insight.

Furthermore, we evaluated the effect of a random disorder in the models, and investigated the spin-spin correlations behaviour with different disorder strengths. In the short and intermediate regime the disorder affects the correlations, decaying very quickly with a strong disorder.

In the time evolutions considered in our simulations, we observed no disorder effect in the long-range interactions regime. We consider a further analysis that could be done to study a possible disorder strength threshold where the correlations will decay even in the presence of long-range interactions.

Additionally, it would be interesting to extend this study consider the different types of disorder in these kind of models.

There are some open questions where we envision additional considerations will be very interesting. A better understanding of the spread of entanglement distributed by quasi-particles in these models could be investigated by evaluating the von-Neumann entropy in the systems [118, 216, 217].

Further studies of a range of quantum phenomena, including spin transport [218] and thermalisation [206], and their experimental implementations, will help to engineer these systems and probe new physics.

Chapter 8

Conclusions & Outlook

Our journey along this thesis has come to an end. We have investigated different phenomena including in and out-of-equilibrium dynamics in spin models of ultracold bosonic atoms in optical lattices. The possibility to control and tune the parameters in the systems experimentally offers new possibilities to engineer and study strongly correlated many-body systems, and in particular in our field of research, quantum magnetism.

In this thesis, we considered the time-dependent dynamics of magnetic models corresponding to two-component bosons in an optical lattice. By rotating a system of interacting spins from a low-entropy initial state, we investigated how to probe these states using time-dependent dynamics and evaluating the spin currents in the models. Moreover, we studied situations with different interaction ranges and also explored how disorder affects these systems.

We also investigated the correlation length of a XY-ferromagnet in a thermal state, as a function of the entropy/temperature. This offers opportunities to study fundamental properties away from equilibrium and to probe states of the spin models, as well as providing tools to prepare states of lower temperature and entropy.

One of the challenges in working with these systems in the laboratory remains reaching the low temperatures/entropies necessary to produce some particularly sensitive interacting states. Investigating the magnetically ordered quantum states that can be engineered, we study the techniques to prepare states with a very low entropy that can be produced using adiabatic state preparation (potentially further enhanced by non-adiabatic ramps determined using optimal control techniques), where some parameters are varied time dependently. We explored these techniques in more detail, using numerical methods in tensor networks with MPS and MPOs, and based around parameters of

current experiments. We also showed how the same models can give rise to entanglement that is useful for quantum enhanced metrology, and characterised the states we can prepare in terms of their Quantum Fisher Information for collective measurements with Ramsey spectroscopy.

Several directions could be taken following the work discussed in this thesis. First of all, realising these ideas experimentally would be extremely interesting. Furthermore, we propose several theoretical suggestions below.

It would be interesting to extend the study of the spin models in the different interactions regimes (chapters 5 and 7) to include the presence of classical noise and spontaneous emission. Any additional experimental values would help to understand the main differences that could appear between the numerical solutions and those resulting from imperfections in the experiments.

The finite-temperature calculations (chapter 5) for larger systems could be analysed via Monte-Carlo techniques for very small temperatures. This would require a different kind of numerical calculation expertise, but the answers could complete the thermalisation studies in these systems.

We have studied the preparation of magnetic quantum states using adiabatic state preparation techniques in chapter 6. There are several lines of further studies that we propose. For the study of antiferromagnetic states, which were only briefly touched upon here, we consider that exploring this behaviour for larger system sizes using Matrix Product States would be very interesting, and would connect to recent experiments in this area [29–32]. Additionally, more research on alternative optimal control techniques could be done. This field is extremely vast and numerous research studies could be practised in this area. Likewise, studies for the spin-1 model in other magnetic regimes could complete the results here and the ones explored in [153].

As was noted in chapter 7, a disorder strength threshold could be found in the presence of long-range interactions, beyond which the spin-spin correlations will decay even in the presence of long-range interactions. This could be a stimulating study to investigate whether this would be a sharp transition or a crossover, complemented with the considerations of different types of disorder. Further future investigations of the phase diagrams [219] for the different models described with disorder will shed some light on understanding the behaviour of these systems in terms of their magnetic properties.

Other quantum phenomena could be investigated in these many-body systems. The presence of impurities, or further investigations on transport in these models could help to understand and probe the non-equilibrium dynamics in quantum magnetic states [220].

Our findings are immediately relevant for ultracold atoms in optical lattices. However, realising these models in other quantum simulation platforms could provide new interesting physics, such as in ion traps [15] or, in the case of systems with long range interactions, Rydberg atoms [221, 222] or ultracold molecules [84].

The study of these kind of models in higher dimensions would require complementary tensor network techniques, such as PEPS [41] or MERA [114].

A great deal of research work could be still done, and we hope that future collaborations between experimental and theoretical groups will provide answers to some of these remaining questions and further expand the impact of this work in the field of strongly correlated systems in many-body physics.

Appendices

Appendix A

Convergence studies

To handle a many-body problem numerically, we implement a Density Matrix Renormalization Group (DMRG) code, using Matrix Product States (MPS) representation.

For large system sizes, the convergence cannot be studied by comparing with the Exact Diagonalisation (ED) results.

To keep the time-scale required for the numerical calculations manageable, we truncate it by defining a maximum value bond dimension D_{\max} . This truncation is performed by retaining only basis states related to a small weight in the expansion of a reduced density matrix in terms of its eigenstates, for some part of the system.

Note: here we do not make the difference between spin-1 ($\hat{S}_j^x, \hat{S}_j^y, \hat{S}_j^z$) and spin-1/2 ($\hat{s}_j^x, \hat{s}_j^y, \hat{s}_j^z$) operators.

A.1 Time evolution for a large number of spins

Here we include the convergence studies for section 5.3.

An exhaustive convergence analysis is done for a system size $M = 40$ for the time evolution of our spin-1 and spin-1/2 models, by looking at the truncation parameters bond dimension D_{\max} and time-step dt .

A.1.1 Spin-1 model time evolution

All plots in Figures A.1 and A.2 are normalized and calculated with Trotter error 4. The insets are enlarged parts of the bigger graph, having the same axes.

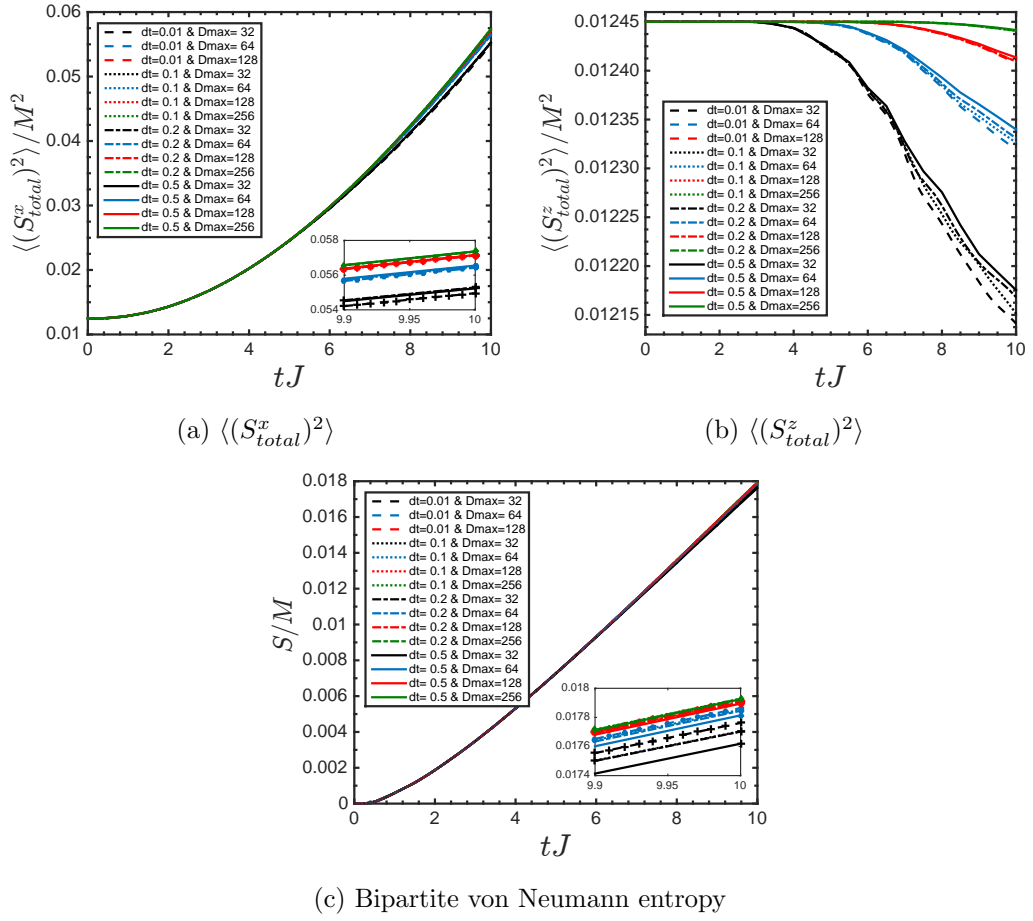


FIGURE A.1: Spin-1: Convergence plots for global quantities and local properties (correlation functions and entropy), for $M = 40$ and $u = 0.2J$, as a function of dt and D_{\max} . The insets provide a zoom at the end of the evolution, for a better understanding of the convergence, having point markers as well as lines, to represent exactly the values result of the simulations. (a) For $\langle (S_{total}^x)^2 \rangle$ at $tJ \approx 7$ there is a divergence for the smallest D_{\max} . Only the end of the evolution we can distinguish the biggest bond dimensions, with a divergence of less than 1%. (b) $\langle (S_{total}^z)^2 \rangle$ shows very early discrepancies with smaller bond dimensions, decaying very fast. At around $tJ = 6$ the divergence between $D_{\max}=128$ and $D_{\max}=256$ appears. Taking the value at the end of the ramp, the discrepancies for these two bond dimensions for a time step $dt=0.1$ is only about 0.02%. (c) The bipartite von Neumann entropy per particle increases with time. The convergence for high bond dimensions is clearly visible. These studies are relevant for plots in Fig. 5.3.

Regarding dt , there is no need to go to values smaller than 0.1. For the bond dimension, a value of $D_{\max} = 128$ will be selected for the further calculations, as the convergence is found for increasingly large D_{\max} with very small total differences.

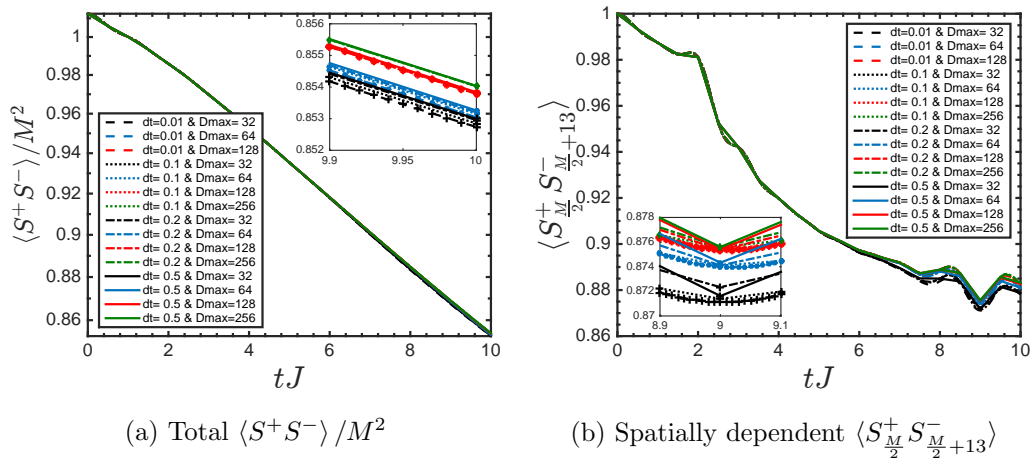


FIGURE A.2: Spin-1: Spatially dependent correlation functions, for $M = 40$ and $u = 0.2J$, as a function of dt and D_{\max} . The insets provide a zoom for a better understanding of the convergence, having point markers as well as lines, to represent exactly the values result of the simulations. (a) The total value of the $\langle S^+ S^- \rangle$ converges at the end of the evolution. (b) In the spatially dependent correlations the divergence starts around $tJ = 6.5$. For higher dimensions the divergence starts around $tJ = 9$. These studies are relevant for plots in figures 5.3 and 5.5.

A.1.2 Spin-1/2 model time evolution

All plots in Figures A.3 and A.4, are normalized and calculated with Trotter error 4. The insets are enlarged parts of the bigger graph, having the same axes.

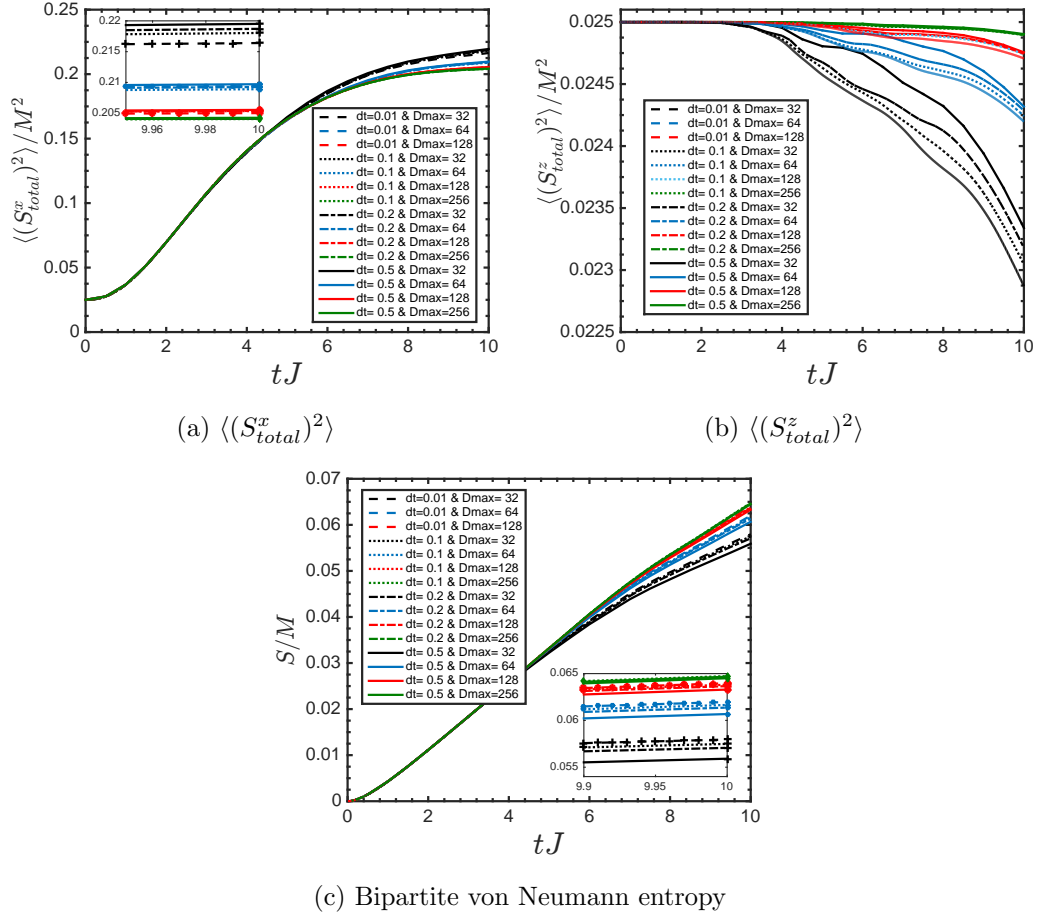


FIGURE A.3: Spin-1/2: Convergence plots for global quantities and local properties (correlation functions and entropy), for $M = 40$ and $\Delta = 0.2J$, as a function of dt and D_{\max} . The insets provide a zoom at the end of the evolution, for a better understanding of the convergence, having point markers as well as lines, to represent exactly the values result of the simulations. (a) For $\langle\langle S_{total}^x \rangle\rangle^2$ it is possible to distinguish a divergence for smaller bond dimensions, starting around $tJ = 5$. (b) $\langle\langle S_{total}^z \rangle\rangle^2$ shows very early discrepancies with smaller bond dimensions, decaying very fast. At around $tJ = 5$ the divergence between $D_{\max}=128$ and $D_{\max}=256$ appears. Taking the value at the end of the ramp, the discrepancies for these two bond dimensions for a time step $dt=0.1$ is only about 1%. (c) The bipartite von Neumann entropy per particle increases with time. The divergence starts around $tJ = 4$ and at the end of the evolution only for high bond dimension the system shows a convergence. These studies are relevant for plots in Fig. 5.4.

Regarding dt , there is no need to go to values smaller than 0.1. For the bond dimension, a value of $D_{\max} = 256$ will be selected for the further calculations, as the convergence is found for increasingly large D_{\max} .

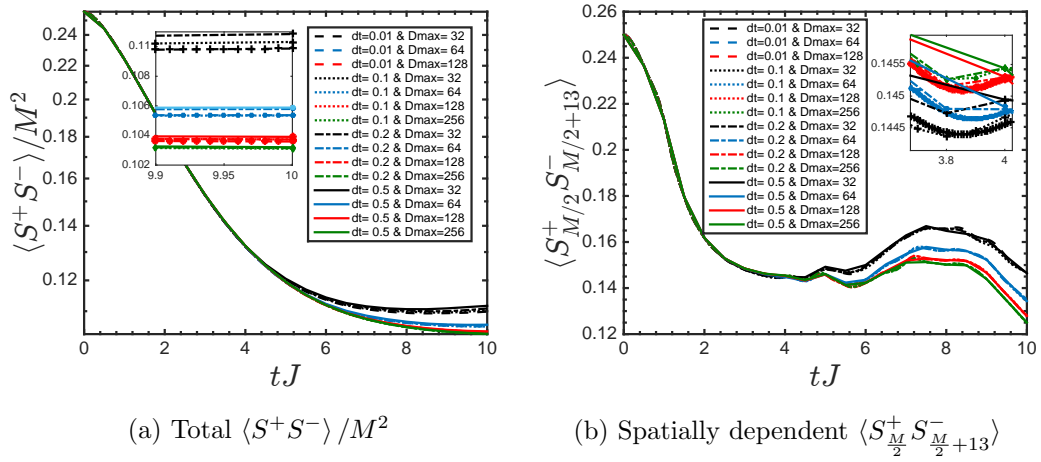


FIGURE A.4: Spin-1/2: Spatially dependent correlation functions, for $M = 40$ and $\Delta = 0.2J$, as a function of dt and D_{\max} , with Trotter error 4. The insets provide a zoom for a better understanding of the convergence, having point markers as well as lines, to represent exactly the values result of the simulations. (a) The total value of the $\langle S^+ S^- \rangle$ converge at the end of the evolution only for higher bond dimensions. (b) In the spatially dependent correlations the divergence even for higher dimensions starts around $tJ = 3.9$. These studies are relevant for plots in figures 5.4 and 5.5.

A.2 Finite temperature calculations

Here we include the convergence studies for section 5.4.2.

The convergence analysis is done for a system size $M = 40$ for the time-propagation at finite temperatures in our spin-1 and spin-1/2 models, by looking at the truncation parameters bond dimension D_{\max} and β_{step} , with $\beta = \frac{1}{k_B T}$, being T the temperature.

Here we use Trotter error 2, since the time needed in CPU for Order 4 will be much longer without a large difference expected.

A.2.1 Spin-1 model finite temperature calculations

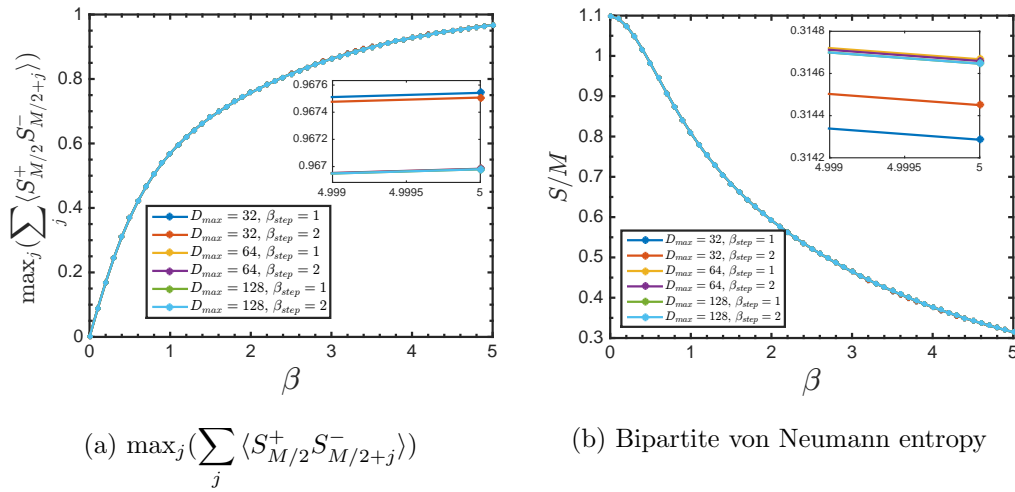


FIGURE A.5: Spin-1: Convergence studies for $M = 40$ and $u = 0.3J$, as a function of D_{\max} and β_{step} . (a) $\max_j \left(\sum_j \langle S_{M/2}^+ S_{M/2+j}^- \rangle \right)$ correlations where just in the inset the divergence for smaller D_{\max} is appreciated. (b) For the bipartite von Neumann entropy S we find the same results, just showing differences at the end of the evolution. The insets are enlarged parts of the bigger graph, having the same axes. These studies are relevant for plots in figures 5.6, 5.8 and 5.9.

The convergence study for spin-1 is summarised in Fig. A.5. According to the results, $D_{\max} = 64$ and $\beta_{\text{step}} = 1$ will be the values selected for the correlation length analysis.

A.2.2 Spin-1/2 model finite temperature calculations

The convergence study for spin-1/2 is summarised in Fig. A.6. According to the results, $D_{\max} = 64$ and $\beta_{step} = 1$ will be the values selected for the correlation length analysis.

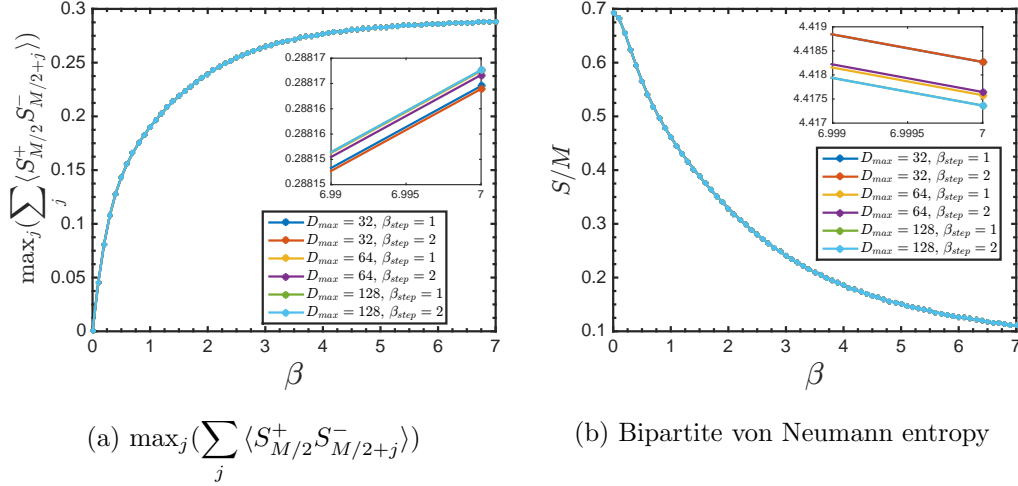


FIGURE A.6: Spin-1/2: Convergence studies for $M = 40$ and $\Delta = 0.2J$, as a function of D_{\max} and β_{step} . (a) $\max_j \left(\sum_j \langle S_{M/2}^+ S_{M/2+j}^- \rangle \right)$ correlations, where just at the end

we see a divergence for smaller bond dimensions. (c) For the bipartite von Neumann entropy S we find the same results, just showing differences in the inset. The insets are enlarged parts of the bigger graph, having the same axes. These studies are relevant for plots in figures 5.7 and 5.10.

A.3 Spin currents

In this section we include the convergence studies for the spin currents study in section 5.5.

The convergence analysis is done for a system size $M = 20$ for the time-propagation of the spin currents \hat{C} in our spin-1 and spin-1/2 models, by looking at the truncation parameters bond dimension D_{\max} and time step dt .

In Fig. A.7 we show the values of the currents at $tJ = 3$ for different bond dimension and time step, for both models.

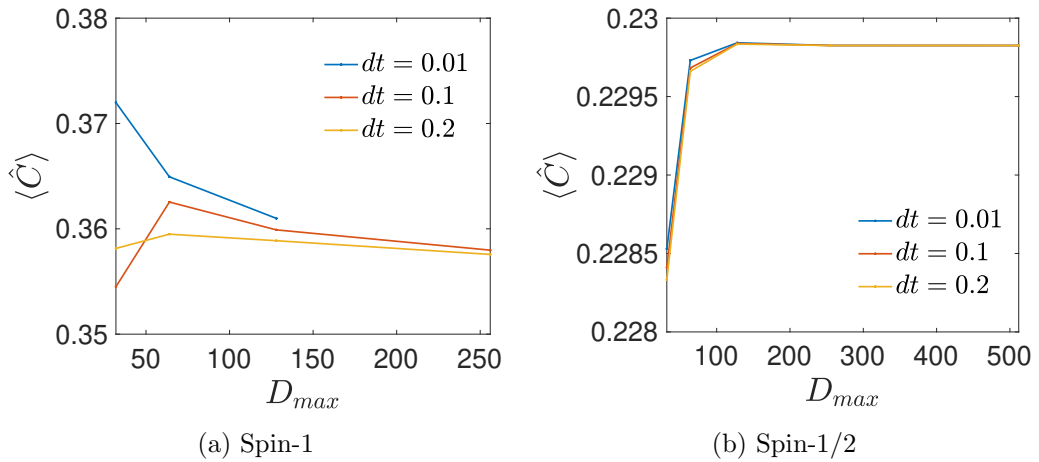


FIGURE A.7: Convergence study for currents in the (a) spin-1 and (b) spin-1/2 model, for $M=20$ and periodic boundary conditions, as a function of dt and D_{\max} , with Trotter error 4. Parameters values are $u, \Delta = 0.5J$ and $\Omega = 0.3\pi$. These studies are relevant for plots in figures 5.15 to 5.21.

As a result of this convergence study, the numerical parameters values chosen are $D_{\max} = 256$ and $dt = 0.1$.

Bibliography

- [1] W. D. Phillips, J. V. Prodan, and H. J. Metcalf. Laser cooling and electromagnetic trapping of neutral atoms. *J. Opt. Soc. Am. B*, **2**(11):1751–1767, Nov 1985.
- [2] J. Dalibard and C. Cohen-Tannoudji. Dressed-atom approach to atomic motion in laser light: the dipole force revisited. *J. Opt. Soc. Am. B*, **2**(11):1707–1720, Nov 1985.
- [3] S. Chu, L. Hollberg, J. E. Bjorkholm, A. Cable, and A. Ashkin. Three-dimensional viscous confinement and cooling of atoms by resonance radiation pressure. *Phys. Rev. Lett.*, **55**:48–51, Jul 1985.
- [4] M. H. Anderson, J. R. Ensher, M. R. Matthews, C. E. Wieman, and E. A. Cornell. Observation of bose-einstein condensation in a dilute atomic vapor. *Science*, **269**(5221):198–201, 1995.
- [5] K. B. Davis, M. O. Mewes, M. R. Andrews, N. J. van Druten, D. S. Durfee, D. M. Kurn, and W. Ketterle. Bose-einstein condensation in a gas of sodium atoms. *Phys. Rev. Lett.*, **75**:3969–3973, Nov 1995.
- [6] C. C. Bradley, C. A. Sackett, J. J. Tollett, and R. G. Hulet. Evidence of bose-einstein condensation in an atomic gas with attractive interactions. *Phys. Rev. Lett.*, **75**:1687–1690, Aug 1995.
- [7] R. P. Feynman. Simulating physics with computers. *International Journal of Theoretical Physics*, **21**(6):467–488, 1982.
- [8] C. Gross, T. Zibold, E. Nicklas, J. Estève, and M. K. Oberthaler. Nonlinear atom interferometer surpasses classical precision limit. *Nature*, **464**(7292):1165–1169, 2010.
- [9] C. Gross and I. Bloch. Quantum simulations with ultracold atoms in optical lattices. *Science*, **357**(6355):995–1001, 2017.

- [10] E. A. Martinez, C. A. Muschik, P. Schindler, D. Nigg, A. Erhard, M. Heyl, P. Hauke, M. Dalmonte, T. Monz, P. Zoller, and R. Blatt. Real-time dynamics of lattice gauge theories with a few-qubit quantum computer. *Nature*, **534** (7608):516–519, 2016.
- [11] J. Argüello-Luengo, A. González-Tudela, T. Shi, P. Zoller, and J. I. Cirac. Analogue quantum chemistry simulation. *Nature*, **574**(7777):215–218, 2019.
- [12] I. Buluta and F. Nori. Quantum simulators. *Science*, **326**(5949):108–111, 2009.
- [13] I. M. Georgescu, S. Ashhab, and F. Nori. Quantum simulation. *Rev. Mod. Phys.*, **86**:153–185, Mar 2014.
- [14] R. Blatt and C. F. Roos. Quantum simulations with trapped ions. *Nature Physics*, **8**(4):277–284, 2012.
- [15] J. G. Bohnet, B. C. Sawyer, J. W. Britton, M. L. Wall, A. M. Rey, M. Foss-Feig, and J. J. Bollinger. Quantum spin dynamics and entanglement generation with hundreds of trapped ions. *Science*, **352**(6291):1297–1301, 2016.
- [16] A. A. Houck, H. E. Türeci, and J. Koch. On-chip quantum simulation with superconducting circuits. *Nature Physics*, **8**(4):292–299, 4 2012.
- [17] A. Aspuru-Guzik and P. Walther. Photonic quantum simulators. *Nature Physics*, **8**(4):285–291, 2012.
- [18] I. Bloch, J. Dalibard, and S. Nascimbene. Quantum simulations with ultracold quantum gases. *Nat Phys*, **8**(4):267–276, Apr 2012.
- [19] J. Hubbard. Electron correlations in narrow energy bands. *Proceedings of the Royal Society of London A: Mathematical, Physical and Engineering Sciences*, **276**(1365):238–257, 1963.
- [20] L. Tarruell and L. Sanchez-Palencia. Quantum simulation of the hubbard model with ultracold fermions in optical lattices. *Comptes Rendus Physique*, **19**:365 – 393, 2018.
- [21] M. P. A. Fisher, P.B. Weichman, G. Grinstein, and D. S. Fisher. Boson localization and the superfluid-insulator transition. *Phys. Rev. B*, **40**:546–570, Jul 1989.
- [22] D. Jaksch, C. Bruder, J. I. Cirac, C. W. Gardiner, and P. Zoller. Cold bosonic atoms in optical lattices. *Phys. Rev. Lett.*, **81**:3108–3111, Oct 1998.
- [23] M. Greiner, O. Mandel, T. Esslinger, T. W. Hansch, and I. Bloch. Quantum phase transition from a superfluid to a mott insulator in a gas of ultracold atoms. *Nature*, **415**(6867):39–44, Jan 2002.

- [24] C. Chin, R. Grimm, P. Julienne, and E. Tiesinga. Feshbach resonances in ultracold gases. *Rev. Mod. Phys.*, **82**:1225–1286, Apr 2010.
- [25] P. W. Anderson. Antiferromagnetism. theory of superexchange interaction. *Phys. Rev.*, **79**:350–356, Jul 1950.
- [26] W. Nolting and A. Ramakanth. *Quantum Theory of Magnetism*. Springer Berlin Heidelberg, 2009.
- [27] S. Trotzky, P. Cheinet, S. Fölling, M. Feld, U. Schnorrberger, A. M. Rey, A. Polkovnikov, E. A. Demler, M. D. Lukin, and I. Bloch. Time-resolved observation and control of superexchange interactions with ultracold atoms in optical lattices. *Science*, **319**(5861):295–299, 2008.
- [28] K. R. A. Hazzard, M. van den Worm, M. Foss-Feig, S. R. Manmana, E. G. Dalla Torre, T. Pfau, M. Kastner, and A. M. Rey. Quantum correlations and entanglement in far-from-equilibrium spin systems. *Phys. Rev. A*, **90**:063622, Dec 2014.
- [29] R. A. Hart, P. M. Duarte, T-L. Yang, X. Liu, T. Paiva, E. Khatami, R. T. Scalettar, N. Trivedi, D. A. Huse, and R. G. Hulet. Observation of antiferromagnetic correlations in the Hubbard model with ultracold atoms. *Nature*, **519**:211–214, 2015.
- [30] L. W. Cheuk, M. A. Nichols, K. R. Lawrence, M. Okan, H. Zhang, and M. W. Zwierlein. Observation of 2d fermionic mott insulators of ^{40}K with single-site resolution. *Phys. Rev. Lett.*, **116**:235301, Jun 2016.
- [31] M. F. Parsons, A. Mazurenko, C. S. Chiu, G. Ji, D. Greif, and M. Greiner. Site-resolved observations of antiferromagnetic correlations in the hubbard model. *arXiv*, **cond-mat/1605.02704**, May 2016.
- [32] M. Boll, T. A. Hilker, G. Salomon, A. Omran, J. Nespolo, L. Pollet, I. Bloch, and C. Gross. Spin- and density-resolved microscopy of antiferromagnetic correlations in fermi-hubbard chains. *Science*, **353**(6305):1257–1260, 2016.
- [33] S. Kuhr, W. Alt, D. Schrader, M. Müller, V. Gomer, and D. Meschede. Deterministic delivery of a single atom. *Science*, **293**(5528):278–280, 2001.
- [34] W. S. Bakr, J. I. Gillen, A. Peng, S. Fölling, and M. Greiner. A quantum gas microscope for detecting single atoms in a hubbard-regime optical lattice. *Nature*, **462**(7269):74–77, 2009.

- [35] J. F. Sherson, C. Weitenberg, M. Endres, M. Cheneau, I. Bloch, and S. Kuhr. Single-atom-resolved fluorescence imaging of an atomic mott insulator. *Nature*, **467**(7311):68–72, 2010.
- [36] J. I. Cirac and P. Zoller. Goals and opportunities in quantum simulation. *Nature Publishing Group*, **8**(4):264–266, 2012.
- [37] D. C. McKay and B. DeMarco. Cooling in strongly correlated optical lattices: prospects and challenges. *Reports on Progress in Physics*, **74**(5):054401, Apr 2011.
- [38] R. M. Noack and S. R. Manmana. Diagonalization- and numerical renormalization-group-based methods for interacting quantum systems. *AIP Conference Proceedings*, **789**(1):93–163, 2005.
- [39] S. R. White. Density matrix formulation for quantum renormalization groups. *Phys. Rev. Lett.*, **69**:2863–2866, Nov 1992.
- [40] S. R. White. Density-matrix algorithms for quantum renormalization groups. *Phys. Rev. B*, **48**:10345–10356, Oct 1993.
- [41] F. Verstraete, V. Murg, and J. I. Cirac. Matrix product states, projected entangled pair states, and variational renormalization group methods for quantum spin systems. *Advances in Physics*, **57**(2):143–224, 2008.
- [42] U. Schollwöck. The density-matrix renormalization group in the age of matrix product states. *Annals of Physics*, **326**(1):96 – 192, 2011. Jan 2011 Special Issue.
- [43] G. Vidal. Efficient classical simulation of slightly entangled quantum computations. *Phys. Rev. Lett.*, **91**:147902, Oct 2003.
- [44] G. Vidal. Efficient simulation of one-dimensional quantum many-body systems. *Phys. Rev. Lett.*, **93**:040502, Jul 2004.
- [45] F. Verstraete, J. J. García-Ripoll, and J. I. Cirac. Matrix product density operators: Simulation of finite-temperature and dissipative systems. *Phys. Rev. Lett.*, **93**:207204, 2004.
- [46] I. P. McCulloch. From density-matrix renormalization group to matrix product states. *Journal of Statistical Mechanics: Theory and Experiment*, **2007**(10), Oct 2007.
- [47] M. L. Wall and L. D. Carr. Out-of-equilibrium dynamics with matrix product states. *New Journal of Physics*, **14**(12):125015, 2012.

- [48] J. Haegeman, J. I. Cirac, T. J. Osborne, I. Pižorn, H. Verschelde, and F. Verstraete. Time-dependent variational principle for quantum lattices. *Phys. Rev. Lett.*, **107**:070601, Aug 2011.
- [49] H. Carmichael. An Open Systems Approach to Quantum Optics. *Lecture Notes in Physics Monographs*, **18**, Jan 1993.
- [50] K. Mølmer, Y. Castin, and J. Dalibard. Monte carlo wave-function method in quantum optics. *J. Opt. Soc. Am. B*, **10**(3):524–538, Mar 1993.
- [51] A. J. Daley. Quantum trajectories and open many-body quantum systems. *Advances in Physics*, **63**(2):77–149, 2014.
- [52] M. Greiner and S. Folling. Condensed-matter physics: Optical lattices. *Nature*, **453**:736–738, Jun 2008.
- [53] M. Lewenstein, A. Sanpera, and V. Ahufinger. *Ultracold atoms in optical lattices: simulating Quantum Many-Body systems*. Oxford University Press, 2012.
- [54] A. Venegas-Gomez, A. S. Buyskikh, J. Schachenmayer, W. Ketterle, and A. J. Daley. Dynamics of rotated spin states and magnetic ordering with two-component bosonic atoms in optical lattices. *Phys. Rev. A*, **102**:023321, Aug 2020.
- [55] A. Venegas-Gomez, A. S. Buyskikh, J. Schachenmayer, W. Ketterle, and A. J. Daley. Adiabatic preparation of entangled, magnetically ordered states with cold bosons in optical lattices. *arXiv*, **cond-mat/ 2003.10905**, 2020.
- [56] I. Dimitrova, N. Jepsen, A. Buyskikh, A. Venegas-Gomez, J. Amato-Grill, A. Daley, and W. Ketterle. Enhanced superexchange in a tilted mott insulator. *Phys. Rev. Lett.*, **124**:043204, Jan 2020.
- [57] J. Sebby-Strabley, M. Anderlini, P. S. Jessen, and J. V. Porto. Lattice of double wells for manipulating pairs of cold atoms. *Phys. Rev. A*, **73**:033605, Mar 2006.
- [58] C. Orzel. *Quantum Simulation*. 2399-2891. IOP Publishing, 2017.
- [59] V. S. Letokhov. The narrowing of doppler broadened line in standing light wave. *JETP Lett.*, **7**, 1968.
- [60] C. Salomon, J. Dalibard, A. Aspect, H. Metcalf, and C. Cohen-Tannoudji. Channeling atoms in a laser standing wave. *Phys. Rev. Lett.*, **59**:1659–1662, Oct 1987.
- [61] C. Gerry and P. Knight. *Introductory Quantum Optics*. Cambridge University Press, 2004.

- [62] K. R. A. Hazzard. *Quantum Phase Transitions in Cold Atoms and Low Temperature Solids*. Springer, 2011.
- [63] C. J. Pethick and H. Smith. *Bose-Einstein condensation in dilute gases*. Cambridge University Press, 2nd edition, 2008.
- [64] R. Grimm, M. Weidemüller, and Y. B. Ovchinnikov. Optical Dipole Traps for Neutral Atoms. *Advances in Atomic Molecular and Optical Physics*, **42**:95–170, 2000.
- [65] C. Salomon, G. Shlyapnikov, and L. F. Cugliandolo. *Many-body Physics with Ultracold Gases: Lecture Notes of the Les Houches Summer School*, volume **94**. Oxford University Press, 28 June to 23 July 2010.
- [66] D. Jaksch, H.-J. Briegel, J. I. Cirac, C. W. Gardiner, and P. Zoller. Entanglement of atoms via cold controlled collisions. *Phys. Rev. Lett.*, **82**:1975–1978, Mar 1999.
- [67] O. Mandel, M. Greiner, A. Widera, T. Rom, T. W. Hänsch, and I. Bloch. Coherent transport of neutral atoms in spin-dependent optical lattice potentials. *Phys. Rev. Lett.*, **91**:010407, Jul 2003.
- [68] D. McKay and B. DeMarco. Thermometry with spin-dependent lattices. *New Journal of Physics*, **12**(5):055013, May 2010.
- [69] N. W. Ashcroft and N. D. Mermin. *Solid state physics*. Science: Physics. Saunders College, 1976.
- [70] D. Jaksch and P. Zoller. The cold atom hubbard toolbox. *Annals of Physics*, **315**(1):52 – 79, 2005. Special Issue.
- [71] P. Törmä and K. Sengstock, editors. *Quantum Gas Experiments - Exploring Many-Body States*. Cold Atoms Series. Imperial College Press, 2014.
- [72] P. L. Knight, S. Scheel, et al. *Springer handbook of atomic, molecular, and optical physics*, pages 1219–1234. Springer, 2006.
- [73] P. B. Blakie and C. W. Clark. Wannier states and bose–hubbard parameters for 2d optical lattices. *Journal of Physics B: Atomic, Molecular and Optical Physics*, **37**(7):1391–1404, Mar 2004.
- [74] I. Bloch. Quantum gases in optical lattices. *Physics World*, **17**(4):25, 2004.
- [75] Endres M. *Probing Correlated Quantum Many-Body Systems at the Single-Particle Level*. Springer, 2014.

- [76] I. Bloch, J. Dalibard, and W. Zwerger. Many-body physics with ultracold gases. *Rev. Mod. Phys.*, **80**:885–964, Jul 2008.
- [77] G. K. Campbell, J. Mun, M. Boyd, P. Medley, A. E. Leanhardt, L. G. Marcassa, D. E. Pritchard, and W. Ketterle. Imaging the mott insulator shells by using atomic clock shifts. *Science*, **313**(5787):649–652, 2006.
- [78] W. S. Bakr, A. Peng, M. E. Tai, R. Ma, J. Simon, J. I. Gillen, S. Fölling, L. Pollet, and M. Greiner. Probing the superfluid–to–mott insulator transition at the single-atom level. *Science*, **329**(5991):547–550, 2010.
- [79] M. Miranda, R. Inoue, Y. Okuyama, A. Nakamoto, and M. Kozuma. Site-resolved imaging of ytterbium atoms in a two-dimensional optical lattice. *Phys. Rev. A*, **91**:063414, Jun 2015.
- [80] E. Haller, J. Hudson, A. Kelly, D. A. Cotta, B. Peaudecerf, G. D. Bruce, and S. Kuhr. Single-atom imaging of fermions in a quantum-gas microscope. *Nature Physics*, **11**(9):738–742, 2015.
- [81] P. Cheneau, M. and Barmettler, D. Poletti, M. Endres, P. Schauß, T. Fukuhara, C. Gross, I. Bloch, C. Kollath, and S. Kuhr. Light-cone-like spreading of correlations in a quantum many-body system. *Nature*, **481**(7382):484–487, 2012.
- [82] M. Lewenstein, A. Sanpera, V. Ahufinger, B. Damski, A. Sen(De), and U. Sen. Ultracold atomic gases in optical lattices: mimicking condensed matter physics and beyond. *Advances in Physics*, **56**(2):243–379, 2007.
- [83] T. Manthey, T. Niederprüm, O. Thomas, and H. Ott. Dynamically probing ultracold lattice gases via rydberg molecules. *New Journal of Physics*, **17**(10):103024, Oct 2015.
- [84] J. A. Blackmore, L. Caldwell, P. D. Gregory, E. M. Bridge, R. Sawant, J. Aldegunde, J. Mur-Petit, D. Jaksch, J. M. Hutson, B. E. Sauer, M. R. Tarbutt, and S. L. Cornish. Ultracold molecules for quantum simulation: rotational coherences in CaF and RbCs. *Quantum Science and Technology*, **4**(1):014010, Dec 2018.
- [85] J. J. García-Ripoll and J. I. Cirac. Spin dynamics for bosons in an optical lattice. *New Journal of Physics*, **5**(1):76, 2003.
- [86] P. L. Knight, E. A. Hinds, M. B. Plenio, J. J. García-Ripoll, and J. I. Cirac. Quantum computation with cold bosonic atoms in an optical lattice. *Philosophical Transactions of the Royal Society of London*, **361**, 2003.

- [87] J. H. Lee, E. Montano, I. H. Deutsch, and P. S. Jessen. Robust site-resolvable quantum gates in an optical lattice via inhomogeneous control. *Nature Communications*, **4**(1):2027, 2013.
- [88] G. De las Cuevas and T. S. Cubitt. Simple universal models capture all classical spin physics. *Science*, **351**(6278):1180–1183, 2016.
- [89] D. M. Weld and W. Ketterle. Towards quantum magnetism with ultracold atoms. *Journal of Physics: Conference Series*, **264**:012017, Jan 2011.
- [90] I. B. Spielman. Atomic physics: A route to quantum magnetism. *Nature*, **472**:301–302, Apr 2011.
- [91] J. Spałek. Effect of pair hopping and magnitude of intra-atomic interaction on exchange-mediated superconductivity. *Phys. Rev. B*, **37**:533–536, Jan 1988.
- [92] J. Quintanilla and C. Hooley. The strong-correlations puzzle. *Physics World*, **22**(6):32–37, 6 2009.
- [93] M. Inguscio, W. Ketterle, S. Stringari, and G. Roati. *Quantum Matter at Ultralow Temperatures*. International School of Physics Enrico Fermi Series. IOS Press, 2016.
- [94] R. C. Brown, R. Wyllie, S. B. Koller, E. A. Goldschmidt, M. Foss-Feig, and J. V. Porto. Two-dimensional superexchange-mediated magnetization dynamics in an optical lattice. *Science*, **348**(6234):540–544, 2015.
- [95] L.-M. Duan, E. Demler, and M. D. Lukin. Controlling spin exchange interactions of ultracold atoms in optical lattices. *Phys. Rev. Lett.*, **91**:090402, Aug 2003.
- [96] A. B. Kuklov and B. V. Svistunov. Counterflow superfluidity of two-species ultracold atoms in a commensurate optical lattice. *Phys. Rev. Lett.*, **90**:100401, Mar 2003.
- [97] E. Altman, W. Hofstetter, E. Demler, and M. D. Lukin. Phase diagram of two-component bosons on an optical lattice. *New Journal of Physics*, **5**:113, 2003.
- [98] J. Sólyom and T. A. L. Ziman. Ground-state properties of axially anisotropic quantum heisenberg chains. *Phys. Rev. B*, **30**:3980–3992, Oct 1984.
- [99] W. Chen, K. Hida, and B. C. Sanctuary. Ground-state phase diagram of $s = 1$ XXZ chains with uniaxial single-ion-type anisotropy. *Phys. Rev. B*, **67**:104401, Mar 2003.

- [100] T. Stöferle, H. Moritz, C. Schori, M. Köhl, and T. Esslinger. Transition from a strongly interacting 1d superfluid to a mott insulator. *Phys. Rev. Lett.*, **92**:130403, Mar 2004.
- [101] J. Cullum and R. A. Willoughby. Computing eigenvalues of very large symmetric matrices—an implementation of a lanczos algorithm with no reorthogonalization. *Journal of Computational Physics*, **44**(2):329 – 358, 1981.
- [102] U. M. Ascher. *Computer Methods for Ordinary Differential Equations and Differential-Algebraic Equations*. Cambridge University Press, 1998.
- [103] R. B. Sidje. EXPOKIT. A software package for computing matrix exponentials. *ACM Trans. Math. Softw.*, **24**(1):130–156, 1998.
- [104] J. Eisert, M. Cramer, and M. B. Plenio. Colloquium: Area laws for the entanglement entropy. *Rev. Mod. Phys.*, **82**:277–306, Feb 2010.
- [105] S. Östlund and S. Rommer. Thermodynamic limit of density matrix renormalization. *Phys. Rev. Lett.*, **75**:3537–3540, Nov 1995.
- [106] S. Rommer and S. Östlund. Class of ansatz wave functions for one-dimensional spin systems and their relation to the density matrix renormalization group. *Phys. Rev. B*, **55**:2164–2181, Jan 1997.
- [107] U. Schollwöck. The density-matrix renormalization group. *Reviews of modern physics*, **77**(1):259, 2005.
- [108] A. J. Daley, C. Kollath, U. Schollwöck, and G. Vidal. Time-dependent density-matrix renormalization-group using adaptive effective hilbert spaces. *Journal of Statistical Mechanics: Theory and Experiment*, **2004**(04):P04005, 2004.
- [109] M. Suzuki. Fractal decomposition of exponential operators with applications to many-body theories and monte carlo simulations. *Physics Letters A*, **146**(6):319 – 323, 1990.
- [110] J. J. García-Ripoll. Time evolution of matrix product states. *New Journal of Physics*, **8**(12):305–305, Dec 2006.
- [111] A. E. Feiguin and S. R. White. Finite-temperature density matrix renormalization using an enlarged hilbert space. *Phys. Rev. B*, **72**:220401, Dec 2005.
- [112] G. De las Cuevas, N. Schuch, D. Pérez-García, and J. I. Cirac. Purifications of multipartite states: limitations and constructive methods. *New J. Phys.*, **15**(12):123021, 2013.
- [113] C. W. Gardiner and P. Zoller. *Quantum Noise*. Springer, 2nd edition, 2000.

- [114] G. Vidal. Class of quantum many-body states that can be efficiently simulated. *Phys. Rev. Lett.*, **101**:110501, Sep 2008.
- [116] P. Barmettler, M. Punk, V. Gritsev, E. Demler, and E. Altman. Relaxation of antiferromagnetic order in spin-1/2 chains following a quantum quench. *Phys. Rev. Lett.*, **102**:130603, Apr 2009.
- [117] E. H. Lieb and D. W. Robinson. The finite group velocity of quantum spin systems. *Communications in Mathematical Physics*, **28**(3):251–257, 1972.
- [118] A. S. Buyskikh, M. Fagotti, J. Schachenmayer, F. Essler, and A. J. Daley. Entanglement growth and correlation spreading with variable-range interactions in spin and fermionic tunneling models. *Phys. Rev. A*, **93**:053620, May 2016.
- [119] D. I. Khomskii. *Basic Aspects of the Quantum Theory of Solids: Order and Elementary Excitations*. Cambridge University Press, 2010.
- [120] T. Koffel, M. Lewenstein, and L. Tagliacozzo. Entanglement entropy for the long range Ising chain. *Phys. Rev. Lett.*, **109**(26):267203, 2012.
- [121] J. Haegeman, T. J. Osborne, and F. Verstraete. Post-matrix product state methods: To tangent space and beyond. *Phys. Rev. B*, **88**(7):075133, 2013.
- [122] J. Haegeman, C. Lubich, I. Oseledets, B. Vandereycken, and F. Verstraete. Unifying time evolution and optimization with matrix product states. *Phys. Rev. B*, **94**:165116, 2016.
- [123] J. M. Deutsch. Quantum statistical mechanics in a closed system. *Phys. Rev. A*, **43**(4):2046–2049, 1991.
- [124] M. Srednicki. Chaos and quantum thermalization. *Phys. Rev. E*, **50**(2):888–901, Aug 1994.
- [125] L. D’Alessio, Y. Kafri, A. Polkovnikov, and M. Rigol. From quantum chaos and eigenstate thermalization to statistical mechanics and thermodynamics. *Adv. Phys.*, **65**(3):239–362, May 2016.
- [126] A. Polkovnikov and D. Sels. Thermalization in small quantum systems. *Science*, **353**(6301):752–753, 2016.
- [127] A. M. Kaufman, M. E. Tai, A. Lukin, M. Rispoli, R. Schittko, P. M. Preiss, and M. Greiner. Quantum thermalization through entanglement in an isolated many-body system. *Science*, **353**(6301):794–800, 2016.
- [128] M. Rigol, V. Dunjko, and M. Olshanii. Thermalization and its mechanism for generic isolated quantum systems. *Nature*, **452**(7189):854–858, 2008.

- [129] R. Nandkishore and D. A. Huse. Many-Body Localization and Thermalization in Quantum Statistical Mechanics. *Annu. Rev. Condens. Matter Phys.*, **6**(1):15–38, Mar 2015.
- [130] J. Eisert, M. Friesdorf, and C. Gogolin. Quantum many-body systems out of equilibrium. *Nat. Phys.*, **11**:124, Feb 2015.
- [131] J. M. Deutsch. Eigenstate thermalization hypothesis. *Rep. Prog. Phys.*, **81**(8):082001, Jul 2018.
- [132] J. Schachenmayer, L. Pollet, M. Troyer, and A. J. Daley. Spontaneous emission and thermalization of cold bosons in optical lattices. *Phys. Rev. A*, **89**(1):1–7, 2014.
- [133] J. Schachenmayer, L. Pollet, M. Troyer, and A. J. Daley. Thermalization of strongly interacting bosons after spontaneous emissions in optical lattices. *EPJ Quantum Technol.*, **2**(1):1–14, 2015.
- [134] W. Han, S.i Maekawa, and X-C. Xie. Spin current as a probe of quantum materials. *Nature Materials*, **19**(2):139–152, 2020.
- [135] J. Schachenmayer, G. Pupillo, and A. J. Daley. Time-dependent currents of one-dimensional bosons in an optical lattice. *New J. Phys.*, **12**:025014, 2010.
- [136] X. Zotos, F. Naef, and P. Prelovsek. Transport and conservation laws. *Phys. Rev. B*, **55**:11029–11032, May 1997.
- [137] E. B. Sonin. Spin currents and spin superfluidity. *Advances in Physics*, **59**(3):181–255, 2010.
- [138] G. Vidal. Classical simulation of infinite-size quantum lattice systems in one spatial dimension. *Phys. Rev. Lett.*, **98**:070201, Feb 2007.
- [139] J. Mun, P. Medley, G. K. Campbell, L. G. Marcassa, D. E. Pritchard, and W. Ketterle. Phase Diagram for a Bose-Einstein Condensate Moving in an Optical Lattice. *Phys. Rev. Lett.*, **99**(15):150604, Oct 2007.
- [140] E. Altman, E. Demler, and M. D. Lukin. Probing many-body states of ultracold atoms via noise correlations. *Phys. Rev. A*, **70**:013603, Jul 2004.
- [141] M. Greiner, C. A. Regal, J. T. Stewart, and D. S. Jin. Probing pair-correlated fermionic atoms through correlations in atom shot noise. *Phys. Rev. Lett.*, **94**:110401, Mar 2005.

- [142] A. Polkovnikov, E. Altman, E. Demler, B. Halperin, and M. D. Lukin. Decay of superfluid currents in a moving system of strongly interacting bosons. *Phys. Rev. A*, **71**:063613, Jun 2005.
- [143] E. Altman, A. Polkovnikov, E. Demler, B. I. Halperin, and M. D. Lukin. Superfluid-insulator transition in a moving system of interacting bosons. *Phys. Rev. Lett.*, **95**:020402, Jul 2005.
- [144] D. M. Weld, H. Miyake, P. Medley, D. E. Pritchard, and W. Ketterle. Thermometry and refrigeration in a two-component mott insulator of ultracold atoms. *Phys. Rev. A*, **82**:051603, Nov 2010.
- [145] G. Baym and C. J. Pethick. Landau critical velocity in weakly interacting bose gases. *Phys. Rev. A*, **86**:023602, Aug 2012.
- [146] J. H. P. Colpa. Diagonalization of the quadratic boson hamiltonian. *Physica A Statistical Mechanics and its Applications*, **93**(3):327–353, Sep 1978.
- [147] T. Schneider and E. Stoll. *Excitation Spectrum of Ferromagnetic xxz -Chains*, pages 201–212. Springer US, Boston, MA, 1983.
- [148] S. Trebst, U. Schollwöck, M. Troyer, and P. Zoller. d -wave resonating valence bond states of fermionic atoms in optical lattices. *Phys. Rev. Lett.*, **96**:250402, Jun 2006.
- [149] A. Kantian, A. J. Daley, and P. Zoller. η condensate of fermionic atom pairs via adiabatic state preparation. *Phys. Rev. Lett.*, **104**:240406, Jun 2010.
- [150] A. S. Sørensen, E. Altman, M. Gullans, J. V. Porto, M. D. Lukin, and E. Demler. Adiabatic preparation of many-body states in optical lattices. *Phys. Rev. A*, **81**:061603, Jun 2010.
- [151] J. Schachenmayer, I. Lesanovsky, A. Micheli, and A. J. Daley. Dynamical crystal creation with polar molecules or rydberg atoms in optical lattices. *New Journal of Physics*, **13**(5):059503, May 2011.
- [152] M. Lubasch, V. Murg, U. Schneider, J. I. Cirac, and M-C. Bañuls. Adiabatic preparation of a heisenberg antiferromagnet using an optical superlattice. *Phys. Rev. Lett.*, **107**:165301, Oct 2011.
- [153] J. Schachenmayer, D. M. Weld, H. Miyake, G. A. Siviloglou, W. Ketterle, and A. J. Daley. Adiabatic cooling of bosons in lattices to magnetically ordered quantum states. *Phys. Rev. A*, **92**:041602, Oct 2015.

- [154] S. Inouye, M. R. Andrews, J. Stenger, H. J. Miesner, D. M. Stamper-Kurn, and W. Ketterle. Observation of feshbach resonances in a bose–einstein condensate. *Nature*, **392**(6672):151–154, 1998.
- [155] E. Timmermans, P. Tommasini, M. Hussein, and A. Kerman. Feshbach resonances in atomic bose–einstein condensates. *Physics Reports*, **15**(1):199 – 230, 1999.
- [156] W-F. Liu, J. Ma, and X. Wang. Quantum fisher information and spin squeezing in the ground state of the xy model. *Journal of Physics A: Mathematical and Theoretical*, **46**(4):045302, Jan 2013.
- [157] E-J. Ye, Z-D. Hu, and W. Wu. Scaling of quantum fisher information close to the quantum phase transition in the xy spin chain. *Physica B: Condensed Matter*, **502**:151 – 154, 2016.
- [158] Kajtoch, D., Witkowska, E., and Sinatra, A. Spin-squeezed atomic crystal. *EPL*, **123**(2):20012, 2018.
- [159] M. M. Rams, P. Sierant, O. Dutta, P. Horodecki, and J. Zakrzewski. At the limits of criticality-based quantum metrology: Apparent super-heisenberg scaling revisited. *Phys. Rev. X*, **8**:021022, Apr 2018.
- [160] I. Frérot and T. Roscilde. Quantum critical metrology. *Phys. Rev. Lett.*, **121**:020402, Jul 2018.
- [161] I. Frérot and T. Roscilde. Reconstructing the quantum critical fan of strongly correlated systems using quantum correlations. *Nature Communications*, **10**(1):577, 2019.
- [162] L. Lucchesi and M. L. Chiofalo. Many-body entanglement in short-range interacting fermi gases for metrology. *Phys. Rev. Lett.*, **123**:060406, Aug 2019.
- [163] J. M. E. Fraïsse, J-G. Baak, and U. R. Fischer. Many-body quantum metrology with scalar bosons in a single potential well. *Phys. Rev. A*, **99**:043618, Apr 2019.
- [164] B. Lücke, M. Scherer, J. Kruse, L. Pezzé, F. Deuretzbacher, P. Hyllus, O. Topic, J. Peise, W. Ertmer, J. Arlt, L. Santos, A. Smerzi, and C. Klempt. Twin matter waves for interferometry beyond the classical limit. *Science*, **334**(6057):773–776, 2011.
- [165] Z. Zhang and L. M. Duan. Quantum metrology with dicke squeezed states. *New Journal of Physics*, **16**(10):103037, Oct 2014.
- [166] K. Lange, J. Peise, B. Lücke, I. Kruse, G. Vitagliano, I. Apellaniz, M. Kleinmann, G. Tóth, and C. Klempt. Entanglement between two spatially separated atomic modes. *Science*, **360**(6387):416–418, 2018.

- [167] Y-Q. Zou, L-N. Wu, Q. Liu, X-Y. Luo, S-F. Guo, J-H. Cao, M. K. Tey, and L. You. Beating the classical precision limit with spin-1 dicke states of more than 10,000 atoms. *Proceedings of the National Academy of Sciences*, **115**(25):6381–6385, 2018.
- [168] A. Evrard, V. Makhalov, T. Chalopin, L. A. Sidorenkov, J. Dalibard, R. Lopes, and S. Nascimbene. Enhanced magnetic sensitivity with non-gaussian quantum fluctuations. *Phys. Rev. Lett.*, **122**:173601, May 2019.
- [169] C. Zener. Non-adiabatic crossing of energy levels. *Proceedings of the Royal Society of London A: Mathematical, Physical and Engineering Sciences*, **137**(833):696–702, 1932.
- [170] J. Oreg, F. T. Hioe, and J. H. Eberly. Adiabatic following in multilevel systems. *Phys. Rev. A*, **29**:690–697, Feb 1984.
- [171] J. Roland and N. J. Cerf. Quantum search by local adiabatic evolution. *Phys. Rev. A*, **65**:042308, Mar 2002.
- [172] N. V. Vitanov, A. A. Rangelov, B. W. Shore, and K. Bergmann. Stimulated raman adiabatic passage in physics, chemistry, and beyond. *Rev. Mod. Phys.*, **89**:015006, Mar 2017.
- [173] M. Born and V. Fock. Beweis des adiabatensatzes. *Zeitschrift für Physik*, **51**(3):165–180, 1928.
- [174] G. Nenciu. On the adiabatic theorem of quantum mechanics. *Journal of Physics A: Mathematical and General*, **13**(2):L15–L18, Feb 1980.
- [175] L. E. Ballentine. *Quantum mechanics: a modern development; 2nd ed.* World Scientific, Hackensack, NJ, Sep 2014.
- [176] D. J. Griffiths and D. F. Schroeter. *Introduction to Quantum Mechanics.* Cambridge University Press, 3rd edition, 2018.
- [177] A. M. Rey, V. Gritsev, I. Bloch, E. Demler, and M. D. Lukin. Preparation and detection of magnetic quantum phases in optical superlattices. *Phys. Rev. Lett.*, **99**:140601, Oct 2007.
- [178] T-L. Ho and Q. Zhou. Intrinsic heating and cooling in adiabatic processes for bosons in optical lattices. *Phys. Rev. Lett.*, **99**:120404, Sep 2007.
- [179] S. Gammelmark and A. Eckardt. Quantum crystal growing: adiabatic preparation of a bosonic antiferromagnet in the presence of a parabolic inhomogeneity. *New Journal of Physics*, **15**(3):033028, Mar 2013.

- [180] S. E. Pollack, D. Dries, M. Junker, Y. P. Chen, T. A. Corcovilos, and R. G. Hulet. Extreme tunability of interactions in a ^7Li bose-einstein condensate. *Phys. Rev. Lett.*, **102**:090402, Mar 2009.
- [181] S. L. Braunstein and C. M. Caves. Statistical distance and the geometry of quantum states. *Phys. Rev. Lett.*, **72**:3439–3443, May 1994.
- [182] M. G. A. Paris. Quantum estimation for quantum technology. *International Journal of Quantum Information*, **07**(supp01):125–137, 2009.
- [183] L. Pezzè and A. Smerzi. Quantum theory of phase estimation. *arXiv*, **quant-ph/1411.5164**, 2014.
- [184] L. Pezzè, A. Smerzi, M. K. Oberthaler, R. Schmied, and P. Treutlein. Quantum metrology with nonclassical states of atomic ensembles. *Rev. Mod. Phys.*, **90**:035005, Sep 2018.
- [185] A. Polkovnikov and V. Gritsev. Breakdown of the adiabatic limit in low-dimensional gapless systems. *Nature Physics*, **4**(6):477–481, 2008.
- [186] P. Richerme, C. Senko, J. Smith, A. Lee, S. Korenblit, and C. Monroe. Experimental performance of a quantum simulator: Optimizing adiabatic evolution and identifying many-body ground states. *Phys. Rev. A*, **8**:012334, Jul 2013.
- [187] A. H. Skelt, R. W. Godby, and I. D’Amico. Measuring adiabaticity in nonequilibrium quantum systems. *Phys. Rev. A*, **98**:012104, Jul 2018.
- [188] E. Torrontegui, S. Ibáñez, S. Martínez-Garaot, M. Modugno, A. del Campo, D. Guéry-Odelin, A. Ruschhaupt, X. Chen, and J. G. Muga. Chapter 2 - shortcuts to adiabaticity. In *Advances in Atomic, Molecular, and Optical Physics*, volume **63**, pages 117 – 169. Academic Press, 2013.
- [189] S. Campbell and S. Deffner. Trade-off between speed and cost in shortcuts to adiabaticity. *Phys. Rev. Lett.*, **118**:100601, Mar 2017.
- [190] A. del Campo and K. Kim. Focus on shortcuts to adiabaticity. *New Journal of Physics*, **21**(5):050201, May 2019.
- [191] J. Werschnik and E. K. U. Gross. Quantum optimal control theory. *Journal of Physics B: Atomic, Molecular and Optical Physics*, **40**(18):R175–R211, Sep 2007.
- [192] C. Brif, R. Chakrabarti, and H. Rabitz. Control of quantum phenomena: past, present and future. *New Journal of Physics*, **12**(7):075008, Jul 2010.
- [193] P. Doria, T. Calarco, and S. Montangero. Optimal control technique for many-body quantum dynamics. *Phys. Rev. Lett.*, **106**:190501, May 2011.

- [194] S. J. Glaser, U. Boscain, T. Calarco, C. P. Koch, W. Köckenberger, R. Kosloff, I. Kuprov, B. Luy, S. Schirmer, T. Schulte-Herbrüggen, D. Sugny, and F. K. Wilhelm. Training schrödinger’s cat: quantum optimal control. *The European Physical Journal D*, **69**(12):279, Dec 2015.
- [195] S. van Frank, M. Bonneau, J. Schmiedmayer, S. Hild, C. Gross, M. Cheneau, I. Bloch, T. Pichler, A. Negretti, T. Calarco, and S. Montangero. Optimal control of complex atomic quantum systems. *Scientific Reports*, **6**(1):34187, 2016.
- [196] T. Caneva, T. Calarco, and S. Montangero. Chopped random-basis quantum optimization. *Phys. Rev. A*, **84**:022326, Aug 2011.
- [197] C. Brif, M. D. Grace, M. Sarovar, and K. C. Young. Exploring adiabatic quantum trajectories via optimal control. *New Journal of Physics*, **16**(6):065013, Jun 2014.
- [198] P. Barmettler, M. Punk, V. Gritsev, E. Demler, and E. Altman. Quantum quenches in the anisotropic spin-1/2 Heisenberg chain: different approaches to many-body dynamics far from equilibrium. *New Journal of Physics*, **12**(5):055017, 2010.
- [199] H. Pichler, A. J. Daley, and P. Zoller. Nonequilibrium dynamics of bosonic atoms in optical lattices: Decoherence of many-body states due to spontaneous emission. *Phys. Rev. A*, **82**:063605, Dec 2010.
- [200] B. Zhu, J. Schachenmayer, M. Xu, F. Herrera, J. G. Restrepo, M. J. Holland, and A. M. Rey. Synchronization of interacting quantum dipoles. *New Journal of Physics*, **17**(8):083063, Sep 2015.
- [201] R. Khasseh, R. Fazio, S. Ruffo, and A. Russomanno. Many-body synchronization in a classical hamiltonian system. *Phys. Rev. Lett.*, **123**:184301, Oct 2019.
- [202] A. Browaeys, D. Barredo, and T. Lahaye. Experimental investigations of dipole–dipole interactions between a few rydberg atoms. *Journal of Physics B: Atomic, Molecular and Optical Physics*, **49**(15):152001, Jun 2016.
- [203] J. Zeiher, J-Y. Choi, A. Rubio-Abadal, T. Pohl, R. van Bijnen, I. Bloch, and C. Gross. Coherent many-body spin dynamics in a long-range interacting ising chain. *Phys. Rev. X*, **7**:041063, Dec 2017.
- [204] B. Yan, S. A. Moses, B. Gadway, J. P. Covey, K. R. A. Hazzard, A. M. Rey, D. S. Jin, and J. Ye. Observation of dipolar spin-exchange interactions with lattice-confined polar molecules. *Nature*, **501**(7468):521–525, 2013.

- [205] J. Zhang, G. Pagano, P. W. Hess, A. Kyprianidis, P. Becker, H. Kaplan, A. V. Gorshkov, Z. X. Gong, and C. Monroe. Observation of a many-body dynamical phase transition with a 53-qubit quantum simulator. *Nature*, **551**(7682):601–604, 2017.
- [206] L. Cevolani, G. Carleo, and L. Sanchez-Palencia. Spreading of correlations in exactly solvable quantum models with long-range interactions in arbitrary dimensions. *New Journal of Physics*, **18**:093002, Sep 2016.
- [207] I. Frérot, P. Naldesi, and T. Roscilde. Entanglement and fluctuations in the xxz model with power-law interactions. *Phys. Rev. B*, **95**:245111, Jun 2017.
- [208] D. J. Luitz and Y. Bar Lev. Emergent locality in systems with power-law interactions. *Phys. Rev. A*, **99**:010105, Jan 2019.
- [209] M. D. Mulanix, Demetrius Almada, and Ehsan Khatami. Numerical linked-cluster expansions for disordered lattice models. *Phys. Rev. B*, **99**:205113, May 2019.
- [210] M. A. Cazalilla, R. Citro, T. Giamarchi, E. Orignac, and M. Rigol. One dimensional bosons: From condensed matter systems to ultracold gases. *Rev. Mod. Phys.*, **83**:1405–1466, Dec 2011.
- [211] F. Alet and N. Laflorencie. Many-body localization: An introduction and selected topics. *Comptes Rendus Physique*, **19**(6):498 – 525, 2018.
- [212] M. P. Kwasigroch and N. R. Cooper. Bose-einstein condensation and many-body localization of rotational excitations of polar molecules following a microwave pulse. *Phys. Rev. A*, **90**:021605, Aug 2014.
- [213] M. P. Kwasigroch and N. R. Cooper. Synchronization transition in dipole-coupled two-level systems with positional disorder. *Phys. Rev. A*, **96**:053610, Nov 2017.
- [214] D. Clément, A. F. Varón, J. A. Retter, L. Sanchez-Palencia, A. Aspect, and P. Bouyer. Experimental study of the transport of coherent interacting matter-waves in a 1d random potential induced by laser speckle. *New Journal of Physics*, **8**(8):165–165, Aug 2006.
- [215] G. Gomez-Santos and J. D. Joannopoulos. Application of spin-wave theory to the ground state of xy quantum hamiltonians. *Phys. Rev. B*, **36**:8707–8711, Dec 1987.
- [216] J. Schachenmayer, B. P. Lanyon, C. F. Roos, and A. J. Daley. Entanglement growth in quench dynamics with variable range interactions. *Phys. Rev. X*, **3**:031015, Sep 2013.

- [217] P. Jurcevic, B. P. Lanyon, P. Hauke, C. Hempel, P. Zoller, R. Blatt, and C. F. Roos. Quasiparticle engineering and entanglement propagation in a quantum many-body system. *Nature*, **511**(7508):202–205, 2014.
- [218] B. Kloss and Y. Bar Lev. Spin transport in a long-range-interacting spin chain. *Phys. Rev. A*, **99**:032114, Mar 2019.
- [219] A. Hubener, M. Snoek, and W. Hofstetter. Magnetic phases of two-component ultracold bosons in an optical lattice. *Phys. Rev. B*, **80**:245109, Dec 2009.
- [220] S. Hild, T. Fukuhara, P. Schauß, J. Zeiher, M. Knap, E. Demler, I. Bloch, and C. Gross. Far-from-equilibrium spin transport in heisenberg quantum magnets. *Phys. Rev. Lett.*, **113**:147205, Oct 2014.
- [221] H. Labuhn, D. Barredo, S. Ravets, S. de Léséleuc, T. Macrì, T. Lahaye, and A. Browaeys. Tunable two-dimensional arrays of single rydberg atoms for realizing quantum ising models. *Nature*, **534**(7609):667–670, 2016.
- [222] T. L. Nguyen, J. M. Raimond, C. Sayrin, R. Cortiñas, T. Cantat-Moltrecht, F. Assemat, I. Dotsenko, S. Gleyzes, S. Haroche, G. Roux, Th. Jolicoeur, and M. Brune. Towards quantum simulation with circular rydberg atoms. *Phys. Rev. X*, **8**:011032, Feb 2018.